Advanced computational methods for studying noble metal nanoclusters: From quantum chemistry to machine learning

by

Yuchen Wang

B.S., Anhui Normal University, China, 2019

AN ABSTRACT OF A DISSERTATION

submitted in partial fulfillment of the requirements for the degree

DOCTOR OF PHILOSOPHY

Department of Chemistry
College of Arts and Sciences

KANSAS STATE UNIVERSITY
Manhattan, Kansas

2024

Abstract

Gold and silver nanoparticles can exhibit unique physical and chemical properties such as plasmonic resonance characters. Those types of plasmonic nanoparticles usually exist in large sizes, which leads to difficulty in computing their optical properties using quantum chemistry methods. Facing these challenges, this dissertation will focus on employing different computational approaches to investigate the physical and chemistry properties of noble metal nanoclusters.

The two central techniques in this dissertation will be DFT (density functional theory) and TDDFT (time-dependent density functional theory), which are two quantum chemistry approaches that have been widely used for ground-state and excited-state calculations, respectively. In addition, we also applied other techniques such as molecular dynamics (both Born-Oppenheimer molecular dynamics and non-adiabatic molecular dynamics) and a machine learning model to assist with the study of noble metal nanoclusters.

In the first part of the dissertation, our goal is to employ a reasonable model system to examine the plasmon-induced catalytic process involving nanocluster/nanowire systems for small molecule activation/dissociation. In chapter 3, we examine the dissociation of a nitrogen molecule on atomically-thin silver nanowires with different lengths and on a Ag_{19} nanorod. We also applied different field strengths to the system and examine field strength effects on the N_2 dissociation properties. In chapter 4, we study how a transition metal dopant affects the system's electronic structure and its plasmon-enhanced N_2 dissociation properties. In chapter 5, to study the effects of different electric fields, we apply both static electric fields and continuous wave fields to gold/silver triangle nanoclusters@H_2 systems and examine the system evolution as various external fields are applied. For these three projects, linear-response TDDFT provides the

absorption spectra information, real-time TDDFT calculations show the electronic transitions and population of electrons, and Ehrenfest dynamics provides information about the motion of nuclei during the dynamics process.

In addition, it is also possible to develop new computational methods with lower computational costs in order to accelerate the calculations. In the second part of the dissertation, we develop new methods to examine the properties of large metal nanoclusters. In chapter 6, we develop a new method called TDDFT-aas, which is an approximate method to TDDFT. In this method, instead of calculating the exact two electron integrals in the *K* coupling matrix when solving the Casida equations, we approximate the integrals in the *K* coupling matrix, which therefore reduces the computational cost. In chapter 7, we apply the DFT method to examine the gold thiolate-protected nanoparticle growth mechanism in a diglyme solvent environment. DFT approaches can be successfully applied to calculate relatively small metal nanocluster systems, but larger systems are difficult to study, including the dimers of interest in this work. Therefore, in chapter 8, we develop a type of machine learning force field that shows success in predicting energies for gold thiolate-protected nanoclusters not only in the training database but also outside the database.

Overall, in this dissertation, we both apply theoretical approaches and develop new computational methods to study different aspects of noble metal nanoclusters.

Advanced computational methods for studying noble metal nanoclusters: From quantum chemistry to machine learning

by

Yuchen Wang

B.S., Anhui Normal University, China, 2019

A DISSERTATION

submitted in partial fulfillment of the requirements for the degree

DOCTOR OF PHILOSOPHY

Department of Chemistry
College of Arts and Sciences

KANSAS STATE UNIVERSITY
Manhattan, Kansas

2024

Approved by:

Major Professor
Christine M. Aikens

Copyright

© Yuchen Wang 2024.

Abstract

Gold and silver nanoparticles can exhibit unique physical and chemical properties such as plasmonic resonance characters. Those types of plasmonic nanoparticles usually exist in large sizes, which leads to difficulty in computing their optical properties using quantum chemistry methods. Facing these challenges, this dissertation will focus on employing different computational approaches to investigate the physical and chemistry properties of noble metal nanoclusters.

The two central techniques in this dissertation will be DFT (density functional theory) and TDDFT (time-dependent density functional theory), which are two quantum chemistry approaches that have been widely used for ground-state and excited-state calculations, respectively. In addition, we also applied other techniques such as molecular dynamics (both Born-Oppenheimer molecular dynamics and non-adiabatic molecular dynamics) and a machine learning model to assist with the study of noble metal nanoclusters.

In the first part of the dissertation, our goal is to employ a reasonable model system to examine the plasmon-induced catalytic process involving nanocluster/nanowire systems for small molecule activation/dissociation. In chapter 3, we examine the dissociation of a nitrogen molecule on atomically-thin silver nanowires with different lengths and on a Ag_{19} nanorod. We also applied different field strengths to the system and examine field strength effects on the N_2 dissociation properties. In chapter 4, we study how a transition metal dopant affects the system's electronic structure and its plasmon-enhanced N_2 dissociation properties. In chapter 5, to study the effects of different electric fields, we apply both static electric fields and continuous wave fields to gold/silver triangle nanoclusters@H_2 systems and examine the system evolution as various external fields are applied. For these three projects, linear-response TDDFT provides the

absorption spectra information, real-time TDDFT calculations show the electronic transitions and population of electrons, and Ehrenfest dynamics provides information about the motion of nuclei during the dynamics process.

In addition, it is also possible to develop new computational methods with lower computational costs in order to accelerate the calculations. In the second part of the dissertation, we develop new methods to examine the properties of large metal nanoclusters. In chapter 6, we develop a new method called TDDFT-aas, which is an approximate method to TDDFT. In this method, instead of calculating the exact two electron integrals in the *K* coupling matrix when solving the Casida equations, we approximate the integrals in the *K* coupling matrix, which therefore reduces the computational cost. In chapter 7, we apply the DFT method to examine the gold thiolate-protected nanoparticle growth mechanism in a diglyme solvent environment. DFT approaches can be successfully applied to calculate relatively small metal nanocluster systems, but larger systems are difficult to study, including the dimers of interest in this work. Therefore, in chapter 8, we develop a type of machine learning force field that shows success in predicting energies for gold thiolate-protected nanoclusters not only in the training database but also outside the database.

Overall, in this dissertation, we both apply theoretical approaches and develop new computational methods to study different aspects of noble metal nanoclusters.

Table of Contents

List of Figures xii
List of Tables xxiv
Acknowledgements xxvii
Dedication xxix
Chapter 1 - Introduction 1
1.1 Plasmon-induced catalyzed reactions 2
1.2 Noble metal nanoparticles (NPs) 4
1.3 Solvent effects in metal nanoparticle synthesis 6
1.4 Challenges in modeling noble metal nanoparticles 7
1.5 Objectives of this dissertation 9
1.6 References 10
Chapter 2 - Theory and methods 13
2.1 The Schrödinger equation and the Born-Oppenheimer approximation 14
2.2 Density functional theory 15
2.3 Basis sets 17
2.4 Time-dependent density functional theory (TDDFT) 18
2.4.1 Linear-response TDDFT (LR-TDDFT) 19
2.4.2 Real-time TDDFT (RT-TDDFT) 20
2.5 Time-dependent density functional theory related approximation methods 20
2.6 Nonadiabatic dynamics 21
2.7 Solvent models 24
2.8 Machine learning models 26
2.9 References 29
Chapter 3 - Effects of field strength and silver nanowire size on plasmon-enhanced N_2 dissociation 34
3.1 Abstract 34
3.2 Introduction 35
3.3 Computational methods 37
3.4 Results and discussion 38

3.4.1 Binding energies analysis 38
3.4.2 Molecular orbitals 39
3.4.3 LR-TDDFT calculations 40
3.4.4 RT-TDDFT calculations 42
3.4.5 Nonadiabatic dynamics simulations 46
3.4.6 Plasmon-enhancement of Ag_{19} cluster 50
3.5 Conclusion 52
3.6 Acknowledgement 53
3.7 Supporting information 53
3.8 References 54
Chapter 4 - Effects of nanowire doping on plasmon-enhanced N_2 dissociation 59
4.1 Abstract 59
4.2 Introduction 59
4.3 Computational details 61
4.4 Results and discussion 63
4.4.1 Binding energy analysis 63
4.4.2 Linear response TDDFT absorption spectra 64
4.4.3 90º structure 67
4.4.4 Mean-field Ehrenfest dynamics 69
4.4.5 Ag_5CuN_2 vs Ag_5AuN_2 72
4.5 Conclusions 77
4.6 Supporting information 78
4.7 Acknowledgment 78
4.8 References 78
Chapter 5 - Connectivity between static field and continuous wave field effects on excitation-induced H_2 activation 85
5.1 Abstract 85
5.2 Introduction 86
5.3 Computational methods 88
5.4 Results and discussion 89
5.4.1 Static fields effect 89

5.4.2 Resonant electric fields 96
5.5 Conclusions 101
5.6 Supporting information 102
5.7 Acknowledgments 102
5.8 References 103
Chapter 6 - Implementation of energy and gradient for the TDDFT- approximate auxiliary function (aas) method 108
6.1 Abstract 108
6.2 Introduction 108
6.3 Theory and code implementation 111
6.4 Results and discussion 112
6.4.1 Optimized tuning parameter 112
6.4.2 Comparison of methods for nanocluster absorption spectra 113
6.4.3 Numerical and analytical gradients 116
6.4.4 Excited state geometry optimization 117
6.4.5 Comparison between computational cost 122
6.5 Discussion 124
6.6 Conclusion 125
6.7 Acknowledgment 125
6.8 References 126
Chapter 7 - Effects of diglyme on Au nanocluster formation: mechanism, ^{1}H NMR, and bonding 129
7.1 Abstract 129
7.2 Introduction 129
7.3 Computational Details 131
7.4 Results and discussion 132
7.5 Conclusion 146
7.6 Supporting Information 147
7.7 Acknowledgements 147
7.8 References 147

Chapter 8 - A Gaussian process approach to constructing transferable force fields for gold thiolate-protected nanoclusters 151
8.1 Abstract 151
8.2 Introduction 151
8.3 Theoretical background and computational details 153
8.4 Results and discussion 160
8.5 Conclusions 171
8.6 Supporting information 172
8.7 Conflicts 172
8.8 Acknowledgment 172
8.9 References 173
Chapter 9 - Final conclusion and outlook 177
Appendix A - Supporting information for: Effects of field strength and silver nanowire size on plasmon-enhanced N_2 dissociation 180
Appendix B - Supporting information for: Effects of nanowire doping on plasmon-enhanced N_2 dissociation 182
Appendix C - Supporting information for: Connectivity between static field and continuous wave field effects on excitation-induced H_2 activation 186
Appendix D - Supporting information for: Implementation of energy and gradient for the TDDFT- approximate auxiliary function (aas) method 192
Appendix E - Supporting Information for: Effects of diglyme on Au nanocluster formation: mechanism, ^{1}H NMR, and bonding 195
Appendix F - Supporting information for: A Gaussian process approach to constructing transferable force fields for gold thiolate-protected nanoclusters 211

List of Figures

Figure 1.1 Schematic of plasmon oscillation for a sphere, showing the displacement of the conduction electron charge cloud relative to the nuclei. Reprinted with permission from *J. Phys. Chem. B* 2003, 107, 3, 668–677. Copyright 2003 American Chemical Society. 1

Figure 1.2 Silver nanoparticle (NP) coupled with the N_2 molecule, with a laser pulse applied to the system. Reprinted with permission from ACS Nanosci. Au 2023, 3, 4, 269–279 Copyright 2023. This publication is licensed under CC-BY 4.0. 2

Figure 1.3 Plasmon excitation at t = 0 and subsequent generation of hot electron–hole pairs within the metal, then thermalization via electron–electron, electron–phonon scattering (this leads to a Fermi-Dirac distribution of charge carriers representing the elevated temperature) and further via thermal dissipation via phonon–phonon scattering. E_F indicates the Fermi level, and yellow and red areas indicate hole and electron energies, respectively. Reprinted with permission from *Commun Mater* 2021, 2, 114 Copyright 2021. This publication is licensed under CC-BY 4.0. 3

Figure 1.4 A. Au_{23} core with labeling of the surface Au atoms involved in determining the symmetry of the ligand layer. B. Chiral D_3 arrangement of the Au−S atoms. C. C_{3h} arrangement of the Au−S atoms. D. Optimal SCH_3 distribution on structure. Reprinted with permission from *J. Am. Chem. Soc.* 2010, 132, 23, 8210–8218. Copyright 2010 American Chemical Society. 5

Figure 1.5 Timeline of some key milestones in the field of atomically precise metal nanoclusters. The key developments presented in each box are focused on gold-based metal nanoclusters because they have been studied most intensively and promoted the development of their silver- and copper-based counterparts. Au, gold; DFT, density functional theory; ESI-MS, electrospray ionization mass spectrometry; NCs, nanoclusters; SAMs, self-assembling monolayers; SR, thiolate. Note: Reference numbers in the figure refer to references in Nat Rev Mater 8, 372–389 (2023). Reprinted with permission from Nat Rev Mater 8, 372–389 (2023) Copyright 2023, Springer Nature Limited 6

Figure 1.6 Combined orbital contours of the twice-degenerate HOMO of the computed diglyme-linked $Au_{20}(SCH_3)_{15}$ dimer. Reprinted with permission from ACS Nano 2015, 9, 12, 11690–11698. Copyright 2015 American Chemical Society. 7

Figure 1.7 (a) Schematic diagram of H_2 molecule adsorbed on the NP surface. The electric field is in x direction. (b) Bonding and (c) antibonding (AB) wave functions of H_2 in the x–z plane. Panel c indicates that (1) the AB state is 1.48 eV above the Fermi energy, which offers the possibility of transferring the hot-electron generated in the metallic NPs to the AB state; and (2) the AB WF is hybridized with the NP, which can facilitate the hot-electron transfer. The red circle indicates the surface of the NP. (d) LDOS of H_2 adsorbed on NP surface. The dashed line indicates the Fermi energy (shifted to 0) of the NP + H_2 system with equilibrium H–H bond length. The evolution of peaks in LDOS for different H–H bond lengths roughly reflects the PES of the H_2 molecule. (e) Absorption spectrum of NP and NP + H_2. Reprinted with permission from ACS Nano 2018, 12, 8, 8415–8422 Copyright 2018 American Chemical Society 8

Figure 2.1 Quantum-chemical (QC) wavefunction methods can conveniently deal with small molecules with great accuracy. Density functional theory (DFT) is a major workhorse dealing with monolayer-protected cluster (MPC) electronic structure, optical properties, and reactions, but with limited time scales. Classical force fields generated for molecular mechanics (MM) and molecular dynamics (MD) simulations can give valuable details on MPC-environment interactions such as with viruses as shown here. Finally, processes and properties in self-assembling MPC systems may need to be dealt with coarse-grained (CG) methods where each MPC is described as a "unified atom". Reprinted with permission from *Nat Commun* 12, 2197 (2021) Copyright 2021. This publication is licensed under CC-BY 4.0..... 13

Figure 2.2 Relationships among several different computational methods. Reprinted with permission from *J. Chem. Phys* 144, 184103 (2016) of AIP Publishing..... 21

Figure 2.3 Schematic illustration of the adiabatic energies and nonadiabatic couplings (NAC) as a function of time. In a weak-coupling region (left side), the width of the nonadiabatic coupling peak may be of the same order of the integration time step, ~0.5 fs. Reprinted with permission from Chem. Rev. 2018, 118, 15, 7026-7068. Copyright 2018, American Chemical Society 22

Figure 2.4 Schematic illustration of the mean field Ehrenfest dynamics. The trajectory is run on a surface averaged over all electronic states weighted by their respective electronic

population. Reprinted with permission from Chem. Rev. 2018, 118, 15, 7026-7068. Copyright 2018, American Chemical Society 23
Figure 2.5 Three-time-scale integration scheme for Ehrenfest dynamics. Reprinted with permission from *J. Chem. Phys* 123, 084106 (2005) of AIP Publishing..... 24
Figure 2.6 Calculated optical absorption spectrum in gas phase and in implicit solvent for $Au_{25}(SH)_{18}^-$. Reprinted with permission from *J. Phys. Chem. A* 2009, 113, 40, 10811–10817. Copyright 2009 American Chemical Society 25
Figure 2.7 A. Structure of alizarin. The electron–hole difference density plot of the lowest dipole-allowed transition of a single MD frame (frame 5) of alizarin, as calculated in B. implicit solvent; C. in 6 Å of explicit water; D. in 10 Å of explicit water. The hole density is displayed in orange, while the electron density is shown in cyan. Reprinted with permission from *J. Chem. Theory Comput.* 2016, 12, 4, 1853–1861. Copyright 2016 American Chemical Society 26
Figure 2.8 Basic elements of GPR as discussed in the present section: (1) observations of an unknown function at a number of locations; (2) basis functions (only one of them shown for clarity), centered at the data locations; (3) an estimation $\boldsymbol{y}$ defined by the set of coefficients, c_m, and the corresponding basis functions; $\boldsymbol{y}$ is the prediction of the GPR model. Reprinted with permission from *Chem. Rev.* 2021, 121, 16, 10073–10141 Copyright 2021 The Authors. Published by American Chemical Society. This publication is licensed under CC-BY 4.0. 27
Figure 2.9 a. At each time-step of the MD simulation, local energies, forces, and stresses are computed with the SGP model. If the uncertainty on a local energy exceeds the chosen threshold Δ_{DFT}, a DFT calculation is performed, and the model is updated. b. Mapping of local environments ρ_i onto multielement descriptors derived from the atomic cluster expansion. The environment is first mapped onto an equivariant descriptor c_i, products of which are used to compute the rotationally invariant descriptor d_i that serves as an input to the model. C. Mapping of a $\xi = 2$ SGP force field onto an equivalent quadratic model. The prediction cost of the SGP scales linearly with the number of sparse environments N_S, while the cost of the corresponding polynomial model is independent of N_S. Reprinted with permission from *Nat Commun* 13, 5183 (2022) *Copyright 2022 by the Authors,* this is an open access article distributed under the terms of the Creative Commons CC BY license. 29

Figure 3.1 Selected molecular orbitals (from HOMO to LUMO+5) for A. Ag_6N_2; B. Ag_8N_2; C. $Ag_{10}N_2$; D. $Ag_{12}N_2$ 40
Figure 3.2 Linear response TDDFT absorption spectra for Ag_nN_2 (n = 6, 8, 10, 12) molecular systems 41
Figure 3.3 Variation of the population of selected molecular orbitals in the first 40 fs of the RT-TDDFT simulation. The electric fields were applied at frequencies corresponding to the longitudinal plasmon frequency of each system. Systems: Ag_6N_2 with applied field intensity of A. 0.03 au, B. 0.04 au, and C. 0.05 au. Ag_8N_2 with applied field intensity of D. 0.03 au, E. 0.04 au, and F. 0.05 au. $Ag_{10}N_2$ with applied field intensity of G. 0.03 au, H. 0.04 au, and I. 0.05 au. $Ag_{12}N_2$ with applied field intensity of J. 0.03 au, K. 0.04 au, and L. 0.05 au. 43
Figure 3.4 Off-diagonal elements (Pov) analysis in RT-TDDFT simulations for four systems. The x-axis represents the occupied orbital number and the y axis represents the virtual orbital number. The color represents the maximum value of the Pov (Mpov) during the electron dynamics across the first 40 fs. A dark-blue color indicates a relatively strong transition, while the light-yellow color shows a weak transition. Systems: Ag_6N_2 with an applied field intensity of A. 0.03 au, B. 0.04 au, and C. 0.05 au. Ag_8N_2 with an applied field intensity of D. 0.03 au, E. 0.04 au, and F. 0.05 au. $Ag_{10}N_2$ with an applied field intensity of G. 0.03 au, H. 0.04 au, and I. 0.05 au. $Ag_{12}N_2$ with an applied field intensity of J. 0.03 au, K. 0.04 au, and L. 0.05 au. 45
Figure 3.5 Variation of the N_2 bond length with selected field strengths when interacting with different silver nanowires. A. Ag_6N_2 B. Ag_8N_2 C. $Ag_{10}N_2$ D. $Ag_{12}N_2$ 48
Figure 3.6 A. Selected molecular orbitals (HOMO to LUMO+5) of $Ag_{19}N_2^{+1}$. B. Visualization of ground state optimized structure of $Ag_{19}N_2^{+1}$. Key: silver = silver, nitrogen = blue. C. LR-TDDFT absorption spectrum of $Ag_{19}N_2^{+1}$. 50
Figure 3.7 A. Comparison of N-N bond variation in Ehrenfest dynamics for $Ag_{19}N_2^{+1}$ with z-polarized and x-polarized electric fields with field intensities of 0.030 au. B. Comparison of N-N bond variation in Ehrenfest dynamics for wire-N_2 and $Ag_{19}N_2^{+1}$ systems with a 0.040 au field strength using z-polarized excitations. 52
Figure 4.1 Linear-response excitation spectra for A. group X doped systems, B. group XI doped systems, and C. group XII doped systems. 65

Figure 4.2 Kohn-Sham ground state molecular orbitals diagram of selected orbitals for A. Ag_5AuN_2 and B. Ag_5CuN_2 (isovalue =0.01). 66
Figure 4.3 Ground state optimized geometries for parallel and 90º structures. A. Optimized parallel structure for the Ag_6NiN_2 system. B. Optimized structure for the 90º Ag_6NiN_2 system. Key: silver=silver, nickel=green, and nitrogen=blue..... 68
Figure 4.4 Comparison of the linear-response excitation spectra between parallel structure and 90º structure in A: Ag_6NiN_2, B: Ag_6PdN_2, and C: Ag_6PtN_2 systems. 69
Figure 4.5 Variation of the N-N distance during nonadiabatic dynamics using the A. 0.03 au, B. 0.04 au, and C. 0.05 au electric fields with frequencies corresponding to the longitudinal excitation of each parallel system. 70
Figure 4.6 Comparison of Ehrenfest dynamics results between parallel structure and 90º structure for the Ag_6NiN_2 system with A. 0.03 au, B. 0.04 au, and C. 0.05 au electric field strengths excited at the longitudinal excitation energy. 71
Figure 4.7 Snapshot of the Ag_6NiN_2 geometry at 50 fs for parallel structure and 90º structure from the 0.05 au electric field simulation. Key: silver=silver, nickel=green, and nitrogen=blue. 71
Figure 4.8 Variation of the N-N distance in Ehrenfest dynamics at different initial temperatures A. Ag_5Cu (parallel system) B. Ag_5Au (parallel system) in 0.04 au electric field..... 73
Figure 4.9 Comparison of orbital population results between the Ag_5AuN_2 and Ag_5CuN_2 parallel systems using RT-TDDFT calculations. 75
Figure 4.10 Selected KS ground state molecular orbitals for Ag_5CuN_2 at different constrained N-N bond lengths (isovalue =0.01). For the 1.1 Å system, the LUMO+1 and LUMO+2 form a degenerate set; images are shown from the x and y directions. For the 1.35 Å system, LUMO and LUMO+1 form a degenerate set; images are shown from the x and y directions. 76
Figure 5.1 Optimized geometries of A. Au_6H_2 and B. Ag_6H_2 systems at zero applied electric field 90
Figure 5.2 Selected molecular orbitals of optimized Ag_6H_2 under different static applied electric fields. (All molecular orbitals are oriented using a front view, except the orbitals involving H_2 σ*, which are oriented using the side view for the sake of clarity.) 92

Figure 5.3 Bonding and antibonding characters between cluster and H_2 molecule. A. Au_6H_2 and B. Ag_6H_2 93
Figure 5.4 Orbital energy differences between A. bonding and antibonding orbitals, B. LUMO and bonding character orbitals with the change of applied field. 94
Figure 5.5 Mulliken charge analysis for A. Au_6H_2 B. Ag_6H_2. 95
Figure 5.6 Linear absorption spectra for A. Au_6H_2 B. Ag_6H_2. 96
Figure 5.7 Variation of H-H bond distance during Ehrenfest dynamics simulations for the Au_6H_2 system with the 0.01 au electric field strength. 97
Figure 5.8 Variation of H-H bond distance during Ehrenfest dynamics simulations for the Ag_6H_2 system with the 0.01 au electric field strength. 98
Figure 5.9 Orbital population analysis of Au_6H_2 system in RT-TDDFT simulations 99
Figure 5.10 Orbital population analysis of Ag_6H_2 system in RT-TDDFT simulations. 100
Figure 6.1 Absorption spectra for tetrahedral clusters A. Ag_{20} and B. Au_{20} calculated by the TDDFT-aas method with different α values. TDDFT and TDDFT+TB calculation results are included for comparison. 113
Figure 6.2 Comparison of the absorption results using TDDFT-aas and TDDFT+TB for pure gold nanoclusters. A. Au_{38}^{+4} B. Au_{55}^{+5} 114
Figure 6.3 Comparison of the absorption results using TDDFT-aas to calculate pure gold nanoclusters. A. Ag_{38}^{+4} B. Ag_{55}^{+5} 115
Figure 6.4 Comparison of the absorption results using TDDFT-aas to calculate thiolate-protected gold nanocluster. A. $Au_{25}(SCH_3)_{18}^-$ B. $Au_{38}(SCH_3)_{24}$ 116
Figure 6.5 Potential energy surfaces for the A. H_2 and B. Li_2 systems. In the key, S0 represents the PES for the ground state. S1: TDDFT-aas represents the PES for the S_1 state using TDDFT-aas methods with α=0.2. S1: TDDFT-aas-0.1 represents the PES for the S_1 state using TDDFT-aas methods with α=0.1. S1: TDDFT+TB represents the PES for the S_1 state using TDDFT+TB methods. S1: TDDFT represents the PES for the S_1 state using TDDFT methods. 118
Figure 6.6 Emission energy differences among TDDFT-aas, TDDFT+TB, and TDDFT for organic molecules from the Thiel test set. 120

Figure 7.1 Three products in the Au-Au linking reactions. A. $(AuCl_3)dg$ B. $(AuCl_3)_2dg$ C. $(AuCl_3)_3dg$ Key: gold = gold, chlorine = green, carbon = grey, oxygen = red and hydrogen = white. 133
Figure 7.2 Three generated products for thiol addition reactions. The $-(CH_2)_2$-Ph (phenylethane) group is shown using a stick model. A. $(AuCl_2)PET(AuCl_3)dg$ B. $(AuCl_2PET)_2dg$ C. $(AuCl_2)PET(AuCl)dg$ Key: gold = gold, sulfur = light yellow, chlorine = green, carbon = grey, oxygen = red and hydrogen = white. 134
Figure 7.3 Three generated products for thiol addition reactions without diglyme; the $-(CH_2)_2$-Ph group is shown using a stick model. A. $(AuCl_2)PET(AuCl_3)$ B. $(AuCl_2PET)_2$ C. $(AuCl_2)PET(AuCl)$ Key: gold = gold, sulfur = light yellow and chlorine = green. 135
Figure 7.4 Four possible products formed in pathway 1 and pathway 2. The $-(CH_2)_2$-Ph group is shown using a stick model. A. $(AuClPET)_2dg$ B. $(AuClPET)Au(PET)_2dg$ C. $(AuCl)PET(AuHPET)dg$ D. $(AuCl)_2dg$ Key: gold = gold, sulfur = light yellow, chlorine = green, carbon = grey, oxygen = red and hydrogen = white. 136
Figure 7.5 Optimized structures for A. $AuCl_3dg$, B. $(AuCl_2PET)_2dg$, and C. $(AuCl)PET(AuHPET)dg$. Selected geometric information and atom labels are also included. Full coordinates are given in the SI. Key: gold = gold, sulfur = light yellow, chlorine = green, carbon = grey, oxygen = red and hydrogen = white. 139
Figure 7.6 Dominant ETS-NOCV deformation density contribution for diglyme and $AuCl_3$ interaction. The charge flux is red to blue (isovalue = 0.001 au). Key: gold = gold, chlorine = green, carbon = grey, oxygen = red and hydrogen = white. 142
Figure 7.7 Dominant ETS-NOCV deformation density contributions for diglyme and $(AuCl_2PET)_2$ interaction. The charge flux is red to blue (isovalue = 0.001 au). Key: gold = gold, sulfur = light yellow, chlorine = green, carbon = grey, oxygen = red and hydrogen = white. 143
Figure 7.8 Dominant ETS-NOCV deformation density contribution for diglyme and $(AuCl)PET(AuHPET)$ interaction. The charge flux is red to blue (isovalue = 0.001 au) Key: gold = gold, sulfur = light yellow, chlorine = green, carbon = grey, oxygen = red and hydrogen = white. 144

Figure 7.9 Dominant ETS-NOCV deformation density contribution for diglyme and $Au_{20}(SCH_3)_{15}^+$ interaction. The charge flux is red to blue (isovalue = 0.001 au). Key: gold = gold, sulfur = light yellow, carbon = grey, oxygen = red and hydrogen = white. 145
Figure 8.1 A. $Au_{20}(SCH_3)_{16}$: DFT. B. $Au_{20}(SCH_3)_{16}$: crystal. C. Basic motif in $Au_{20}(SCH_3)_{16}$ nanocluster. D. Basic motif in $Au_{20}(SCH_3)_{16}$ nanocluster. E. Au core in $Au_{20}(SCH_3)_{16}$: DFT structure. F. Au core in $Au_{20}(SCH_3)_{16}$: crystal structure. Color code: Gold = orange, carbon = gray, sulfur = yellow, and hydrogen = white. 155
Figure 8.2 Visualization of the gold nanoclusters and their corresponding kernel structure. 157
Figure 8.3 The training-testing-training working flowchart. 158
Figure 8.4 Overlap between the LAMMPS optimized and DFT optimized geometries. A. $Au_{18}(SCH_3)_{14}$ system front view. B. $Au_{18}(SCH_3)_{14}$ system side view. C. $Au_{44}(SCH_3)_{28}$ system front view. D. $Au_{44}(SCH_3)_{28}$ system side view. Color code: orange: DFT optimized geometry. Iceblue: LAMMPS optimized geometry. 161
Figure 8.5 Comparison of the energy from the ML-MD LAMMPS simulation results and DFT calculated energy for the $Au_{18}(SCH_3)_{14}$ system. 162
Figure 8.6 Comparison of the energy from the ML-MD LAMMPS simulation results and DFT calculated energy for the $Au_{20}(SCH_3)_{16:}$ crystal system. 163
Figure 8.7 Comparison of the energy from the ML-MD LAMMPS simulation results and DFT calculated energy for the $Au_{25}(SCH_3)_{18}$ system. 163
Figure 8.8 Comparison of the energy from the ML-MD LAMMPS simulation results and DFT calculated energy for the $Au_{28}(SCH_3)_{20:}$ crystal system. 164
Figure 8.9 Comparison of the energy from the ML-MD LAMMPS simulation results and DFT calculated energy for the $Au_{36}(SCH_3)_{24}$ system. 164
Figure 8.10 Comparison of the energy from the ML-MD LAMMPS simulation results and DFT calculated energy for the $Au_{38}(SCH_3)_{24}$ system. Simulation started without energy minimization. 165
Figure 8.11 Comparison of the energy from the ML-MD LAMMPS simulation results and DFT calculated energy for the $Au_{44}(SCH_3)_{28}$ system. 165
Figure 8.12 Comparison of the energy from the ML-MD LAMMPS simulation results and DFT calculated energy for the $Au_{20}(SCH_3)_{16}$ system at 400 K. 167

Figure 8.13 Comparison of the energy from the LAMMPS simulation results and DFT calculated energy for the $Au_{25}(SCH_3)_{18}$ system at 200 K. 167
Figure 8.14 A. Mean bond length variation. B. C-S---S-C dihedral angle count for various angle ranges. C. Au atom count for each individual Au-Au coordination numbers. D. PCA visualization of the bonding parameters for different training configurations of $Au_{20}(SCH_3)_{16}$ at 400K (PC - principal component). Each graph demonstrates results from a hundred configurations (one snapshot per picosecond). 169
Figure 8.15 A. Mean bond length variation. B. C-S---S-C dihedral angle count for various angle ranges. C. Au atom count for each individual Au-Au coordination numbers. D. PCA visualization of the bonding parameters for different training configurations of $Au_{25}(SCH_3)_{18}$ at 200K (PC - principal component). Each graph demonstrates results from a hundred configurations (one snapshot per picosecond). 170
Figure 8.16 A. Mean bond length variation. B. C-S---S-C dihedral angle count for various angle ranges. C. Au atom count for each individual Au-Au coordination numbers. D. PCA visualization of the bonding parameters for different training configurations of $Au_{44}(SCH_3)_{28}$ at 300K (PC - principal component). Each graph demonstrates results from a hundred configurations (one snapshot per picosecond). 171

Appendix Figure A.1 Selected molecular orbitals (HOMO-4 to LUMO+6) of $Ag_{19}N_2^{+1}$ 180
Appendix Figure B.1 Selected molecular orbitals (from HOMO-4 to LUMO+3) for A. Ag_6NiN_2; B. Ag_6PdN_2; C. Ag_6PtN_2 (isovalue =0.01). 182
Appendix Figure B.2 Selected molecular orbitals (from HOMO-4 to LUMO+3) for A. Ag_5CuN_2; B. Ag_6N_2; C. Ag_5AuN_2 (isovalue =0.01). 183
Appendix Figure B.3 Selected molecular orbitals (from HOMO-4 to LUMO+3) for A. Ag_6ZnN_2; B. Ag_6CdN_2; C. Ag_6HgN_2. (isovalue =0.01). 184
Appendix Figure B.4 Variation of the doped metal-N1 distance during nonadiabatic dynamics using the A. 0.03 au, B. 0.04 au, and C. 0.05 au electric fields with frequencies corresponding to the longitudinal excitation of each parallel system. 184
Appendix Figure B.5 Comparison of Ehrenfest dynamics results between parallel structure and 90º structure of Ag_6PtN_2 system with A. 0.03 au, B. 0.04 au, and C. 0.05 au electric field strengths excited at the longitudinal excitation energy. 185

Appendix Figure C.1 Selected molecular orbitals of optimized Au_6H_2 under different static applied electric fields. (All molecular orbitals are oriented using a front view, except the orbitals involving H_2 σ*, which are oriented using the side view for the sake of clarity.). 187
Appendix Figure C.2 Selected unoccupied orbital energies (59 denotes LUMO; 69 denotes LUMO+10) for A. Au_6H_2 and B. Ag_6H_2. 188
Appendix Figure C.3 Hirshfeld charge analysis for A. Au_6H_2 B. Ag_6H_2. 189
Appendix Figure C.4 Off-diagonal elements (Pov) analysis for Au_6H_2 in RT-TDDFT simulations; the x-axis represents the occupied orbital number and the y-axis represents the virtual orbital number. The color represents the maximum number of the Pov (MPov) during the electron dynamics in the first 40fs. The dark-blue color shows a relatively strong transition, while the light-yellow color shows a weak transition. 190
Appendix Figure C.5 Off-diagonal elements (Pov) analysis of Ag_6H_2 system in RT-TDDFT simulations; the x-axis represents the occupied orbital number and the y-axis represents the virtual orbital number. The color represents the maximum number of the Pov (MPov) during the electron dynamics in the first 40fs. The dark-blue color shows a relatively strong transition, while the light-yellow color shows a weak transition. 191
Appendix Figure D.1 Stick spectra for the Au_{38}^{+4} system A. TDDFT-aas calculated results; B. TDDFT calculated results. 192
Appendix Figure D.2 Stick spectra for the Au_{55}^{+5} system A. TDDFT-aas calculated results; B. TDDFT calculated results. 192
Appendix Figure D.3 BP86 calculated results using TDDFT-aas, TDDFT+TB and TDDFT for the $Au_{25}(SCH_3)_{18}^-$ system. 193
Appendix Figure E.1 Labeled hydrogen atoms on HPET. Key: sulfur = light yellow, carbon = grey, and hydrogen = white. 195
Appendix Figure E.2 Hydrogen atoms on PET and HPET in (AuCl)PET(AuHPET)]dg. Diglyme is displayed with a stick model. Key: gold = gold, sulfur = light yellow, chlorine = green, carbon = grey, oxygen = red and hydrogen = white. 197
Appendix Figure E.3 Optimized geometries for $(AuCl_3)$dg isomers and their relative energies. 200
Appendix Figure E.4 Optimized geometries for $(AuCl_2)$PET(AuCl)dg isomers and their relative energies. 201

Appendix Figure E.5 Optimized geometries for $(AuCl)_2$dg isomers and their relative energies. 201
Appendix Figure E.6 Optimized geometries for $(AuClPET)_2$dg isomers and their relative energies. 201
Appendix Figure E.7 Graphical form of chemical shift results for $(AuCl_3)$dg (orange), $(AuCl_2PET)_2$dg (blue) and (AuCl)PET(AuHPET)dg (purple) systems. 202
Appendix Figure F.1 Comparison of the energy from the ML-MD LAMMPS simulation results and DFT calculated energy for the $Au_{25}(SCH_3)_{18}$ system at 300 K. 211
Appendix Figure F.2 Comparison of the energy from the ML-MD LAMMPS simulation results and DFT calculated energy for the $Au_{28}(SCH_3)_{20}$ system at 300 K. 212
Appendix Figure F.3 Comparison of the energy from the ML-MD LAMMPS simulation results and DFT calculated energy for the $Au_{36}(SCH_3)_{24}$ system at 300 K. 212
Appendix Figure F.4 Comparison of the energy from the ML-MD LAMMPS simulation results and DFT calculated energy for the $Au_{38}(SCH_3)_{24}$ system at 300 K. 213
Appendix Figure F.5 Comparison of the energy from the ML-MD LAMMPS simulation results and DFT calculated energy for the $Au_{44}(SCH_3)_{30}$ system at 300 K. 213
Appendix Figure F.6 Comparison of the energy from the ML-MD LAMMPS simulation results and DFT calculated energy for the $Au_{25}(SCH_3)_{18}$ system at 200 K. 214
Appendix Figure F.7 A. Mean bond length variation. B. C-S---S-C dihedral angle count for various angle ranges. C. Au atom count for each individual Au-Au coordination numbers. D. PCA visualization of the bonding parameters for different training configurations of $Au_{20}(SCH_3)_{16}$ at 400K (using a 14.85% increase in covalent radii). Each graph demonstrates results from a hundred configurations (one snapshot per picosecond). 215
Appendix Figure F.8 A. Mean bond length variation. B. C-S---S-C dihedral angle count for various angle ranges. C. Au atom count for each individual Au-Au coordination numbers. D. PCA visualization of the bonding parameters for different training configurations of $Au_{20}(SCH_3)_{16}$ at 400K (using a 30.00% increase in covalent radii). Each graph demonstrates results from a hundred configurations (one snapshot per picosecond). 216
Appendix Figure F.9 A. Mean bond length variation. B. C-S---S-C dihedral angle count for various angle ranges. C. Au atom count for each individual Au-Au coordination numbers. D. PCA visualization of the bonding parameters for different training configurations of

$Au_{25}(SCH_3)_{18}$ at 200K (using a 14.85% increase in covalent radii). Each graph demonstrates results from a hundred configurations (one snapshot per picosecond). 217
Appendix Figure F.10 A. Mean bond length variation. B. C-S---S-C dihedral angle count for various angle ranges. C. Au atom count for each individual Au-Au coordination numbers. D. PCA visualization of the bonding parameters for different training configurations of $Au_{25}(SCH_3)_{18}$ at 200K (using a 30.00% increase in covalent radii). Each graph demonstrates results from a hundred configurations (one snapshot per picosecond). 218
Appendix Figure F.11 A. Mean bond length variation. B. C-S---S-C dihedral angle count for various angle ranges. C. Au atom count for each individual Au-Au coordination numbers. D. PCA visualization of the bonding parameters for different training configurations of $Au_{44}(SCH_3)_{28}$ at 200K (using a 14.85% increase in covalent radii). Each graph demonstrates results from a hundred configurations (one snapshot per picosecond). 219

List of Tables

Table 3.1 Ground state geometric information for the Ag_nN_2 (n = 6, 8, 10, 12) systems. The nitrogen atom that is closest to the wire is denoted N1, whereas the nitrogen atom that is the furthest from the Ag_n system is denoted N2. 39

Table 3.2 Main electronic transitions for longitudinal excitation mode in the Ag_nN_2 (n = 6, 8, 10, 12) systems from LR-TDDFT calculations. 42

Table 3.3 Maximum N-N bond distance across 100 fs for Ehrenfest dynamics simulations on Ag_nN_2 (n = 6, 8, 10, 12) systems. Orange: N_2 bond is not activated; Blue: N_2 bond is activated but not dissociated; Green: N_2 bond is dissociated. 47

Table 4.1 Binding energies between N_2 molecule and wire systems in the parallel configuration. The pure Ag_6 (Ag_5-Ag) wire is included as well for the comparison. Binding energies were calculated using the equation: $\boldsymbol{E}binding = \boldsymbol{E}(wire) + \boldsymbol{E}(\boldsymbol{N2}) - \boldsymbol{E}(wire{+}\boldsymbol{N2}\ system)$ 63

Table 4.2 Longitudinal excitation mode energy and the corresponding electronic transitions and their contributions for each linear doped system. 67

Table 4.3 Binding energies for different configurations of group X metal-doped systems. 68

Table 4.4 Orbital energy, orbital character, contributions of N1 and N2 atomic orbitals to the molecular orbitals, and two selected energy gaps for Ag_5AuN_2 and Ag_5CuN_2 parallel system. 74

Table 4.5 Constrained geometry optimization results for Ag_5CuN_2 and Ag_5AuN_2. During the optimization process, the N-N bond length is fixed at 1.2 Å, 1.3 Å, 1.4 Å, 1.5 Å, and 1.6 Å. The relative energy for each system is calculated based on the equilibrium structure energy as reference. 76

Table 5.1 Selected bond length information (Å) for Au_6H_2 and Ag_6H_2 systems optimized with static applied electric fields. Atom numbers are provided in Figure 5.1. 90

Table 6.1 Numerical vs. analytical gradient differences (Hartree/Å) for representative molecular systems. 117

Table 6.2 Emission energy for five diatomic molecules (unit: eV) calculated at different level of theories, TDDFT failed in calculating the emission energy of H_2. 118

Table 6.3 Emission energy differences between TDDFT and TDDFT+TB for the gold nanoclusters. 122

Table 6.4 Comparison between the computational time (minutes) for TDDFT-aas, TDDFT+TB and TDDFT energy calculations. 123
Table 6.5 Comparison between the computational time (minutes) for TDDFT-aas, TDDFT+TB and TDDFT gradient calculations for three organic systems. 123
Table 6.6 Comparison between the computational time (minutes) for TDDFT-aas, TDDFT+TB and TDDFT gradient calculations for the $Au_{25}(SCH_2CH_2CH_3)_{18}^{-1}$ and Au_7^{3+} systems. 123
Table 7.1 Reaction energies for thiol addition steps (1B, 2B, 3B: diglyme present; 1B', 2B', 3B': no diglyme present). 135
Table 7.2 Calculated reaction energies (eV) for each step in the investigated reaction pathways. 138
Table 7.3 Calculated NMR chemical shifts (ppm) for hydrogen atoms in diglyme ligand for $AuCl_3$dg, $(AuCl_2PET)_2$dg, and (AuCl)PET(AuHPET)dg. 140
Table 7.4 Binding energy (kJ/mol) calculated using Eq. (1) between diglyme molecule and the gold moiety for three featured molecular systems. Charge analysis for three gold-diglyme systems using ETS-NOCV theory. The system is split into two fragments: diglyme and gold motif. 142
Table 7.5 Bonding energy decomposition results for selected systems. 146
Table 8.1 Database information for each round of the training procedure. The table contains information on the total number of data points in the database and the type of nanocluster included in the database. 156
Table 8.2 Parameters and hyperparameters for each round of the training procedure. 159

Appendix Table A.1 Dominant electronic transitions for two excitations in the $Ag_{19}N_2^{+1}$systems from LR-TDDFT calculations. 181
Appendix Table C.1 Selected bond lengths (Å) after ground state geometry optimizations using PBE and LC-ωPBE functionals. 186
Appendix Table C.2 Selected orbital energies (in eV) for two systems. "Bonding" denotes the orbital that shows bonding character for the interaction between H_2 and the cluster. "Antibonding" denotes the orbital that shows antibonding character for the interaction between H_2 and the cluster. Electric fields are given in atomic units. 188

Appendix Table D.1 Emission energy differences for five diatomic molecules (unit: eV) calculated at different level of theories; TDDFT failed in calculating the emission energy of H_2. 193
Appendix Table D.2 Emission energy differences among TDDFT-aas, TDDFT+TB, and TDDFT for organic molecules from the Thiel test set. Unit: eV 194
Appendix Table E.1 Calculated ^{1}H NMR results for hydrogen atoms in HPET. 196
Appendix Table E.2 Calculated ^{1}H NMR results for hydrogen atoms on PET and HPET in (AuCl)PET(AuHPET)]dg. 198
Appendix Table E.3 Calculated free energies (eV) at 298.15 K for each step in the investigated reaction pathways. 203

Acknowledgements

In the first place, I would like to express my deepest gratitude to my incredible fantastic, knowledgeable advisor Prof. Christine Aikens. She provides so many hand-on instructions, which makes me feel always being supported in the research. Meanwhile, she also gives me space to work on the project I am interested in and helps me learn to work more independently. Besides research, she is a great mentor and makes my journey at K-State so wonderful. Thank you, Christine!

I would like to thank my committee members: Prof. Paul Smith, Prof. Christer Aakeröy and Prof. Bin Liu. Thanks so much for giving me so many valuable suggestions, feedback, and support from different perspectives during the past five years!

I would like to thank my research collaborators: Prof. Xiaosong Li, Prof. Chris Ackerson, Dr. Vera Truttmann, Dr. Elizabeth Ploetz, Prof. Noelia Barrabés, Prof. Di Sun, and Prof. Hui Shen for their knowledge and input. I always learn a lot of new things through the collaborations.

I am so grateful to be a member of Aikens group, and I want to thank everyone in the group for their friendship and all the help/valuable discussion: Dr. Gowri Udayangani Kuda-Singappulige, Dr. Pratima Pandeya, Dr. Zhen Liu, Dr. Olivia Hull, Dr. Shana Havenridge, Sulalith Samarasinghe, Paul Javed, Gayathri Habarakadage, Dmitri Leenatali, Jonathan Bvunzawabaya, and Brie Little. I also wanted to thank Prof. Bin Liu and Prof. Bin Liu's group members for the joint group meeting every Friday. Thanks to Hao Deng for his help in the machine learning project; I am so happy this project eventually worked!

I also want to thank my friends in the chemistry department: Chao An, Aloka Marasinghe, Wei Wu and Ying Zhang. Thank you for making my workday filled with so much fun.

I am grateful to my undergraduate advisor, Prof. Sufan Wang. She introduced the area of quantum chemistry to me and gave me so much support during my college time. Specifically, she provided me the opportunity to go to the summer school at Beijing Normal University, where I met Prof. Weihai Fang and Prof. Run Long. That unforgettable experience convinced me to choose excited state dynamics as my future research area. Thank you, Prof. Wang! And I also want to express my gratefulness to Prof. Yucheng Huang, Prof. Yongjia Shang, Prof. Yonghong Ni, Prof. Ying Sun, and Prof. Yali Xie for helping me with the graduate school application. I could not be a member of K-State and the Aikens group without their help!

I want to thank my cool friends who help me bridge the connections between art and science: Dr. Qian-Yuan Tang at Hong Kong Baptist University always helps me understand physics concepts in an easier way. Dr. Natasha Rozhkovskaya in the math department at K-State is an expert in finding the beauty behind math and she organizes a fantastic Art&Math seminar. I also want to thank my violin teacher Russell Clark, and he is the best violin teacher.

During my journey at K-State, I met so many lovely friends, and we shared so much happiness together; specifically, I want to thank: Xiaoting Xu, Fengqing Di, Natalie Liptak, Nenghan Wan, Yizhi Wang, Zixian Wang, Zhen Liu, Hao Deng, and Fan Liu.

Lastly, I want to thank Yue Wang, Yanping Xu, Yijie Shen, and Xinxue Bi for being such great friends for ten years and always being by my side. I want to express my love to my family: Mom and Dad, thank you for your constant love. Grandpa and Grandma (from both mother's and father's side), thank you for always believing in me and encouraging me to go further. I also want to thank our big family for always making me feel loved. And Timi, thank you for being the best cat in the world.

yé ye and wài pó, I will miss you forever.

庭有枇杷树 今已亭亭如盖。

Dedication

"Everything is beautiful, the whole secret lies in knowing how to interpret."

– Camille Pissarro

Chapter 1 - Introduction

Why do water molecules come together and form snowflakes with distinct and beautiful patterns? How is it that a flock of birds lacks a unified command, yet moves as a cohesive whole, freely changing formations? And what enables a symphony orchestra to produce intricate music that differs significantly from a soloist's performance? Those phenomena can be all classified as emergence. Emergence phenomena can be found everywhere in the world including in science, math, and art.[1,2] According to Goldstein,[3] emergence refers to "*the arising of novel and coherent structures, patterns, and properties during the process of self-organization in complex systems*." However, the principal mechanism behind many of those emergence characters is still not clear, largely because the emergence effect occurs in the complex system, and the behavior of the total system is different from each individual component of the system.

The emergence phenomenon can also be observed in noble metal nanoparticle systems. For example, when small nanoclusters self-assemble into a large system, the properties of the system are non-scalable with the size of the system.[4] Plasmonic character is also a kind of emergence phenomenon existing in noble metal nanoparticles. Since this dissertation will include a focus on modeling plasmonic systems, let us first answer the question: what is a plasmon?

When an external field (for example, from a laser) is applied to the system and its frequency aligns with the plasmonic frequency of the system, the valence electrons within the noble metal nanocluster become collectively excited, oscillating back and forth. A schematic picture of the plasmon resonance is shown in Figure 1.1. This process can convert light energy into electronic excitation energy, which offers potential applications in diverse fields such as biosensing, photo-catalysis, and energy harvesting.[5,6]

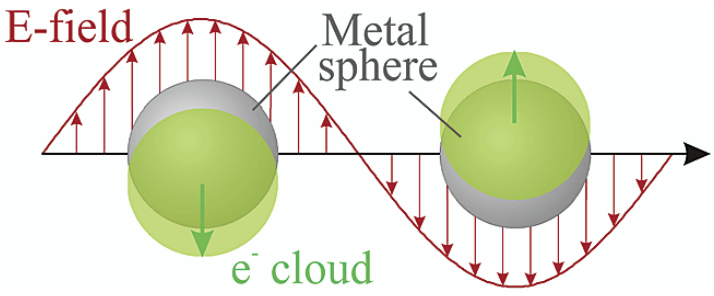


Figure 1.1 Schematic of plasmon oscillation for a sphere, showing the displacement of the conduction electron charge cloud relative to the nuclei. Reprinted with permission from *J. Phys. Chem. B* 2003, 107, 3, 668–677. Copyright 2003 American Chemical Society.

1.1 Plasmon-induced catalyzed reactions

As mentioned above, systems with plasmonic character have potential applications in diverse fields. However, the intrinsic mechanism underlying the plasmon-induced catalytic process remains unclear, which leads to difficulty in designing efficient catalysts, finding active reaction sites, and optimizing the conditions for the plasmon-induced reactions.

Several recent review articles have discussed the plasmon-induced catalytic reaction from different aspects.[5,7–10] In this section, I will employ a coupled noble metal nanoparticle@molecule system (a visualization is shown in Figure 1.2) as an example to briefly illustrate the plasmon catalytic process. A schematic diagram is shown in Figure 1.3.

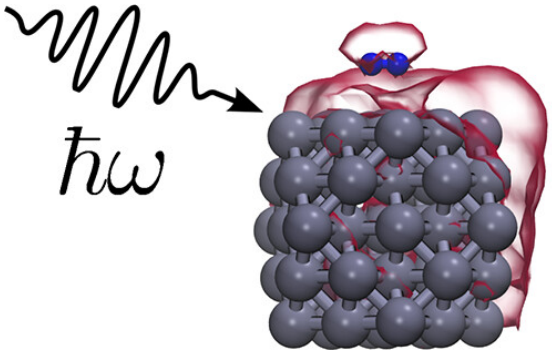


Figure 1.2 Silver nanoparticle (NP) coupled with the N_2 molecule, with a laser pulse applied to the system. Reprinted with permission from ACS Nanosci. Au 2023, 3, 4, 269–279 Copyright 2023. This publication is licensed under CC-BY 4.0.

In the first step, an external field (for example, a laser) will be applied to the system, leading to the plasmon excitation (Figure 1.3). Upon excitation, hot electrons will redistribute throughout the system, leading to the plasmonic system being in a non-equilibrium state. Energy transfer may occur between the metal system and N_2 through three different processes,[5,7–10] including (1) Hot-carrier injection, which suggests that charge transfer (CT) occurs from the metal to absorbate, incorporating the electron-electron scattering process. (2) Thermal heating. This process involves electron-phonon coupling, which will serve to thermalize the excited carriers. (3) Direct excitation, which includes both far-field (light emission) and near-field (resonance energy transfer) interactions. The subsequent vibrational resonance occurs on a time scale of

approximately 10−100 ps. In the last step, the plasmonic system can be coupled to the bath through thermal dissipation, which has an approximate time scale of 100 ps to 10 ns.[8]

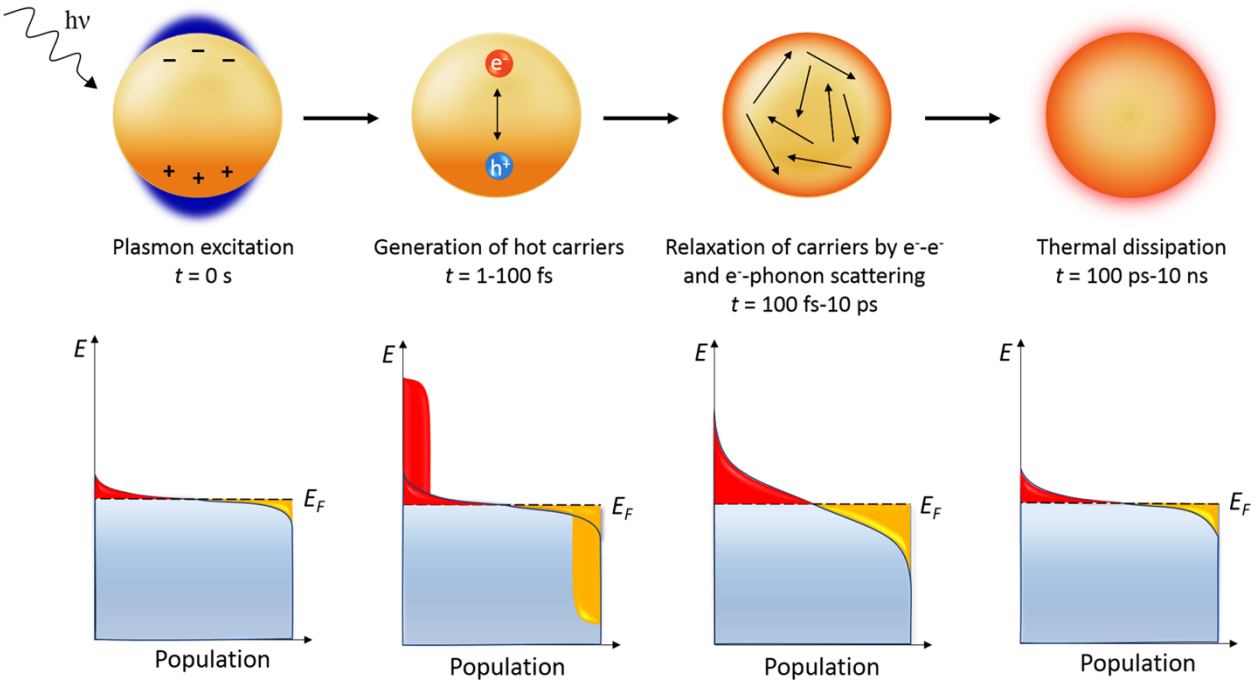


Figure 1.3 Plasmon excitation at t = 0 and subsequent generation of hot electron–hole pairs within the metal, then thermalization via electron–electron, electron–phonon scattering (this leads to a Fermi-Dirac distribution of charge carriers representing the elevated temperature) and further via thermal dissipation via phonon–phonon scattering. E_F indicates the Fermi level, and yellow and red areas indicate hole and electron energies, respectively. Reprinted with permission from *Commun Mater* 2021, 2, 114 Copyright 2021. This publication is licensed under CC-BY 4.0.

As shown in Figure 1.3, there is a broad time scale for each sub-step, spanning from the femtosecond to nanosecond range, which leads to difficulty in thoroughly studying the whole process. Another major challenge lies in the diverse physical phenomena manifesting in different plasmonic systems; for example, the plasmon decay process can proceed through different channels, and there might be competition between radiative and nonradiative decay.[11,12] Thus, it is important to figure out the exact mechanism involved in each specific process.

1.2 Noble metal nanoparticles (NPs)

Noble metal nanoparticles generally refer to metal nanoparticles constructed of silver, gold or copper. Noble metal nanoparticles have gained significant attention due to their unique LSPR (localized surface plasmon resonance) properties that lead to strong light scattering and absorption.[13,14] LSPR properties will vary depending on the type of the elements: gold and silver nanospheres with similar radii will show different excitation wavelengths for their corresponding LSPR peaks.[15] Gold nanoparticles show more splitting in the absorption peaks because of their d-band electrons, while silver nanoparticles tend to show one sharp peak in their LSPR region.[16]

Nanoparticles which can be determined with atomic precision are often called nanoclusters.[17] The properties of a nanocluster can be modified by dressing the nanocluster with different ligands, and these types of nanoclusters are named ligand-protected nanoclusters.[18,19] Thiolate-protected metal nanoclusters are one of the most widely discussed in the ligand-protected nanocluster family. The nanoclusters consist of a metal kernel in the center and a thiolate-protected motif (usually built from a basic unit of SR-Au-SR) around the kernel; an example $Au_{38}(SR)_{24}$ nanocluster is shown in Figure 1.4.

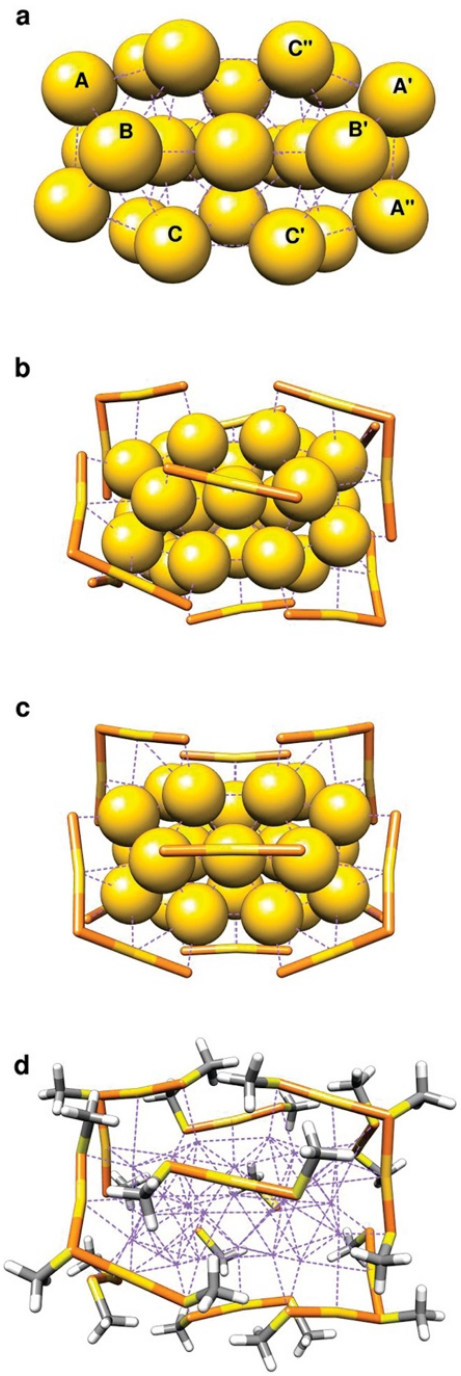


Figure 1.4 A. Au_{23} core with labeling of the surface Au atoms involved in determining the symmetry of the ligand layer. B. Chiral D_3 arrangement of the Au−S atoms. C. C_{3h} arrangement of the Au−S atoms. D. Optimal SCH_3 distribution on structure. Reprinted with permission from *J. Am. Chem. Soc.* 2010, 132, 23, 8210–8218. Copyright 2010 American Chemical Society.

A brief introduction of the history of gold thiolate-protected nanoclusters is shown in Figure 1.5. The first density functional theory (DFT) model of thiolate protected nanocluster was proposed in 1999.[20] $Au_{25}(SR)_{18}^-$ is one of the first thiolate-protected nanoparticles whose X-ray crystal structure was determined and showed a good correlation with the DFT-predicted results.[21–23] Since the structure can be determined with atomic precision, it provides an opportunity to use quantum chemistry calculations to investigate the physical and chemical properties of the noble metal nanoclusters.[19,24–26] Currently, DFT calculations have been successfully applied to study the geometric information, electronic structures, and optical properties of the ligand-protected noble metal nanoclusters. The electronic structure and luminescence properties will vary depending on the size, shape, ligand types, and doping of the nanocluster.[27–30]

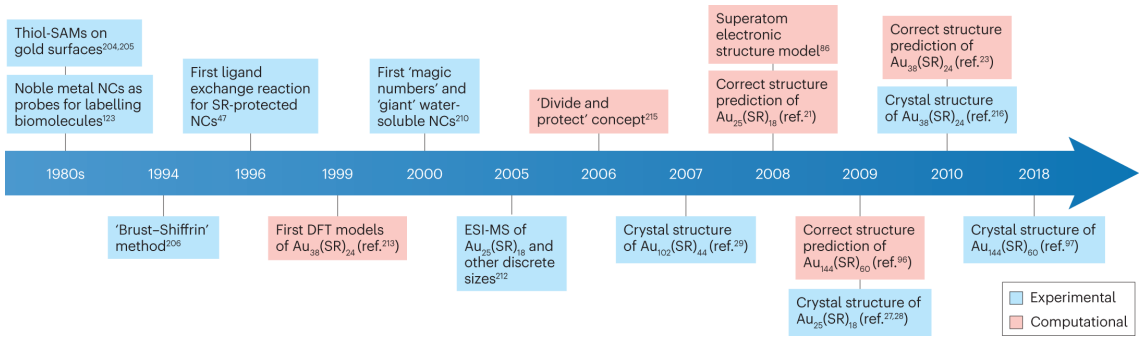


Figure 1.5 Timeline of some key milestones in the field of atomically precise metal nanoclusters. The key developments presented in each box are focused on gold-based metal nanoclusters because they have been studied most intensively and promoted the development of their silver- and copper-based counterparts. Au, gold; DFT, density functional theory; ESI-MS, electrospray ionization mass spectrometry; NCs, nanoclusters; SAMs, self-assembling monolayers; SR, thiolate. Note: Reference numbers in the figure refer to references in Nat Rev Mater 8, 372–389 (2023). Reprinted with permission from Nat Rev Mater 8, 372–389 (2023) Copyright 2023, Springer Nature Limited

1.3 Solvent effects in metal nanoparticle synthesis

Many of the current synthesis work on thiolate-protected gold nanoclusters employs the straightforward Brust–Schiffrin synthesis, which includes a two-phase reduction starting from the $AuCl_4^-$ in a mixture of water/toluene solvent.[31] Recently, diglyme (dg) has been applied as a co-solvent in the gold nanoparticle synthesis process and can mediate the self-assembly process of

the gold nanoparticles.[32–34] When using diglyme as the solvent, both the monomer gold nanocluster and dimer gold nanocluster (with bridging diglyme) were observed in the final products. A computational model of the dimerized structure was first proposed in 2015.[32] In the model, the diglyme was placed in the middle of two gold nanoparticles, and the HOMO orbital (described as doubly-degenerate) was computed (Figure 1.6). Compared with the single $Au_{20}(SCH_3)_{15}$dg cluster with a large HOMO-LUMO gap, the dimerized structure $(Au_{20}(SCH_3)_{15})_2$dg shows a triplet state in the ground state.

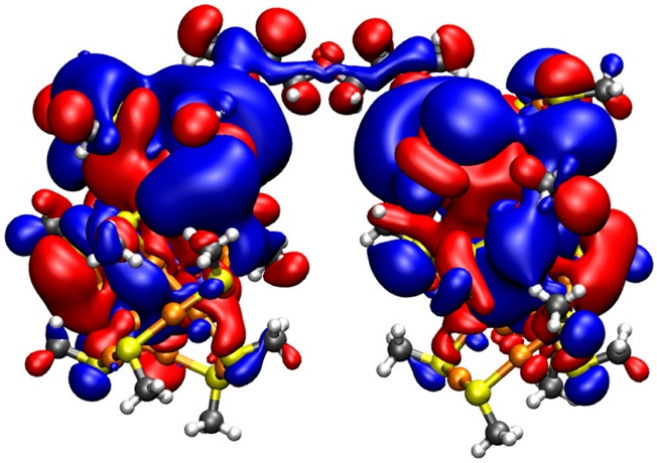


Figure 1.6 Combined orbital contours of the twice-degenerate HOMO of the computed diglyme-linked $Au_{20}(SCH_3)_{15}$ dimer. Reprinted with permission from ACS Nano 2015, 9, 12, 11690–11698. Copyright 2015 American Chemical Society.

In the real solvent, gold nanocluster will interact with a massive number of solvent molecules, rather than just one molecule. In addition, determining the optimal ratio between gold nanoclusters and diglyme molecules is crucial for facilitating the reactions. In that way, it is important to figure out a good model to describe the interaction between the diglyme molecules and gold nanocluster in a computationally efficient manner.

1.4 Challenges in modeling noble metal nanoparticles

Plasmonic noble metal nanoparticles usually exist with a large size. Thus, if we want to model the system using quantum chemistry methods, the computational cost (in terms of computational memory and time) will be very expensive.

The Jellium model (aka the uniform electron gas model) is a cheaper alternative to approximate the metal nanoclusters. In the model, instead of calculating the atomically precise

structure of the metal nanocluster system, the whole system is treated as a giant spherical positive charge, and a visualized example is shown in Figure 1.7.a. The radius of the Jellium model is related to the resonant frequency of the system. The Jellium model has been successfully applied to investigate the plasmon-enhanced H_2 dissociation, and the simplified model makes it possible to examine the TDDFT absorption spectra and excited state potential energy surface of the plasmonic dimer@H_2 system with reasonable computational costs.[35]

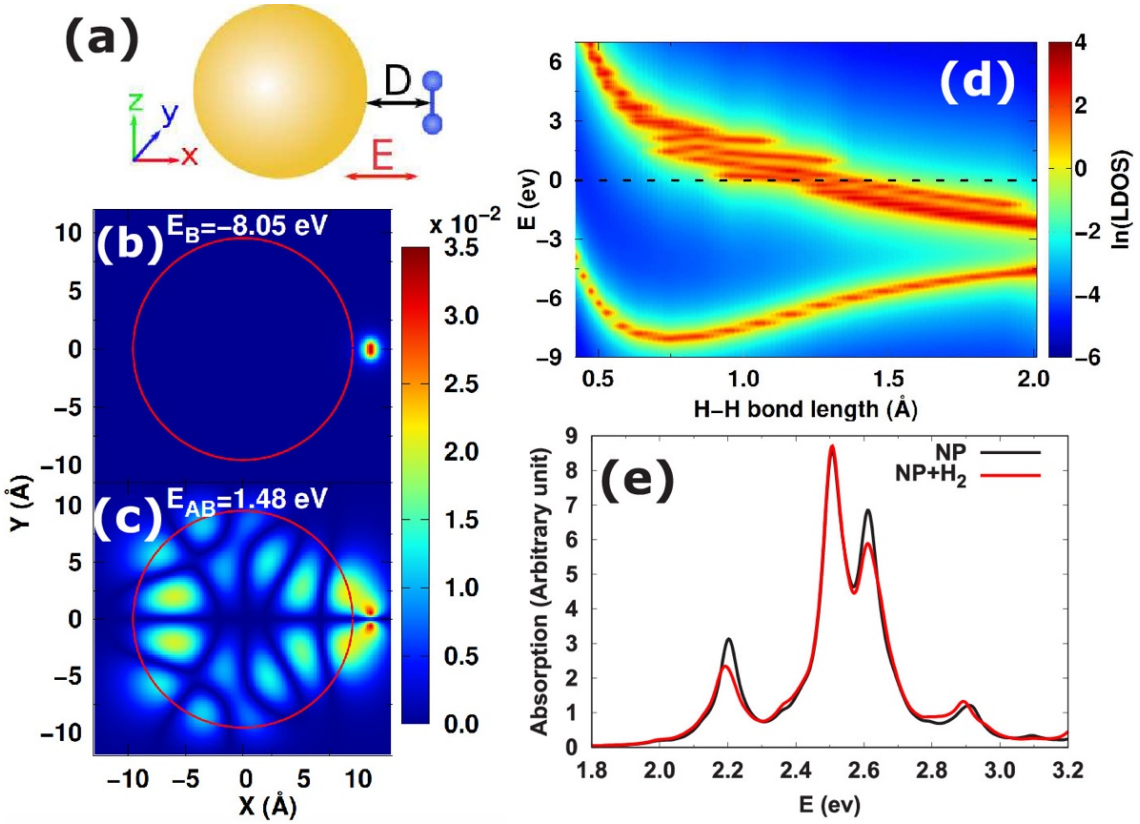


Figure 1.7 (a) Schematic diagram of H_2 molecule adsorbed on the NP surface. The electric field is in x direction. (b) Bonding and (c) antibonding (AB) wave functions of H_2 in the x–z plane. Panel c indicates that (1) the AB state is 1.48 eV above the Fermi energy, which offers the possibility of transferring the hot-electron generated in the metallic NPs to the AB state; and (2) the AB WF is hybridized with the NP, which can facilitate the hot-electron transfer. The red circle indicates the surface of the NP. (d) LDOS of H_2 adsorbed on NP surface. The dashed line indicates the Fermi energy (shifted to 0) of the NP + H_2 system with equilibrium H–H bond length. The evolution of peaks in LDOS for different H–H bond lengths roughly reflects the PES of the H_2 molecule. (e) Absorption spectrum of NP and NP + H_2. Reprinted with permission from ACS Nano 2018, 12, 8, 8415–8422 Copyright 2018 American Chemical Society

While the approximate Jellium method can significantly reduce computational costs, it cannot be used to study the interaction between metal atoms and the absorbate, as the nanoparticle

loses precise atomic structure information. Another direction is to keep the atomically precise structure of the nanocluster but use a smaller cluster instead to model the plasmon-like process. This approach can be rationalized based on the configuration interaction (CI) treatment of a plasmonic system: a plasmon consists of a constructive superposition of single-particle transitions. Therefore, a plasmon can be considered as the mixing of N single-particle transitions represented by determinants. As the size of the nanoparticle decreases, fewer determinants contribute to the plasmon excitation.[36,37] In that way, it is reasonable to use a small system with fewer single-particle transitions to model the plasmon-induced process. A third way to enable calculations on large systems is to develop other types of methods that can reduce the computational cost, which will be described further in this dissertation.

1.5 Objectives of this dissertation

In this dissertation, the objective is to apply different approaches to model and examine the properties of noble nanoclusters. In Chapters 3, 4, and 5, I have applied electronic structure (DFT, linear-response time-dependent DFT (TDDFT), and real-time TDDFT) calculations combined with nonadiabatic dynamics approaches to investigate the plasmon-induced catalytic process of nanowire/nanocluster systems. By employing these various computational methods, we studied: (1) The nanowire length and electric field strength effects on the plasmon-enhanced N_2 dissociation on a Ag nanowire. (2) The effects of doping the Ag nanowire on plasmon-enhanced N_2 dissociation. (3) The effects of different types of electric fields (static electric field and continuous wave field) on the Ag/Au nanocluster@H_2 system. In summary, in these three projects, we have used small sizes of nanowires and nanoclusters to model the plasmon-like process to reduce the computational cost. In Chapter 6, I develop the TDDFT- approximate auxiliary function s (aas) method, which is an approximate method based on standard TDDFT. TDDFT-aas can reduce the computational cost for calculating the optical properties of large-size nanoclusters. In Chapter 7, I applied DFT methods to examine the diglyme effects on the gold nanocluster growth process. In Chapter 8, I developed a type of machine learning-based force field to accelerate the molecular dynamics of gold thiolate-protected nanoclusters with force fields that can reach the DFT level of accuracy.

1.6 References

(1) Kivelson, S.; Kivelson, S. A. Defining Emergence in Physics. *npj Quant Mater* **2016**, *1* (1), 16024.

(2) Clayton, P.; Davies, P. *The Re-Emergence of Emergence*; Oxford University Press, 2008.

(3) Goldstein, J. Emergence as a Construct: History and Issues. *Emergence* **1999**, *1* (1), 49–72.

(4) Landman, U.; Luedtke, W. D. Small Is Different: Energetic, Structural, Thermal, and Mechanical Properties of Passivated Nanocluster Assemblies. *Faraday Disc.* **2004**, *125*, 1.

(5) Yu, H.; Peng, Y.; Yang, Y.; Li, Z.-Y. Plasmon-Enhanced Light–Matter Interactions and Applications. *npj Comput Mater* **2019**, *5* (1), 45.

(6) Dong, Y.; Hu, C.; Xiong, H.; Long, R.; Xiong, Y. Plasmonic Catalysis: New Opportunity for Selective Chemical Bond Evolution. *ACS Catal.* **2023**, *13* (10), 6730–6743.

(7) Kazuma, E. Key Factors for Controlling Plasmon-Induced Chemical Reactions on Metal Surfaces. *J. Phys. Chem. Lett.* **2024**, *15* (1), 59–67.

(8) Ahlawat, M.; Mittal, D.; Govind Rao, V. Plasmon-Induced Hot-Hole Generation and Extraction at Nano-Heterointerfaces for Photocatalysis. *Commun Mater* **2021**, *2* (1), 114.

(9) Herring, C. J.; Montemore, M. M. Recent Advances in Real-Time Time-Dependent Density Functional Theory Simulations of Plasmonic Nanostructures and Plasmonic Photocatalysis. *ACS Nanosci. Au* **2023**, *3* (4), 269–279.

(10) Cortés, E.; Besteiro, L. V.; Alabastri, A.; Baldi, A.; Tagliabue, G.; Demetriadou, A.; Narang, P. Challenges in Plasmonic Catalysis. *ACS Nano* **2020**, *14* (12), 16202–16219.

(11) Khurgin, J. B. How to Deal with the Loss in Plasmonics and Metamaterials. *Nature Nanotech* **2015**, *10* (1), 2–6.

(12) Brown, A. M.; Sundararaman, R.; Narang, P.; Goddard, W. A.; Atwater, H. A. Nonradiative Plasmon Decay and Hot Carrier Dynamics: Effects of Phonons, Surfaces, and Geometry. *ACS Nano* **2016**, *10* (1), 957–966.

(13) Gong, C.; Leite, M. S. Noble Metal Alloys for Plasmonics. *ACS Photonics* **2016**, *3* (4), 507–513.

(14) Hartland, G. V. Optical Studies of Dynamics in Noble Metal Nanostructures. *Chem. Rev.* **2011**, *111* (6), 3858–3887.

(15) Kelly, K. L.; Coronado, E.; Zhao, L. L.; Schatz, G. C. The Optical Properties of Metal Nanoparticles: The Influence of Size, Shape, and Dielectric Environment. *J. Phys. Chem. B* **2003**, *107* (3), 668–677.

(16) Bernardi, M.; Mustafa, J.; Neaton, J. B.; Louie, S. G. Theory and Computation of Hot Carriers Generated by Surface Plasmon Polaritons in Noble Metals. *Nat Commun* **2015**, *6* (1), 7044.

(17) Jin, R.; Zeng, C.; Zhou, M.; Chen, Y. Atomically Precise Colloidal Metal Nanoclusters and Nanoparticles: Fundamentals and Opportunities. *Chem. Rev.* **2016**, *116* (18), 10346–10413.

(18) Lopez-Acevedo, O.; Tsunoyama, H.; Tsukuda, T.; Häkkinen, H.; Aikens, C. M. Chirality and Electronic Structure of the Thiolate-Protected Au_{38} Nanocluster. *J. Am. Chem. Soc.* **2010**, *132* (23), 8210–8218.

(19) Aikens, C. M. Electronic and Geometric Structure, Optical Properties, and Excited State Behavior in Atomically Precise Thiolate-Stabilized Noble Metal Nanoclusters. *Acc. Chem. Res.* **2018**, *51* (12), 3065–3073.

(20) Häkkinen, H.; Barnett, R. N.; Landman, U. Electronic Structure of Passivated $Au_{38}(SCH_3)_{24}$ Nanocrystal. *Phys. Rev. Lett.* **1999**, *82* (16), 3264–3267.

(21) Zhu, M.; Aikens, C. M.; Hollander, F. J.; Schatz, G. C.; Jin, R. Correlating the Crystal Structure of A Thiol-Protected Au_{25} Cluster and Optical Properties. *J. Am. Chem. Soc.* **2008**, *130* (18), 5883–5885.

(22) Akola, J.; Walter, M.; Whetten, R. L.; Häkkinen, H.; Grönbeck, H. On the Structure of Thiolate-Protected Au_{25}. *J. Am. Chem. Soc.* **2008**, *130* (12), 3756–3757.

(23) Heaven, M. W.; Dass, A.; White, P. S.; Holt, K. M.; Murray, R. W. Crystal Structure of the Gold Nanoparticle $[N(C_8H_{17})_4][Au_{25}(SCH_2CH_2Ph)_{18}]$. *J. Am. Chem. Soc.* **2008**, *130* (12), 3754–3755.

(24) Matus, M. F.; Häkkinen, H. Understanding Ligand-Protected Noble Metal Nanoclusters at Work. *Nat Rev Mater* **2023**, *8* (6), 372–389.

(25) Sun, F.; Tang, Q.; Jiang, D. Atomically Precise Metal Nanoclusters as Electrocatalysts: From Experiment to Computational Insights. In *Atomically Precise Nanochemistry*; Jin, R., Jiang, D., Eds.; Wiley, 2023; pp 195–225.

(26) Xiong, L.; Pei, Y. Gold Nanoclusters with Atomic Precision: Optical Properties. In *Atomically Precise Nanoclusters*; Zhu, Y., Jin, R., Eds.; Jenny Stanford Publishing, 2021; pp 165–225.

(27) Aikens, C. M. Effects of Core Distances, Solvent, Ligand, and Level of Theory on the TDDFT Optical Absorption Spectrum of the Thiolate-Protected Au_{25} Nanoparticle. *J. Phys. Chem. A* **2009**, *113* (40), 10811–10817.

(28) Wei, J.; MacLeod Carey, D.; Halet, J.-F.; Kahlal, S.; Saillard, J.-Y.; Muñoz-Castro, A. From 8- to 18-Cluster Electrons Superatoms: Evaluation via DFT Calculations of the Ligand-Protected $W@Au_{12}(DPPM)_6$ Cluster Displaying Distinctive Electronic and Optical Properties. *Inorg. Chem.* **2023**, *62* (7), 3047–3055.

(29) Vanzan, M.; Corni, S. Role of Organic Ligands Orientation on the Geometrical and Optical Properties of $Au_{25}(SCH_3)_{18}^0$. *J. Phys. Chem. A* **2018**, *122* (34), 6864–6872.

(30) Havenridge, S.; Weerawardene, K. L. D. M.; Aikens, C. M. Characterization of Pt-Doping Effects on Nanoparticle Emission: A Theoretical Look at $Au_{24}Pt(SH)_{18}$ and $Au_{24}Pt(SC_3H_7)_{18}$. *Faraday Discuss.* **2023**, *242*, 464–477.

(31) Brust, M.; Walker, M.; Bethell, D.; Schiffrin, D. J.; Whyman, R. Synthesis of Thiol-Derivatised Gold Nanoparticles in a Two-Phase Liquid–Liquid System. *J. Chem. Soc., Chem. Commun.* **1994**, *0* (7), 801–802.

(32) Compel, W. S.; Wong, O. A.; Chen, X.; Yi, C.; Geiss, R.; Häkkinen, H.; Knappenberger, K. L.; Ackerson, C. J. Dynamic Diglyme-Mediated Self-Assembly of Gold Nanoclusters. *ACS Nano* **2015**, *9* (12), 11690–11698.

(33) Herbert, P. J.; Yi, C.; Compel, W. S.; Ackerson, C. J.; Knappenberger, K. L. Relaxation Dynamics of Electronically Coupled $Au_{20}(SC_8H_9)_{15}$-*n*-Glyme-$Au_{20}(SC_8H_9)_{15}$ Monolayer-Protected Cluster Dimers. *J. Phys. Chem. C* **2018**, *122* (33), 19251–19258.

(34) Herbert, P. J.; Ackerson, C. J.; Knappenberger, K. L. Size-Scalable Near-Infrared Photoluminescence in Gold Monolayer Protected Clusters. *J. Phys. Chem. Lett.* **2021**, *12* (31), 7531–7536.

(35) Zhang, Y.; Nelson, T.; Tretiak, S.; Guo, H.; Schatz, G. C. Plasmonic Hot-Carrier-Mediated Tunable Photochemical Reactions. *ACS Nano* **2018**, *12* (8), 8415–8422.

(36) Guidez, E. B.; Aikens, C. M. Quantum Mechanical Origin of the Plasmon: From Molecular Systems to Nanoparticles. *Nanoscale* **2014**, *6* (20), 11512–11527.

(37) Guidez, E. B.; Aikens, C. M. Plasmon Resonance Analysis with Configuration Interaction. *Phys. Chem. Chem. Phys.* **2014**, *16* (29), 15501.

Chapter 2 - Theory and methods

Since the dissertation focuses on employing different computational approaches to calculate the noble metal nanoclusters, in this chapter I will introduce the theoretical background behind the computational methods that are involved in this dissertation. Figure 2.1 provides an intuitive comparison of the computational time scale and system size scale for these approaches; certain methods are better for particular ranges of computational time scales and system sizes.

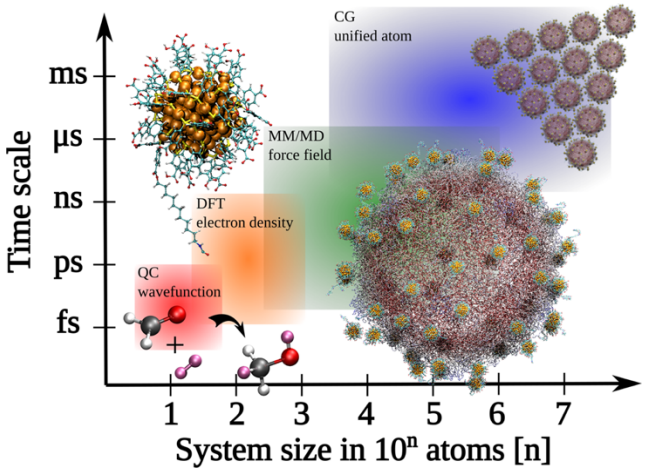


Figure 2.1 Quantum-chemical (QC) wavefunction methods can conveniently deal with small molecules with great accuracy. Density functional theory (DFT) is a major workhorse dealing with monolayer-protected cluster (MPC) electronic structure, optical properties, and reactions, but with limited time scales. Classical force fields generated for molecular mechanics (MM) and molecular dynamics (MD) simulations can give valuable details on MPC-environment interactions such as with viruses as shown here. Finally, processes and properties in self-assembling MPC systems may need to be dealt with coarse-grained (CG) methods where each MPC is described as a "unified atom". Reprinted with permission from *Nat Commun* 12, 2197 (2021) Copyright 2021. This publication is licensed under CC-BY 4.0.

Wavefunction-based methods are suitable for calculating small systems with few atoms. As the system size increases, the dimensions of the wavefunction increase dramatically. For example, for a system with N electrons, the wavefunction of the system depends on 3N spatial functions and N spin functions. In this way, the computational cost increases significantly with the increase of the system size (the computation time scale can vary from N^4 to N!).[1]

One alternative approach to reduce the dimensions of the system is to introduce the concept of density to describe the system instead of using wavefunction. Nowadays, density functional theory (DFT) stands out as the foremost and most widely employed electronic structure method in chemistry research. DFT has significantly increased the size of systems that can be accurately calculated, from hundreds to thousands of atoms, compared to wavefunction-based methods. DFT can reduce the computational time scale of the system to N^3.

Going further to larger systems, molecular mechanics (MM) and molecular dynamics (MD) enable the study of atomistic nanostructures containing millions of atoms over microsecond time scales. Furthermore, in coarse-grained (CG) simulations, the system's dynamics are described by interactions between those unified atoms rather than individual real atoms, which means that the nanoclusters lose their precise atomic structures. Overall, all methods involve a trade-off between accuracy and computational cost.

2.1 The Schrödinger equation and the Born-Oppenheimer approximation

Solving quantum chemistry problems can start by solving the Schrödinger equation $\widehat{\mathcal{H}}\Psi = E\Psi$. The Hamiltonian of interest ($\widehat{\mathcal{H}}$) can be written as:

$$\widehat{\boldsymbol{\mathcal{H}}} = -\sum_I \frac{\hbar^2}{2M_I}\nabla_I^2 - \sum_i \frac{\hbar^2}{2m_e}\nabla_i^2 + \sum_{i<j} \frac{e^2}{|\mathbf{r}_i-\mathbf{r}_j|} - \sum_{I,i} \frac{e^2 Z_I}{|\mathbf{R}_I-\mathbf{r}_i|} + \sum_{I<J} \frac{e^2 Z_I Z_J}{|\mathbf{R}_I-\mathbf{R}_J|} \quad \textbf{(Equation 2.1)}$$

where in Equation 2.1, the first two terms are kinetic energy operators for nuclei (using *I* and *J* to denote the nuclei index) and electrons (using *i* and *j* to denote the electrons index) respectively, the third term is the electron-electron interaction operator, the fourth term is the nuclear-electron interaction operator, and the last term is related to the nuclear-nuclear interaction.

Based on the Born-Oppenheimer approximation,[2] since nuclei are heavier than electrons, we can neglect the first term and treat the last term as a constant potential for equation 1. The Born-Oppenheimer approximation simplifies the equation; however, the third term is still challenging to deal with due to the many-body effects of the electronic wavefunction. Therefore, the biggest question lies in how to treat this many-body term.

2.2 Density functional theory

Modern density functional theory is closely related to the Hohenberg–Kohn (HK) theorems and the Kohn-Sham theorem.[3,4] The first HK theorem states that there is a unique one-to-one mapping between a ground-state wavefunction and its density.[3] Then, the second HK theorem applies variational principle to prove that the ground-state electron density minimizes the energy functional.[3] Kohn and Sham introduced the concept of a non-interacting system (Kohn-Sham (KS) system).[4] In this way, a many-body system of interacting electrons can be treated as a non-interacting electron system (ϕ_i^{KS}) in an effective potential ($v_{eff} = v_{ext}(r) + \int \frac{\rho(r')}{|r-r'|} dr' + v_{XC}(r)$). The effective potential includes the external potential term ($v_{ext}(r)$), the electron-electron repulsion term ($\int \frac{\rho(r')}{|r-r'|} dr'$), and the exchange-correlation term ($v_{XC}(r)$).

The pseudoeigenvalue equations (aka the Kohn-Sham equations) can be written as Equation 2.2:

$$\widehat{\boldsymbol{h}}\boldsymbol{\phi}_{\boldsymbol{i}}^{\boldsymbol{KS}} = \left[-\frac{\boldsymbol{\nabla^2}}{\boldsymbol{2}} + \boldsymbol{v_{ext}(r)} + \int \frac{\boldsymbol{\rho(r')}}{\boldsymbol{|r-r'|}} \boldsymbol{dr'} + \boldsymbol{v_{XC}(r)}\right] \boldsymbol{\phi}_{\boldsymbol{i}}^{\boldsymbol{KS}} = \boldsymbol{\epsilon_i \phi}_{\boldsymbol{i}}^{\boldsymbol{KS}} \quad \textbf{(Equation 2.2)}$$

where $-\frac{\nabla^2}{2}$ is the kinetic operator, ϵ_i is the Kohn-Sham orbital energy, ϕ_i^{KS} is the Kohn-Sham orbital, and $\rho(\mathbf{r}) = \sum_{i=1}^{N} \left|\phi_i^{KS}(\mathbf{r})\right|^2$ is the ground state density for the system. Since $\rho(\mathbf{r})$ appears on both sides of the equation, the pseudoeigenvalue equation must be solved self-consistently.

Theoretically, the exact exchange-correlation energy term ($v_{XC}(r)$) will lead to the exact solution; however, since the exchange-correlation energy functionals are related to the many-body effects of the system, the exact form of the density is unknown, which leads to the next question: how to get a relatively good exchange-correlation energy functional term?

Currently, there have been a diverse set of DFT functionals proposed to calculate the properties of physical and chemical systems, and the key differences between them lie in the exchange-correlation part. As a general summary of those functionals, the local density approximation (LDA) uses ideas from the uniform electron gas when considering the exchange-correlation energy term; the exchange-correlation energy ($E_{\mathrm{xc}}^{\mathrm{LDA}}[\rho]$) for the system is calculated using Equation 2.3, where ρ represents the density.

$$\boldsymbol{E_{xc}^{LDA}[\rho]} = \int \boldsymbol{d^3 r f(\rho)} \qquad \textbf{(Equation 2.3)}$$

Based on LDA, the local spin density approximation (LSDA) slightly improves by incorporating the effects of spin density differences (i.e. differences between ρ_α and ρ_β), and the exchange energy part can be written as Equation 2.4:

$$\boldsymbol{E_{xc}^{LSDA}[\rho_\alpha, \rho_\beta] = \int d^3\mathbf{r} f(\rho_\alpha, \rho_\beta)} \quad \textbf{(Equation 2.4)}$$

In this way, LDA and LSDA are interchangeable when treating closed-shell systems.

Since the real system's electron density does not vary slowly like a uniform electron gas, one direction for improvement is to make the exchange and correlation energies dependent not only on the electron density but also on derivatives of the density, which is known as the generalized gradient approximation (GGA) method.[5–7] For a GGA functional, the exchange-correlation functional energy can be written as:

$$\boldsymbol{E_{xc}^{GGA}[\rho_\alpha, \rho_\beta] = \int d^3\mathbf{r} f(\rho_\alpha, \rho_\beta, \nabla\rho_\alpha, \nabla\rho_\beta)} \quad \textbf{(Equation 2.5)}$$

where $\nabla\rho_\alpha$ and $\nabla\rho_\beta$ are the gradient terms concerning densities.

However, for both LDA/LSDA and GGA functionals, the exchange term stills need to be improved. To address this, hybrid functionals aim to improve this problem by adding the Hartree-Fock (HF) exchange term when calculating the exchange-correlation energy term (E_{XC}) as shown in Equation 2.6:[8]

$$\boldsymbol{E_{XC} = (1 - a)E_{XC}^{DFT} + aE_X^{HF}} \quad \textbf{(Equation 2.6)}$$

where a ranges between 0 and 1, which is a parameter that can be applied to change the percentage between DFT (E_{XC}^{DFT}) and HF (E_X^{HF}).

Applying long-range corrected functionals (LRCF) can improve the local character of the approximate exchange-correlation functional. In the LRCF, the electron repulsion operator $\frac{1}{r_{12}}$ is divided into short-range (SR) and long-range (LR) terms, as shown in Equation 2.7:

$$\boldsymbol{\frac{1}{r_{12}} = \frac{1-\mathrm{erf}(\mu r_{12})}{r_{12}} + \frac{\mathrm{erf}(\mu r_{12})}{r_{12}}} \quad \textbf{(Equation 2.7)}$$

where "erf" denotes the error function. μ is the parameter that determines the proportion between the two ranges depending on the value of r_{12}. For Equation 2.7, the first term is related to the short-range interaction and is described using a DFT exchange functional; the second term related to the long-range exchange interaction is described using the HF exchange integral.

In this dissertation, for chapters 3, 4, and 5, we investigated the plasmon-enhanced catalysis reaction of a small molecule in the presence of a nanowire/nanocluster. Since LRCF has shown

success in capturing the charge-transfer character between small molecule and silver nanowire systems, we employed the LC-ωPBE functional[9] in these three projects.

Adding a dispersion correction is another direction to improve the locality of a LDA/GGA functional. This method can be straightforward by integrating empirical potentials represented by the formula $\frac{-C_6}{R^6}$, where the C_6 coefficients denote pairwise atomic parameters.[10] In this dissertation, for the project on studying the interaction between diglyme and gold nanocluster (chapter 7), we employed the BP86-D3[7,11,10] method to better describe the dispersion interaction between two systems.

2.3 Basis sets

Besides the choice of the functionals, basis sets are another important part of the level of theory that needs to be carefully chosen in DFT calculations.[12] For the calculation of a finite system, slater-type orbitals (STO) and Gaussian-type orbitals (GTO) are two popular types of basis sets in quantum chemistry calculation packages, and both STOs and GTOs are atomic-centered basis functions. Their formulas are shown in Equation 2.8 and Equation 2.9 respectively.

Slater-type orbitals (STO):

$$\boldsymbol{\chi_{\zeta,n,l,m}(r,\theta,\varphi) = NY_{l,m}(\theta,\varphi)r^{n-1}e^{-\zeta r}} \qquad \textbf{(Equation 2.8)}$$

Gaussian-type orbitals (GTO):

$$\boldsymbol{\chi_{\zeta,n,l,m}(r,\theta,\varphi) = NY_{l,m}(\theta,\varphi)r^{2n-2-l}e^{-\zeta r^2}} \qquad \textbf{(Equation 2.9)}$$

In both Equations 2.8 and 2.9, *N* represents the normalization factor. *n*, *l*, and *m* represent the principle, angular, and magnetic quantum numbers respectively. $Y_{l,m}(\theta,\varphi)$ represents the spherical harmonic. ζ represents the Slater/Gaussian orbital exponent, and *r* represents the distance between the electron and atom center. In general, STOs provide a more accurate description of molecular orbitals, such as the decay behaviors; however, GTOs are easier to solve analytically compared with STOs because of their formula.

For systems with periodic symmetry, all cell-periodic functions are expanded in plane waves. The principal idea is to assume the system is being placed in a unit cell defined by unit vectors $\vec{a}_1, \vec{a}_2$ and $\vec{a}_3$. (The volume of the unit cell can be written as: $\Omega = [\vec{a}_1, \vec{a}_2, \vec{a}_3]$). The plane wave basis expansion can be written as $u_n(\vec{r}) = \frac{1}{\sqrt{\Omega}}\sum_{\vec{G}} e^{i\vec{G}\cdot\vec{r}}$, where $\vec{G}$ represents a wave vector,

and $e^{i\vec{G}\cdot\vec{r}}$ is a plane wave. Because of periodicity, plane wave basis sets are widely used in solid-state physics calculations.[13]

In this dissertation, for Chapters 3, 4, and 5, we employed the LANL2DZ basis set in the Gaussian package, which is a double zeta (dz, means the valence orbitals are described by two basis functions) basis set developed at Los Alamos National Laboratory (LANL).[14,15] For Chapter 6 and 7, the main quantum chemistry calculations are performed using the ADF software,[16] and ADF utilizes STO basis sets. For Chapter 8, we employed the VASP[17–19] software in the DFT calculation parts; VASP utilizes plane-wave basis sets.

2.4 Time-dependent density functional theory (TDDFT)

To examine time-dependent properties, Runge and Gross extended DFT by incorporating a time-dependent external potential into the Hohenberg-Kohn DFT formalism.[20] In that way, the Kohn-Sham equation can be written as in Equation 2.10:

$$\left[-\frac{1}{2}\nabla^2 + \boldsymbol{V_{ext}}(\mathbf{r},t) + \int \boldsymbol{v}(\mathbf{r},\mathbf{r}')\boldsymbol{\rho}(\mathbf{r}',t)d\mathbf{r}' + \boldsymbol{V_{xc}}([\boldsymbol{\rho}],\mathbf{r},t)\right]\boldsymbol{\phi_i}(\mathbf{r},t) = \boldsymbol{i}\frac{\partial}{\partial t}\boldsymbol{\phi_i}(\mathbf{r},t)$$

(Equation 2.10)

where $V_{ext}(\mathbf{r},t)$ denotes the external potential term, $\int v(\mathbf{r},\mathbf{r}')\rho(\mathbf{r}',t)d\mathbf{r}'$ denotes the electron-electron repulsion term, and $V_{xc}([\rho],\mathbf{r},t)$ denotes the exchange correlation potential. As we can see from the equation, $V_{xc}([\rho],\mathbf{r},t)$ depends on the density for all times. Analogous to the Kohn-Sham equation when we are solving the energy of the system in the ground state, the exact time-dependent exchange-correlation in the equation is still unknown, which leads to difficulty in solving the exact solution for the TDDFT problem.[21]

An external potential affects the density, which can be written as in Equation 2.11:

$$\boldsymbol{\rho}(\boldsymbol{r},\boldsymbol{t}) = \boldsymbol{\rho_0}(\boldsymbol{r}) + \boldsymbol{\delta\rho}(\boldsymbol{r},\boldsymbol{t}) \quad \textbf{(Equation 2.11)}$$

where $\rho_0(r)$ is the reference density and can be considered to be the initial density without an external perturbation (where the total potential can be defined as v_0). $\delta\rho(r,t)$ can be considered as the density variation with respect to the external perturbation (where the external potential can be defined as v_1), and $v = v_0 + v_1$ represents the total potential of the system after the perturbation is applied. The density can be written as a Taylor expansion form in equation 2.12:

$$\boldsymbol{\rho[v](r,t) = \rho[v_0 + v_1](r,t)}$$
$$\boldsymbol{= \rho[v_0](r,t)}$$
$$\boldsymbol{+ \int \left.\frac{\delta\rho[v](r,t)}{\delta v(r',t')}\right|_{v_0} v_1(r',t')\mathrm{d}^3r'\mathrm{d}t'}$$
$$\boldsymbol{+ \frac{1}{2}\iint \left.\frac{\delta^2\rho[\mathrm{v}](\mathrm{rt})}{\delta v(\mathrm{r}',\mathrm{t}')\delta v(\mathrm{r}'',\mathrm{t}'')}\right|_{v} v_1(r',t')v_1(r'',t'')\mathrm{d}^3r\mathrm{d}^3r''\mathrm{d}t'\mathrm{d}t''} \quad \textbf{(Equation 2.12)}$$

From the equation, the second term is the linear density response of the interacting system, and $\chi_{\mathrm{s}(r,t,r',t')} = \left.\frac{\delta\rho[v](r,t)}{\delta v(r',t')}\right|_{V_0[\rho_0]}$ is defined as the density-density response function of interacting system.

Although it is challenging to solve the exact solution for the TDDFT equation, in practice the problem of finding the excited state energies can be solved by calculating poles in the response of the ground state density to an external field. This leads to the linear response equations. The linear response equations can be transformed into a matrix formula, which is also known as the Casida equations.[22] The Casida equations will be discussed in more detail in next subsection.

2.4.1 Linear-response TDDFT (LR-TDDFT)

The Casida equations can be applied to solve the linear formalism of TDDFT,[22,23] which can be written as Equation 2.13:

$$\begin{pmatrix} \mathbf{A} & \mathbf{B} \\ \mathbf{B}^* & \mathbf{A} \end{pmatrix}\begin{pmatrix} \mathbf{X} \\ \mathbf{Y} \end{pmatrix} = \boldsymbol{\omega}\begin{pmatrix} \mathbf{1} & \mathbf{0} \\ \mathbf{0} & \mathbf{-1} \end{pmatrix}\begin{pmatrix} \mathbf{X} \\ \mathbf{Y} \end{pmatrix} \quad \textbf{(Equation 2.13)}$$

where **A** and **B** represent rotational Hessian matrices, ω represents excitation energy, and **X** and **Y** are eigenvectors that correspond to the excitation and deexcitation respectively. The linear Casida equation (2.13) can be transformed into the formalism of $\boldsymbol{\Omega\mathbf{F} = \omega^2\mathbf{F}}$, where $\mathbf{F} = (\mathbf{A} - \mathbf{B})^{-\frac{1}{2}}(\mathbf{X} + \mathbf{Y})$ and $\boldsymbol{\Omega} = (\mathbf{A} - \mathbf{B})^{\frac{1}{2}}(\mathbf{A} + \mathbf{B})(\mathbf{A} - \mathbf{B})^{\frac{1}{2}}$.[23] To solve the equation, $\mathbf{A} + \mathbf{B}$ and $\mathbf{A} - \mathbf{B}$ need to be calculated, and the matrices have the following formulas:

$$\boldsymbol{A_{ia,jb} + B_{ia,jb} = \delta_{ab}\delta_{ij}(\epsilon_a - \epsilon_i) + 2(ia \mid jb) + 2(ia|f_{xc}|jb) - a_x((ij \mid ab) + (ib \mid ja))}$$
(Equation 2.14)

$$\boldsymbol{A_{ia,jb} - B_{ia,jb} = \delta_{ab}\delta_{ij}(\epsilon_a - \epsilon_i) - a_x((ij \mid ab) - (ib \mid ja))} \quad \textbf{(Equation 2.15)}$$

where *i, j* represent occupied orbitals and *a, b* represent virtual orbitals; $(\epsilon_a - \epsilon_i)$ represents the orbital energy difference between orbital index *i and a;* a_x is the amount of Hartree-Fock exchange; and $(ia \mid jb)$ and $(ia|f_{xc}|jb)$ are the usual two-electron integrals.

2.4.2 Real-time TDDFT (RT-TDDFT)

The linear-response formalism can be applied to calculate photo-absorption spectra. However, the LR-TDDFT method is not applicable if we want to investigate the properties of a system beyond a linear response regime, such as when strong electric fields are applied to a system. Therefore, it is important to introduce the real-time TDDFT (RT-TDDFT) technique. The basic principle behind RT-TDDFT is to propagate the density matrix ($\boldsymbol{P}(t)$) numerically with time. In that way, the TDDFT equation can be written in the following formula:[24,25]

$$\boldsymbol{i}\frac{\boldsymbol{dP(t)}}{\boldsymbol{dt}} = [\boldsymbol{H(t)}, \boldsymbol{P(t)}] \qquad \textbf{(Equation 2.16)}$$

where $\boldsymbol{H}(t)$ is the matrix form of the time-dependent Kohn-Sham operator. Density matrix elements can be expanded using $P_{\mu\nu}(t) = \sum_i c^*_{\mu i}(t)c_{vi}(t)$, where $c_{\mu i}(t)$ represents the time-dependent expansion coefficients of molecular orbital i on the μ'th basis function ϕ_μ, such that molecular orbital $\varphi_i = \sum_\mu c_\mu(t)\phi_\mu$.

In this dissertation, we employed the real-time TDDFT algorithm developed by Prof. Xiaosong Li's group,[24] in which $\boldsymbol{H}(t)$ can be written as $\boldsymbol{H}(t) = \boldsymbol{E}(t) \cdot \boldsymbol{\mu}$, where $\boldsymbol{\mu}$ is the dipole moment.

2.5 Time-dependent density functional theory related approximation methods

As the size of the system increases, the computational time and memory increase significantly for TDDFT. To reduce the computational cost, some approximation methods to TDDFT have been proposed, such as TD-DFTB,[26,27] sTDDFT,[28] sTDA,[29,30] TDDFT+TB,[31] TDDFT-as (TDDFT for auxiliary basis function s),[32] and TDDFT-ris.[33] These approximation methods share similarities but also show differences, and we can classify them by starting the approximations from ground-state calculations (such as TD-DFTB) or starting the approximations from excited-state calculations (such as TDDFT+TB), as shown in Figure 2.2. For example, TD-DFTB starts with semiempirical density functional tight-binding (DFTB) ground state

calculations, where trial densities are applied instead of using actual densities. The trial density is a superposition of atomic contributions and needs to be parameterized; in general, DFTB calculations incorporate many parameters that must be determined in advance for each pair of atoms[34,35]

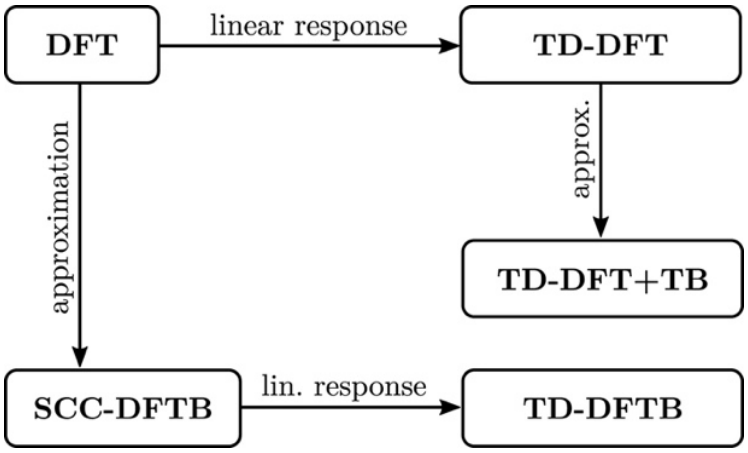


Figure 2.2 Relationships among several different computational methods. Reprinted with permission from *J. Chem. Phys* 144, 184103 (2016) of AIP Publishing

To avoid the need for extensive parameterization, several recent methods have combined aspects of DFT and DFTB. For sTDA and sTDDFT, standard DFT is employed for the ground state calculations. Therefore, an approximation is only used in the excited state calculation. The related TDDFT+TB method is motivated by sTDA and sTDDFT; it also uses standard DFT for the ground state calculations. For the excited-state calculations, both TD-DFTB and TDDFT+TB use the K coupling matrix, although Löwdin population analysis is used to calculate the q.

2.6 Nonadiabatic dynamics

Born-Oppenheimer molecular dynamics (BOMD) is a type of molecular dynamics in which we can treat the electronic and nuclear degrees of freedom separately, based on the statement in the Born-Oppenheimer approximation that nuclei move slower than electrons. In this way, for molecular dynamics of a chemical system, the nuclear motions can be treated classically whereas electron motions can be treated quantum mechanically. Therefore, BOMD neglects coupling between electronic states and nuclear motion.[36]

BOMD has shown its success in molecular dynamics for many ground-state chemistry problems, such as simulations at room temperature. However, if we want to study some processes such as charge carrier dynamics, excitation energy transfer, or vibrational excitation energy

relaxation, a quantum-mechanical description is required that goes beyond the common Born-Oppenheimer approximations and accurately accounts for nonadiabatic effects. A schematic illustration of the weak and strong nonadiabatic coupling is shown in Figure 2.3.

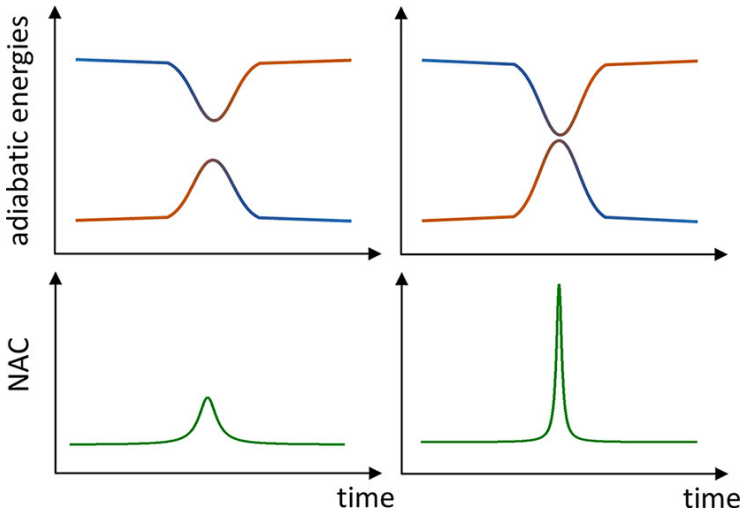


Figure 2.3 Schematic illustration of the adiabatic energies and nonadiabatic couplings (NAC) as a function of time. In a weak-coupling region (left **side), the width of the nonadiabatic coupling peak may be of the same order of the integration time step, ~0.5 fs. Reprinted with permission from Chem. Rev. 2018, 118, 15, 7026-7068. Copyright 2018, American Chemical Society**

Currently, there are several types of nonadiabatic dynamics. Mean-field Ehrenfest dynamics, trajectory surface hopping, multiple spawning method and exact factorization are some of the most extensively used techniques.[37–39] In this dissertation, we employed the mean-field Ehrenfest dynamics methods approach developed by Xiaosong Li's group,[40–42] where the method is a "mixed quantum-classical" method, which propagates the classical nuclei on a superposition of electronic states. A schematic picture of mean-field Ehrenfest dynamics in shown in Figure 2.4.

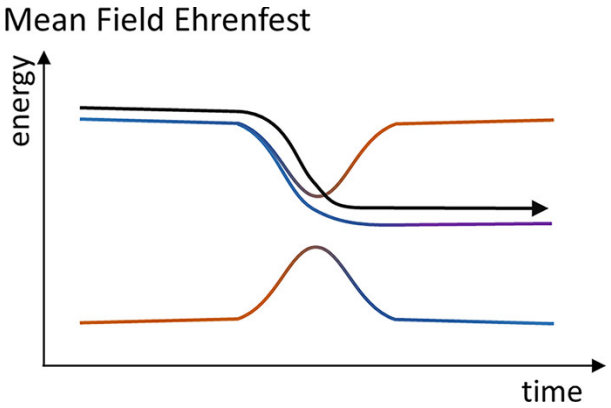
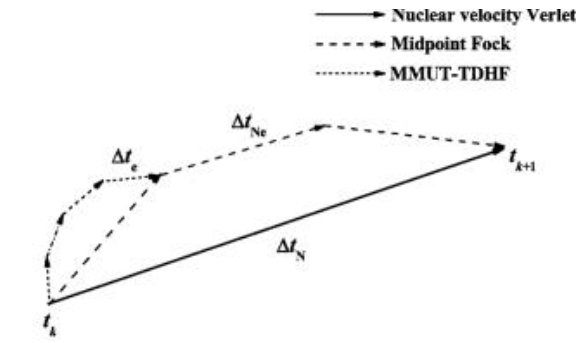


Figure 2.4 Schematic illustration of the mean field Ehrenfest dynamics. The trajectory is run on a surface averaged over all electronic states weighted by their respective electronic population. Reprinted with permission from Chem. Rev. 2018, 118, 15, 7026-7068. **Copyright 2018, American Chemical Society**

As shown in Figure 2.4, in mean-field Ehrenfest the system is propagated by solving a quantum equation of motion for the classical coordinates with the average force calculated by weighing all electronic states according to their electronic populations. For the mean-field Ehrenfest codes we utilized in this dissertation, a three-step technique is employed (Figure 2.5).



$\Delta t_{Ne} = \Delta t_N / n$, $\Delta t_e = \Delta t_{Ne} / m$

Do k
  $t_k = t_{k-1} + \Delta t_N$
  Calculate $g(t_k)$ at $x(t_k)$ [eq. 13]
  Calculate $p(t_{k+1/2})$ and $x(t_{k+1})$ [eq. 10, 11]
  Do j = 1, n
    $t' = t_k + (j-1)\,\Delta t_{Ne}$
    $\mathbf{x}(t' + \frac{1}{2}\Delta t_{Ne}) = \mathbf{x}(t_k) + (t' + \frac{1}{2}\Delta t_{Ne})\,p(t_{k+1/2})/M$
    Calculate $\mathbf{h}'$, $(\mu\nu||\lambda\sigma)$, $\mathbf{S}$ and $\mathbf{V} = \mathbf{S}^{1/2}$
    Do i = 1, m
      $\tau = t' + (i-1)\,\Delta t_e$
      $\mathbf{P}'(\tau) = \mathbf{V}^{-1}\,\mathbf{P}(\tau)\,\mathbf{V}^{-T}$
      Form $\mathbf{F}'(\tau)$ using $\mathbf{P}'(\tau)$ and the current integrals
      $\mathbf{F}(\tau) = \mathbf{V}^{-1}\,\mathbf{F}'(\tau)\,\mathbf{V}^{-T}$, $\mathbf{U} = \exp(i\,2\,\Delta t_e\,\mathbf{F}(\tau))$
      $\mathbf{P}(\tau+\Delta t_e) = \mathbf{U}\,\mathbf{P}(\tau-\Delta t_e)\,\mathbf{U}^{T}$
      End Do
    End Do
  End Do

Figure 2.5 Three-time-scale integration scheme for Ehrenfest dynamics. Reprinted with permission from *J. Chem. Phys* 123, 084106 (2005) of AIP Publishing

STEP 1. Each nuclear Verlet step (Δt_N) is divided into n smaller Δt_{Ne} steps;

STEP 2. The Fock matrix is calculated based on the integrals calculated at the midpoint of Δt_{Ne} and the density at this time step;

STEP 3. The density is propagated using the MMUT-TDHF (modified midpoint and unitary transformation-time-dependent Hartree-Fock) method using steps of Δt_e.

This Ehrenfest dynamics strategy demonstrates a reasonable computational cost and can account for nonadiabatic electronic excitations within superposition states.

2.7 Solvent models

Since many chemical reactions and process procced in solvent, it is important to have appropriate solvent model for computational modeling as well. In this section, I will summarize the solvent models involved in this dissertation. In general, solvent models can be classified into

three categories: (1) polarizable continuum model (PCM), (2) molecular mechanics (MM) solvent model, and (3) quantum mechanics (QM) solvent model.

PCM is also known as an implicit model. The principal idea of the implicit model is to consider the solvent as a continuum medium. Therefore, a dielectric constant will be applied to the system when using the PCM model. PCM can be applied to describe a non-equilibrium state, such as the Frank-Condon (vertical) excited state where the nuclei are frozen upon excitation; PCM has successfully been applied to investigate the solvent effect on the TDDFT absorption spectra (Figure 2.6) of the $Au_{25}(SH)_{18}^-$ nanocluster.[43] However, in general the structure of the solvent molecules is missing in the PCM model and the model fails to describe the interactions between the system and solvent molecules.

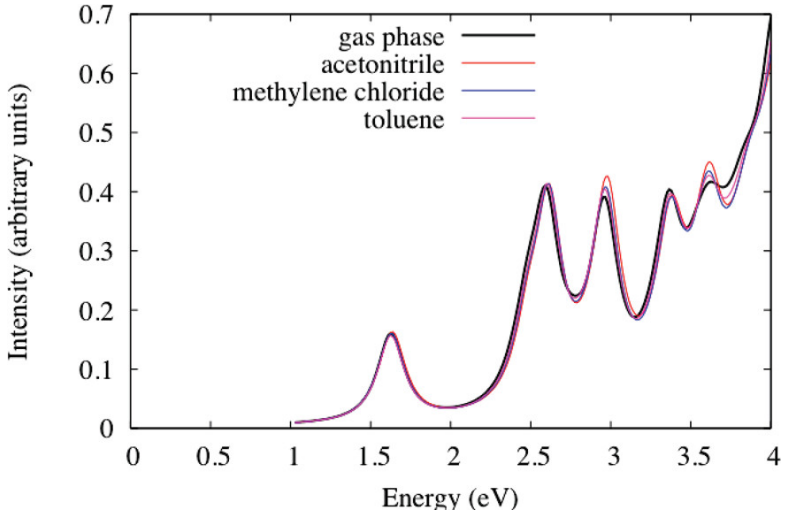


Figure 2.6 Calculated optical absorption spectrum in gas phase and in implicit solvent for $Au_{25}(SH)_{18}^-$. Reprinted with permission from *J. Phys. Chem. A* 2009, 113, 40, 10811–10817. Copyright 2009 American Chemical Society

Compared to the PCM model, the QM model includes explicit solvent molecules in the ensemble when modeling the system. A visualized comparison between implicit and explicit solvent model is shown in Figure 2.7.[44] For both the implicit model and explicit model, the excited state shows the same character for the alizarin molecule. Meanwhile, one can observe that fractions of the electron densities are delocalized onto the solvent molecules when using the explicit solvent model. Therefore, explicit solvent can better describe interactions such as electron transfer or energy transfer between the solvent and system.

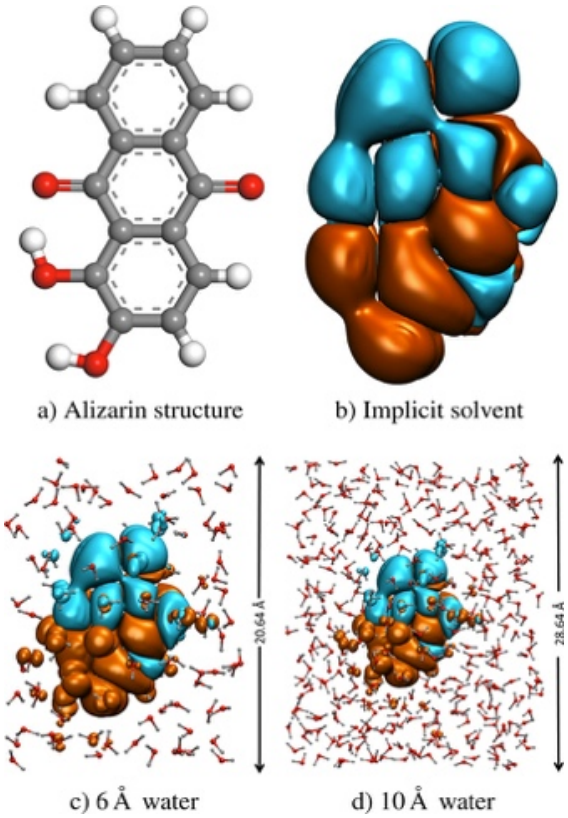


Figure 2.7 A. Structure of alizarin. The electron–hole difference density plot of the lowest dipole-allowed transition of a single MD frame (frame 5) of alizarin, as calculated in B. implicit solvent; C. in 6 Å of explicit water; D. in 10 Å of explicit water. The hole density is displayed in orange, while the electron density is shown in cyan. Reprinted with permission from *J. Chem. Theory Comput.* 2016, 12, 4, 1853–1861. Copyright 2016 American Chemical Society

Overall, there is always a trade-off in choosing a reasonable solvent model, depending on which kind of scientific question we want to solve. In the chapter 7 of this dissertation, I have employed both the implicit solvent model and the explicit solvent model to study the solvent effect on the physical and chemical properties of noble metal nanoclusters.

2.8 Machine learning models

The above-mentioned techniques are all related to quantum chemistry methods. In this dissertation, I also applied a machine learning model to explore the potential of accelerating the calculation (chapter 8). Different machine learning models will match well with different specific

systems or solving different scientific problems. Currently, machine learning has been successfully applied in many fields in chemistry. [45–47]

In this dissertation, the machine learning model employed is the Gaussian process regression (GPR) model, specifically, the sparse Gaussian process (SGP) model, where only novel atomic environments will be added into the training data set. SGP thus largely reduces the computational cost. A schematic workflow is shown in Figure 2.8, where the Gaussian process can be generally classified into three steps: observation, choosing basis function and estimation. [48]

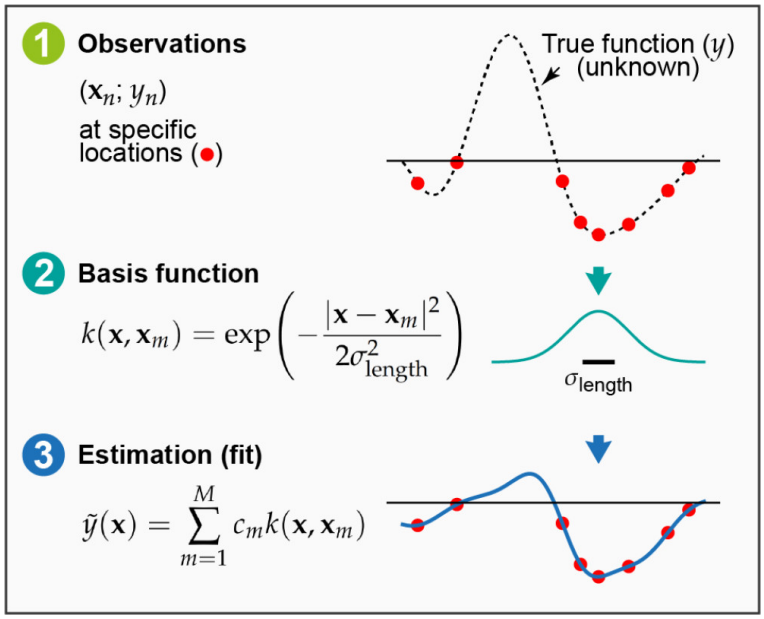


Figure 2.8 Basic elements of GPR as discussed in the present section: (1) observations of an unknown function at a number of locations; (2) basis functions (only one of them shown for clarity), centered at the data locations; (3) an estimation $\tilde{y}$ defined by the set of coefficients, c_m, and the corresponding basis functions; $\tilde{y}$ is the prediction of the GPR model. Reprinted with permission from *Chem. Rev.* 2021, 121, 16, 10073–10141 Copyright 2021 The Authors. Published by American Chemical Society. This publication is licensed under CC-BY 4.0.

The first step is to make the observations. For example, for a chemical system, if our goal is to correlate the structure-property relationships, we need to know the information about the structure (x_i) and (y_i) and integrate this datapoint (x_i, y_i) into the training database (labeled as index i). In the second step, a type of basis function (kernel function) needs to be chosen; the basis function should have a Gaussian type of distribution function with the data point located at the peak of the function. In the third step, a linear combination of the basis functions will be applied to fit the output y. In summary, the training process is intended to optimize the kernel function k.

Machine learning models can be generally divided into two main categories: supervised learning models and unsupervised learning models. In a supervised learning model, all the data are labeled. The user trains a model using labeled training data sets and teaches the model to yield certain output directly or through some kernel space. However, one big challenge for the current supervised learning strategy is the redundant work of creating a training database and labeling data points. In that way, active learning (also known as on-the-fly learning), which is a type of semi-supervised learning, provides new insights that make the training and database generation process work simultaneously.

In brief, the active learning strategy will identify the most valuable data points for collection and labeling, allowing us to train more efficiently. A workflow for the active Gaussian learning process is shown in Figure 2.9.[49] At the beginning, we need a starting geometry as input to perform a DFT calculation. Then, mapped Gaussian processes were applied to construct a Bayesian force field, and predicted variance was calculated to quantify the uncertainty of the force fields. If the uncertainty is lower than the tolerance value, the algorithm will proceed to the MD simulations section using the current trained force fields. Normally, DFT calculations will be frequently called in the beginning steps of the simulations, and DFT will be called infrequently when a relatively stable force field has been obtained.

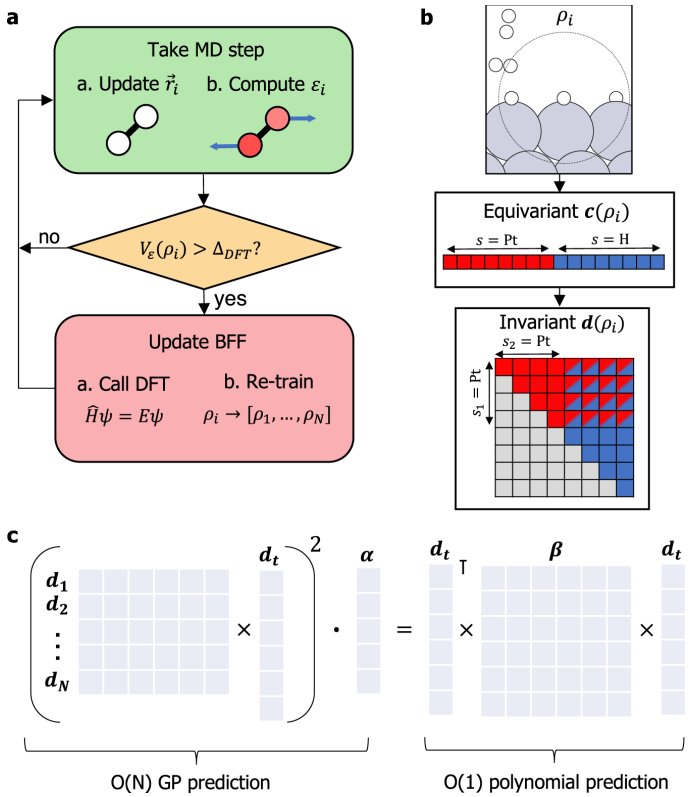


Figure 2.9 a. At each time-step of the MD simulation, local energies, forces, and stresses are computed with the SGP model. If the uncertainty on a local energy exceeds the chosen threshold Δ_{DFT}, a DFT calculation is performed, and the model is updated. b. Mapping of local environments ρ_i onto multielement descriptors derived from the atomic cluster expansion. The environment is first mapped onto an equivariant descriptor c_i, products of which are used to compute the rotationally invariant descriptor d_i that serves as an input to the model. C. Mapping of a $\xi = 2$ SGP force field onto an equivalent quadratic model. The prediction cost of the SGP scales linearly with the number of sparse environments N_S, while the cost of the corresponding polynomial model is independent of N_S. Reprinted with permission from *Nat Commun* 13, 5183 (2022) *Copyright 2022 by the Authors,* this is an open access article distributed under the terms of the Creative Commons CC BY license.

2.9 References

(1) Kurth, S.; Perdew, J. P. Role of the Exchange-Correlation Energy: Nature's Glue. *Int. J. Quant. Chem.* **2000**, *77* (5), 814–818.

(2) Born, M.; Oppenheimer, R. Zur Quantentheorie Der Molekeln. *Annalen der Physik* **1927**, *389* (20), 457–484.

(3) Hohenberg, P.; Kohn, W. Inhomogeneous Electron Gas. *Phys. Rev.* **1964**, *136* (3B), B864–B871.

(4) Kohn, W.; Sham, L. J. Self-Consistent Equations Including Exchange and Correlation Effects. *Phys. Rev.* **1965**, *140* (4A), A1133–A1138.

(5) Perdew, J. P.; Chevary, J. A.; Vosko, S. H.; Jackson, K. A.; Pederson, M. R.; Singh, D. J.; Fiolhais, C. Atoms, Molecules, Solids, and Surfaces: Applications of the Generalized Gradient Approximation for Exchange and Correlation. *Phys. Rev. B* **1992**, *46* (11), 6671–6687.

(6) Langreth, D. C.; Mehl, M. J. Beyond the Local-Density Approximation in Calculations of Ground-State Electronic Properties. *Phys. Rev. B* **1983**, *28* (4), 1809–1834.

(7) Becke, A. D. Density-Functional Exchange-Energy Approximation with Correct Asymptotic Behavior. *Phys. Rev. A* **1988**, *38* (6), 3098–3100.

(8) Arbuznikov, A. V. Hybrid Exchange Correlation Functionals and Potentials: Concept Elaboration. *J Struct Chem* **2007**, *48* (S1), S1–S31.

(9) Rohrdanz, M. A.; Martins, K. M.; Herbert, J. M. A Long-Range-Corrected Density Functional That Performs Well for Both Ground-State Properties and Time-Dependent Density Functional Theory Excitation Energies, Including Charge-Transfer Excited States. *J. Chem. Phys* **2009**, *130* (5), 054112.

(10) Grimme, S.; Antony, J.; Ehrlich, S.; Krieg, H. A Consistent and Accurate *Ab Initio* Parametrization of Density Functional Dispersion Correction (DFT-D) for the 94 Elements H-Pu. *J. Chem. Phys* **2010**, *132* (15), 154104.

(11) Perdew, J. P. Density-Functional Approximation for the Correlation Energy of the Inhomogeneous Electron Gas. *Phys. Rev. B* **1986**, *33* (12), 8822–8824.

(12) Davidson, E. R.; Feller, D. Basis Set Selection for Molecular Calculations. *Chem. Rev.* **1986**, *86* (4), 681–696.

(13) Monkhorst, H. J.; Pack, J. D. Special Points for Brillouin-Zone Integrations. *Phys. Rev. B* **1976**, *13* (12), 5188–5192.

(14) Wadt, W. R.; Hay, P. J. *Ab Initio* Effective Core Potentials for Molecular Calculations. Potentials for Main Group Elements Na to Bi. *J. Chem. Phys* **1985**, *82* (1), 284–298.

(15) Hay, P. J.; Wadt, W. R. *Ab Initio* Effective Core Potentials for Molecular Calculations. Potentials for the Transition Metal Atoms Sc to Hg. *J. Chem. Phys* **1985**, *82* (1), 270–283.

(16) te Velde, G.; Bickelhaupt, F. M.; Baerends, E. J.; Fonseca Guerra, C.; van Gisbergen, S. J. A.; Snijders, J. G.; Ziegler, T. Chemistry with ADF. *J. Comput. Chem.* **2001**, *22* (9), 931–967.

(17) Kresse, G.; Hafner, J. *Ab Initio* Molecular Dynamics for Liquid Metals. *Phys. Rev. B* **1993**, *47* (1), 558–561.

(18) Kresse, G.; Furthmüller, J. Efficiency of Ab-Initio Total Energy Calculations for Metals and Semiconductors Using a Plane-Wave Basis Set. *Computational Materials Science* **1996**, *6* (1), 15–50.

(19) Kresse, G.; Furthmüller, J. Efficient Iterative Schemes for *Ab Initio* Total-Energy Calculations Using a Plane-Wave Basis Set. *Phys. Rev. B* **1996**, *54* (16), 11169–11186.

(20) Runge, E.; Gross, E. K. U. Density-Functional Theory for Time-Dependent Systems. *Phys. Rev. Lett.* **1984**, *52* (12), 997–1000.

(21) Van Leeuwen, R. Key Concepts in Time-Dependent Density-Functional Theory. *Int. J. Mod. Phys. B* **2001**, *15* (14), 1969–2023.

(22) Casida, M. E.; Huix-Rotllant, M. Progress in Time-Dependent Density-Functional Theory. *Annu. Rev. Phys. Chem.* **2012**, *63* (1), 287–323.

(23) Casida, M. E. Time-Dependent Density Functional Response Theory for Molecules. In *Recent Advances in Computational Chemistry*; World Scientific, 1995; Vol. 1, pp 155–192.

(24) Goings, J. J.; Lestrange, P. J.; Li, X. Real-time Time-dependent Electronic Structure Theory. *WIREs Comput Mol Sci* **2018**, *8* (1), e1341.

(25) Yabana, K.; Nakatsukasa, T.; Iwata, J. -I.; Bertsch, G. F. Real-time, Real-space Implementation of the Linear Response Time-dependent Density-functional Theory. *Physica Status Solidi (b)* **2006**, *243* (5), 1121–1138.

(26) Niehaus, T. A.; Suhai, S.; Della Sala, F.; Lugli, P.; Elstner, M.; Seifert, G.; Frauenheim, Th. Tight-Binding Approach to Time-Dependent Density-Functional Response Theory. *Phys. Rev. B* **2001**, *63* (8), 085108.

(27) Trani, F.; Scalmani, G.; Zheng, G.; Carnimeo, I.; Frisch, M. J.; Barone, V. Time-Dependent Density Functional Tight Binding: New Formulation and Benchmark of Excited States. *J. Chem. Theory Comput.* **2011**, *7* (10), 3304–3313.

(28) Bannwarth, C.; Grimme, S. A Simplified Time-Dependent Density Functional Theory Approach for Electronic Ultraviolet and Circular Dichroism Spectra of Very Large Molecules. *Computational and Theoretical Chemistry* **2014**, *1040–1041*, 45–53.

(29) Grimme, S. A Simplified Tamm-Dancoff Density Functional Approach for the Electronic Excitation Spectra of Very Large Molecules. *J. Chem. Phys* **2013**, *138* (24), 244104.

(30) Risthaus, T.; Hansen, A.; Grimme, S. Excited States Using the Simplified Tamm–Dancoff-Approach for Range-Separated Hybrid Density Functionals: Development and Application. *Phys. Chem. Chem. Phys.* **2014**, *16* (28), 14408–14419.

(31) Rüger, R.; Van Lenthe, E.; Heine, T.; Visscher, L. Tight-Binding Approximations to Time-Dependent Density Functional Theory — A Fast Approach for the Calculation of Electronically Excited States. *J. Chem. Phys* **2016**, *144* (18), 184103.

(32) Giannone, G.; Della Sala, F. Minimal Auxiliary Basis Set for Time-Dependent Density Functional Theory and Comparison with Tight-Binding Approximations: Application to Silver Nanoparticles. *J. Chem. Phys* **2020**, *153* (8), 084110.

(33) Zhou, Z.; Della Sala, F.; Parker, S. M. Minimal Auxiliary Basis Set Approach for the Electronic Excitation Spectra of Organic Molecules. *J. Phys. Chem. Lett.* **2023**, *14* (7), 1968–1976.

(34) Porezag, D.; Frauenheim, Th.; Köhler, Th.; Seifert, G.; Kaschner, R. Construction of Tight-Binding-like Potentials on the Basis of Density-Functional Theory: Application to Carbon. *Phys. Rev. B* **1995**, *51* (19), 12947–12957.

(35) Seifert, G.; Porezag, D.; Frauenheim, Th. Calculations of Molecules, Clusters, and Solids with a Simplified LCAO-DFT-LDA Scheme. *Int. J. Quantum Chem.* **1996**, *58* (2), 185–192.

(36) Tully, J. C. Perspective on "Zur Quantentheorie Der Molekeln." *Theoretical Chemistry Accounts: Theory, Computation, and Modeling (Theoretica Chimica Acta)* **2000**, *103* (3–4), 173–176.

(37) Agostini, F.; Curchod, B. F. E. Different Flavors of Nonadiabatic Molecular Dynamics. *WIREs Comput Mol Sci* **2019**, *9* (5), e1417.

(38) Crespo-Otero, R.; Barbatti, M. Recent Advances and Perspectives on Nonadiabatic Mixed Quantum–Classical Dynamics. *Chem. Rev.* **2018**, *118* (15), 7026–7068.

(39) Nelson, T. R.; White, A. J.; Bjorgaard, J. A.; Sifain, A. E.; Zhang, Y.; Nebgen, B.; Fernandez-Alberti, S.; Mozyrsky, D.; Roitberg, A. E.; Tretiak, S. Non-Adiabatic Excited-State Molecular Dynamics: Theory and Applications for Modeling Photophysics in Extended Molecular Materials. *Chem. Rev.* **2020**, *120* (4), 2215–2287.

(40) Li, X.; Tully, J. C.; Schlegel, H. B.; Frisch, M. J. *Ab Initio* Ehrenfest Dynamics. *J. Chem. Phys* **2005**, *123* (8), 084106.

(41) Ding, F.; Van Kuiken, B. E.; Eichinger, B. E.; Li, X. An Efficient Method for Calculating Dynamical Hyperpolarizabilities Using Real-Time Time-Dependent Density Functional Theory. *J. Chem. Phys* **2013**, *138* (6), 064104.

(42) Li, X.; Smith, S. M.; Markevitch, A. N.; Romanov, D. A.; Levis, R. J.; Schlegel, H. B. A Time-Dependent Hartree–Fock Approach for Studying the Electronic Optical Response of Molecules in Intense Fields. *Phys. Chem. Chem. Phys.* **2005**, *7* (2), 233–239.

(43) Aikens, C. M. Effects of Core Distances, Solvent, Ligand, and Level of Theory on the TDDFT Optical Absorption Spectrum of the Thiolate-Protected Au_{25} Nanoparticle. *J. Phys. Chem. A* **2009**, *113* (40), 10811–10817.

(44) Zuehlsdorff, T. J.; Haynes, P. D.; Hanke, F.; Payne, M. C.; Hine, N. D. M. Solvent Effects on Electronic Excitations of an Organic Chromophore. *J. Chem. Theory Comput.* **2016**, *12* (4), 1853–1861.

(45) Xia, S.; Chen, E.; Zhang, Y. Integrated Molecular Modeling and Machine Learning for Drug Design. *J. Chem. Theory Comput.* **2023**, *19* (21), 7478–7495.

(46) Westermayr, J.; Marquetand, P. Machine Learning for Electronically Excited States of Molecules. *Chem. Rev.* **2021**, *121* (16), 9873–9926.

(47) Dral, P. O. Quantum Chemistry in the Age of Machine Learning. *J. Phys. Chem. Lett.* **2020**, *11* (6), 2336–2347.

(48) Deringer, V. L.; Bartók, A. P.; Bernstein, N.; Wilkins, D. M.; Ceriotti, M.; Csányi, G. Gaussian Process Regression for Materials and Molecules. *Chem. Rev.* **2021**, *121* (16), 10073–10141.

(49) Vandermause, J.; Xie, Y.; Lim, J. S.; Owen, C. J.; Kozinsky, B. Active Learning of Reactive Bayesian Force Fields Applied to Heterogeneous Catalysis Dynamics of H/Pt. *Nat Commun* **2022**, *13* (1), 5183.

Chapter 3 - Effects of field strength and silver nanowire size on plasmon-enhanced N_2 dissociation

Reprinted with permission from *J. Phys. Chem. A* 2023, 127, 27, 5609–5619. Copyright 2023 American Chemical Society

Yuchen Wang, Christine M. Aikens*

Department of Chemistry, Kansas State University, Manhattan, KS 66506, USA

*Email: cmaikens@ksu.edu; Phone: 1-785-532-0954

3.1 Abstract

Dissociation of the nitrogen molecule via plasmon-enhanced catalysis using noble metal nanoparticles has been investigated both experimentally and computationally in recent years. However, the mechanism of plasmon-enhanced nitrogen dissociation is still not very clear. In this work, we apply theoretical approaches to examine the dissociation of a nitrogen molecule on atomically-thin Ag_n nanowires (n = 6, 8, 10, 12) and a Ag_{19}^+ nanorod. Ehrenfest dynamics provides information about the motion of nuclei during the dynamics process and real-time TDDFT calculations show the electronic transitions and population of electrons over the first 10s of fs time scale. The activation and dissociation of nitrogen is typically enhanced when the electric field strength increases. However, the enhancement is not always monotonic with field strength. As the length of the Ag wire increases, nitrogen is typically easier to dissociate and thus requires lower field strengths, even though the plasmon frequency is lower. The Ag_{19}^+ nanorod leads to faster dissociation of N_2 than the atomically-thin nanowires. Overall, our detailed study yields insights into the mechanisms involved in plasmon-enhanced N_2 dissociation, as well as provides information about factors that can be used to improve adsorbate activation.

3.2 Introduction

The Haber-Bosch process is the primary method for NH_3 formation; however, the reaction needs high pressure and temperature to proceed.[1] The key step in the NH_3 formation reaction is the bond breaking of N_2. Because the nitrogen bond has a very strong bonding energy, it is very important to figure out a plausible way to catalyze N_2 activation or dissociation. The reactivity of N_2 activation was examined on different metal surfaces and clusters both experimentally and theoretically in recent years, including examining the properties of N_2 on various metal surfaces and applying different methods (i.e. electrochemical and photoelectrochemical reactions) to investigate N_2 reduction or oxidation.[2–10] Among those studies, the catalytic N_2 reaction can be divided into two groups: ground-state catalytic reactions and photocatalytic reactions. Compared with the ground-state catalytic pathway, photo-induced chemical reactions gained recent interest by providing new insights into the dissociation of nitrogen molecules in the excited states.[11–13] However, the reaction mechanism of the photocatalytic reaction will be more complicated because excited states are involved in the reaction pathway.[14]

Due to their broad application in the areas of molecular sensing,[15] biomedical research,[16] and photocatalysis,[17–19] noble metal nanoparticles (NPs) have been investigated intensively in recent years, and one of the unique properties of noble metal NPs is the localized surface plasmon resonance (LSPR).[20,21] When a gold or silver nanoparticle is present in an electromagnetic field with photon frequencies that are equal to a natural frequency of the valence electrons' collective oscillation, a strong peak will appear in the absorption spectrum. Different sizes of plasmonic nanoparticles have different plasmon frequencies and absorption intensities. For nanorods, the longitudinal plasmon resonance is particularly sensitive to the aspect ratio. In the area of small molecule reactions, plasmonic nanoparticles can be applied to drive plasmon-enhanced processes such as catalytic CO_2 reduction,[22–25] water splitting,[26–28] N_2 dissociation,[11,12,25,29] and the transformation of organic compounds.[30] From previous research, the LSPR process consists of detailed steps including plasmon dephasing (including Landau damping) (0 ~ 20 fs), electron-electron scattering (including hot carrier generation) (20 ~ 100 fs), electron-phonon coupling (100 fs ~ 1 ps), and coupling with the bath (thermalization) (1 ps ~ 10 ps).[31–36] Since these steps span a wide time scale, this causes difficulties in studying the mechanism of plasmon-driven catalytic reactions in detail. Various theoretical studies of plasmon-enhanced photochemical reactions have

been undertaken to unravel the mechanisms behind these processes. For example, plasmon-enhanced catalytic H_2 dissociation has been studied by using a jellium model as well as on atomically precise gold nanoclusters.[37,38] Compared with the dissociation of H_2, the dissociation of N_2 will be different due to its very strong bond energy.

Modeling atomically precise plasmonic nanoparticles can be computationally expensive due to their large size. As mentioned in the previous paragraph, one approach to overcoming this barrier is to use the jellium model approximation, which treats the nanoparticle as a single giant sphere with a constant electron density. While this approximation method can significantly reduce computational costs, it cannot be used to study the interaction between metal atoms and small molecules, as the nanoparticle lose precise atomic structure information. Another direction is to apply a small metal nanocluster with less computational cost to model the effects of plasmon-like resonances on photocatalytic processes. Previous examples include using a tetrahedral Au_{20} cluster to study plasmon-driven water splitting,[28] using a tetrahedral Ag_8 cluster to study excitation-induced oxygen activation,[39] and using planar triangular Au_6 cluster to study the photo-induced dissociation of H_2.[38] In the last two studies, although the clusters are too small to show plasmonic character, they exhibits certain degrees of similarity to plasmon-induced process. Treating the plasmon system using ultrasmall clusters will enable us to study the interaction between metal atoms and a small molecule by using atomically-precise models.

A variety of approaches have been reported to identify the plasmonic character of a system.[40–42] According to the configuration interaction (CI) treatment of plasmonic system,[40] a plasmon consists of a constructive superposition of single-particle transitions. Therefore, a plasmon can be considered as the mixing of N single-particle transitions represented by determinants. As the size of the nanoparticle decreases, fewer determinants contribute to the plasmon excitation. This makes the atomic-thickness nanowire a limiting case where N approaches 1. Several previous studies have effectively employed to study plasmon-enhanced photocatalysis on silver atomic wires. Meng and co-workers examined H_2 dissociation on resonantly and nonresonantly excited silver wires.[43] Hull and Aikens studied the electronic structure and nonadiabatic dynamics of N_2 coupled with Ag_n (n = 6, 8, 10) systems in 2020. N_2 molecule gained a greater degree of activation when the longitudinal excitation mode was excited compared to the charge-transfer and transverse excitation modes.[44] The same researchers then compared N_2 and H_2

activation/dissociation when these adsorbates interact with Ag_n systems.[45] The orientation of small molecules on the nanowire were compared and the parallel orientation was found to lead to a greater degree of charge transfer between the wire and the N_2 and H_2 molecules, which can aid the dissociation of the adsorbate.

However, for this specific system, questions remain. What is the threshold electric field strength needed to initiate nitrogen dissociation? Moreover, what are the relationships between the Ag nanowire length and its plasmon-enhanced catalytic properties. Therefore, in this work, Ag_6, Ag_8, Ag_{10}, and Ag_{12} linear wires are chosen to study the effect of the length of the silver wire on the plasmon-enhanced N_2 dissociation. Then, the Ag_{19} nanorod is considered to study the effect of changing the width of the system. At first, linear response TDDFT (LR-TDDFT) calculations are performed to get the plasmonic excitation energies of each system. Then, Ehrenfest nonadiabatic dynamics and fixed-nuclei real-time TDDFT (RT-TDDFT) calculations are applied to evaluate nuclear and electron motion of the Ag wire-N_2 system under the presence of the electromagnetic field. RT-TDDFT calculations can provide real-time dipole moments, orbital populations, and off-diagonal density matrix elements information at each time step. Ehrenfest dynamics is a type of excited state nonadiabatic nuclear-electron dynamics that can be applied to examine the motion of the nitrogen molecule after an external electric field is applied,[46,47] The method has already been applied to study the optical properties of gold and silver nanowires and nanoclusters.[48–50] In this way, the effect of electric field strength and the effect of Ag nanowire size on the plasmon-enhanced N_2 dissociation will be examined throughout the work.

3.3 Computational methods

All calculations were performed at the LC-ωPBE[51]/LanL2DZ[52–54] level of theory using a development version of the Gaussian software package.[55] The atomic silver nanowire-N_2 system is a simple model to study plasmon-enhanced processes; the atomic silver nanowires do not exist as global minima unless supported on a surface. For the ground state geometry optimization steps, the geometry of the Ag wire was initially optimized, and for the geometry optimization of the combined Ag wire-N_2 systems, Ag atoms were fixed while nitrogen atoms were relaxed. Then, LR-TDDFT calculations were performed to obtain the absorption spectra. For Ehrenfest dynamics,[46,47] an electric field is turned on at 0 fs and turned off at 20 fs. When applying an electric

field to the molecular system, the field is ramped up (first 1 fs) and then ramped down (final 1 fs) in strength with a trapezoidal envelope. The frequencies of the electric field are equivalent to the longitudinal excitation energies for each molecular system in order to simulate excitation at the longitudinal plasmon resonance. The electric field is polarized along the z-direction, which is parallel to the Ag wire. For the Ehrenfest dynamics, the electronic step size is 0.00025 fs and the nuclear step size is 0.1 fs, and the initial velocity of all the systems are set to zero. For the real-time RT-TDDFT calculations, the electronic step is set to be 0.002 fs.

3.4 Results and discussion

3.4.1 Binding energies analysis

Binding energies between Ag nanowires and the N_2 molecule were calculated in this work using Equation 1. Although there is a slight dependence of the binding energy on the nanowire length, the binding energy difference between $Ag_{12}N_2$ and Ag_6N_2 is just 1.3 kJ/mol, which indicates that the binding energy is not greatly affected by the Ag wire length (Table 3.1). The binding energy between Ag_6 and N_2 is found to be the lowest, while the binding energy between Ag_{12} and N_2 is the highest. The bond distance between the terminal silver atom and the closest nitrogen atom (denoted N1) is found to slightly decrease with increasing chain length, which corresponds with the increase in binding energy. Meanwhile, the bond distance between the two nitrogen atoms stays the same in all four molecular systems, which indicates that the N-N bond length (and corresponding N-N bond strength) is not affected by the Ag wire length in the ground state of these systems.

$$E_{binding} = E_{(Ag\ wire)} + E_{(N_2)} - E_{(AgN_2\ system)} \qquad \textbf{Equation 3.1}$$

Table 3.1 Ground state geometric information for the Ag_nN_2 (n = 6, 8, 10, 12) systems. The nitrogen atom that is closest to the wire is denoted N1, whereas the nitrogen atom that is the furthest from the Ag_n system is denoted N2.

	Binding Energy (kJ/mol)	Ag-N1 bond (Å)	N1-N2 bond (Å)
Ag_6N_2	29.9	2.486	1.119
Ag_8N_2	30.5	2.482	1.119
$Ag_{10}N_2$	30.9	2.479	1.119
$Ag_{12}N_2$	31.2	2.477	1.119

3.4.2 Molecular orbitals

Previous work on silver nanowires has demonstrated that silver *s* orbitals form molecular orbitals that are delocalized along the entire nanocluster.[40,44] For atomic wires, these orbitals can be described as Σ_n and Π_n orbitals, where the orbitals have sigma or pi character similar to σ and π orbitals, the capital letter denotes delocalized nanocluster orbitals, and the orbitals have n axial lobes (i.e. number of nodes + 1). As the length of the Ag nanowire increases, more electrons are involved in the molecular systems. Some differences in the orbitals can be noted in the four systems examined in this work (Figure 3.1). Addition of a N_2 molecule to a nanowire system does not greatly perturb the orbitals, so the Σ_n and Π_n description for silver-based orbitals is still useful. Nitrogen π* orbitals are located in the frontier region; these interact to a small degree with the Π_n orbitals. In this work, orbitals that primarily arise from the π* orbitals of nitrogen are denoted $\pi^*_{N_2}$, whereas the orbitals that primarily arise from silver are denoted as Π_n orbitals.

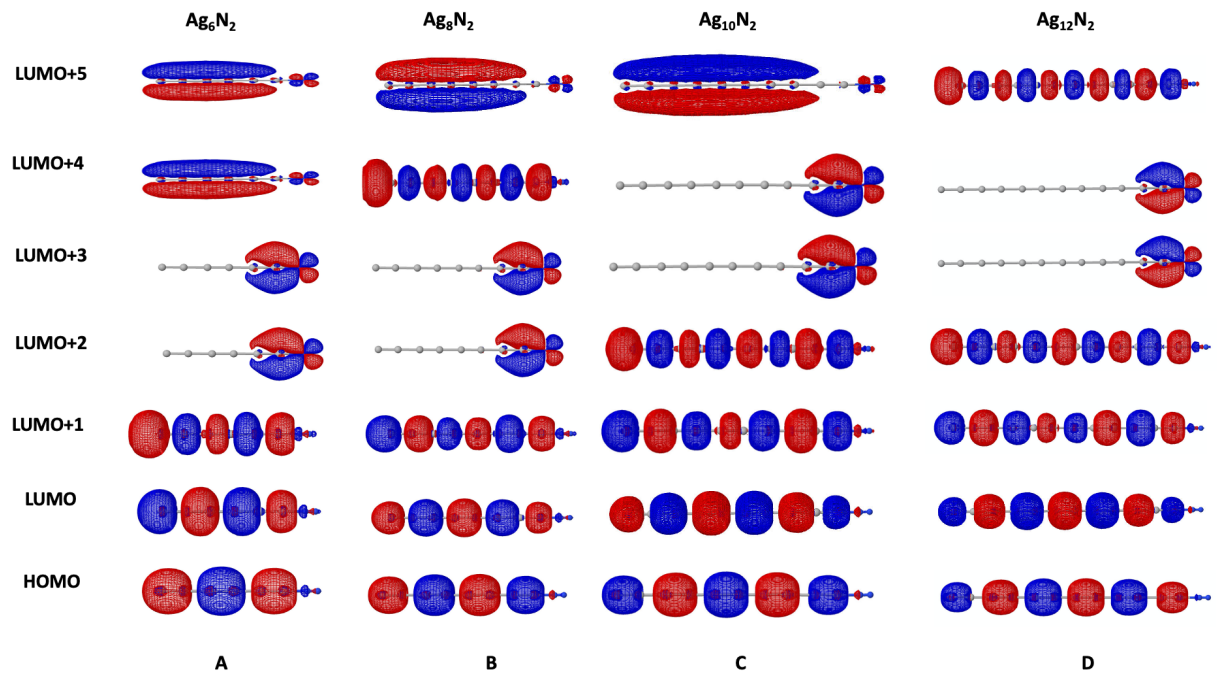


Figure 3.1 Selected molecular orbitals (from HOMO to LUMO+5) for A. Ag_6N_2; B. Ag_8N_2; C. $Ag_{10}N_2$; D. $Ag_{12}N_2$

For both Ag_6N_2 and Ag_8N_2, the LUMO+2 and LUMO+3 show doubly degenerate $\pi^*_{N_2}$ character, and the electron densities are localized on the two terminal Ag atoms and the N_2 molecule. For both $Ag_{10}N_2$ and $Ag_{12}N_2$, the LUMO+3 and LUMO+4 are the doubly degenerate $\pi^*_{N_2}$ orbitals, which show similarity with the LUMO+2/LUMO+3 in Ag_6N_2 and Ag_8N_2. The order of the orbitals also changes in these systems. For Ag_6N_2 and $Ag_{10}N_2$, no Σ_n orbitals are present between the $\pi^*_{N_2}$ and Π_n orbitals, whereas in Ag_8N_2 and $Ag_{12}N_2$, a Σ_n orbital is present between the $\pi^*_{N_2}$ and Π_n orbitals.

3.4.3 LR-TDDFT calculations

To examine the properties of Ag_nN_2 systems upon excitation, LR-TDDFT calculations were performed to obtain their linear response optical absorption spectra (Figure 3.2). From the absorption spectra, intense peaks are observed in two regions: one is around 1-2 eV (related to the longitudinal excitation mode), and the other is around 4-6 eV (related to the transverse mode).

For the longitudinal plasmon excitation, Ag_6N_2, Ag_8N_2, $Ag_{10}N_2$, and $Ag_{12}N_2$ show energies of 1.88 eV, 1.58 eV, 1.39 eV, and 1.26 eV respectively, which indicates that $Ag_{12}N_2$ has the lowest longitudinal plasmon energy and Ag_6N_2 has the highest longitudinal plasmon energy. In general, as the length of the nanowire increases, the longitudinal plasmon energies become lower. However, the oscillator strength of $Ag_{12}N_2$ is twice as intense as Ag_6N_2, which is consistent with previous optical spectra studies of silver nanorods.[56] Thus, this set of nanowire-N_2 systems provides an opportunity to examine whether the excitation energy or the intensity of the excitation is the more important factor for plasmon-enhanced photocatalysis; the longest system has the lowest plasmon energy but the highest oscillator strength.

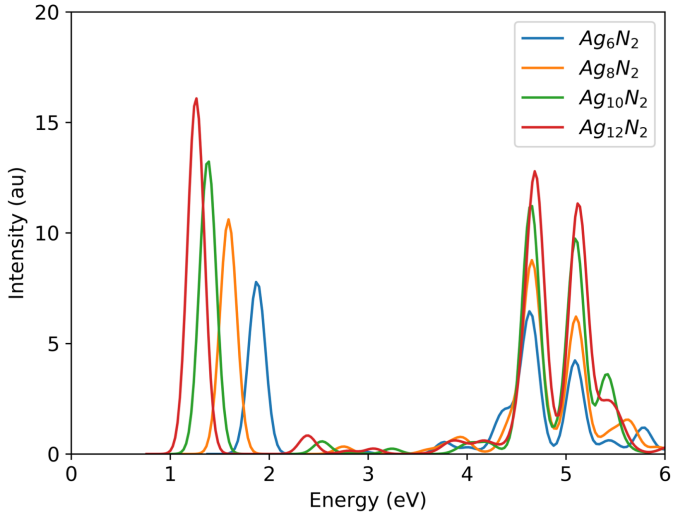


Figure 3.2 Linear response TDDFT absorption spectra for Ag_nN_2 (n = 6, 8, 10, 12) molecular systems

For Ag_6N_2 and Ag_8N_2 systems, the main electronic transitions for the longitudinal excitation mode are HOMO → LUMO and HOMO-1 → LUMO+1. For $Ag_{10}N_2$ and $Ag_{12}N_2$ molecular systems, the main electronic transitions for the longitudinal excitation mode are HOMO → LUMO, HOMO-1 → LUMO+1, and HOMO-2 → LUMO+2. All of these transitions are Σ → Σ type transitions, which demonstrates that the Σ → Σ transitions play the leading role in longitudinal excitations in nanowire systems. With the increasing nanowire length, the contribution from HOMO → LUMO decreases, and the contributions from HOMO-1 → LUMO+1 and HOMO-2 → LUMO+2 increases (Table 3.2).

Table 3.2 Main electronic transitions for longitudinal excitation mode in the Ag_nN_2 (n = 6, 8, 10, 12) systems from LR-TDDFT calculations.

	Excitation energy (eV)	Transition	Contribution
Ag_6N_2	1.88	HOMO → LUMO	91.3%
		HOMO-1 → LUMO+1	6.08%
Ag_8N_2	1.58	HOMO → LUMO	86.6%
		HOMO-1 → LUMO+1	9.26%
$Ag_{10}N_2$	1.39	HOMO → LUMO	81.5%
		HOMO-1 → LUMO+1	11.9%
		HOMO-2 → LUMO+2	2.92%
$Ag_{12}N_2$	1.26	HOMO → LUMO	76.4%
		HOMO-1 → LUMO+1	14.2%
		HOMO-2 → LUMO+2	4.09%

3.4.4 RT-TDDFT calculations

Electron-only (fixed nuclear) RT-TDDFT calculations were then performed to provide dynamic insights into electron populations and electronic transitions upon application of an external field. Physical insights are achieved by examining the electron density matrix, in which diagonal elements are related to orbital populations (Figure 3.3) and off-diagonal elements (Pov) represent the electronic transitions during the electron dynamics process (Figure 3.4).

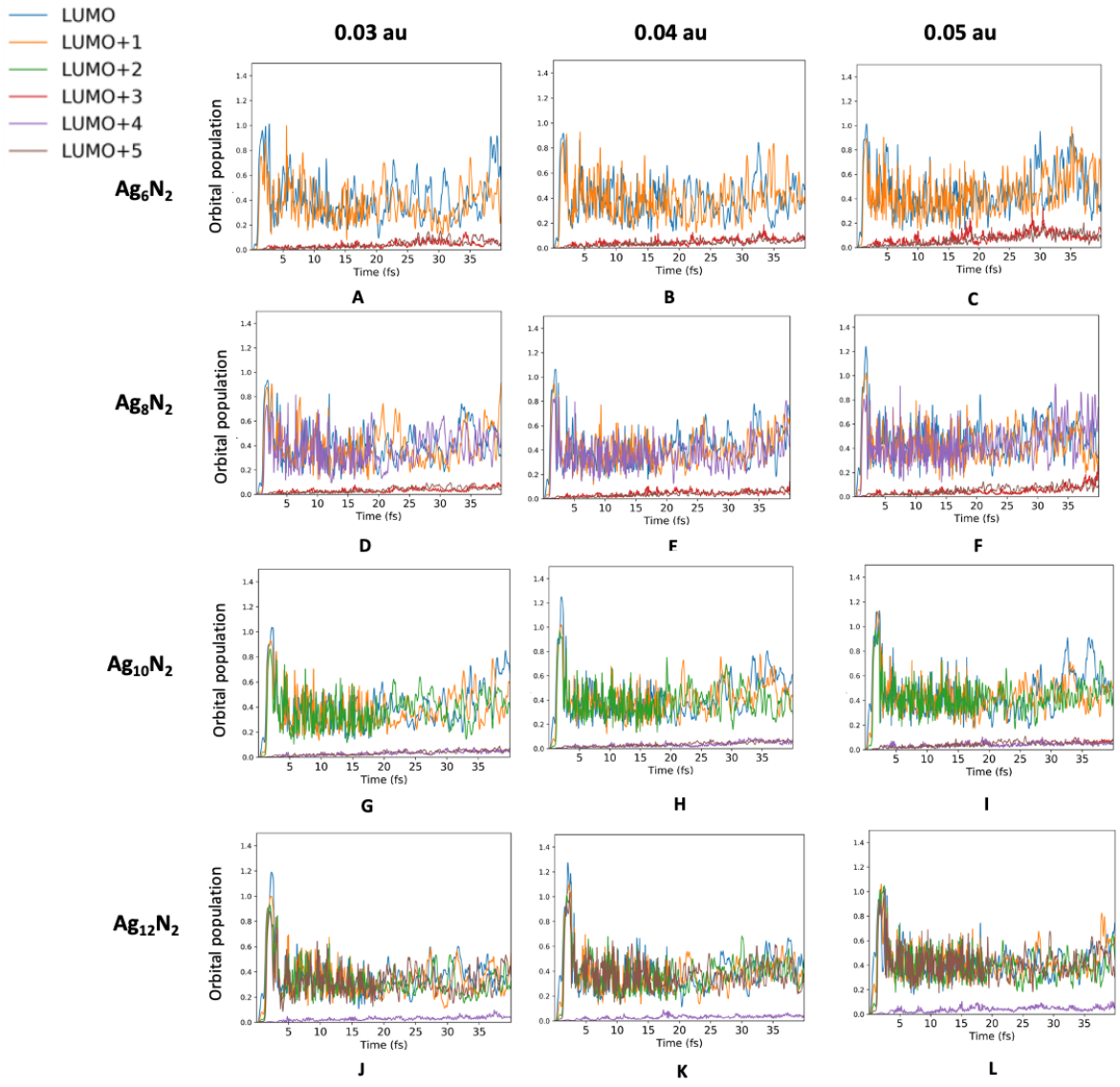


Figure 3.3 Variation of the population of selected molecular orbitals in the first 40 fs of the RT-TDDFT simulation. The electric fields were applied at frequencies corresponding to the longitudinal plasmon frequency of each system. Systems: Ag_6N_2 with applied field intensity of A. 0.03 au, B. 0.04 au, and C. 0.05 au. Ag_8N_2 with applied field intensity of D. 0.03 au, E. 0.04 au, and F. 0.05 au. $Ag_{10}N_2$ with applied field intensity of G. 0.03 au, H. 0.04 au, and I. 0.05 au. $Ag_{12}N_2$ with applied field intensity of J. 0.03 au, K. 0.04 au, and L. 0.05 au.

According to our previous research, the orbital populations of virtual orbitals will increase with more intense electric fields, since more electrons can be excited to virtual orbitals under the irradiation of the electric field.[44] In this work, we examine four Ag_nN_2 systems to investigate the effect of the silver wire length on the orbital populations. From the orbital population results of those four systems, strong orbital populations can be observed in Σ type orbitals and essentially

zero populations can be observed in Π type orbitals, which is logical due to the symmetry of the excitation. For the Ag_6N_2 system, LUMO and LUMO+1 have a relatively high orbital population compared to other orbitals. A similar trend can also be observed in Ag_8N_2: the population number of LUMO, LUMO+1, and LUMO+4 is quite high, while LUMO+2, LUMO+3, and LUMO+5 have comparatively low population numbers. For the $Ag_{10}N_2$ system, the LUMO, LUMO+1, and LUMO+2 populations play the dominant role, and for the $Ag_{12}N_2$ system, the LUMO, LUMO+1, LUMO+2, and LUMO+5 populations play the dominant role. All orbitals that show higher population numbers are Σ-type orbitals. For Ag_6N_2 and Ag_8N_2, LUMO+2 and LUMO+3 are doubly degenerate orbitals, with essentially zero population (Figure 3.3; the green curves (LUMO+2) are overlapped by the red curves (LUMO+3)). These two orbitals exhibit $\pi^*_{N_2}$ character and are localized on the terminal Ag atoms and two nitrogen atoms (Figure 3.1). Therefore, if electrons are excited to those two orbitals, a direct charge transfer process would occur which could lead to fast dissociation of the N_2 molecule.[57,58] However, the maximum population number of LUMO+2 and LUMO+3 is no more than 0.3 in the first 40 fs, and that value is rather low compared with the population number of Σ type virtual orbitals, which is expected due to the symmetry of the excitation. Similar phenomena can also be observed in $Ag_{10}N_2$, and $Ag_{12}N_2$: LUMO, LUMO+1 and LUMO+2 are Σ-type orbitals, whereas LUMO+3 and LUMO+4 are the two $\pi^*_{N_2}$ orbitals in those two systems and their population is lower than 0.2 in the first 40 fs simulations. The above results demonstrate that the direct charge transfer process does not occur with longitudinal excitation. Previous work has also shown that direct excitation of charge transfer transitions does not lead to a greater degree of N_2 dissociation; excitation of the longitudinal mode preferentially leads to nitrogen dissociation,[44] so we focus on this excitation in our current work.

When an electric field is applied, an intense peak in the orbital population of the LUMO appears between 0 – 5 fs (Figure 3.3). For the Ag_6N_2 system, the peak with the 0.04 au field is less intense than the peak with the 0.03 au field. For the Ag_8N_2 system, the peak intensity increases with the higher intensity field. For the $Ag_{10}N_2$ and $Ag_{12}N_2$ systems, the peaks with the 0.04 au field are more intense than in the 0.05 au field. The above results indicate that orbital population does not show a strong correlation with the field intensity.

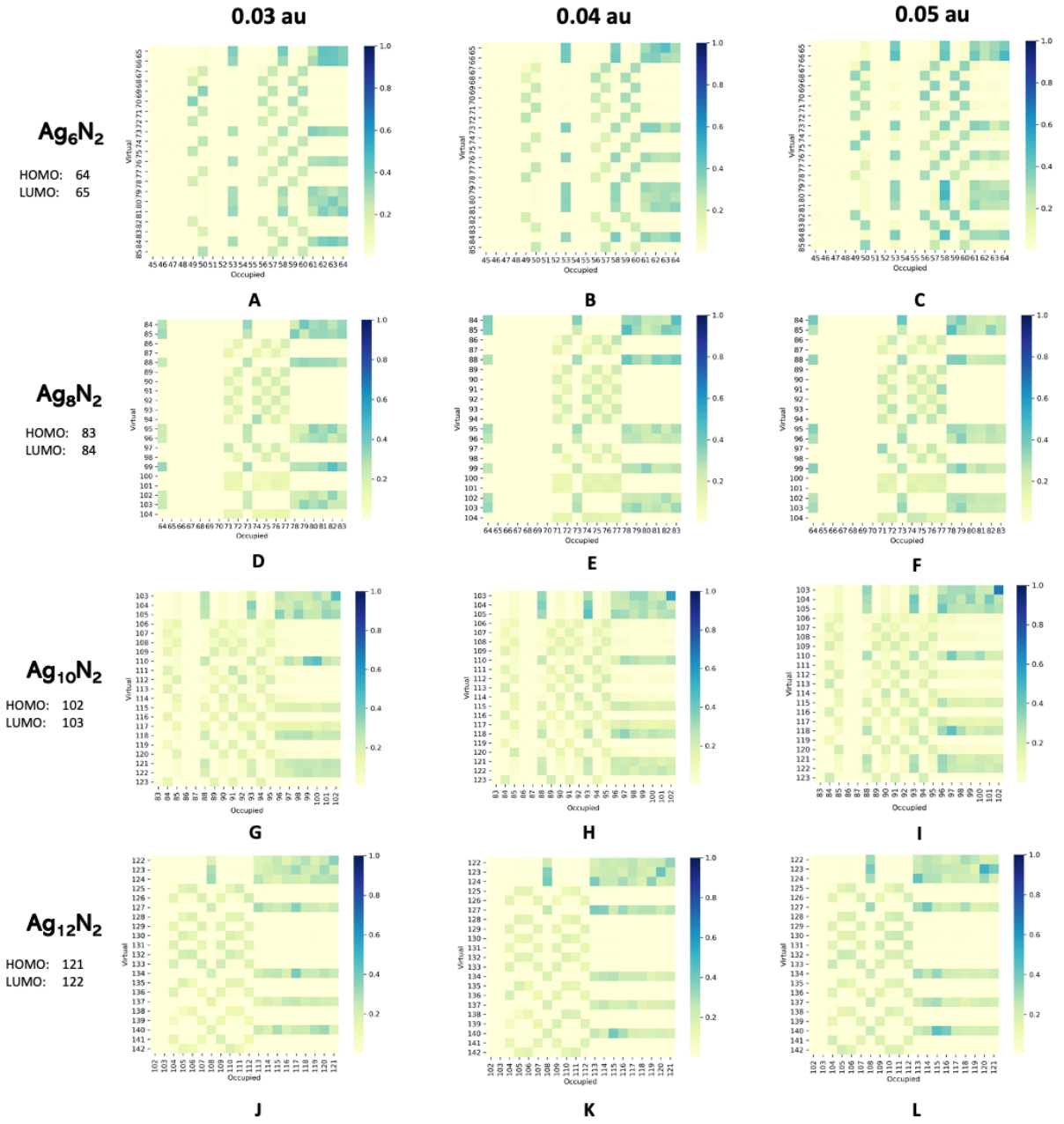


Figure 3.4 Off-diagonal elements (Pov) analysis in RT-TDDFT simulations for four systems. The x-axis represents the occupied orbital number and the y axis represents the virtual orbital number. The color represents the maximum value of the Pov (Mpov) during the electron dynamics across the first 40 fs. A dark-blue color indicates a relatively strong transition, while the light-yellow color shows a weak transition. Systems: Ag_6N_2 with an applied field intensity of A. 0.03 au, B. 0.04 au, and C. 0.05 au. Ag_8N_2 with an applied field intensity of D. 0.03 au, E. 0.04 au, and F. 0.05 au. $Ag_{10}N_2$ with an applied field intensity of G. 0.03 au, H. 0.04 au, and I. 0.05 au. $Ag_{12}N_2$ with an applied field intensity of J. 0.03 au, K. 0.04 au, and L. 0.05 au.

The maximum Pov (Mpov) value of for the main electronic transitions occurring during the first 40 fs of the simulations was plotted in a 2D heatmap (Figure 3.4). For the Ag_6N_2 system, the Mpov of the HOMO → LUMO transition is not monotonically increasing with the more intense electric fields, and HOMO → LUMO has the lowest Mpov with the 0.04 au field. With increasing field intensity, the dominant electronic transitions have changed; rather than occurring between frontier orbitals, they arise from several lower occupied orbitals → higher virtual orbitals. For example, HOMO-6 → LUMO+14 and HOMO-6 → LUMO+15 show higher Mpov in the 0.05 au field for the Ag_6N_2 system. For the Ag_8N_2 system, the HOMO → LUMO transition shows the highest Mpov for the 0.04 au electric field and the lowest Mpov with the 0.05 au electric field. For the $Ag_{10}N_2$ system, Mpov of the HOMO → LUMO transition increases with the higher field intensities. For the $Ag_{12}N_2$ system, Mpov of the HOMO → LUMO transition shows the lowest intensities with the 0.05 au electric field; however, the HOMO-1 → LUMO+1 transition shows the highest Mpov with the 0.05 au electric field. The Mpov studies in the RT-TDDFT calculations indicate that different lengths of Ag wires show various Pov results with the applied field, and electronic transitions do not linearly depend on the field intensity for these strong fields.

3.4.5 Nonadiabatic dynamics simulations

N_2 bond length with different field intensities

We then applied nonadiabatic dynamics simulations to investigate the motion of nitrogen atoms when interacting with the plasmonic silver nanowires (Ag_n, n = 6, 8, 10, 12). Ehrenfest dynamics are performed for intense field strengths ranging from 0.03 au (1.53×10^{15} W/cm^2) to 0.05 au (1.76×10^{15} W/cm^2) with increments of 0.001 au (3.57×10^{13} W/cm^2). Although these high electric field strengths are beyond the perturbative regime, the electric field is applied only in the first 20 fs, which keeps it feasible to apply this strong field strength to the systems. As the nanoparticle size increases, we expect that a lower intensity electric field will need to be applied to induce dissociation, which is shown in section 6.

To classify the Ehrenfest dynamics results, we define N_2 activation and N_2 dissociation as follows:

1. If the bond distance between two nitrogen atoms fluctuates between 1.5 Å and 2 Å, it is defined as N_2 activation.

2. If the bond distance between two nitrogen atoms passes 2 Å, it is defined as N_2 dissociation.

Table 3.3 Maximum N-N bond distance across 100 fs for Ehrenfest dynamics simulations on Ag_nN_2 (n = 6, 8, 10, 12) systems. Orange: N_2 bond is not activated; Blue: N_2 bond is activated but not dissociated; Green: N_2 bond is dissociated.

	Ag_6N_2	Ag_8N_2	$Ag_{10}N_2$	$Ag_{12}N_2$
0.030 au	1.45	1.51	1.36	1.35
0.031 au	1.48	1.39	1.37	1.76
0.032 au	1.38	1.45	1.44	1.30
0.033 au	1.51	1.57	1.46	1.40
0.034 au	1.58	1.49	1.42	1.61
0.035 au	1.65	1.37	1.61	1.39
0.036 au	1.41	1.68	1.47	1.38
0.037 au	1.75	1.62	1.67	1.50
0.038 au	1.69	1.51	1.42	2.50
0.039 au	1.44	1.48	2.30	1.90
0.040 au	1.57	1.52	4.09	2.35
0.041 au	1.76	1.56	2.86	2.42
0.042 au	1.69	1.68	3.98	1.64
0.043 au	3.12	1.62	4.43	2.10
0.044 au	3.98	1.68	4.01	3.29
0.045 au	1.51	1.67	5.55	3.09
0.046 au	2.19	2.78	3.07	1.91
0.047 au	1.70	1.46	5.25	4.58
0.048 au	4.78	5.89	5.43	4.59
0.049 au	5.80	1.85	6.44	6.69
0.050 au	6.24	1.63	6.68	6.48

Effects of the silver nanowire length

As shown in Table 3.3, for the Ag_6N_2 system, the N_2 started to be dissociated with a field strength of 0.043 au. For the Ag_8N_2 system, the N_2 began to be dissociated with the 0.046 au field. N_2 in the $Ag_{10}N_2$ system started to be dissociated with a field strength of 0.039 au, while for $Ag_{12}N_2$, N_2 started to be dissociated with the 0.038 au field. Therefore, the plasmon enhancement arising from the Ag_{12} wire can lead to N_2 dissociation with the lowest field strength in those four Ag wires, whereas the Ag_8 wire needs the highest field strength for plasmon-enhanced N_2

dissociation. Meanwhile, compared with the $Ag_{10}N_2$ and $Ag_{12}N_2$, although $Ag_{12}N_2$ shows the lowest field intensity required for dissociation (0.038 au), the nitrogen molecule in $Ag_{10}N_2$ shows a faster dissociation rate for several field intensities (0.040 au, 0.041 au, 0.042 au, and 0.043 au electric field) compared to $Ag_{12}N_2$, and the maximum N-N bond distances in $Ag_{10}N_2$ are higher than in $Ag_{12}N_2$ for those several field strengths (Figure 3.5). Again, it is clear that the effects of field strength are not monotonic with the length of the wire. However, in general longer wires aid in N_2 activation and dissociation.

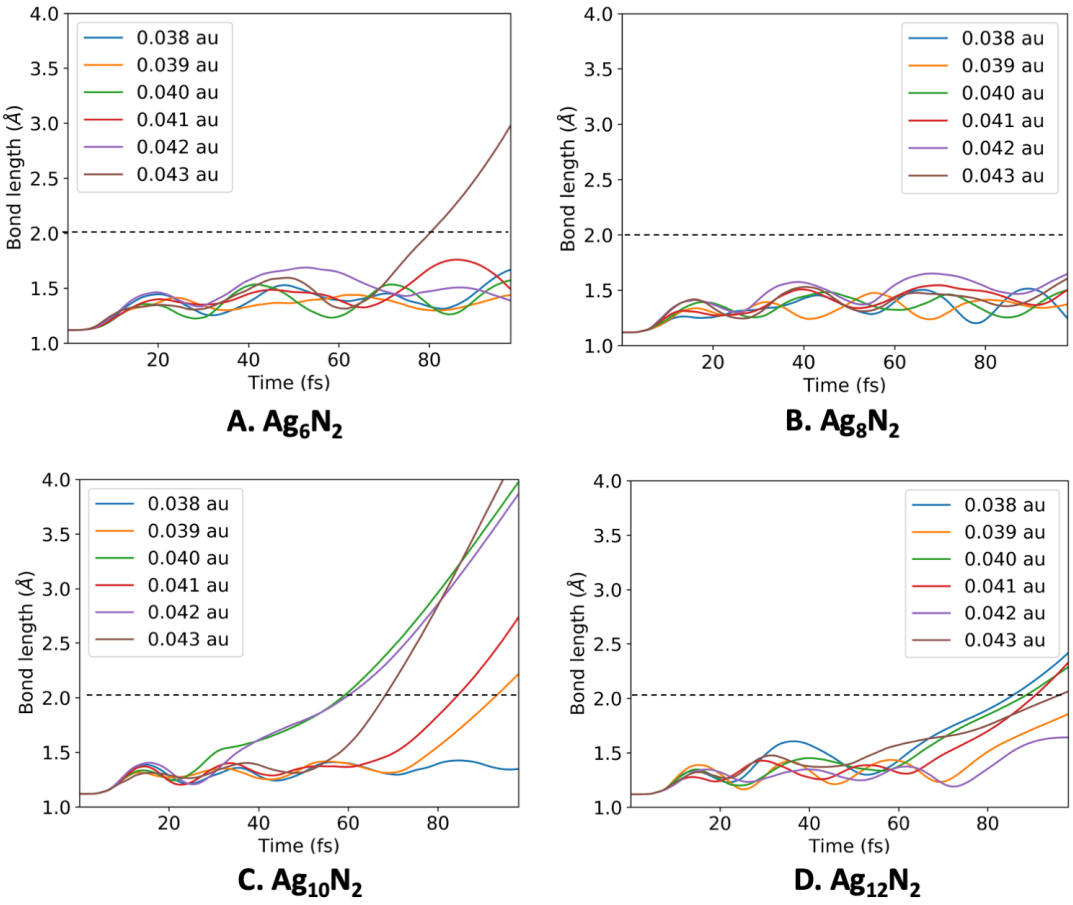


Figure 3.5 Variation of the N_2 bond length with selected field strengths when interacting with different silver nanowires. A. Ag_6N_2 B. Ag_8N_2 C. $Ag_{10}N_2$ D. $Ag_{12}N_2$

Effects of field strengths

The Ehrenfest dynamics simulation results show that the maximum N-N bond distance does not have a linear correlation with field intensity. For Ag_6N_2, the N_2 bond can be activated

with the 0.033 au field strength; however, it cannot be activated with the 0.036 au and 0.039 au field strengths (Table 3.3). N_2 started to be dissociated with the 0.043 au field; however, N_2 cannot be dissociated with fields of 0.045 au and 0.047 au (Table 3.3).

Similar trends can also be observed in other Ag_nN_2 systems: for the Ag_8N_2 system, N_2 has already been activated with the 0.030 au field; however, it is not activated with several other intense electric fields (0.034 au, 0.035 au, and 0.039 au). For the $Ag_{10}N_2$ system, N_2 can be activated with the 0.035 au field but cannot be activated with the 0.036 au and 0.038 au fields. For the $Ag_{12}N_2$ system, N_2 can be dissociated with a field strength of 0.038 au; however, it did not dissociate with the field strengths of 0.039 au and 0.042 au. Therefore, a more intense field can lead to higher degrees of activation or dissociation of N_2 molecule in general; however, the dissociation and activation abilities will not increase monotonically with the field intensities, and the above results also indicates the N_2 activation or dissociation is sensitive to the electric field intensity. This may be due in part to the complicated electron dynamics occurring in these processes.

Because the real-time electron-only TDDFT calculations results in section 4 show that the orbital populations also have a non-linear correlation with electric field intensities, the non-monotonic variation of N-N bond may be related in part to these electronic transitions during the Ehrenfest dynamics simulations. However, the behavior is complicated and counterexamples exist. In the Ag_6N_2 system, we observe more intense bond activation using a field with an intensity of 0.04 au than an intensity of 0.03 au. However, the LUMO exhibits more population (compared using the maximum population number in electron-only dynamics. Figure 3.3) in 0.03 au than in 0.04 au. Similar trends can be observed in other systems. For the $Ag_{10}N_2$ and $Ag_{12}N_2$ system, N_2 exhibits a greater degree of dissociation for the 0.05 au field than with 0.04 au. Meanwhile, the LUMO shows more population with 0.04 au than with 0.05 au. The above observation suggests that the degree of N_2 activation or dissociation may not be directly related to the LUMO populations. Instead, a collective excitation induced by the applied field may contribute to the dynamics and affect the N-N bond dissociation. In the highly non-linear bond dissociation process, various interferences occur as the electrons slosh along the wire and into (and out of) the adsorbate, which begins to vibrate; changes to the electronic structure that occur as the nuclear geometry changes can thus affect the activation process.

3.4.6 Plasmon-enhancement of Ag_{19} cluster

In addition to our work with the linear Ag nanowire model, we have also examined the plasmon-enhanced catalytic properties of the Ag_{19}^{+1} nanocluster. This system is one of the smallest three-dimensional silver nanorods, with four interior silver atoms surrounded by three pentagonal rings. The double-icosahedron structure is one of the lowest energy minima of the Ag_{19} cluster.[59,60] This system thus provides an opportunity to examine how N_2 dissociation is affected by increasing the nanocluster width using a system that could be experimentally achieved.

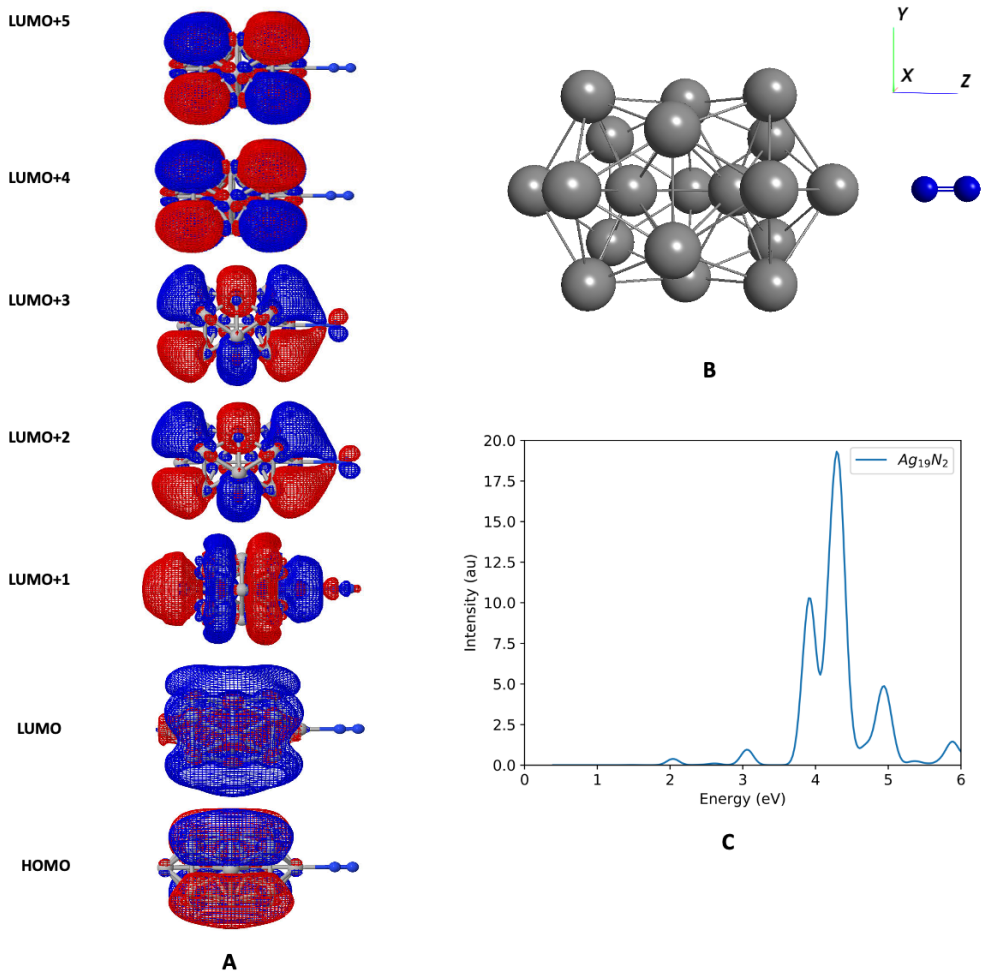


Figure 3.6 A. Selected molecular orbitals (HOMO to LUMO+5) of $Ag_{19}N_2^{+1}$. B. Visualization of ground state optimized structure of $Ag_{19}N_2^{+1}$. Key: silver = silver, nitrogen = blue. C. LR-TDDFT absorption spectrum of $Ag_{19}N_2^{+1}$.

For the geometry optimization, all atoms are relaxed during the ground state geometry optimization process of the $Ag_{19}N_2^{+1}$ system (Figure 3.6B). In the ground state, the N-N bond length in the $Ag_{19}N_2^{+1}$ system is the same as in the wire-like Ag_nN_2 systems (i.e. 1.119 Å). From the molecular orbitals, the $Ag_{19}N_2^{+1}$ system does not have a localized $\pi^*_{N_2}$ type orbital (Figure 3.6A), unlike the similar wire-N_2 systems. Instead, the $\pi^*_{N_2}$ orbitals mix with Π_3 orbitals of Ag_{19}^+ (LUMO+2 and LUMO+3). A more comprehensive molecular orbital diagram is shown in Figure A.1. The calculated binding energy between N_2 and the Ag_{19} cluster is 41.5 kJ/mol. The absorption spectrum (Figure 3.6C) displays two intense peaks at 3.9 eV and 4.2 eV. The smoothed peak at 3.9 eV is the result of two excited states at 3.86 eV and 3.94 eV. The excitation at 3.86 eV arises from two degenerate excitations with transition dipole moments in the x and y directions (i.e. a transverse excitation), and the excitation at 3.94 eV is polarized along the z direction (i.e. longitudinal excitation). The LR-TDDFT results show that both the longitudinal and transverse excitations in $Ag_{19}N_2^{+1}$ exhibit collective electronic transitions, compared to the Ag_n wire system, in which only the HOMO to LUMO transition played a dominant role in the longitudinal excitation. The top three dominant electronic transitions contributing to the transverse excitation at 3.86 eV are HOMO-2/HOMO-3 → LUMO+6, HOMO-2/HOMO-3 → LUMO+4 and HOMO-2/HOMO-3 → LUMO+5. The top three dominant electronic transitions contributing to the longitudinal excitation at 3.94 eV are HOMO-3 → LUMO+2, HOMO-2 → LUMO+3 and HOMO-4 → LUMO+1 (Table A.1). The oscillator strengths of these two excitations are 0.4390 a.u. (for each of the two degenerate states at 3.86 eV) and 1.5664 a.u., respectively.

Then, Ehrenfest dynamics simulations were initiated with both x and z polarizations and an applied electric field at a frequency of 3.9 eV to excite the transverse and longitudinal excitations. With a field intensity of 0.030 au, when the electric field is applied in the x direction, the N_2 molecule is not dissociated within 35 fs. However, when the electric field is applied in the z direction, the N_2 molecule can be dissociated within 30 fs (Figure 3.7A). Thus, excitation of the longitudinal plasmon leads to a greater degree of dissociation than excitation of the transverse plasmon for this system, similar to previous results with nanowires.

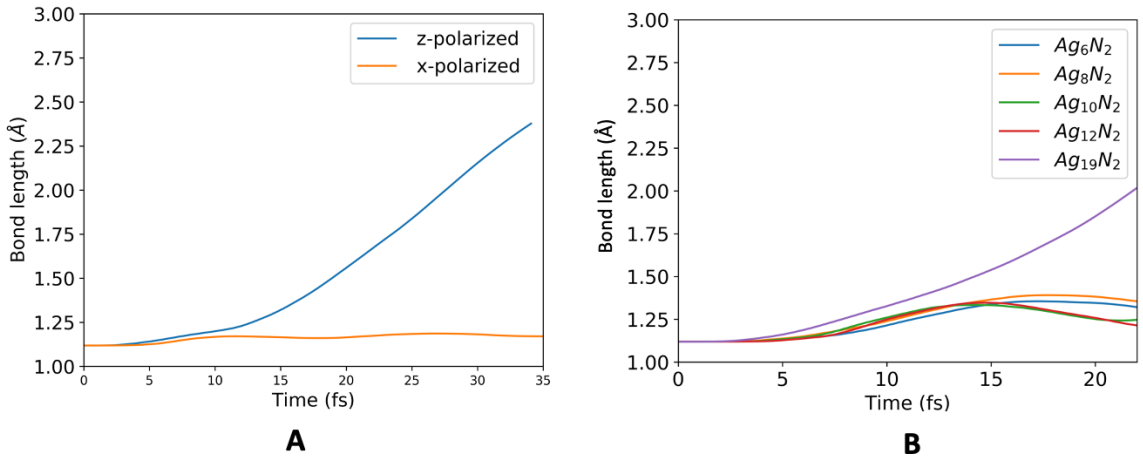


Figure 3.7 A. Comparison of N-N bond variation in Ehrenfest dynamics for $Ag_{19}N_2^{+1}$ with z-polarized and x-polarized electric fields with field intensities of 0.030 au. B. Comparison of N-N bond variation in Ehrenfest dynamics for wire-N_2 and $Ag_{19}N_2^{+1}$ systems with a 0.040 au field strength using z-polarized excitations.

With a larger field intensity of 0.04 au and an electric field polarized along the z direction, we can observe N_2 dissociation after only 22 fs (Figure 3.7B; the N-N bond length at 22 fs is 2.02 Å). Overall, although the oscillator strength (*f*) of the longitudinal peak in the Ag_{19} cluster is lower than the Ag_{12} nanowire ($Ag_{19}N_2^{+1}$: $f = 1.57$ for the 3.94 eV excitation; $Ag_{12}N_2$: $f = 3.43$ for the 1.26 eV excitation), the results show that N_2 starts to dissociate with a lower field intensity when it is adsorbed to the Ag_{19} cluster compared with Ag_n nanowires (n = 6, 8, 10, 12), and the dissociation process on the Ag_{19} cluster occurs faster than for Ag_n nanowires. The above results indicate that the number of the Ag atoms in the plasmon-enhanced system will affect the N_2 dissociation rate, and the oscillator strength of the excitation is not the only factor that determines the plasmon-enhanced dissociation ability of silver nanorods and nanowires.

3.5 Conclusion

In this work, we examine the effects of field strength and Ag nanowire size on plasmon-enhanced N_2 dissociation. Ground state calculations show that the length of the nanowire has very slight effects on the binding energies with the N_2 molecule. Linear response TDDFT calculations show that the longitudinal plasmon frequencies shift to lower energies when increasing the length of the silver nanowire. Real-time TDDFT calculations demonstrate that the LUMO orbital

populations do not increase monotonically with field strength for strong electric fields. Ehrenfest nonadiabatic dynamics were applied to examine the behavior of the system using applied electric fields with different intensities. The results showed that stronger field strengths lead to plasmon-enhanced N_2 dissociation in general; however, the N_2 dissociation or activation ability does not always monotonically increase with the field strength, which might be related to the nonlinear electronic transition and orbital population values observed for different electric field strengths. Longer nanowires typically require lower field strengths for activation/dissociation of N_2, even though their plasmon energy decreases with length, which suggests that the oscillator strength of the transition is a more dominant factor than the frequency of the plasmon resonance. Finally, we examined the plasmon-enhancement properties of the Ag_{19} nanocluster and found that this can lead to fast N_2 dissociation within 30 fs with a 0.030 au field intensity if the electric field is polarized along the z axis (longitudinal excitation). However, the N_2 bond distance remains nearly unchanged if the field is polarized along the x axis (transverse excitation) with the 0.030 au field intensity. The Ag_{19}^+ nanorod leads to faster dissociation of N_2 than the atomically-thin nanowires such as Ag_{12}. Overall, these results demonstrate that the size of the plasmonic nanostructures will affect the plasmon-enhanced catalytic process of N_2 dissociation, with larger clusters leading to more facile dissociation and activation.

3.6 Acknowledgement

This material is based on work supported by the Department of Energy under grant DE-SC0012273. The computing for this work was performed on the Beocat Research Cluster at Kansas State University, which is in part funded by the NSF (Grant Nos. CHE-1726332, CNS-1006860, EPS-1006860, and EPS-0919443). The authors thank Gowri Udayangani Kuda-Singappulige and Olivia Hull for their help and discussion during this project. The authors thank Prof. Xiaosong Li for the RT-TDDFT and Ehrenfest Dynamics code.

3.7 Supporting information

Supporting information provides information on the Selected molecular orbitals of $Ag_{19}N_2^{+1}$ and electronic transitions information for two main excitations of $Ag_{19}N_2^{+1}$systems.

3.8 References

(1) van der Ham, C. J. M.; Koper, M. T. M.; Hetterscheid, D. G. H. Challenges in Reduction of Dinitrogen by Proton and Electron Transfer. *Chem Soc Rev* **2014**, *43* (15), 5183–5191.

(2) Honkala, K.; Hellman, A.; Remediakis, I. N.; Logadottir, A.; Carlsson, A.; Dahl, S.; Christensen, C. H.; Nørskov, J. K. Ammonia Synthesis from First-Principles Calculations. *Science* **2005**, *307* (5709), 555–558.

(3) Jiang, G.-D.; Mou, L.-H.; Chen, J.-J.; Li, Z.-Y.; He, S.-G. Reactivity of Neutral Tantalum Sulfide Clusters Ta_3S_n (n = 0–4) with N_2. *J. Phys. Chem. A* **2020**, *124* (38), 7749–7755.

(4) Kumar, D.; Pal, S.; Krishnamurty, S. N_2 Activation on Al Metal Clusters: Catalyzing Role of BN-Doped Graphene Support. *Phys. Chem. Chem. Phys.* **2016**, *18* (40), 27721–27727.

(5) Casey-Stevens, C. A.; Lambie, S. G.; Ruffman, C.; Skúlason, E.; Garden, A. L. Geometric and Electronic Effects Contributing to N_2 Dissociation Barriers on a Range of Active Sites on Ru Nanoparticles. *J. Phys. Chem. C* **2019**, *123* (50), 30458–30466.

(6) Rochana, P.; Lee, K.; Wilcox, J. Nitrogen Adsorption, Dissociation, and Subsurface Diffusion on the Vanadium (110) Surface: A DFT Study for the Nitrogen-Selective Catalytic Membrane Application. *J. Phys. Chem. C* **2014**, *118* (8), 4238–4249.

(7) Kulkarni, B. S.; Krishnamurty, S.; Pal, S. Size- and Shape-Sensitive Reactivity Behavior of Al_n (n = 2–5, 13, 30, and 100) Clusters Toward the N_2 Molecule: A First-Principles Investigation. *J. Phys. Chem. C* **2011**, *115* (30), 14615–14623.

(8) Romanowski, Z.; Krukowski, S.; Grzegory, I.; Porowski, S. Surface Reaction of Nitrogen with Liquid Group III Metals. *J. Chem. Phys* **2001**, *114* (14), 6353–6363.

(9) Iriawan, H.; Andersen, S. Z.; Zhang, X.; Comer, B. M.; Barrio, J.; Chen, P.; Medford, A. J.; Stephens, I. E. L.; Chorkendorff, I.; Shao-Horn, Y. Methods for Nitrogen Activation by Reduction and Oxidation. *Nat. Rev. Methods Primer* **2021**, *1* (1), 56.

(10) Liu, D.; Zhao, W.; Yuan, Q. Breaking the Linear Relation in the Dissociation of Nitrogen on Iron Surfaces. *ChemPhysChem* **2022**, *23* (17).

(11) Martirez, J. M. P.; Carter, E. A. Prediction of a Low-Temperature N_2 Dissociation Catalyst Exploiting near-IR–to–Visible Light Nanoplasmonics. *Sci. Adv.* **2017**, *3* (12), eaao4710.

(12) Martirez, J. M. P.; Carter, E. A. Excited-State N_2 Dissociation Pathway on Fe-Functionalized Au. *J. Am. Chem. Soc.* **2017**, *139* (12), 4390–4398.

(13) Banerjee, A.; Yuhas, B. D.; Margulies, E. A.; Zhang, Y.; Shim, Y.; Wasielewski, M. R.; Kanatzidis, M. G. Photochemical Nitrogen Conversion to Ammonia in Ambient Conditions with FeMoS-Chalcogels. *J. Am. Chem. Soc.* **2015**, *137* (5), 2030–2034.

(14) Cortés, E.; Besteiro, L. V.; Alabastri, A.; Baldi, A.; Tagliabue, G.; Demetriadou, A.; Narang, P. Challenges in Plasmonic Catalysis. *ACS Nano* **2020**, *14* (12), 16202–16219.

(15) Loiseau, A.; Zhang, L.; Hu, D.; Salmain, M.; Mazouzi, Y.; Flack, R.; Liedberg, B.; Boujday, S. Core–Shell Gold/Silver Nanoparticles for Localized Surface Plasmon Resonance-Based Naked-Eye Toxin Biosensing. *ACS Appl. Mater. Interfaces* **2019**, *11* (50), 46462–46471.

(16) Hooshmand, N.; Thoutam, A.; Anikovskiy, M.; Labouta, H. I.; El-Sayed, M. Localized Surface Plasmon Resonance as a Tool to Study Protein Corona Formation on Nanoparticles. *J. Phys. Chem. C* **2021**, *125* (45), 24765–24776.

(17) Mou, T.; Quiroz, J.; Camargo, P. H. C.; Wang, B. Localized Orbital Excitation Drives Bond Formation in Plasmonic Catalysis. *ACS Appl. Mater. Interfaces* **2021**, *13* (50), 60115–60124.

(18) Kim, H. Y.; Henkelman, G. CO Oxidation at the Interface between Doped CeO_2 and Supported Au Nanoclusters. *J. Phys. Chem. Lett.* **2012**, *3* (16), 2194–2199.

(19) Aslam, U.; Rao, V. G.; Chavez, S.; Linic, S. Catalytic Conversion of Solar to Chemical Energy on Plasmonic Metal Nanostructures. *Nat. Catal.* **2018**, *1* (9), 656–665.

(20) Mayer, K. M.; Hafner, J. H. Localized Surface Plasmon Resonance Sensors. *Chem. Rev.* **2011**, *111* (6), 3828–3857.

(21) Jain, P. K.; Huang, X.; El-Sayed, I. H.; El-Sayed, M. A. Review of Some Interesting Surface Plasmon Resonance-Enhanced Properties of Noble Metal Nanoparticles and Their Applications to Biosystems. *Plasmonics* **2007**, *2* (3), 107–118.

(22) Choi, K. M.; Kim, D.; Rungtaweevoranit, B.; Trickett, C. A.; Barmanbek, J. T. D.; Alshammari, A. S.; Yang, P.; Yaghi, O. M. Plasmon-Enhanced Photocatalytic CO_2 Conversion within Metal–Organic Frameworks under Visible Light. *J. Am. Chem. Soc.* **2017**, *139* (1), 356–362.

(23) García-García, I.; Lovell, E. C.; Wong, R. J.; Barrio, V. L.; Scott, J.; Cambra, J. F.; Amal, R. Silver-Based Plasmonic Catalysts for Carbon Dioxide Reduction. *ACS Sustain. Chem. Eng.* **2020**, *8* (4), 1879–1887.

(24) Gu, M.; Liu, D.; Ding, T.; Liu, X.; Chen, T.; Shen, X.; Yao, T. Plasmon-Assisted Photocatalytic CO_2 Reduction on Au Decorated ZrO_2 Catalysts. *Dalton Trans.* **2021**, *50* (18), 6076–6082.

(25) Yang, J.; Guo, Y.; Lu, W.; Jiang, R.; Wang, J. Emerging Applications of Plasmons in Driving CO_2 Reduction and N_2 Fixation. *Adv. Mater.* **2018**, *30* (48), 1802227.

(26) Kim, H. J.; Lee, S. H.; Upadhye, A. A.; Ro, I.; Tejedor-Tejedor, M. I.; Anderson, M. A.; Kim, W. B.; Huber, G. W. Plasmon-Enhanced Photoelectrochemical Water Splitting with Size-Controllable Gold Nanodot Arrays. *ACS Nano* **2014**, *8* (10), 10756–10765.

(27) Mascaretti, L.; Dutta, A.; Kment, Š.; Shalaev, V. M.; Boltasseva, A.; Zbořil, R.; Naldoni, A. Plasmon-Enhanced Photoelectrochemical Water Splitting for Efficient Renewable Energy Storage. *Adv. Mater.* **2019**, *31* (31), 1805513.

(28) Huang, J.; Zhao, X.; Huang, X.; Liang, W. Understanding the Mechanism of Plasmon-Driven Water Splitting: Hot Electron Injection and a near Field Enhancement Effect. *Phys. Chem. Chem. Phys.* **2021**, *23* (45), 25629–25636.

(29) Hu, C.; Chen, X.; Jin, J.; Han, Y.; Chen, S.; Ju, H.; Cai, J.; Qiu, Y.; Gao, C.; Wang, C.; Qi, Z.; Long, R.; Song, L.; Liu, Z.; Xiong, Y. Surface Plasmon Enabling Nitrogen Fixation in Pure Water through a Dissociative Mechanism under Mild Conditions. *J. Am. Chem. Soc.* **2019**, *141* (19), 7807–7814.

(30) Gellé, A.; Jin, T.; de la Garza, L.; Price, G. D.; Besteiro, L. V.; Moores, A. Applications of Plasmon-Enhanced Nanocatalysis to Organic Transformations. *Chem. Rev.* **2020**, *120* (2), 986–1041.

(31) Christopher, P.; Moskovits, M. Hot Charge Carrier Transmission from Plasmonic Nanostructures. *Annu. Rev. Phys. Chem.* **2017**, *68* (1), 379–398.

(32) Román Castellanos, L.; Hess, O.; Lischner, J. Single Plasmon Hot Carrier Generation in Metallic Nanoparticles. *Commun. Phys.* **2019**, *2* (1), 47.

(33) Zhang, Y. Theory of Plasmonic Hot-Carrier Generation and Relaxation. *J. Phys. Chem. A* **2021**, *125* (41), 9201–9208.

(34) Khurgin, J. B. Hot Carriers Generated by Plasmons: Where Are They Generated and Where Do They Go from There? *Faraday Discuss.* **2019**, *214*, 35–58.

(35) Cortés, E.; Besteiro, L. V.; Alabastri, A.; Baldi, A.; Tagliabue, G.; Demetriadou, A.; Narang, P. Challenges in Plasmonic Catalysis. *ACS Nano* **2020**, *14* (12), 16202–16219.

(36) Hartland, G. V.; Besteiro, L. V.; Johns, P.; Govorov, A. O. What's so Hot about Electrons in Metal Nanoparticles? *ACS Energy Lett.* **2017**, *2* (7), 1641–1653.

(37) Zhang, Y.; Nelson, T.; Tretiak, S.; Guo, H.; Schatz, G. C. Plasmonic Hot-Carrier-Mediated Tunable Photochemical Reactions. *ACS Nano* **2018**, *12* (8), 8415–8422.

(38) Wu, Q.; Zhou, L.; Schatz, G. C.; Zhang, Y.; Guo, H. Mechanistic Insights into Photocatalyzed H_2 Dissociation on Au Clusters. *J. Am. Chem. Soc.* **2020**, *142* (30), 13090–13101.

(39) Kuda-Singappulige, G. U.; Aikens, C. M. Theoretical Insights into Excitation-Induced Oxygen Activation on a Tetrahedral Ag_8 Cluster. *J. Phys. Chem. A* **2021**, *125* (43), 9450–9458.

(40) Guidez, E. B.; Aikens, C. M. Quantum Mechanical Origin of the Plasmon: From Molecular Systems to Nanoparticles. *Nanoscale* **2014**, *6* (20), 11512–11527.

(41) Langford, J.; Xu, X.; Yang, Y. Plasmon Character Index: An Accurate and Efficient Metric for Identifying and Quantifying Plasmons in Molecules. *J. Phys. Chem. Lett.* **2021**, *12* (38), 9391–9397.

(42) Gieseking, R. L. M. Plasmons: Untangling the Classical, Experimental, and Quantum Mechanical Definitions. *Mater. Horiz.* **2022**, *9* (1), 25–42.

(43) Yan, L.; Ding, Z.; Song, P.; Wang, F.; Meng, S. Plasmon-Induced Dynamics of H_2 Splitting on a Silver Atomic Chain. *Appl. Phys. Lett.* **2015**, *107* (8), 083102.

(44) Hull, O. A.; Lingerfelt, D. B.; Li, X.; Aikens, C. M. Electronic Structure and Nonadiabatic Dynamics of Atomic Silver Nanowire–N_2 Systems. *J. Phys. Chem. C* **2020**, *124* (38), 20834–20845.

(45) Hull, O. A.; Aikens, C. M. Theoretical Investigations on the Plasmon-Mediated Dissociation of Small Molecules in the Presence of Silver Atomic Wires. *J. Phys. Chem. A* **2023**, *127* (10), 2228–2241.

(46) Li, X.; Tully, J. C.; Schlegel, H. B.; Frisch, M. J. *Ab Initio* Ehrenfest Dynamics. *J. Chem. Phys* **2005**, *123* (8), 084106.

(47) Ding, F.; Goings, J. J.; Liu, H.; Lingerfelt, D. B.; Li, X. Ab Initio Two-Component Ehrenfest Dynamics. *J. Chem. Phys* **2015**, *143* (11), 114105.

(48) Senanayake, R. D.; Lingerfelt, D. B.; Kuda-Singappulige, G. U.; Li, X.; Aikens, C. M. Real-Time TDDFT Investigation of Optical Absorption in Gold Nanowires. *J. Phys. Chem. C* **2019**, *123* (23), 14734–14745.

(49) Kuda-Singappulige, G. U.; Lingerfelt, D. B.; Li, X.; Aikens, C. M. Ultrafast Nonlinear Plasmon Decay Processes in Silver Nanoclusters. *J. Phys. Chem. C* **2020**, *124* (37), 20477–20487.

(50) Pandeya, P.; Aikens, C. M. Real-Time Electron Dynamics Study of Plasmon-Mediated Photocatalysis on an Icosahedral Al_{13}^{-1} Nanocluster. *J. Phys. Chem. A* **2021**, *125* (22), 4847–4860.

(51) Rohrdanz, M. A.; Martins, K. M.; Herbert, J. M. A Long-Range-Corrected Density Functional That Performs Well for Both Ground-State Properties and Time-Dependent Density Functional Theory Excitation Energies, Including Charge-Transfer Excited States. *J. Chem. Phys* **2009**, *130* (5), 054112.

(52) Hay, P. J.; Wadt, W. R. *Ab Initio* Effective Core Potentials for Molecular Calculations. Potentials for K to Au Including the Outermost Core Orbitals. *J. Chem. Phys* **1985**, *82* (1), 299–310.

(53) Wadt, W. R.; Hay, P. J. *Ab Initio* Effective Core Potentials for Molecular Calculations. Potentials for Main Group Elements Na to Bi. *J. Chem. Phys* **1985**, *82* (1), 284–298.

(54) Hay, P. J.; Wadt, W. R. *Ab Initio* Effective Core Potentials for Molecular Calculations. Potentials for the Transition Metal Atoms Sc to Hg. *J. Chem. Phys* **1985**, *82* (1), 270–283.

(55) Gaussian Development Version, Revision I.13+, M. J. Frisch, G. W. Trucks, H. B. Schlegel, G. E. Scuseria, M. A. Robb, J. R. Cheeseman, G. Scalmani, V. Barone, G. A. Petersson, H. Nakatsuji, X. Li, M. Caricato, A. V. Marenich, J. Bloino, B. G. Janesko, R. Gomperts, B. Mennucci, H. P. Hratchian, J. V. Ortiz, A. F. Izmaylov, J. L. Sonnenberg, D. Williams-Young, F. Ding, F. Lipparini, F. Egidi, J. Goings, B. Peng, A. Petrone, T. Henderson, D. Ranasinghe, V. G. Zakrzewski, J. Gao, N. Rega, G. Zheng, W. Liang, M. Hada, M. Ehara, K. Toyota, R. Fukuda, J. Hasegawa, M. Ishida, T. Nakajima, Y. Honda, O. Kitao, H. Nakai, T. Vreven, K. Throssell, J. A. Montgomery, Jr., J. E. Peralta, F. Ogliaro, M. J. Bearpark, J. J. Heyd, E. N. Brothers, K. N. Kudin, V. N. Staroverov, T. A. Keith, R. Kobayashi, J. Normand, K. Raghavachari, A. P. Rendell, J. C. Burant, S. S. Iyengar, J. Tomasi, M. Cossi, J. M. Millam, M. Klene, C. Adamo, R. Cammi, J. W. Ochterski, R. L. Martin, K. Morokuma, O. Farkas, J. B. Foresman, and D. J. Fox, Gaussian, Inc., Wallingford CT, 2018.

(56) Johnson, H. E.; Aikens, C. M. Electronic Structure and TDDFT Optical Absorption Spectra of Silver Nanorods. *J. Phys. Chem. A* **2009**, *113* (16), 4445–4450.

(57) Kale, M. J.; Avanesian, T.; Christopher, P. Direct Photocatalysis by Plasmonic Nanostructures. *ACS Catal.* **2014**, *4* (1), 116–128.

(58) Kumar, P. V.; Rossi, T. P.; Marti-Dafcik, D.; Reichmuth, D.; Kuisma, M.; Erhart, P.; Puska, M. J.; Norris, D. J. Plasmon-Induced Direct Hot-Carrier Transfer at Metal–Acceptor Interfaces. *ACS Nano* **2019**, *13* (3), 3188–3195.

(59) Alamanova, D.; Grigoryan, V. G.; Springborg, M. Theoretical Study of the Structure and Energetics of Silver Clusters. *J. Phys. Chem. C* **2007**, *111* (34), 12577–12587.

(60) Yang, M.; Jackson, K. A.; Jellinek, J. First-Principles Study of Intermediate Size Silver Clusters: Shape Evolution and Its Impact on Cluster Properties. *J. Chem. Phys* **2006**, *125* (14), 144308.

Chapter 4 - Effects of nanowire doping on plasmon-enhanced N_2 dissociation

Yuchen Wang, Christine M. Aikens*

Department of Chemistry, Kansas State University, Manhattan, KS 66506, USA

*Email: cmaikens@ksu.edu

4.1 Abstract

Doping a transition metal element into plasmonic systems can tune the optical properties of the system, which will potentially facilitate the plasmon-enhanced catalytic process. In this study, we applied the linear-response time-dependent density functional theory (LR-TDDFT) method, with real-time electron dynamics and mean-field Ehrenfest dynamics methods to computationally investigate the effects of doping silver nanowires on plasmon-enhanced N_2 dissociation. We calculated the absorption spectra for different doped systems and then applied an external electric field to the system and performed mean-field Ehrenfest dynamics to examine how plasmonic excitation will affect the N_2 activation or dissociation. In addition, we also studied how the transition metal dopant affects the system's electronic structure and potential energy surface.

4.2 Introduction

When metal nanoparticles are irradiated by light with a certain frequency, the valence electrons will be excited and slosh back and forth collectively, which results in one or more excitation energies with a strong oscillator strength. This phenomenon is called Localized Surface Plasmon Resonance (LSPR), and these excitation energies can be utilized in plasmon-driven processes. LSPR is one of the unique properties found in plasmonic metal nanoparticles.[1–4] The plasmonic character of nanoparticles can be applied in a broad range of fields, such as molecular sensing, biological chemistry, and photocatalytic reactions.[5–8] In catalysis, there is great interest in the catalytic N_2 dissociation process since this is one of the very important sub-steps in the NH_3 synthesis process. Due to the very high N-N bonding energy, the dissociation of N_2 usually requires

conditions of high temperature and high pressure when conventional methods such as the Haber-Bosch process are used.[9,10] In recent years, photo-induced reactions have opened a new way to proceed with the N_2 dissociation process, and plasmonic systems can be applied to enhance the N_2 activation or dissociation process. Because plasmonic metals such as gold, silver, and aluminum are often not the best catalysts, combining another transition metal element with the plasmonic metal can tune the optical properties of the plasmonic system and can potentially show better catalytic properties than the pure system. The hybridized system can be combined catalytic-plasmonic metal systems, such as Al-Pd,[11–13] Au-Pd,[14,15] Au-Pt,[16–18] Ag-Pt,[19] Ag-Pd,[20] and Au-Fe systems,[21,22] and also can be combined plasmonic-plasmonic systems, e.g., Ag-Au systems.[23–25]

In this work, to investigate the effects of doping on the plasmon-enhanced process occurring on silver nanoparticles, we build up a simplified model consisting of a linear silver nanowire with a doped transition metal at the terminal site of the silver nanowire. Because quantum chemistry calculations on the atomic precisely plasmonic nanoparticles are computationally expensive, using such a simplified model can thus reduce the computational cost. Moreover, the reasonability for using 1D silver nanowires to model plasmonic character has been validated based on a series of previous studies. Experimentally, the one-dimensional band structure of Au chains was characterized and their plasmon resonance character was observed using a scanning tunneling microscope (STM).[26] Theoretically, Kümmel and co-workers showed in 2001 that the excitations can be considered as collective plasmons in few-atom metal clusters.[27] TDDFT calculations have demonstrated the collective excitations in various atomic metal chains of more than 10 atoms.[28–32] Johnson et al. and Picinni et al. examined the intense absorption peak in the absorption spectrum for Au and Ag nanochain/nanorods systems and suggested that the peak differs from single-particle transitions and can be identified as plasmon excitation.[33,34] Therefore, it is reasonable to use the nanowire to model the plasmon-induced process.

The effects of doping on the plasmonic resonance characters of silver and gold nanochains have been studied using TDDFT, and previous work showed that the metal atom dopants can lead to additional electronic excitation modes in the absorption spectrum, which will then enhance the collective excitations.[30,32,35] Compared with the previous studies, our work will be more focused on how doping affects the plasmon-enhanced N_2 dissociation. To study the nuclear motions in excited states, various types of nonadiabatic quantum dynamics have been applied to examine the photo-catalyzed process such as small molecule activation/dissociation.[36–43] In this work, we

applied mean-field Ehrenfest dynamics[44–48] to watch the evolution of N_2 when interacting with a doped plasmonic silver nanowire.

This article is organized into the following steps: First, we built a doped silver nanowire model and the nitrogen molecule was placed parallel to the wire because this orientation has been found to be the best orientation for the plasmon-enhanced N_2 dissociation in pure silver nanowires.[49] We then performed LR-TDDFT calculations to understand the effects of doping on absorption spectra. Then, nonadiabatic molecular dynamics were carried out by applying a continuous wave electric field. The variation of the N-N distance with time gives us an intuitive view of the N_2 activation/dissociation when coupling with different doped systems. In the last section, we focus on elucidating the doping effects of Ag_5Cu and Ag_5Au systems from the aspects of thermal effects, potential energy surface, and electronic structure calculation results.

4.3 Computational details

All the calculations were carried out at the LC-ωPBE[50]/LanL2DZ[51–53] level of theory with a development version of the Gaussian software package.[54] The molecular systems were visualized using MacMolPlt[55] and the molecular orbitals were visualized using Jmol.[56] For the ground state geometry optimization, a transition metal atom (Ni, Pd, Pt, Cu, Au, Zn, Cd, Hg) was doped at the terminal site of the Ag wire. For the group X and group XII dopants, the dopant is appended to an Ag_6 wire (Ag_6X, X = doped atom). For the group XI dopants, Ag_5 is chosen as the wire (Ag_5X, X = doped atom) so that we focus on closed shell system models in this work; all systems discussed in this work have singlet multiplicity. Because we have chosen to examine closed shell systems in this work, we have not examined other transition metals such as Fe that are also of interest for N_2 dissociation. The linear doped silver wires were optimized in the first step. In the next step, for the geometry optimization of the wire-N_2 systems, the wire was fixed while nitrogen atoms were relaxed. Then, LR-TDDFT calculations were performed to obtain the absorption spectra. Previous work has shown that the linear structure for the Ag_6N_2 systems is more stable than the T-shaped isomer.[38] In addition to the linear isomer, we also considered an L-shaped (90 degree) structure in this work; this is found to be the preferred isomer for group X dopants, but does not optimize for group XI and group XII dopants. The T-shaped isomer is found to be a higher energy isomer for

group XII dopants and does not optimize for group X or XI dopants (instead, the T-shaped isomer becomes an L-shaped isomer for group X dopants).

Real-time TDDFT (RT-TDDFT) calculations with fixed nuclei are also carried out to examine the electronic populations and transitions occurring after excitation. These simulations are referred to as electron-only dynamics and use the optimized ground state geometry. The applied electric field strengths are set to 0.03 au, 0.04 au, and 0.05 au, the frequencies for the applied electric field are equivalent to the longitudinal excitation energies for the doping nanowire.[57–59]

The mean field Ehrenfest dynamics scheme is coupled with the RT-TDDFT method,[44–48] and the nuclei are propagated based on a superposition of electronic states at a given time step. For the Ehrenfest dynamics simulations, the electronic step size used is 0.00025 fs and the nuclear step size is 0.1 fs. The metal atom coordinates are fixed and the nitrogen atoms are allowed to move during the simulations. Initial velocities for the system are set to zero unless otherwise noted, and the metal atoms are frozen during the dynamics. All Ehrenfest dynamics simulations start at the optimized ground state geometry. A single Ehrenfest trajectory is performed for all simulations; because the initial velocities are zero, sampling is not expected to change these results. It should be noted that Ehrenfest dynamics is a mean-field approach, and several issues such as lack of detailed balance can arise because the dynamics take place on an average potential surface.[60,61]

For both Ehrenfest dynamics and real-time TDDFT, a continuous wave electric field is turned on at 0 fs and turned off at 20 fs, and the field is ramped up (first 1 fs) and then down (final 1 fs) in strength with a trapezoidal envelope; the equation describing the field is shown in Equation 1:

$$
\begin{aligned}
&\boldsymbol{E(t) = t * \mathrm{E}_{max} \times \sin(\omega t)} && \textbf{for } \mathbf{0 \le t \le 1} \\
&\boldsymbol{E(\mathrm{t}) = \mathrm{E}_{max} \times \sin(\omega t)} && \textbf{for } \mathbf{1 \le t \le 19} \\
&\boldsymbol{E(\mathrm{t}) = (20 - t)\mathrm{E}_{max} \times \sin(\omega t)} && \textbf{for } \mathbf{19 \le t \le 20} \\
&\boldsymbol{E(t) = 0} && \textbf{for } \boldsymbol{t < 0 \text{ and } t > 20}
\end{aligned}
\qquad \textbf{Equation 4.1}
$$

where $\mathbf{E}_{max}$ is the electric field strength, and the frequency (ω) of the applied electric field is equivalent to the longitudinal excitation energy (determined from LR-TDDFT absorption spectra) for each system. The electric field is applied parallel with the Ag nanowire and the field strengths are set to 0.03 au, 0.04 au, and 0.05 au. These field strengths are larger than typical experimental field strengths. However, the N_2 will be dissociated at lower strength with the increasing size of

the nanowire;[40,62] therefore, it is reasonable to choose relatively intense electric fields for small nanowire systems.

4.4 Results and discussion

4.4.1 Binding energy analysis

Binding energy results for parallel configurations (Table 4.1) show that N_2 has the strongest binding with the Ag_6Pt wire and has the weakest binding with the Ag_6Hg wire. Generally, group X doped systems have relatively stronger binding energies than group XI doped systems, and group XII doped systems have the weakest binding energies. Systems with dopant atoms in the same group also show differences in binding energy results. For group XI doped systems, the Cu doped wire has a greater binding energy than the Au doped wire. For the group XII doped systems, the Zn doped wire has the strongest binding energy and the Hg doped wire has the weakest binding energy. For comparison, the heat of adsorption for N_2 on the Ag(111) surface has been reported to be 103 meV/atom (4.75 kcal/mol) at 42 K, and was previously measured to be 223 meV/atom (10.28 kcal/mol) at 77 K on the Ag(110) surface.[63] Pure platinum surfaces have N_2 adsorption energies of 0.20 eV (4.61 kcal/mol) for Pt(111)[64] and 0.36 eV (8.30 kcal/mol) for Pt(100).[65] The group X dopants in our model systems are highly undercoordinated, and the binding energies for these model systems are found to be larger than the binding energies to pure Pt metal.

Table 4.1 Binding energies between N_2 molecule and wire systems in the parallel configuration. The pure Ag_6 (Ag_5-Ag) wire is included as well for the comparison. Binding energies were calculated using the equation: $E_{binding} = E_{(wire)} + E_{(N_2)} - E_{(wire+N_2\ system)}$

Doped Wire	Binding Energy (kcal/mol)
Ag_6Ni	29.8
Ag_6Pd	13.3
Ag_6Pt	86.8
Ag_5Cu	14.6
Ag_6(Ag_5-Ag)	7.2
Ag_5Au	5.7
Ag_6Zn	2.7
Ag_6Cd	2.2
Ag_6Hg	2.0

4.4.2 Linear response TDDFT absorption spectra

The linear-response TDDFT absorption spectra for doped systems are shown in Figure 4.1. Based on the reported literature,[66] we sorted the plasmon excitations of doping Ag nanowires into two categories: longitudinal excitation mode and transverse excitation mode. Longitudinal excitations occur in the range of 1-2 eV, and transverse excitations occur in the range of 4-6 eV. According to previous results, the longitudinal excitation energy for the undoped Ag_6N_2 system is 1.88 eV; HOMO → LUMO and HOMO-1 → LUMO+1 are involved in the longitudinal excitation, with the HOMO → LUMO transition being dominant.[40] For the Ag_6NiN_2 doped system, the longitudinal excitation energy is 1.68 eV. HOMO → LUMO, HOMO-1 → LUMO+1, HOMO-4 → LUMO and HOMO-4 → LUMO+1 transitions are involved in the longitudinal excitation, and again the HOMO → LUMO transition has the greatest weight in the excited state. (Molecular orbitals for each system are shown in Figures B.1, B.2 and B.3.) For the Ag_6PdN_2 system, instead of one sharp peak, two split peaks are observed for the longitudinal excitation modes, with corresponding plasmonic excitation energies of 1.47 eV and 1.82 eV. This arises because the normal HOMO → LUMO transition that dominates the strong longitudinal excitations for other systems mixes with transitions from the HOMO-3 into the LUMO and LUMO+1 for Ag_6PdN_2. This causes peak splitting and intensity borrowing for the normally weak transition out of HOMO-3 into LUMO and LUMO+1. As shown in Figure B.1B, the HOMO-3 for this system is primarily located on the Pd atom and the two neighboring silver atoms. For the Ag_6PtN_2 system, the longitudinal excitation energy is 1.59 eV, and the electronic transitions involved in this excitation are HOMO → LUMO (dominant) and HOMO-1 → LUMO+1.

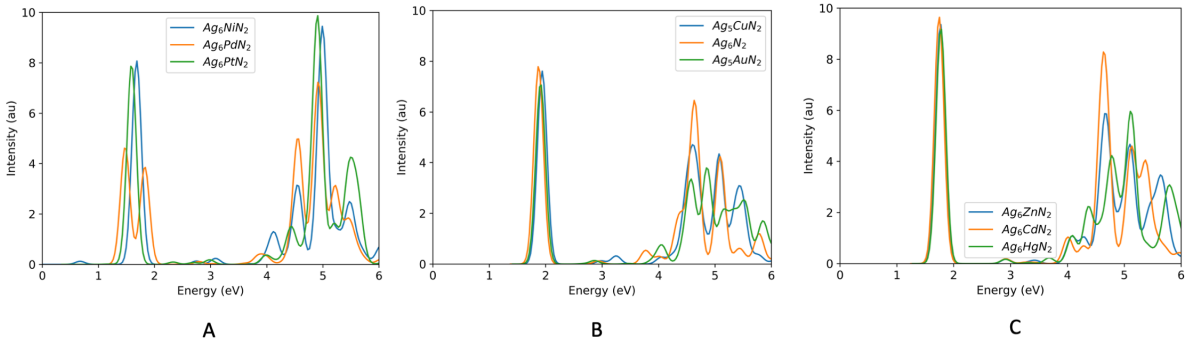


Figure 4.1 Linear-response excitation spectra for A. group X doped systems, B. group XI doped systems, and C. group XII doped systems.

For group XI doped systems (Au, Cu), the longitudinal excitation energies are 1.91 eV and 1.94 eV for Ag_5AuN_2 and Ag_5CuN_2, respectively. For Ag_5AuN_2, transitions involved in the longitudinal excitation are HOMO-1 → LUMO+1 and HOMO → LUMO. For the Ag_5CuN_2 system, the involved electronic transitions for the longitudinal excitation are HOMO-1 → LUMO+3 and HOMO → LUMO. It is notable that LUMO+3 in Ag_5CuN_2 and LUMO+1 in Ag_5AuN_2 have very similar orbital characters, as shown in Figure 4.2.

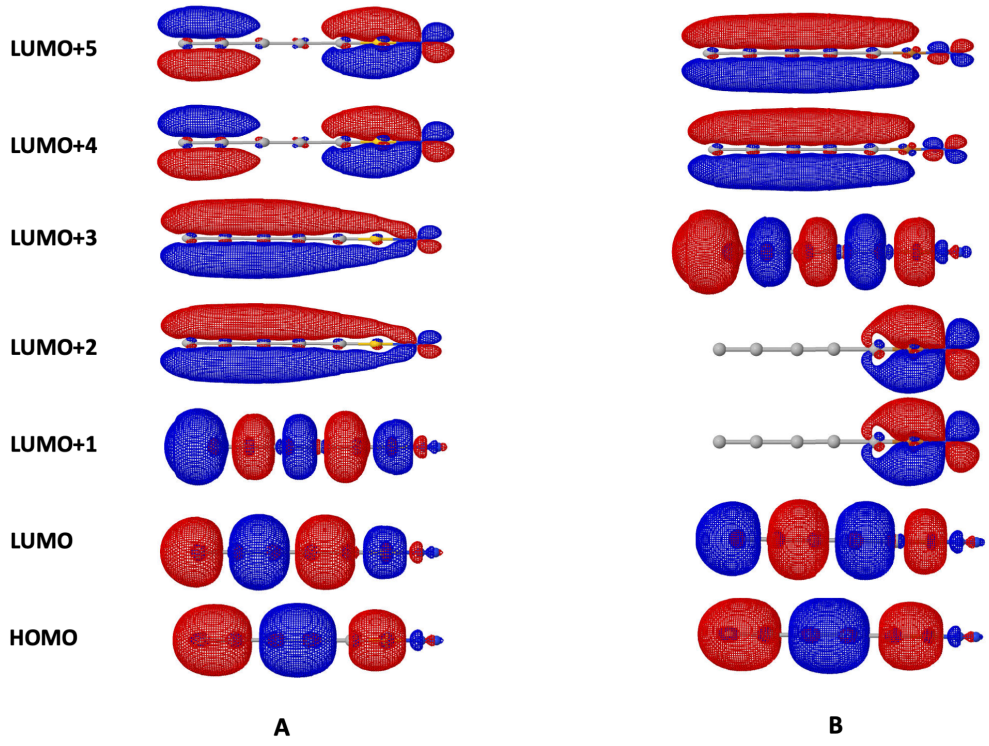


Figure 4.2 Kohn-Sham ground state molecular orbitals diagram of selected orbitals for A. Ag_5AuN_2 and B. Ag_5CuN_2 (isovalue =0.01).

When doping the Ag wire with a transition metal from group XII (Zn, Cd, and Hg), the longitudinal excitation energies are 1.77 eV, 1.75 eV, and 1.78 eV for Ag_6ZnN_2, Ag_6CdN_2, and Ag_6HgN_2, respectively. The electronic transitions involved in the longitudinal excitation mode are HOMO-1 → LUMO+1 and HOMO → LUMO.

As a summary of the linear response TDDFT results, the dominant transition in the longitudinal excitation mode is HOMO → LUMO for all systems (Table 4.2). For different systems, the longitudinal excitation energies are similar when the metal dopants are in the same group. However, when a Pd atom is doped in the Ag wire, the absorption spectrum exhibits two low-energy peaks due to a splitting in the longitudinal excitation mode, and more molecular orbitals are involved in the electronic transitions.

Table 4.2 Longitudinal excitation mode energy and the corresponding electronic transitions and their contributions for each linear doped system.

	Excitation energy (eV)	Transition	Contribution
Ag_6NiN_2	1.68	HOMO-4 → LUMO	2.0%
		HOMO-4 → LUMO+1	7.2%
		HOMO-1 → LUMO	2.7%
		HOMO → LUMO	84.6%
Ag_6PdN_2	1.48	HOMO-3 → LUMO	14.9%
		HOMO-3 → LUMO+1	14.6%
		HOMO-3 → LUMO+2	6.2%
		HOMO-1 → LUMO	3.4%
		HOMO-1 → LUMO+1	7.6%
		HOMO → LUMO	44.3%
	1.83	HOMO-3 → LUMO	19.5%
		HOMO-3 → LUMO+1	17.7%
		HOMO-3 → LUMO+2	6.0%
		HOMO-2 → LUMO+1	2.9%
		HOMO → LUMO	44.5%
Ag_6PtN_2	1.59	HOMO-1 → LUMO+1	8.8%
		HOMO → LUMO	86.3%
Ag_5CuN_2	1.94	HOMO-1 → LUMO+3	5.7%
		HOMO → LUMO	91.6%
Ag_5AuN_2	1.91	HOMO-1 → LUMO+1	5.4%
		HOMO → LUMO	91.9%
Ag_6ZnN_2	1.77	HOMO-1 → LUMO+1	6.7%
		HOMO → LUMO	90.0%
Ag_6CdN_2	1.75	HOMO-1 → LUMO+1	6.9%
		HOMO → LUMO	89.8%
Ag_6HgN_2	1.78	HOMO-1 → LUMO+1	6.8%
		HOMO → LUMO	90.2%

4.4.3 90° structure

In the preceding section, calculations were performed on linear geometries in which the adsorbate is parallel to the doped nanowire (Figure 4.3A). Geometry optimization of the group X

metal-doped system indicates that a different binding configuration between the N_2 molecule and the wire, in which the N_2 molecule is bound to the wire at an almost 90º angle (Figure 4.3B), is preferred. The 90º structure has a higher binding energy than the parallel structure (Table 4.3), indicating that the N_2 molecule is more stable at a 90º angle.

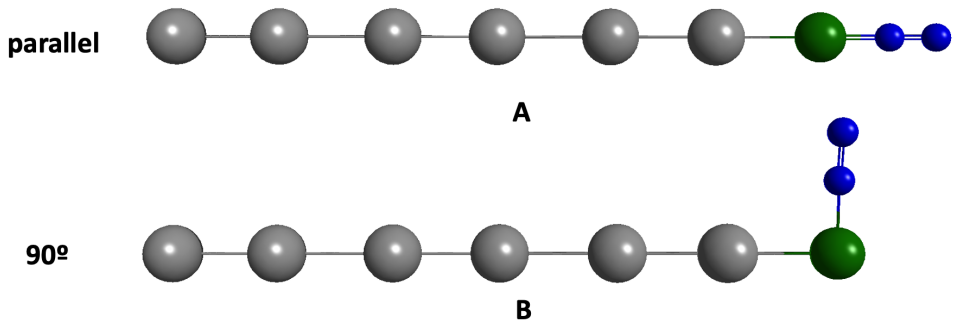


Figure 4.3 Ground state optimized geometries for parallel and 90º structures. A. Optimized parallel structure for the Ag_6NiN_2 system. B. Optimized structure for the 90º Ag_6NiN_2 system. Key: silver=silver, nickel=green, and nitrogen=blue.

Table 4.3 Binding energies for different configurations of group X metal-doped systems.

	Binding Energy (kcal/mol)	
	parallel	**90º**
Ag_6Ni	29.8	41.1
Ag_6Pd	13.3	19.4
Ag_6Pt	86.8	94.8

The LR-TDDFT absorption spectra show that the 90º structures have an intense peak in the longitudinal excitation mode for these three systems (Figure 4.4). For Ag_6NiN_2, the two configurations show almost identical absorption peaks in the longitudinal excitation, and the parallel structure shows a more intense peak than the 90º structure at around 5 eV in the absorption spectra. For the Ag_6PdN_2 system, the parallel structure shows two split peaks, whereas the 90º structure shows only one intense peak in the longitudinal excitation mode. For the Ag_6PtN_2 system, the parallel structure shows slightly higher absorption intensity than the 90º structure for the longitudinal excitation mode, and the parallel structure shows an intense peak at around 5 eV. Overall, the location of the adsorbate primarily affects the longitudinal mode of Ag_6PdN_2 due to the peak splitting in this system.

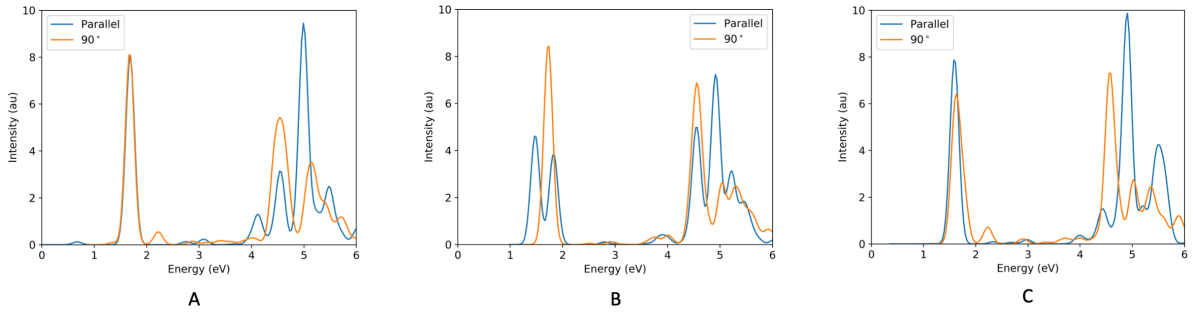


Figure 4.4 Comparison of the linear-response excitation spectra between parallel structure and 90° structure in A: Ag_6NiN_2, B: Ag_6PdN_2, and C: Ag_6PtN_2 systems.

4.4.4 Mean-field Ehrenfest dynamics

As discussed in the preceding sections, linear-response TDDFT calculations have provided electronic excitation information for each doped system. In this section, an external field with a frequency corresponding to the longitudinal excitation energy will be applied to each system to examine their dynamic features. Mean-field Ehrenfest dynamics are performed to understand the motion of N atoms with different doped wires under different applied field strengths.

The N-N distance variation with time is shown in Figure 4.5 for seven doped systems. The N-N bond distance remained unchanged for approximately the first 5 fs. This may indicate that the plasmonic excitation of the wire takes at least 5 fs to transfer to the N_2 molecule and/or the fact that it takes several fs for charge on N_2 to build up.[38] In the 0.03 au field, nitrogen shows a small degree of activation in all systems; the N-N distance oscillates between 1.0 Å and 1.5 Å during the 100 fs of simulation. However, N_2 does not dissociate with this field strength for any of these systems. When increasing the electric field intensity to 0.04 au, we observe an ultrafast N_2 dissociation in the Ag_5AuN_2 system (dissociation occurs within around 40 fs, where dissociation is defined as an N-N distance greater than 2.0 Å). N_2 is also dissociated on Ag_6HgN_2 and almost dissociated on Ag_6ZnN_2 (N-N distance is 1.94 Å) within 100 fs; however, the N_2 dissociation starts after 80 fs and the dissociation rate is slow compared to the N_2 dissociation for Ag_5AuN_2. In the other systems that do not dissociate, longer average bond lengths and a lower frequency of bond length oscillation are noted, which are indicative of a weaker N-N bond in agreement with previous work that focused on the activation of the N-N bond.[38] Upon increasing the field strength to 0.05 au, N_2 can be dissociated in all systems except Ag_5CuN_2. N_2 shows the fastest dissociation in the

Ag_5AuN_2 system. It should be noted that previous work has shown that N_2 is not dissociated in similar applied fields without the presence of a nanowire.[67]

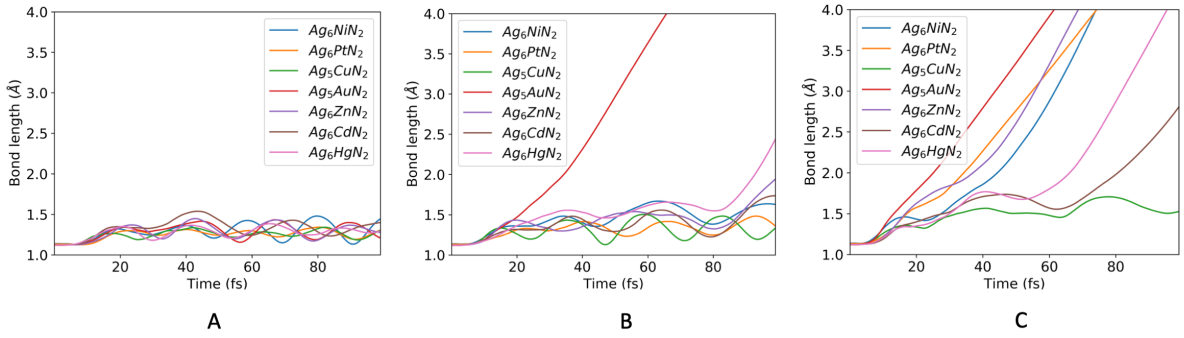


Figure 4.5 Variation of the N-N distance during nonadiabatic dynamics using the A. 0.03 au, B. 0.04 au, and C. 0.05 au electric fields with frequencies corresponding to the longitudinal excitation of each parallel system.

The distance between the terminal doped metal atom and N1 (the nitrogen which is closest to the wire) is shown in Figure B.4. The results show that the nitrogen atoms gradually fly away from the system during the dynamics.

Ehrenfest dynamics were also performed for the 90º structure systems. The N-N variation with time for the Ag_6NiN_2 system is shown in Figure 4.6. With the 0.03 au and 0.04 au field strength, N_2 is not dissociated for either the parallel structure or the 90º structure, and the N_2 shows a higher degree of activation in the parallel structure than in the 90º structure. In the 0.05 au field for the parallel structure, the N_2 bond distance initially increased to 1.5 Å followed by a slight decrease to 1.4 Å around 20 fs. Then, N_2 exhibited a fast dissociation after 20 fs in the parallel structure. Meanwhile, for the 90º structure, the N_2 bond distance increases up to 1.5 Å within the first 60 fs and then shows a flat curve after 60 fs.

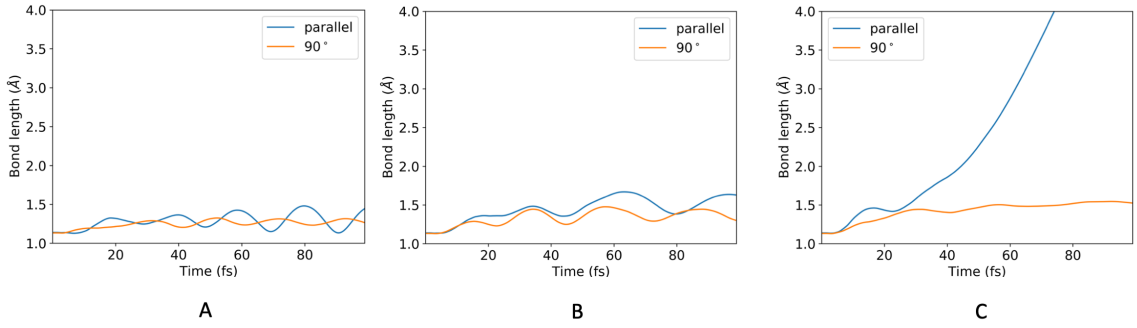


Figure 4.6 Comparison of Ehrenfest dynamics results between parallel structure and 90º structure for the Ag_6NiN_2 system with A. 0.03 au, B. 0.04 au, and C. 0.05 au electric field strengths excited at the longitudinal excitation energy.

For the Ag_6NiN_2 systems, the geometries at 50 fs in Ehrenfest dynamics were extracted and shown in Figure 4.7. For the parallel structure, the N-N bond length has reached up to 2.6 Å at 50 fs, and we can observe the two N atoms have already desorbed from the wire. There is no rotation in the N_2 molecule. Meanwhile, for the 90º structure, the N_2 molecule did not dissociate at 50 fs, and we can observe rotation of the N_2 molecule in the Ehrenfest dynamics.

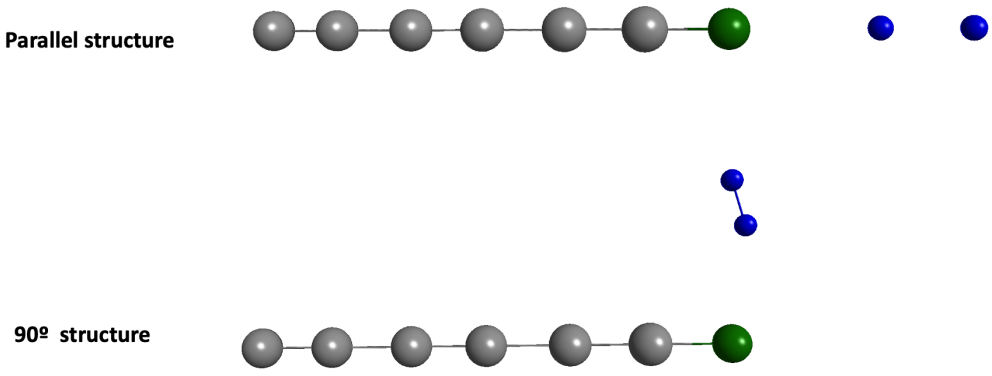


Figure 4.7 Snapshot of the Ag_6NiN_2 geometry at 50 fs for parallel structure and 90º structure from the 0.05 au electric field simulation. Key: silver=silver, nickel=green, and nitrogen=blue.

The N-N variation with time for the Ag_6PtN_2 system is shown in Figure B.5. N_2 is not dissociated in both parallel and 90º structures using the 0.03 au and 0.04 au fields. With the 0.05 au field, N_2 can be dissociated very fast (within 40 fs) in the parallel structure. For the 90º structure,

N_2 can be more intensely activated with the 0.05 au electric field than with the 0.03 au and 0.04 au electric fields, but is still not dissociated.

The comparison between the parallel structure and the 90º structure indicates that the parallel structure will generally show better plasmon-enhancement properties for N_2 dissociation than the 90º structure upon excitation of the longitudinal excitation mode, despite the stronger binding energy of the 90° structure.

4.4.5 Ag_5CuN_2 vs Ag_5AuN_2

The nonadiabatic dynamics results (Figure 4.5) indicate that Ag_5Au shows significantly better plasmon-enhanced N_2 dissociation properties than Ag_5Cu in parallel configurations. To unravel the mechanism behind this, we studied these two systems in more detail, including aspects of thermal effects, electronic structure, and potential energy surfaces.

To study how initial temperature affects the Ehrenfest dynamics results, we chose 0K, 30K, 90K, and 300K as the initial temperature for the system and performed the Ehrenfest dynamics simulations again. The way we incorporated temperature into the system is to add a total nuclear kinetic energy to the system, which is equivalent to the translational energy at that specific temperature. For example, for an initial velocity of 30K, we add 0.00009 au to the total nuclear kinetic energy. Variation of the N-N distance results (Figure 4.8) indicate that initial temperature will affect the Ehrenfest dynamics results; however, the N_2 dissociation rate is not linearly correlated with the initial temperature. For Ag_5CuN_2, N_2 can only be activated, regardless of the temperature. For Ag_5AuN_2, N_2 shows the highest dissociation rate with the initial temperature at 0K, although N_2 is not dissociated with the initial temperature at 90K. The results likely occur due to the stochastic features of the plasmon-induced processes occurring on Ag nanowires. Additional sampling could be useful in the future to analyze the temperature effects.

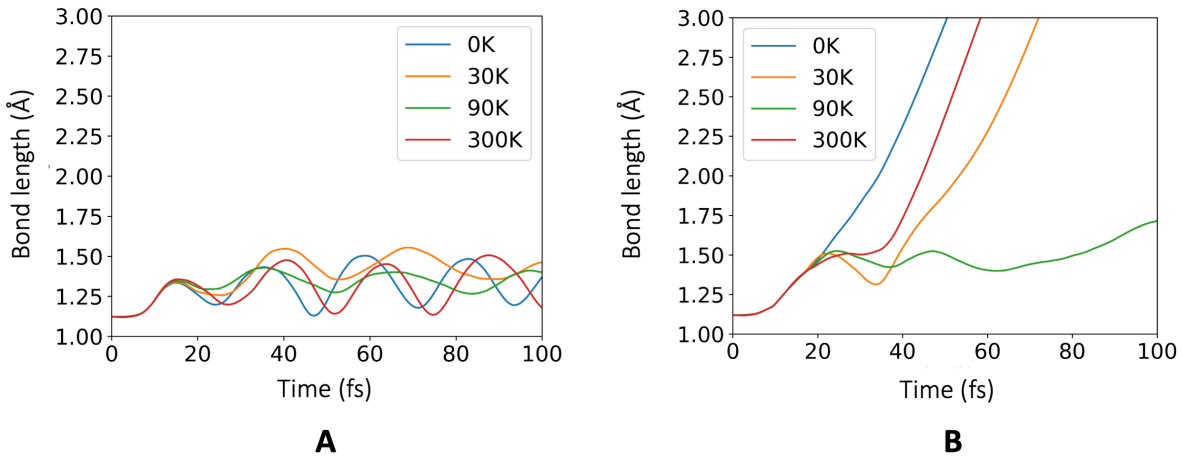


Figure 4.8 Variation of the N-N distance in Ehrenfest dynamics at different initial temperatures A. Ag_5Cu (parallel system) B. Ag_5Au (parallel system) in 0.04 au electric field.

Orbitals in the range from HOMO to LUMO+5 were analyzed to investigate their electronic structures; Kohn-Sham (KS) orbitals are plotted in Figure 4.2. The orbital ordering is different between the Ag_5CuN_2 and Ag_5AuN_2 molecular systems: the LUMO+1 shows Σ_5 character in Ag_5AuN_2, whereas LUMO+3 shows Σ_5 character in Ag_5CuN_2. Although the orbital orderings show differences between the two systems, the HOMO-LUMO gap energies are very similar (4.88 eV and 4.90 eV), and the energy gap between Σ_3 and Σ_5 is the same (6.55 eV), as shown in Table 4.

Table 4.4 Orbital energy, orbital character, contributions of N1 and N2 atomic orbitals to the molecular orbitals, and two selected energy gaps for Ag_5AuN_2 and Ag_5CuN_2 parallel system.

	Ag_5AuN_2				Ag_5CuN_2			
Orbital	**Energy (eV)**	**Character**	**N1 (%)**	**N2 (%)**	**Energy (eV)**	**Character**	**N1 (%)**	**N2 (%)**
HOMO	-7.04	Σ_3	1.03	0.12	-6.56	Σ_3	1.06	0.13
LUMO	-2.16	Σ_4	1.87	0.22	-1.66	Σ_4	2.25	0.24
LUMO+1	-0.50	Σ_5	3.27	0.46	-0.33	π_{N2}^*	40.22	49.77
LUMO+2	0.41	Π_1	8.32	10.72	-0.33	π_{N2}^*	40.22	49.77
LUMO+3	0.41	Π_1	8.32	10.72	-0.02	Σ_5	3.97	0.31
LUMO+4	0.61	Π_2	30.15	36.62	0.69	Π_1	7.75	5.28
LUMO+5	0.61	Π_2	30.15	36.62	0.69	Π_1	7.75	5.28
Energy Gap	Ag_5AuN_2				Ag_5CuN_2			
$\Sigma_3 \rightarrow \Sigma_4$	4.88 eV				4.90 eV			
$\Sigma_3 \rightarrow \Sigma_5$	6.55 eV				6.55 eV			

Ag_5AuN_2 does not have low energy orbitals with almost exclusively π_{N2}^* character; instead, the LUMO+2/LUMO+3 shows delocalized Π_1 character in the Ag_5AuN_2 system, and the contributions of the two nitrogen atomic orbitals to the Π_1 molecular orbital are 8.32% and 10.72% respectively. LUMO+4/LUMO+5 in Ag_5AuN_2 show Π_2 character, and the contribution of the two nitrogen atomic orbitals to the Π_2 orbital is higher than to the Π_1 orbital; however, this orbital still has significant contribution from the Ag orbitals, unlike the Ag_5CuN_2 system. In Ag_5CuN_2, LUMO+1 and LUMO+2 are π_{N2}^* character orbitals, and the contribution of the two nitrogen atomic orbitals to the π_{N2}^* orbital are 40.22% and 49.77%. LUMO+4 and LUMO+5 show Π_1 character and the contributions of the two nitrogen atomic orbitals to these molecular orbitals are 7.75% and 5.28%.

The electron-only (fixed nuclear) RT-TDDFT orbital population results share similarities between Ag_5AuN_2 and Ag_5CuN_2 systems, as shown in Figure 4.9. We can observe that the orbital population increases in Π character orbitals are rather small compared to the orbital population increases in Σ character orbitals upon longitudinal excitation, which is expected from the symmetry of the orbitals involved.

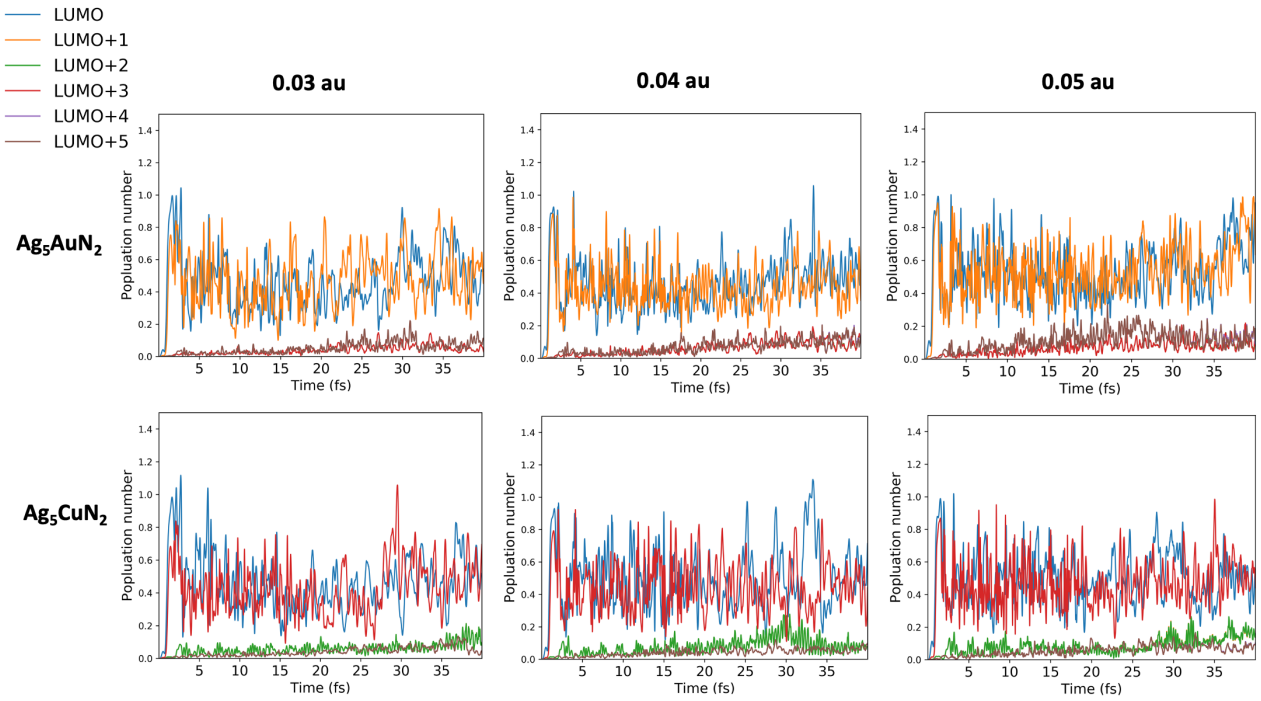


Figure 4.9 Comparison of orbital population results between the Ag_5AuN_2 and Ag_5CuN_2 parallel systems using RT-TDDFT calculations.

Next, geometry optimizations of Ag_5CuN_2 and Ag_5AuN_2 were performed with different constrained N-N bond lengths (1.2 Å, 1.3 Å, 1.4 Å, 1.5 Å, and 1.6 Å). The relative energy and optimized angle (Ag-N-N) results with different N-N distances are shown in Table 5.

For the ground state equilibrium structures, the N-N bond length is 1.12 Å for the Ag_5CuN_2 system and 1.13 Å for the Ag_5AuN_2 system. As the N-N bond length elongates, the energy of the system increases, and the angle between N_2 and the wire changes from a linear to a bent structure. In Ag_5CuN_2, the N_2 molecule starts to access a bent structure when the bond length changes from 1.3 Å to 1.4 Å. In Ag_5AuN_2, the N_2 molecule starts to be bent when elongating the bond length from 1.2 Å to 1.3 Å. This may be due to Ag_5Cu having stronger binding energy with N_2 at equilibrium geometry.

Table 4.5 Constrained geometry optimization results for Ag_5CuN_2 and Ag_5AuN_2. During the optimization process, the N-N bond length is fixed at 1.2 Å, 1.3 Å, 1.4 Å, 1.5 Å, and 1.6 Å. The relative energy for each system is calculated based on the equilibrium structure energy as reference.

Ag_5CuN_2			Ag_5AuN_2		
Bond (Å)	**Angle (°)**	**Relative Energy (eV)**	**Bond (Å)**	**Angle (°)**	**Relative Energy (eV)**
1.2	180.0	0.36	**1.2**	180.0	0.40
1.3	180.0	1.54	**1.3**	141.4	1.56
1.4	148.1	3.54	**1.4**	132.7	3.14
1.5	136	4.60	**1.5**	126.2	4.79
1.6	130.1	6.14	**1.6**	82.4	6.41

KS molecular orbital diagrams for constrained Ag_5CuN_2 optimized structures are shown in Figure 4.10. When the N-N distance is 1.1 Å, LUMO shows Σ_4 character and LUMO+1/LUMO+2 shows π_{N2}^* character. With increasing N-N bond length, the orbital characters are mixed for the 1.3 Å structure. When the N-N bond length is at 1.35 Å, we can observe that the LUMO and LUMO+1 show π_{N2}^* character and LUMO+2 shows Σ_4 character. The above results indicate that the orbital energy of the π_{N2}^* character orbital will become lower than the Σ_4 orbital when the N-N bond length elongates.

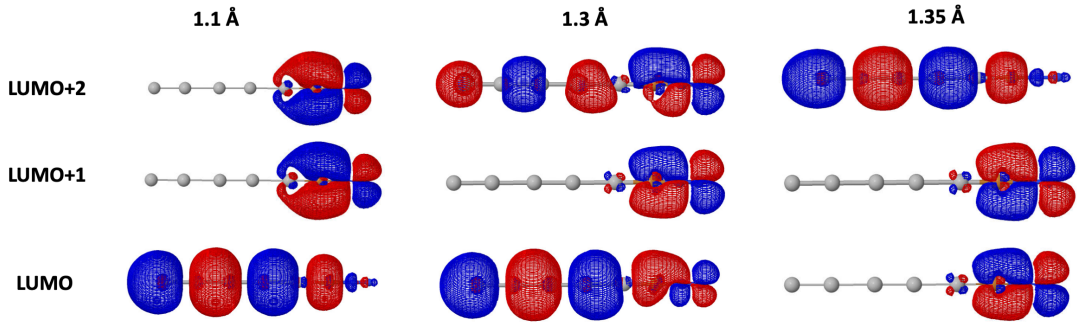


Figure 4.10 Selected KS ground state molecular orbitals for Ag_5CuN_2 at different constrained N-N bond lengths (isovalue =0.01). For the 1.1 Å system, the LUMO+1 and LUMO+2 form a degenerate set; images are shown from the x and y directions. For the 1.35 Å system, LUMO and LUMO+1 form a degenerate set; images are shown from the x and y directions.

Based on the above studies, we analyze several hypotheses to explain the differences in plasmon-enhanced N_2 dissociation properties in Ag_5CuN_2 and Ag_5AuN_2, which appear for all temperatures (i.e., initial velocities) examined in this work. Overall, the differences in plasmon-enhanced N_2 dissociation do not appear to arise from the differences in the ground state KS molecular orbitals for the wire-N_2 systems; both systems have similar energy gaps and excited orbital populations for the Σ_4 and Σ_5 orbitals, which are the ones involved in the transitions responsible for plasmon-enhanced N_2 dissociation. Instead, the more likely hypothesis based on our current work is that the doped transition metal affects the potential energy landscapes, particularly how the electronic structure depends on non-equilibrium geometries, which then may lead to differences in the nuclear motions of the systems in excited states.

4.5 Conclusions

In this work, we applied electronic structure calculations and nonadiabatic dynamics simulations to study the plasmon-enhanced N_2 dissociation process for different doped systems. We found that the excited state dynamics results do not have a direct correlation with the ground state binding energy between the wire and the N_2 molecule. Parallel configurations were considered for all systems. In addition to the parallel structure, a 90º configuration was found for the group X doped systems. By performing Ehrenfest dynamics simulations, we found that the parallel structure shows better plasmon-enhanced dissociation properties than the 90º structure when the longitudinal excitation mode is excited. Interestingly, the N_2 dissociation has little correlation with the binding energy. One possible reason might be that the binding energy arises from the ground state. However, N_2 dissociation is more related to the excited-state potential energy surface, which may differ substantially from the ground-state potential energy surface. Overall, Ag_5Au showed the best plasmon-enhanced catalysis properties for N_2 dissociation with longitudinal excitation. However, the Ag_5Cu system shows quite weak plasmon-enhanced properties for N_2 dissociation with the longitudinal excitation. The differences in plasmon-enhanced properties can be due to the differences in the electronic structure and potential energy surfaces for doped systems. In addition, the initial temperature will play a role in the plasmon-catalyzed process, which will affect the N_2 activation and dissociation.

4.6 Supporting information

Supporting information provides information on the selected molecular orbitals of the doped system, comparison of Ehrenfest dynamics results between parallel structure and 90º structure of Ag_6PtN_2 system, and variation of the doped metal-N1 distance during nonadiabatic dynamics. The ground state optimized structures for all the systems involved in the work are uploaded into the link:

https://github.com/YuchenWang2015/doping-wire/blob/12fe4d7b14a7eb0bbf26b1ee86f1613be97aa604/geometry.rtf

4.7 Acknowledgment

The work is supported by the Department of Energy under grant DE-SC0012273. The computing for this work was performed on the Beocat Research Cluster at Kansas State University, which is partially funded by the NSF (Grant Nos. CHE-1726332, CNS-1006860, EPS-1006860, and EPS-0919443). The authors thank Prof. Xiaosong Li for providing the RT-TDDFT and Ehrenfest Dynamics code.

4.8 References

(1) Christopher, P.; Xin, H.; Linic, S. Visible-Light-Enhanced Catalytic Oxidation Reactions on Plasmonic Silver Nanostructures. *Nature Chem* **2011**, *3* (6), 467–472.

(2) Ekinci, Y.; Solak, H. H.; Löffler, J. F. Plasmon Resonances of Aluminum Nanoparticles and Nanorods. *Journal of Applied Physics* **2008**, *104* (8), 083107.

(3) Mayer, K. M.; Hafner, J. H. Localized Surface Plasmon Resonance Sensors. *Chem. Rev.* **2011**, *111* (6), 3828–3857.

(4) Huang, X.; El-Sayed, M. A. Gold Nanoparticles: Optical Properties and Implementations in Cancer Diagnosis and Photothermal Therapy. *Journal of Advanced Research* **2010**, *1* (1), 13–28.

(5) Verre, R.; Maccaferri, N.; Fleischer, K.; Svedendahl, M.; Odebo Länk, N.; Dmitriev, A.; Vavassori, P.; Shvets, I. V.; Käll, M. Polarization Conversion-Based Molecular Sensing Using Anisotropic Plasmonic Metasurfaces. *Nanoscale* **2016**, *8* (20), 10576–10581.

(6) Taylor, A. B.; Zijlstra, P. Single-Molecule Plasmon Sensing: Current Status and Future Prospects. *ACS Sens.* **2017**, *2* (8), 1103–1122.

(7) Aioub, M.; Kang, B.; Mackey, M. A.; El-Sayed, M. A. Biological Targeting of Plasmonic Nanoparticles Improves Cellular Imaging via the Enhanced Scattering in the Aggregates Formed. *J. Phys. Chem. Lett.* **2014**, *5* (15), 2555–2561.

(8) Dong, Y.; Hu, C.; Xiong, H.; Long, R.; Xiong, Y. Plasmonic Catalysis: New Opportunity for Selective Chemical Bond Evolution. *ACS Catal.* **2023**, *13* (10), 6730–6743.

(9) Shaver, M. P.; Fryzuk, M. D. Activation of Molecular Nitrogen: Coordination, Cleavage and Functionalization of N2 Mediated By Metal Complexes. *Advanced Synthesis & Catalysis* **2003**, *345* (910), 1061–1076.

(10) van der Ham, C. J. M.; Koper, M. T. M.; Hetterscheid, D. G. H. Challenges in Reduction of Dinitrogen by Proton and Electron Transfer. *Chem. Soc. Rev.* **2014**, *43* (15), 5183–5191.

(11) Spata, V. A.; Carter, E. A. Mechanistic Insights into Photocatalyzed Hydrogen Desorption from Palladium Surfaces Assisted by Localized Surface Plasmon Resonances. *ACS Nano* **2018**, *12* (4), 3512–3522.

(12) Swearer, D. F.; Zhao, H.; Zhou, L.; Zhang, C.; Robatjazi, H.; Martirez, J. M. P.; Krauter, C. M.; Yazdi, S.; McClain, M. J.; Ringe, E.; Carter, E. A.; Nordlander, P.; Halas, N. J. Heterometallic Antenna−reactor Complexes for Photocatalysis. *Proc. Natl. Acad. Sci. U.S.A.* **2016**, *113* (32), 8916–8920.

(13) Xiao, Q.; Sarina, S.; Bo, A.; Jia, J.; Liu, H.; Arnold, D. P.; Huang, Y.; Wu, H.; Zhu, H. Visible Light-Driven Cross-Coupling Reactions at Lower Temperatures Using a Photocatalyst of Palladium and Gold Alloy Nanoparticles. *ACS Catal.* **2014**, *4* (6), 1725–1734.

(14) Antosiewicz, T. J.; Apell, S. P.; Wadell, C.; Langhammer, C. Absorption Enhancement in Lossy Transition Metal Elements of Plasmonic Nanosandwiches. *J. Phys. Chem. C* **2012**, *116* (38), 20522–20529.

(15) Sarina, S.; Zhu, H.; Jaatinen, E.; Xiao, Q.; Liu, H.; Jia, J.; Chen, C.; Zhao, J. Enhancing Catalytic Performance of Palladium in Gold and Palladium Alloy Nanoparticles for Organic Synthesis Reactions through Visible Light Irradiation at Ambient Temperatures. *J. Am. Chem. Soc.* **2013**, *135* (15), 5793–5801.

(16) Aoki, Y.; Ishida, T.; Tatsuma, T. Plasmon-Induced Photocatalysis Based on Pt–Au Coupling with Enhanced Oxidation Abilities. *ACS Appl. Nano Mater.* **2022**, *5* (3), 4406–4412.

(17) Ma, L.; Ding, S.-J.; Yang, D.-J. Preparation of Bimetallic Au/Pt Nanotriangles with Tunable Plasmonic Properties and Improved Photocatalytic Activity. *Dalton Trans.* **2018**, *47* (47), 16969–16976.

(18) Suyama, M.; Takano, S.; Tsukuda, T. Synergistic Effects of Pt and Cd Co doping to Icosahedral Au_{13} Superatoms. *J. Phys. Chem. C* **2020**, *124* (43), 23923–23929.

(19) Barcaro, G.; Sementa, L.; Fortunelli, A.; Stener, M. Optical Properties of Pt and Ag–Pt Nanoclusters from TDDFT Calculations: Plasmon Suppression by Pt Poisoning. *J. Phys. Chem. C* **2014**, *118* (48), 28101–28108.

(20) Sulaiman, K. O.; Purves, R. W.; Scott, R. W. J. Exploring the Structure of Atom-Precise Silver–Palladium Bimetallic Clusters Prepared via Improved Single-Pot Co-Reduction Synthesis Protocol. *J. Chem. Phys* **2021**, *155* (8), 084301.

(21) Alexander, D. T. L.; Forrer, D.; Rossi, E.; Lidorikis, E.; Agnoli, S.; Bernasconi, G. D.; Butet, J.; Martin, O. J. F.; Amendola, V. Electronic Structure-Dependent Surface Plasmon Resonance in Single Au–Fe Nanoalloys. *Nano Lett.* **2019**, *19* (8), 5754–5761.

(22) Amendola, V.; Saija, R.; Maragò, O. M.; Iatì, M. A. Superior Plasmon Absorption in Iron-Doped Gold Nanoparticles. *Nanoscale* **2015**, *7* (19), 8782–8792.

(23) Li, Y.; Luo, T.-Y.; Zhou, M.; Song, Y.; Rosi, N. L.; Jin, R. A Correlated Series of Au/Ag Nanoclusters Revealing the Evolutionary Patterns of Asymmetric Ag Doping. *J. Am. Chem. Soc.* **2018**, *140* (43), 14235–14243.

(24) Loiseau, A.; Zhang, L.; Hu, D.; Salmain, M.; Mazouzi, Y.; Flack, R.; Liedberg, B.; Boujday, S. Core–Shell Gold/Silver Nanoparticles for Localized Surface Plasmon Resonance-Based Naked-Eye Toxin Biosensing. *ACS Appl. Mater. Interfaces* **2019**, *11* (50), 46462–46471.

(25) Yin, Z.; Wang, Y.; Song, C.; Zheng, L.; Ma, N.; Liu, X.; Li, S.; Lin, L.; Li, M.; Xu, Y.; Li, W.; Hu, G.; Fang, Z.; Ma, D. Hybrid Au–Ag Nanostructures for Enhanced Plasmon-Driven Catalytic Selective Hydrogenation through Visible Light Irradiation and Surface-Enhanced Raman Scattering. *J. Am. Chem. Soc.* **2018**, *140* (3), 864–867.

(26) Nilius, N.; Wallis, T. M.; Ho, W. Development of One-Dimensional Band Structure in Artificial Gold Chains. *Science* **2002**, *297* (5588), 1853–1856.

(27) Kümmel, S.; Andrae, K.; Reinhard, P.-G. Collectivity in the Optical Response. of Small Metal Clusters. *Applied Physics B: Lasers and Optics* **2001**, *73* (4), 293–297.

(28) Liu, D.-D.; Zhang, H. A Time-Dependent Density Functional Theory Investigation of Plasmon Resonances of Linear Au Atomic Chains. *Chinese Phys. B* **2011**, *20* (9), 097105.

(29) Yan, J.; Yuan, Z.; Gao, S. End and Central Plasmon Resonances in Linear Atomic Chains. *Phys. Rev. Lett.* **2007**, *98* (21), 216602.

(30) Nayyar, N.; Turkowski, V.; Rahman, T. S. Optical Generation of Collective Plasmon Modes in Small Gold Chains Induced by Doping Transition-Metal Impurities. *Phys. Rev. Lett.* **2012**, *109* (15), 157404.

(31) Yan, J.; Gao, S. Plasmon Resonances in Linear Atomic Chains: Free-Electron Behavior and Anisotropic Screening of d Electrons. *Phys. Rev. B* **2008**, *78* (23), 235413.

(32) Li, W.; Chen, F. Effect of Transition Metal (Fe, Cu, Ni, Rh)-Doped Small Silver Chains on Optics of Plasmon Resonances. *Appl. Phys. A* **2013**, *113* (3), 543–548.

(33) Johnson, H. E.; Aikens, C. M. Electronic Structure and TDDFT Optical Absorption Spectra of Silver Nanorods. *J. Phys. Chem. A* **2009**, *113* (16), 4445–4450.

(34) Piccini, G.; Havenith, R. W. A.; Broer, R.; Stener, M. Gold Nanowires: A Time-Dependent Density Functional Assessment of Plasmonic Behavior. *J. Phys. Chem. C* **2013**, *117* (33), 17196–17204.

(35) Conley, K. M.; Nayyar, N.; Rossi, T. P.; Kuisma, M.; Turkowski, V.; Puska, M. J.; Rahman, T. S. Plasmon Excitations in Mixed Metallic Nanoarrays. *ACS Nano* **2019**, *13* (5), 5344–5355.

(36) Li, T. E.; Hammes-Schiffer, S. Nuclear-Electronic Orbital Quantum Dynamics of Plasmon-Driven H_2 Photodissociation. *J. Am. Chem. Soc.* **2023** *145* (33), 18210-1821.

(37) Wu, Q.; Zhou, L.; Schatz, G. C.; Zhang, Y.; Guo, H. Mechanistic Insights into Photocatalyzed H_2 Dissociation on Au Clusters. *J. Am. Chem. Soc.* **2020**, *142* (30), 13090–13101.

(38) Hull, O. A.; Aikens, C. M. Theoretical Investigations on the Plasmon-Mediated Dissociation of Small Molecules in the Presence of Silver Atomic Wires. *J. Phys. Chem. A* **2023**, *127* (10), 2228–2241.

(39) Kuda-Singappulige, G. U.; Aikens, C. M. Theoretical Insights into Excitation-Induced Oxygen Activation on a Tetrahedral Ag_8 Cluster. *J. Phys. Chem. A* **2021**, *125* (43), 9450–9458.

(40) Wang, Y.; Aikens, C. M. Effects of Field Strength and Silver Nanowire Size on Plasmon-Enhanced N_2 Dissociation. *J. Phys. Chem. A* **2023**, *127* (27), 5609–5619.

(41) Wang, Y.; Aikens, C. M. Connectivity between Static Field and Continuous Wave Field Effects on Excitation-Induced H_2 Activation. *J. Phys. Chem. C* **2023** *127* (31), 15375-15384.

(42) Huang, J.; Zhao, X.; Huang, X.; Liang, W. Understanding the Mechanism of Plasmon-Driven Water Splitting: Hot Electron Injection and a near Field Enhancement Effect. *Phys. Chem. Chem. Phys.* **2021**, *23* (45), 25629–25636.

(43) Herring, C. J.; Montemore, M. M. Recent Advances in Real-Time Time-Dependent Density Functional Theory Simulations of Plasmonic Nanostructures and Plasmonic Photocatalysis. *ACS Nanosci. Au* **2023**, *3* (4), 269–279.

(44) Li, X.; Tully, J. C.; Schlegel, H. B.; Frisch, M. J. *Ab Initio* Ehrenfest Dynamics. *J. Chem. Phys* **2005**, *123* (8), 084106.

(45) Ding, F.; Goings, J. J.; Liu, H.; Lingerfelt, D. B.; Li, X. Ab Initio Two-Component Ehrenfest Dynamics. *J. Chem. Phys* **2015**, *143* (11), 114105.

(46) Li, X.; Millam, J. M.; Schlegel, H. B. *Ab Initio* Molecular Dynamics Studies of the Photodissociation of Formaldehyde, $H_2CO \rightarrow H_2+CO$: Direct Classical Trajectory Calculations by MP2 and Density Functional Theory. *J. Chem. Phys* **2000**, *113* (22), 10062–10067.

(47) Li, X.; Millam, J. M.; Schlegel, H. B. Glyoxal Photodissociation. An *Ab Initio* Direct Classical Trajectory Study of $C_2H_2O_2 \rightarrow H_2+2CO$. *J. Chem. Phys* **2001**, *114* (20), 8897–8904.

(48) Li, X.; Millam, J. M.; Schlegel, H. B. Glyoxal Photodissociation. II. An *Ab Initio* Direct Classical Trajectory Study of $C_2H_2O_2 \rightarrow CO+H_2CO$. *J. Chem. Phys* **2001**, *115* (15), 6907–6912.

(49) Hull, O. A.; Lingerfelt, D. B.; Li, X.; Aikens, C. M. Electronic Structure and Nonadiabatic Dynamics of Atomic Silver Nanowire–N_2 Systems. *J. Phys. Chem. C* **2020**, *124* (38), 20834–20845.

(50) Rohrdanz, M. A.; Martins, K. M.; Herbert, J. M. A Long-Range-Corrected Density Functional That Performs Well for Both Ground-State Properties and Time-Dependent Density Functional Theory Excitation Energies, Including Charge-Transfer Excited States. *J. Chem. Phys* **2009**, *130* (5), 054112.

(51) Hay, P. J.; Wadt, W. R. *Ab Initio* Effective Core Potentials for Molecular Calculations. Potentials for K to Au Including the Outermost Core Orbitals. *J. Chem. Phys* **1985**, *82* (1), 299–310.

(52) Wadt, W. R.; Hay, P. J. *Ab Initio* Effective Core Potentials for Molecular Calculations. Potentials for Main Group Elements Na to Bi. *J. Chem. Phys* **1985**, *82* (1), 284–298.

(53) Hay, P. J.; Wadt, W. R. *Ab Initio* Effective Core Potentials for Molecular Calculations. Potentials for the Transition Metal Atoms Sc to Hg. *J. Chem. Phys* **1985**, *82* (1), 270–283.

(54) Gaussian Development Version, Revision I.13+, M. J. Frisch, G. W. Trucks, H. B. Schlegel, G. E. Scuseria, M. A. Robb, J. R. Cheeseman, G. Scalmani, V. Barone, G. A. Petersson, H. Nakatsuji, X. Li, M. Caricato, A. V. Marenich, J. Bloino, B. G. Janesko, R. Gomperts, B. Mennucci, H. P. Hratchian, J. V. Ortiz, A. F. Izmaylov, J. L. Sonnenberg, D. Williams-Young, F. Ding, F. Lipparini, F. Egidi, J. Goings, B. Peng, A. Petrone, T.

Henderson, D. Ranasinghe, V. G. Zakrzewski, J. Gao, N. Rega, G. Zheng, W. Liang, M. Hada, M. Ehara, K. Toyota, R. Fukuda, J. Hasegawa, M. Ishida, T. Nakajima, Y. Honda, O. Kitao, H. Nakai, T. Vreven, K. Throssell, J. A. Montgomery, Jr., J. E. Peralta, F. Ogliaro, M. J. Bearpark, J. J. Heyd, E. N. Brothers, K. N. Kudin, V. N. Staroverov, T. A. Keith, R. Kobayashi, J. Normand, K. Raghavachari, A. P. Rendell, J. C. Burant, S. S. Iyengar, J. Tomasi, M. Cossi, J. M. Millam, M. Klene, C. Adamo, R. Cammi, J. W. Ochterski, R. L. Martin, K. Morokuma, O. Farkas, J. B. Foresman, and D. J. Fox, Gaussian, Inc., Wallingford CT, 2018.

(55) Bode, B. M.; Gordon, M. S. MacMolPlt: A Graphical User Interface for GAMESS. *Journal of Molecular Graphics and Modelling* **1998**, *16* (3), 133–138.

(56) Jmol: An Open-Source Java Viewer for Chemical Structures in 3D. Http://Www.Jmol.Org/ (Accessed 2024-03-11).

(57) Goings, J. J.; Lestrange, P. J.; Li, X. Real-time Time-dependent Electronic Structure Theory. *WIREs Comput Mol Sci* **2018**, *8:e1341*.

(58) Ding, F.; Guidez, E. B.; Aikens, C. M.; Li, X. Quantum Coherent Plasmon in Silver Nanowires: A Real-Time TDDFT Study. *J. Chem. Phys* **2014**, *140* (24), 244705.

(59) Liang, W.; Isborn, C. M.; Li, X. Laser-Controlled Dissociation of $C_2H_2^{2+}$: Ehrenfest Dynamics Using Time-Dependent Density Functional Theory. *J. Phys. Chem. A* **2009**, *113* (15), 3463–3469.

(60) Crespo-Otero, R.; Barbatti, M. Recent Advances and Perspectives on Nonadiabatic Mixed Quantum–Classical Dynamics. *Chem. Rev.* **2018**, *118* (15), 7026–7068.

(61) Parandekar, P. V.; Tully, J. C. Detailed Balance in Ehrenfest Mixed Quantum-Classical Dynamics. *J. Chem. Theory Comput.* **2006**, *2* (2), 229–235.

(62) Giri, S. K.; Schatz, G. C. Photodissociation of H_2 on Ag and Au Nanoparticles: Effect of Size and Plasmon versus Interband Transitions on Threshold Intensities for Dissociation. *J. Phys. Chem. C* **2023** *127* (8), 4115-4123.

(63) Leatherman, G. S.; Diehl, R. D. Thermal and Structural Properties of N_2 or CO on Ag(111). *Langmuir* **1997**, *13* (26), 7063–7067.

(64) Ford, D. C.; Xu, Y.; Mavrikakis, M. Atomic and Molecular Adsorption on Pt(111). *Surface Science* **2005**, *587* (3), 159–174.

(65) Novell-Leruth, G.; Ricart, J. M.; Pérez-Ramírez, J. Pt(100)-Catalyzed Ammonia Oxidation Studied by DFT: Mechanism and Microkinetics. *J. Phys. Chem. C* **2008**, *112* (35), 13554–13562.

(66) Guidez, E. B.; Aikens, C. M. Quantum Mechanical Origin of the Plasmon: From Molecular Systems to Nanoparticles. *Nanoscale* **2014**, *6* (20), 11512–11527.

(67) Pandeya, P. Optical Properties and Electron/Nuclear Dynamics of Nanoparticles. PhD Thesis, 2021. https://er.lib.k-state.edu/login?url=https://www.proquest.com/dissertations-theses/optical-properties-electron-nuclear-dynamics/docview/2584019781/se-2.

Chapter 5 - Connectivity between static field and continuous wave field effects on excitation-induced H_2 activation

Reprinted with permission from *J. Phys. Chem. C* 2023, 127, 31, 15375–15384. Copyright 2023 American Chemical Society

Yuchen Wang, Christine M. Aikens*

Department of Chemistry, Kansas State University, Manhattan, KS 66506, USA

*Email: cmaikens@ksu.edu

5.1 Abstract

Due to the tremendous applications of the plasmon resonance excitation process, such as improvements in catalytic efficiency due to plasmonic enhancement and/or hot electron processes, understanding the mechanism behind these processes has become a popular topic in recent years. In this work, we focus on unraveling the mechanism of excitation-induced H_2 activation using a simplified triangular Au_6/Ag_6 cluster to investigate the effects of the electric field on electron redistribution and bond activation. We applied both static and continuous wave (CW) fields to investigate how these fields affect the systems. Geometrical changes (such as bond lengthening), molecular orbital reordering (affecting the relative energies of orbitals corresponding to hot-electron and charge-transfer excited states), and electronic charge redistribution between the cluster and the adsorbate occur upon application of a static electric field. To study H_2 activation, we apply Ehrenfest dynamics with real-time time-dependent density functional theory (RT-TDDFT) and examine how different excitation frequencies and polarizations affect bond activation. Moreover, electron-only dynamics are examined with RT-TDDFT, and the time-dependent variations in the orbital populations and electronic transitions provide information about the excitation and relaxation processes of hot electrons with applied electric fields. The static field results represent structures that can be accessed during the evolution of the systems when applying continuous wave fields. Through these studies, the effects of static and CW field effects on plasmon-induced H_2 activation can be understood.

5.2 Introduction

If an electric field is applied to gold or silver nanoparticles with a frequency corresponding to a plasmonic resonance frequency of the system, the valence electrons of the nanoparticles will be excited and will slosh back and forth collectively.[1–3] This phenomenon is called localized surface plasmon resonance (LSPR), and LSPRs of gold and silver nanoparticles can be utilized in many areas such as photocatalysis, energy conversion, and biological sensing.[4–8] In the field of photocatalysis, plasmonic systems can be designed as catalysts to enhance chemical reactions such as water splitting, CO_2 reduction, H_2 dissociation, and N_2 dissociation.[9–14] A diverse set of plasmonic systems have been designed to accelerate the rate of the plasmon-driven reactions, and active sites on the plasmonic systems have been examined to improve the efficiency of the catalytic reaction.[15–18] According to current understanding, the LSPR process includes many sub-steps such as hot carrier generation, hot carrier relaxation, and thermalization, which cross over a wide range of time scales.[19–24] Due to the complexity of the plasmon-enhanced photocatalytic process, the mechanism behind this process is not yet fully understood. However, it is of interest to understand this mechanism so that the efficiency of the process can be improved. In this work, we focus on studying plasmon-induced H_2 activation because H_2 activation is one of the most important steps in many chemical engineering processes such as syngas conversion and energy storage.[25,26] In addition, H_2 is the simplest diatomic molecule, and choosing this simple model may help us find the fundamental principles in the plasmon-driven process and guide us in further studies of more complex systems.

The plasmonic properties of both gold and silver nanoclusters have been studied experimentally and theoretically in previous literature, and silver and gold exhibit both similarities and differences in the electronic transitions involved in the plasmon resonance process.[27–31] Generally, the intense dipolar plasmonic resonance peak can be observed with a smaller size of silver nanoclusters compared to gold clusters.[32,33] Silver and gold nanoclusters also show differences in excited states energy distribution and types of electronic transition processes upon excitation.

The experimental work typically employs large nanoparticles that exhibit strong plasmon resonances; however, these large nanoparticles would require high computational memory and runtime costs to model theoretically. Therefore, finding an applicable model to investigate the plasmon-excitation process is necessary. To study the photo-dissociation of small molecules in the

presence of an Au nanoparticle, the jellium model has previously been applied which treats the nanoparticle as a uniform charge density to reduce the computational cost.[12] Other theoretical methods that explicitly consider the nuclei have also been considered.[34–43] Time-dependent density functional theory (TDDFT) has been employed to study plasmon-enhanced photocatalysis with small nanoparticles.[39–42] Computational methods with less expensive costs (i.e., TD-DFTB[34–36] and TDDFT+TB[37,38]) have been developed to deal with larger-sized nanoparticles. In addition, mixed levels of computational methods have been used to study the plasmon-induced H_2 dissociation on an Au(111) slab, in order to reach a balance between computational accuracy and cost.[9]

Au_6/Ag_6 has been demonstrated as a reasonable model and its structure and properties have been calculated and discussed in previous research.[41,44,45] In recent years, the photo-dissociation of H_2 and the corresponding potential energy surfaces for interaction with a triangular Au_6 system have been studied using DFT and TDDFT methods.[41] Excited potential energy surfaces corresponding to hot electrons (electronically excited surfaces corresponding to the metal cluster) and charge transfer surfaces (involving adsorbate antibonding orbitals) were considered.[41] Therefore, although a triangular metal cluster does not have a plasmon, it can still be considered a promising simplified model to study how excitation affects catalytic properties.

In this work, we applied the Au_6/Ag_6 cluster as a model to investigate how electric fields affect the excitation-induced activation of the H_2 molecule. One question that will be answered is: what insights can be achieved by applying a static electric field (which mimics extrema of a continuous wave (CW) field)? We find that static electric field calculations provide insights into geometrical structure changes (such as bond lengthening processes), molecular orbital reordering (which affects the relative energies of orbitals corresponding to hot-electron and charge-transfer excited state surfaces), and the division of the electronic charge distribution between the cluster and the adsorbate. To study the static electric field effects, fields with different strengths are applied during the optimization of the structures. Next, we apply a CW field in order to examine electron and electron-nuclear dynamics in this system. Excited state dynamics is considered an essential tool when studying the dynamic processes of electron-electron scattering and electron-phonon coupling in the plasmonic resonance process.[20,46,47] To study H_2 activation, we apply Ehrenfest dynamics, which is a mean-field nonadiabatic dynamics that is employed to study the motion of both nuclei and electrons in excited states.[48–50] For the excitation-induced activation

process arising from the silver/gold cluster, the system will yield different responses under different excitation frequencies and polarizations. Therefore, this work also focuses on the question: how do excitation frequencies and polarization affect the activation process? Therefore, the CW field was then applied to investigate the systems using frequencies corresponding to certain excitation modes. Electronic dynamics are investigated using real-time TDDFT methods[51,52] and coupled electron-nuclear dynamics are analyzed using Ehrenfest dynamics.[48,49] Real-time TDDFT provides information about electronic transitions and population, which gives us an understanding of the hot-carrier generation and hot-electron relaxation processes with different applied electric fields.

5.3 Computational methods

We first applied both PBE[53] and LC-ωPBE[54] functionals to calculate the geometric structures of Au_6H_2 and Ag_6H_2. PBE and LC-ωPBE show consistent trends when calculating the Ag_6H_2 system; however, H_2 is calculated to bind with an angle to the Au cluster using applied electric fields in the PBE calculations (Table C1). Moreover, the Au_6 nanocluster itself also becomes bent in the geometry optimization process with applied electric fields using the PBE functional. Because the long-range corrected (LC) functionals are expected to be more accurate for metal-adsorbate interactions, all of the following calculations were performed at the LC-ωPBE[54]/LanL2DZ[55–57] level of theory using a development version of the Gaussian software package.[58] The lowest energy structures when H_2 on the nanocluster vertex are shown in Figure 5.1.

When studying the effects of a static electric field, the geometry was optimized with an applied static field. The electric field is applied along the z axis (Figure 5.1), and the strengths of the fields were chosen to be 0.01 au (3.57×10^{14} W/cm^2), 0.005 au (1.79×10^{14} W/cm^2), and 0.001 au (3.57×10^{13} W/cm^2), respectively. The electric fields were chosen based on previous work that shows very weak activation of H_2 (coupled with an Ag_8 nanowire) with a CW electric field strength of 0.001 au and slightly stronger activation for 0.01 au.[39] Electric fields were applied in both the positive z (Z+) and negative z (Z-) directions, which correspond to the maxima of the CW fields.

Linear-response (LR) TDDFT calculations were performed with zero applied field to obtain the absorption spectra, which provides information about frequencies of interest (analogous

to LSPR frequencies) that will be used in electron-only RT-TDDFT (henceforth referred to simply as RT-TDDFT) and combined electron-nuclear (Ehrenfest) calculations. For both RT-TDDFT and Ehrenfest dynamics calculations, a CW electric field is applied for the first 20 fs of total simulation; the field is ramped up during the first 1 fs and then ramped down during the final 1 fs, giving a trapezoidal envelope overall. The maximum strength of the applied electric field is 0.01 au (3.57×10^{14} W/cm^2). Though this is a higher field strength than most experimental CW fields, this compensates in part for the short duration of the field application. Moreover, previous work has shown that smaller nanoclusters typically require stronger applied fields for adsorbate activation, but this decreases with cluster size. [36,59] For RT-TDDFT calculations, the electronic step is set to 0.002 fs. For the Ehrenfest dynamics, the electronic step size is 0.00025 fs and the nuclear step size is 0.1 fs, and the initial velocity of all the systems is set as zero. All of the RT-TDDFT and Ehrenfest calculations were performed using a development version of the Gaussian software package[58] written by Xiaosong Li and co-workers.[48,60,61]

5.4 Results and discussion

5.4.1 Static fields effect

Geometric information

For the ground state geometry optimizations, the Au_6/Ag_6 cluster was oriented in the yz plane and the H_2 molecules were initially placed parallel to the x, y, and z axes. The lowest energy isomer has H_2 parallel to the x axis for both the Ag_6H_2 and Au_6H_2 systems (Figure 5.1). The H-H bond length is 0.75 Å in the ground state for both systems. The distance between the H_2 and the gold cluster (2.41 Å) is smaller than with the silver cluster (3.22 Å) for the zero-field equilibrium structure (Table 5.1). In addition, the binding energy between the H_2 and the gold cluster (6.41 kJ/mol) is higher than with the silver cluster (2.90 kJ/mol) for the zero-field equilibrium structure (using the equation E(binding) = E(H_2) + E(bare cluster) - E(H_2-cluster system)), indicating a stronger bond between the H_2 adsorbate and the gold cluster.

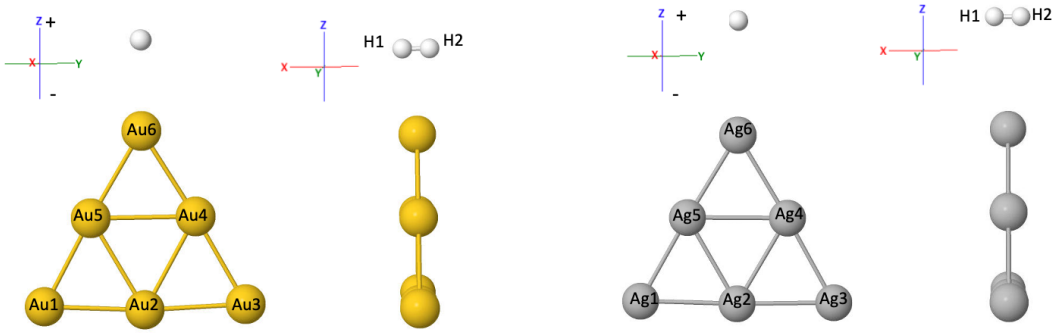


Figure 5.1 Optimized geometries of A. Au_6H_2 and B. Ag_6H_2 systems at zero applied electric field

Table 5.1 Selected bond length information (Å) for Au_6H_2 and Ag_6H_2 systems optimized with static applied electric fields. Atom numbers are provided in Figure 5.1.

		- 0.01 au	- 0.005 au	- 0.001 au	Zero field	0.001 au	0.005 au	0.01 au
	H1-H2	0.77	0.77	0.76	0.75	0.75	0.75	0.75
Au_6H_2	Au6-H1	2.10	2.18	2.33	2.41	2.53	3.25	3.27
	Au6-H2	2.10	2.18	2.33	2.41	2.53	3.33	4.02
	H1-H2	0.76	0.75	0.75	0.75	0.75	0.75	0.74
Ag_6H_2	Ag6-H1	2.34	3.19	3.22	3.22	3.46	4.15	4.93
	Ag6-H2	2.34	3.19	3.22	3.22	3.46	4.15	4.93

For the Au_6H_2 system, when a static electric field is applied in the positive direction along the z-axis (Z+ direction), the H_2 bond length stays the same, but H_2 is rotated from the x-preferred configuration (with H_2 parallel to the x-axis) to the z-preferred configuration (H_2 parallel to the z-axis) as the applied field increases. However, H_2 stays in the x-preferred configuration with Z+ electric fields for the Ag_6H_2 system and the H-H bond length decreases with the more intense field. In the Z- direction, H_2 stays in the x-preferred configuration and the H_2 bond length increases with more intense electric fields for both Ag_6H_2 and Au_6H_2 systems. With the increasing field strength in the Z- direction, we can observe the Au6-H and Ag6-H distances decrease; however, with the

increasing field strength in the Z+ direction, we can observe the Au6-H and Ag6-H distances increase. Therefore, the applied fields in the negative direction shorten the distance between the cluster and the H_2 molecule while simultaneously increasing the H-H bond length, suggesting that these fields lead towards chemisorption of hydrogen, and the applied fields in the positive direction will potentially lead H_2 to desorb from the cluster.

Effects of static electric fields on the molecular orbital diagram

In addition to the geometric changes described above, the applied electric field also leads to modification of molecular orbital energies and the orbital characters in the systems. Molecular orbitals for the optimized structures with zero applied field and for the 0.01 au Z+ and Z- fields are shown in Figure 5.2 for Ag_6H_2 and Figure C1 for Au_6H_2. For Ag_6H_2, the HOMO shows antibonding character between H_2 and the cluster for zero applied field and for the Z+ 0.01 au field. However, this type of orbital character switches to the HOMO-1 for the Z- 0.01 au field. The orbital with H_2 σ^* antibonding character is LUMO+5 for the Z- 0.01 au field, LUMO+6 for the zero applied field, and LUMO+7 for the Z+ 0.01 au field. The switching of the order of the molecular orbital character with different field strengths can also be observed in the Au_6H_2 system (Figure C1), which is consistent with previous literature that examined the ordering of this orbital as a function of H-H and Au-H distances, although the previous work did not examine static applied fields.[41] The crossing of orbitals with different character in the correlated molecular orbital diagrams indicates that the applied static field will modify the ordering of orbitals with different character, which is expected to lead to variations in orbital populations and electronic transitions as a function of different applied fields. For both Au_6H_2 and Ag_6H_2 systems, the applied field has the largest effects on the orbital energies of LUMO, LUMO+2, and LUMO+5 (Figure C2). Because occupation of antibonding orbitals is considered to be a possible mechanism to induce photocatalysis, this implies that application of an electric field (whether static or time-varying) may affect the orbital energies and thus the ability to access states involving these orbitals.

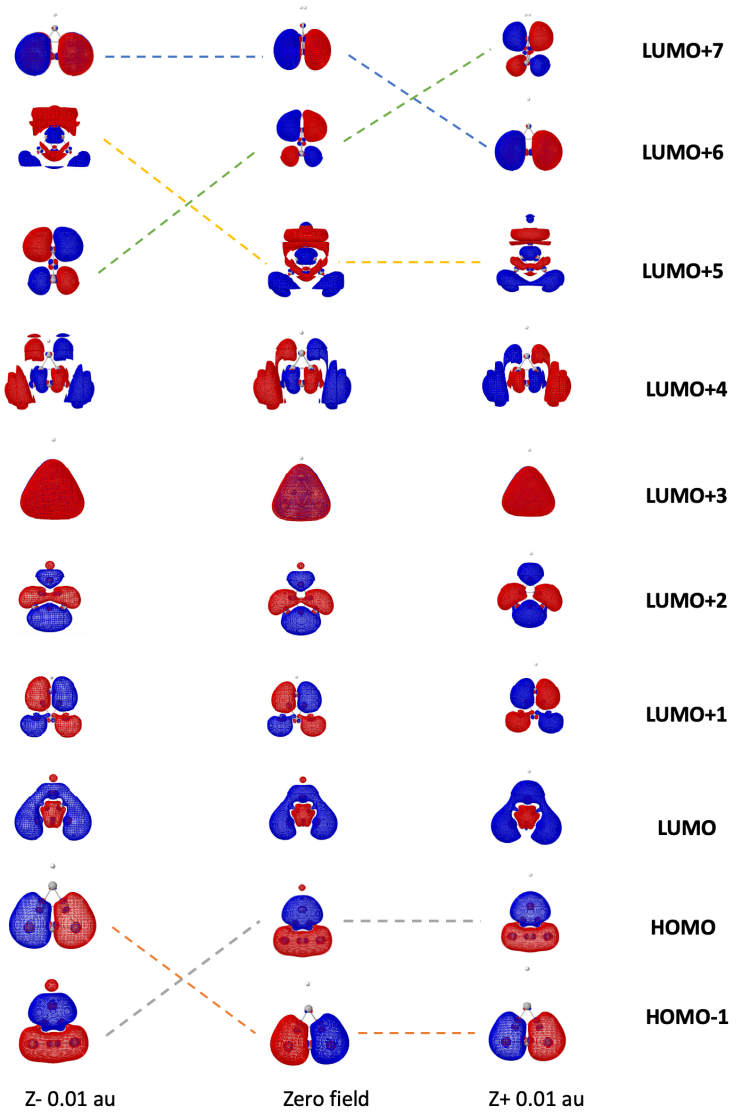


Figure 5.2 Selected molecular orbitals of optimized Ag_6H_2 under different static applied electric fields. (All molecular orbitals are oriented using a front view, except the orbitals involving H_2 σ*, which are oriented using the side view for the sake of clarity.)

Interactions between H_2 and Au_6/Ag_6 cluster

To study the interaction between H_2 and the clusters, we examine the orbitals responsible for bonding between the two subsystems. The molecular orbital that contains bonding character between the H_2 σ orbital and the Au_6 or Ag_6 cluster lies relatively low in energy (orbital index of 25; Figure 5.3) and the corresponding molecular orbital with antibonding character lies close to

the fermi energy (HOMO or HOMO-1, depending on the applied field). The selected orbital energies are shown in Table C2. For the Z- 0.01 au field, orbital 57 (HOMO-1) shows antibonding character between the H_2 molecule and the Ag_6/Au_6 cluster. With the decrease of the field strength in the Z- direction (to Z- 0.001 au), the antibonding character shifts to orbital 58 (HOMO). For the Z+ field, there is less interaction between the molecule and cluster as the field strength increases (Figure 5.3).

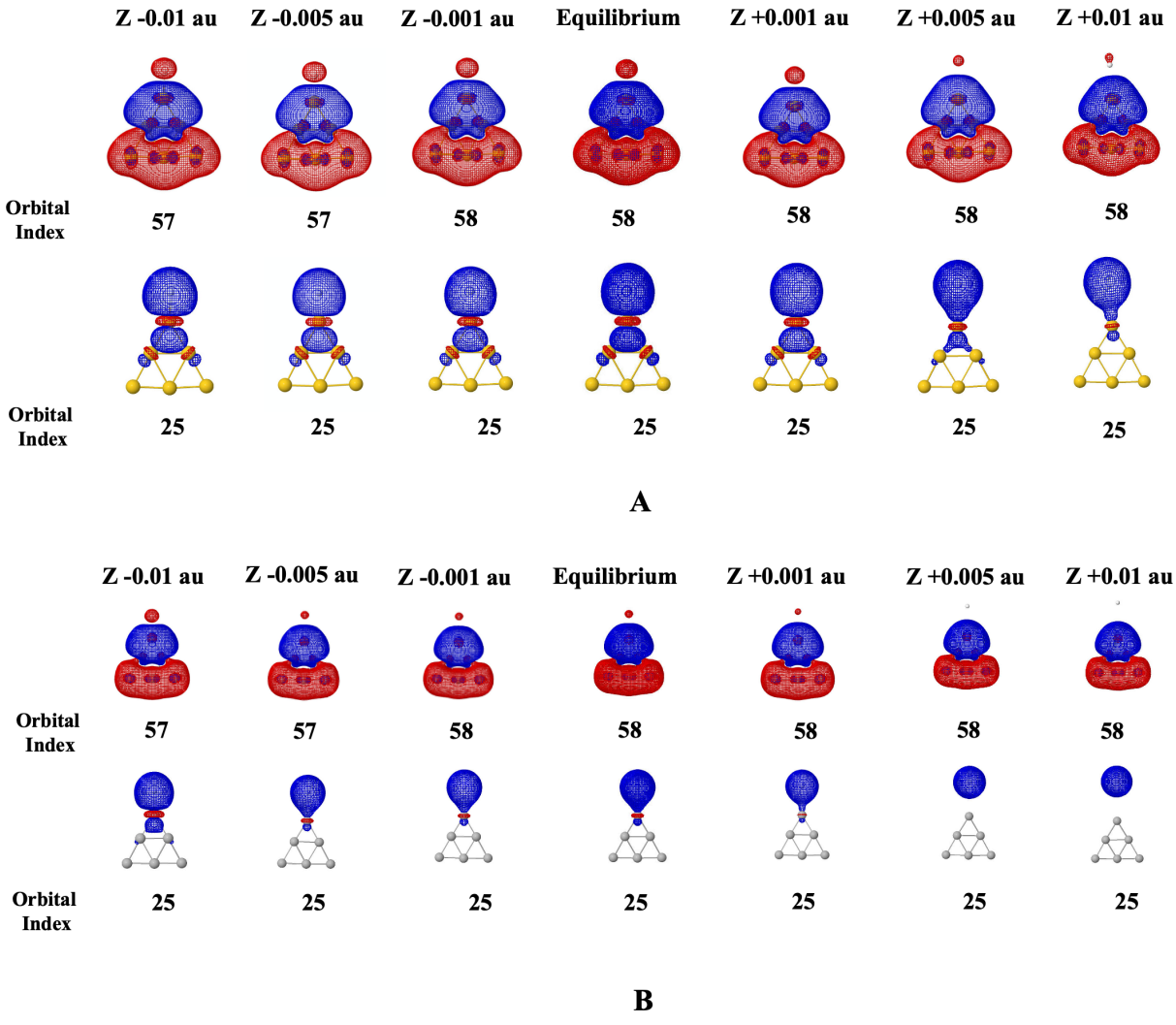


Figure 5.3 Bonding and antibonding characters between cluster and H_2 molecule. A. Au_6H_2 and B. Ag_6H_2

Selected orbital energy differences are shown in Figure 5.4. "Bonding" denotes the orbital that shows bonding character for the interaction between H_2 and the cluster (orbital index 25); "antibonding" denotes the orbital that shows antibonding character for the interaction between H_2 and the cluster (orbital index 57 or 58). Generally, orbital energy differences between bonding and antibonding orbitals show similar trends as the orbital energy differences between the LUMO and the bonding orbital with the applied field. The increased energy difference with a more intense field strength in the Z- direction indicates a stronger coupling between H_2 and the clusters. For the Ag_6H_2 system, the orbital energy differences show a significant decrease when the applied field was decreased from 0.01 au to 0.005 au in the Z- direction. However, the orbital energy differences stay relatively stable in other applied fields. For the Au_6H_2 system, a significant orbital energy difference change occurs when the electric field shifts from Z+ 0.001 au to the Z+ 0.005 au field, and the change may result from the rotation of the H_2 molecule in the system with a stronger static field.

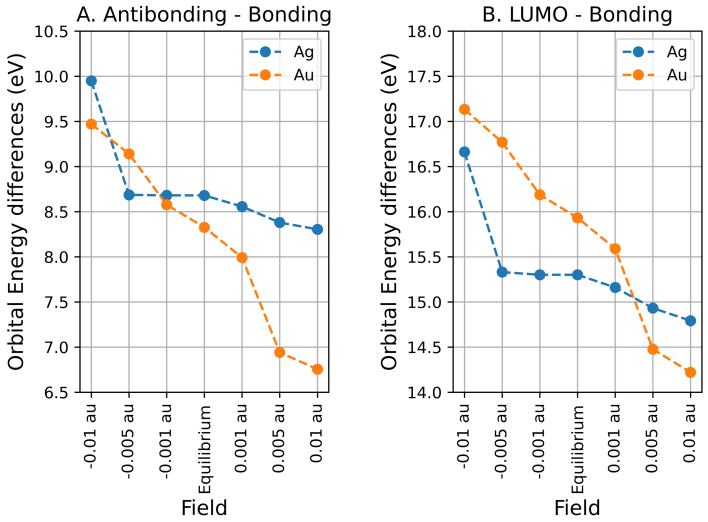


Figure 5.4 Orbital energy differences between A. bonding and antibonding orbitals, B. LUMO and bonding character orbitals with the change of applied field.

Partial charge analysis

To investigate the static field effect on the charge distribution of the systems, the Mulliken (Figure 5.5) and Hirshfeld (Figure C3) partial charge approaches were applied to analyze the partial charges on the atoms. For both the Ag_6H_2 and Au_6H_2 systems, the partial charge on the H

atom is the most positive for the Z- 0.01 au field and shows a monotonic decrease as the Z- field strength decreases and as the field switches to the Z+ direction, indicating that the more intense field along the Z- direction leads to a greater degree of charge transfer between H_2 and the cluster. For both Mulliken and Hirshfeld charge analysis approaches, the sum of the charges on the H atoms when interacting with the Au cluster is larger than for the interaction with the Ag cluster, indicating that there is more charge transfer in Au_6H_2 than in the Ag_6H_2 system.

For the Ag_6H_2 system, the partial charge on the Ag6 atom shows a monotonic decrease with the applied field (except for the Z+ 0.01 au field) using both Mulliken charge and Hirshfeld charge analysis. For the Au_6H_2 system, the Mulliken charge on the Au6 atom shows a monotonic increase with the applied field (except for the Z+ 0.01 au field), and the Hirshfeld charge on Au6 shows a monotonic decrease with the applied field. The above analysis indicates that the applied static field will affect the partial charge distribution of the system, and the partial charge on the hydrogen atoms shows a general correlation with field strength. Similar to Au6, both Au1 and Au3 (which are also vertex atoms) become more negatively charged as the static field becomes greater in the Z- direction.

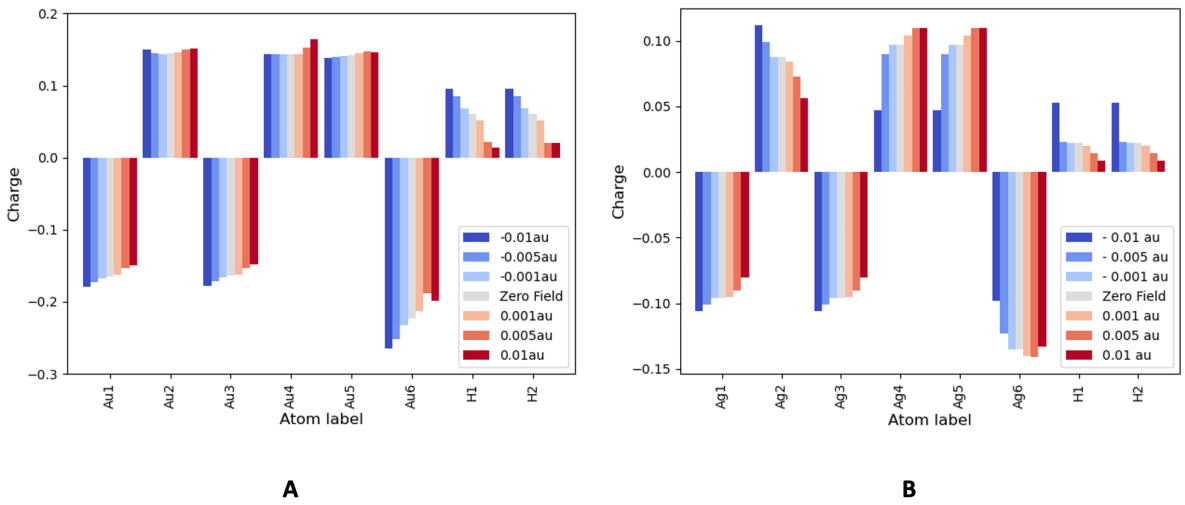


Figure 5.5 Mulliken charge analysis for A. Au_6H_2 B. Ag_6H_2.

5.4.2 Resonant electric fields

Linear response TDDFT

The zero-field absorption spectra of Au_6H_2 and Ag_6H_2 were calculated using linear response TDDFT (Figure 5.6). Ag_6H_2 displays peaks with a greater absorption strength than Au_6H_2 in the range of 3-5 eV, and the strongest peaks in the Ag_6H_2 spectrum are consistent with previous reports.[32,33] For the Au_6H_2 system, excitation 1 and excitation 3 show the two most intense peaks out of the first five peaks from the absorption spectrum. Both peak 1 (excitation 1) and peak 3 (excitation 3) show dominant polarization along the y and z axes, corresponding to the plane of the metal cluster. Compared with Au_6H_2, the Ag_6H_2 system shows two intense dipolar peaks at 3.16 eV (excitation 1) and 3.64 eV (excitation 2); both excitation 1 and excitation 2 (which includes two excited states) are polarized along the y and z axes. For the absorption spectrum of Ag_6H_2, excitation 3 is located at 4.97 eV and is polarized along the x-axis. The strong peaks from the LR-TDDFT calculations are used to select frequencies for applied electric fields that will selectively excite particular excitations within the cluster systems. In the next step, external electric fields with those selected frequencies will be applied to the system and Ehrenfest dynamics will be used to simulate the excitation-induced H_2 activation process when interacting with Au/Ag clusters.

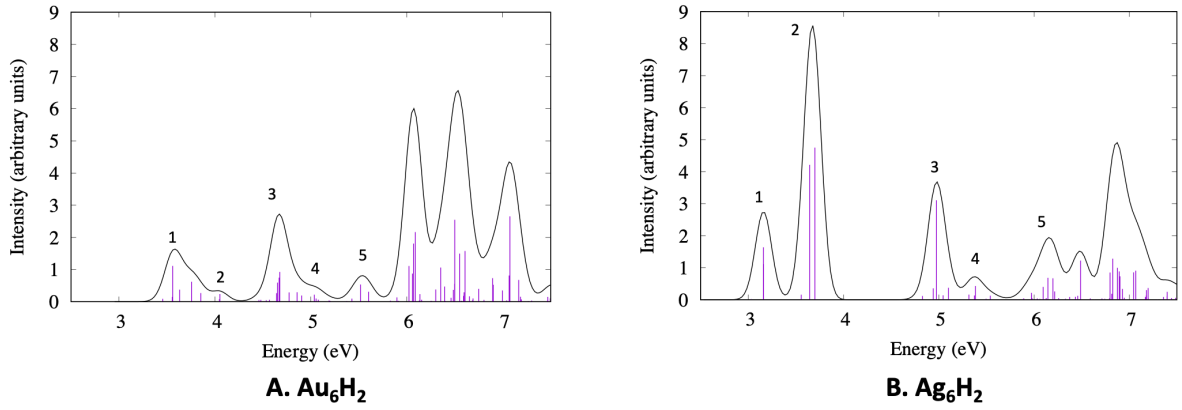


Figure 5.6 Linear absorption spectra for A. Au_6H_2 B. Ag_6H_2.

Nonadiabatic dynamics results

To examine the H_2 bond distance change in the excitation-induced catalytic process, Ehrenfest dynamics were carried out. For the Au_6H_2 system, the applied electric fields were selected to be resonant with excitations 1 and 3 from Figure 5.6A, with all three polarization directions examined for each excitation (Figure 5.7). For the Ag_6H_2 system, fields were chosen to be resonant with excitations 1, 2, and 3 from Figure 5.6B, also with all three polarization directions (Figure 5.8). All simulations were performed with the 0.01 au external field strength. Dynamics were performed over a time period of 100 fs.

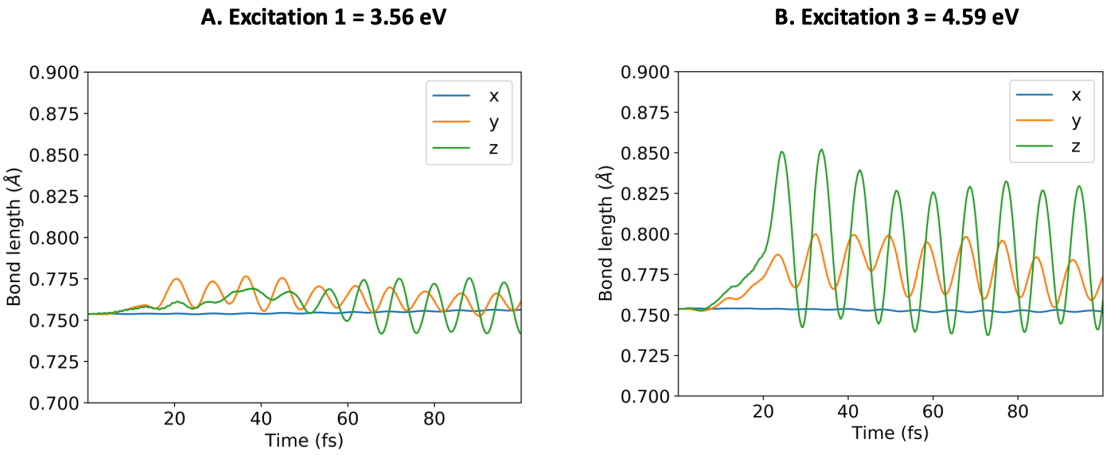


Figure 5.7 Variation of H-H bond distance during Ehrenfest dynamics simulations for the Au_6H_2 system with the 0.01 au electric field strength.

For the Au_6H_2 Ehrenfest dynamics results (Figure 5.7), if the electric field has a frequency corresponding to 3.56 eV (excitation 1), the bond length results show H-H stretching within 100 fs. The maximum H-H bond distance was found to be 0.775 Å for both y- and z-polarized fields, and the H-H bond distance is essentially unchanged for the x-polarized field. For an applied electric field corresponding to 4.59 eV (excitation 3), the H-H bond shows more intense bond stretching for simulations with the y- and z-polarized fields compared with those resonant with excitation 1, and the maximum H-H bond distance reaches up to 0.850 Å for the simulation with z-polarization and 0.800 Å with y-polarization. From the linear response TDDFT spectrum, peak 3 shows a

higher absorption strength than peak 1, which correlates with the greater activation of the H-H bond.

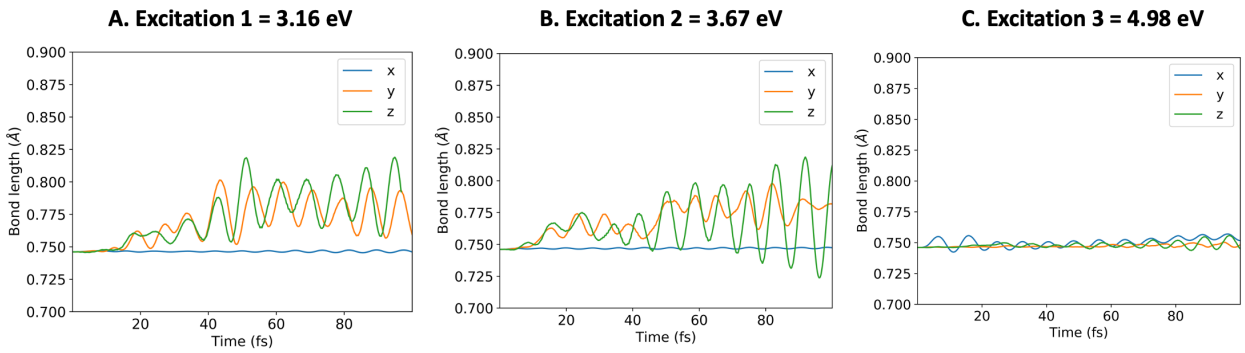


Figure 5.8 Variation of H-H bond distance during Ehrenfest dynamics simulations for the Ag_6H_2 system with the 0.01 au electric field strength.

For the Ag_6H_2 system, for the simulations resonant with excitation 1 (3.16 eV) with y- and z-polarized electric fields, the H-H distance is stable for the first 10 fs, and then displays bond stretching from 20 ~ 100 fs, for which the maximum bond distance can reach up to 0.800 Å (at around 45 fs) with the y-polarized field and 0.820 Å (at around 50 fs) with the z-polarized electric field. For simulations resonant with excitation 2, with the y-polarized electric field the maximum bond distance can reach 0.800 Å (at around 85 fs), and with the z-polarized electric field the maximum bond distance can reach 0.825 Å (at around 95 fs). Although excitation 2 (3.67 eV) has a stronger oscillator strength than excitation 1, the overall bond activation is similar for both simulations. For the simulation resonant with excitation 3 (4.98 eV), the excitation shows a transition dipole moment along the x direction based on LR-TDDFT calculations. However, only weak bond stretching is observed with x-, y-, and z- polarized fields, and the H-H distances do not become longer than 0.775 Å within 100 fs.

The above results indicate that the polarization of the electric field affects the H_2 activation. Ideally, the electric field should have the same polarization as the transition dipole moment of that excitation in order to excite the system, and we observe that the H_2 is not activated if the electric field is polarized along the x axis with excitation 1 and 2 simulations for Ag_6H_2 (Figure 5.8a and Figure 5.8b); as mentioned above, excitations 1 and 2 have transition dipole moments along the y and z axes. However, electric field polarization is not

the only factor that determine the H_2 activation, because the simulation shown in Figure 5.8c indicates that H_2 cannot be activated even when the electric field has the same frequency and is polarized along the same direction as the transition dipole moment of excitation 3. Overall, excitations polarized in the plane of the metal cluster lead to greater adsorbate bond activation.

Real-time TDDFT calculations

RT-TDDFT can be performed with fixed nuclei in order to determine electron-only dynamics. RT-TDDFT simulations were performed to determine the orbital populations (Figure 5.9 and Figure 5.10) and electronic transitions (Figure C4 and Figure C5) using the applied electric fields of interest.

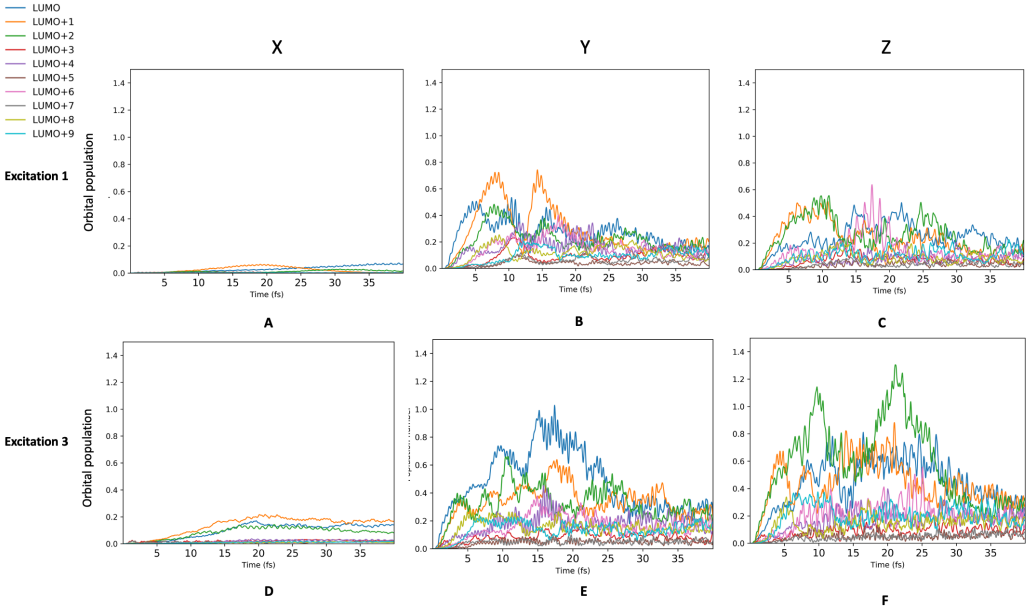


Figure 5.9 Orbital population analysis of Au_6H_2 system in RT-TDDFT simulations

Orbital population results for the Au_6H_2 system (Figure 5.9) indicates that there is almost no orbital population transfer to unoccupied orbitals if the electric field is polarized along the x-axis. We can also observe from Figure 5.9 that more electrons were transferred to the unoccupied orbitals with the field resonant with excitation 3 compared to excitation 1. This can be correlated to the Ehrenfest dynamics results that H-H bonds shows more intense stretching when the frequency corresponds to excitation 3 rather than excitation 1.

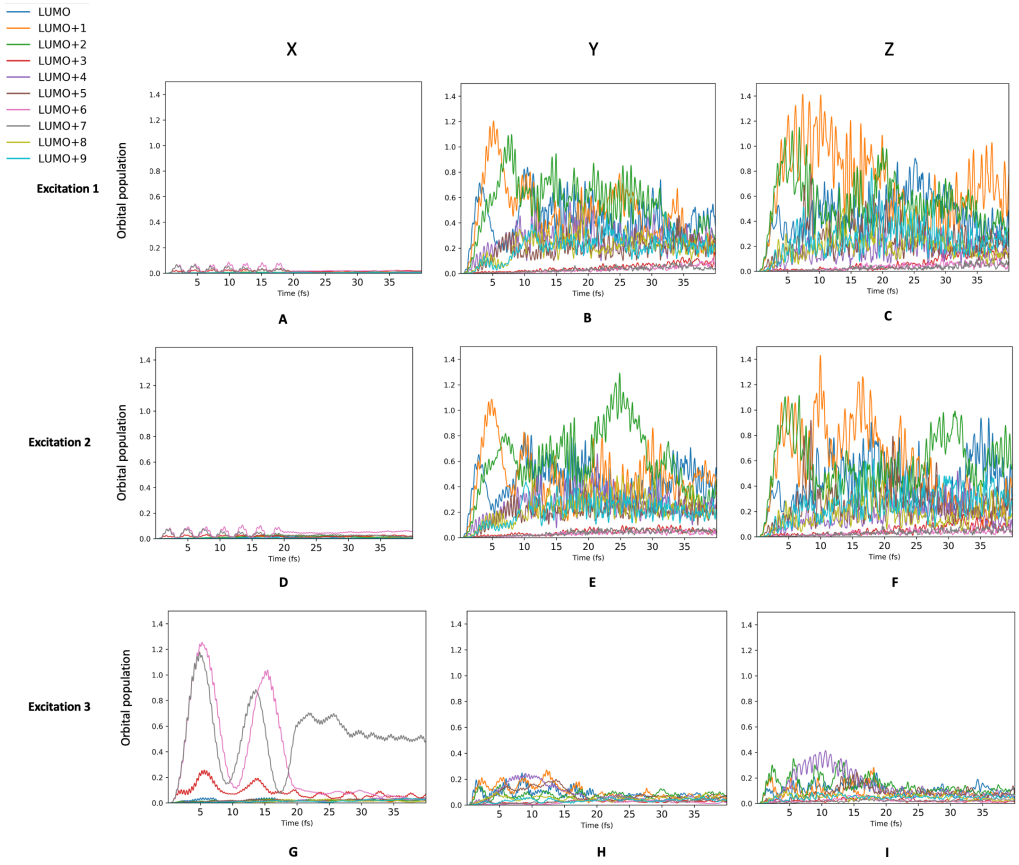


Figure 5.10 Orbital population analysis of Ag_6H_2 system in RT-TDDFT simulations.

For the Ag_6H_2 system, electron-only dynamics results indicate that electron population negligibly transfers into the unoccupied orbitals using the x-polarized electric field when the field is resonant with either excitation 1 or excitation 2. These electron-only dynamics results can be correlated with the Ehrenfest dynamics results in which the H_2 distance stays almost constant during the 100 fs of simulation using x-polarized fields resonant with these two excitations. When the electric field is applied along the y direction for excitation 1, the orbital population of LUMO+1 reaches its highest peak from ~5-6 fs and the population of LUMO+2 reaches its highest peak from ~7-10 fs. LUMO+1 and LUMO+2 play the dominant role for the first 40 fs. For excitation 2, the maximum population of LUMO+1 is lower than for excitation 1 and the population of LUMO+2 reaches its highest peak at around 25 fs, which is 5 fs after the electric field is turned off.

When the electric field is applied along the z direction for excitation 1, the population of LUMO+1 ramped up to 1.4 during ~0-10 fs, and the orbital population of LUMO+2 ramped up to

1.1 during ~0-5 fs. For excitation 3, the populations of LUMO+1 and LUMO+2 share similar trends during ~0-7 fs; however, the population of LUMO+2 ramped down at 10 fs while LUMO+1 population ramped up to reach a maximum peak (with a population number around 1.4).

For excitation 3, electron-only dynamics results show low orbital population transfer with the y and z polarized electric fields. However, with the x polarization, significant population can be observed in LUMO+6 and LUMO+7 during the first 20 fs. Both LUMO+6 and LUMO+7 show two intense peaks at about 5 fs and 15 fs. After 20 fs, the population of LUMO+7 decreases to 0.6 and stays stable across 25-40 fs, and the population of LUMO+6 decreases to 0.1 over 25-40 fs. Since the Ehrenfest dynamics results show that H_2 cannot be activated if the electric field has a frequency corresponding to excitation mode 3 (for all three polarization directions), this demonstrates that electron population is not the only factor that determines the H_2 activation, and H_2 may not be activated even when initially unoccupied orbitals gain electron population upon electric field excitation. It also suggests that electron population in particular types of orbitals is less important than others; interestingly, LUMO+6 is the H_2 σ^* orbital, which would be a logical target for catalysis, yet appears to be unimportant for H_2 activation in this case.

5.5 Conclusions

In this work, we compared the factors involved with activation of adsorbates via excited state activation of silver and gold clusters. First, static electric fields with different varying strengths were applied and we found that both the geometric information and electronic structures were modified with different field strengths and directions. Geometrically, strong positive static fields in the z direction led to a bent adsorbate being preferred for Au_6H_2, while Ag_6H_2 maintained its zero-field orientation. The H-H bond distance increased with increasingly negative static fields, suggesting bond activation is induced by the negative z-direction portion of a CW wave field rather than the positive z-direction portion. Simultaneously, the Au-H bond decreases in length as the field is applied in the negative z direction. Overall, this suggests that the time-varying fields in a CW excitation will alternately increase and decrease the H-H bond length, while also alternately decreasing and increasing the Au-H bond length, leading to excitation. The molecular orbital diagram changes and partial charge analysis results indicate that the applied field also leads to changes in the electronic structure of the system, and we can observe the crossing of the orbital

character with different applied electric fields. Moreover, the applied electric field affects the coupling between the bonding/antibonding of the H_2 σ orbital with the Au/Ag cluster, with the negative z direction field increasing the coupling.

Continuous wave fields with different excitation frequencies were then applied to study how the H_2 adsorbate is activated using the excited state dynamics induced by the silver and gold clusters. The electric fields were polarized along x, y and z for each frequency. Ehrenfest dynamics results indicate that the H_2 activation not only depends on the frequencies of the excitation, but also depends on the configuration between the Ag/Au cluster and the H_2 molecule. Moreover, it shows that H_2 is not activated with an x-polarized field even when the excitation has its transition dipole moment along the x-axis and activates the σ* orbital of the H_2. Instead, the most important excitations correspond to "hot electron" states of the gold or silver cluster. Linear response TDDFT results show that Ag has more intense peaks than Au; however, both of these systems show similar trends in H_2 activation with selected excitations. Therefore, oscillator strength is not the only factor that determines the activation properties, and the nuclear motions play an important role in this excitation-induced process.

5.6 Supporting information

Comparison between PBE and LC-ωPBE functionals, correlated MO diagram of the Au_6H_2 system, orbital energies of selected orbitals, Hirshfeld charge analysis and electronic transitions in RT-TDDFT simulations.

5.7 Acknowledgments

This material is based on work supported by the Department of Energy under grant DE-SC0012273. The computing for this work was performed on the Beocat Research Cluster at Kansas State University, which is in part funded by the NSF (Grant Nos. CHE-1726332, CNS-1006860, EPS-1006860, and EPS-0919443). The authors thank Prof. Xiaosong Li for the RT-TDDFT and Ehrenfest Dynamics code.

5.8 References

(1) Kelly, K. L.; Coronado, E.; Zhao, L. L.; Schatz, G. C. The Optical Properties of Metal Nanoparticles: The Influence of Size, Shape, and Dielectric Environment. *J. Phys. Chem. B* **2003**, *107* (3), 668–677.

(2) Mulvaney, P. Surface Plasmon Spectroscopy of Nanosized Metal Particles. *Langmuir* **1996**, *12* (3), 788–800.

(3) Hartland, G. V. Optical Studies of Dynamics in Noble Metal Nanostructures. *Chem. Rev.* **2011**, *111* (6), 3858–3887.

(4) Mou, T.; Quiroz, J.; Camargo, P. H. C.; Wang, B. Localized Orbital Excitation Drives Bond Formation in Plasmonic Catalysis. *ACS Appl. Mater. Interfaces* **2021**, *13* (50), 60115–60124.

(5) Hooshmand, N.; Thoutam, A.; Anikovskiy, M.; Labouta, H. I.; El-Sayed, M. Localized Surface Plasmon Resonance as a Tool to Study Protein Corona Formation on Nanoparticles. *J. Phys. Chem. C* **2021**, *125* (45), 24765–24776.

(6) Kim, H. Y.; Henkelman, G. CO Oxidation at the Interface between Doped CeO_2 and Supported Au Nanoclusters. *J. Phys. Chem. Lett.* **2012**, *3* (16), 2194–2199.

(7) Aslam, U.; Rao, V. G.; Chavez, S.; Linic, S. Catalytic Conversion of Solar to Chemical Energy on Plasmonic Metal Nanostructures. *Nat. Catal.* **2018**, *1* (9), 656–665.

(8) Hou, W.; Cronin, S. B. A Review of Surface Plasmon Resonance-Enhanced Photocatalysis. *Adv. Funct. Mater.* **2013**, *23* (13), 1612–1619.

(9) Mukherjee, S.; Libisch, F.; Large, N.; Neumann, O.; Brown, L. V.; Cheng, J.; Lassiter, J. B.; Carter, E. A.; Nordlander, P.; Halas, N. J. Hot Electrons Do the Impossible: Plasmon-Induced Dissociation of H_2 on Au. *Nano Lett.* **2013**, *13* (1), 240–247.

(10) Zhou, L.; Zhang, C.; McClain, M. J.; Manjavacas, A.; Krauter, C. M.; Tian, S.; Berg, F.; Everitt, H. O.; Carter, E. A.; Nordlander, P.; Halas, N. J. Aluminum Nanocrystals as a Plasmonic Photocatalyst for Hydrogen Dissociation. *Nano Lett.* **2016**, *16* (2), 1478–1484.

(11) Douglas-Gallardo, O. A.; Box, C. L.; Maurer, R. J. Plasmonic Enhancement of Molecular Hydrogen Dissociation on Metallic Magnesium Nanoclusters. *Nanoscale* **2021**, *13* (25), 11058–11068.

(12) Zhang, Y.; Nelson, T.; Tretiak, S.; Guo, H.; Schatz, G. C. Plasmonic Hot-Carrier-Mediated Tunable Photochemical Reactions. *ACS Nano* **2018**, *12* (8), 8415–8422.

(13) Kumari, G.; Zhang, X.; Devasia, D.; Heo, J.; Jain, P. K. Watching Visible Light-Driven CO_2 Reduction on a Plasmonic Nanoparticle Catalyst. *ACS Nano* **2018**, *12* (8), 8330–8340.

(14) Monyoncho, E. A.; Dasog, M. Photocatalytic Plasmon-Enhanced Nitrogen Reduction to Ammonia. *Adv. Energy Sustain. Res.* **2021**, *2* (3), 2000055.

(15) Jiang, W.; Low, B. Q. L.; Long, R.; Low, J.; Loh, H.; Tang, K. Y.; Chai, C. H. T.; Zhu, H.; Zhu, H.; Li, Z.; Loh, X. J.; Xiong, Y.; Ye, E. Active Site Engineering on Plasmonic Nanostructures for Efficient Photocatalysis. *ACS Nano* **2023**, acsnano.2c12314.

(16) Sayed, M.; Yu, J.; Liu, G.; Jaroniec, M. Non-Noble Plasmonic Metal-Based Photocatalysts. *Chem. Rev.* **2022**, *122* (11), 10484–10537.

(17) Yanagi, R.; Zhao, T.; Solanki, D.; Pan, Z.; Hu, S. Charge Separation in Photocatalysts: Mechanisms, Physical Parameters, and Design Principles. *ACS Energy Lett.* **2022**, *7* (1), 432–452.

(18) Zhan, C.; Yi, J.; Hu, S.; Zhang, X.-G.; Wu, D.-Y.; Tian, Z.-Q. Plasmon-Mediated Chemical Reactions. *Nat. Rev. Methods Primer* **2023**, *3* (1), 12.

(19) Hartland, G. V.; Besteiro, L. V.; Johns, P.; Govorov, A. O. What's so Hot about Electrons in Metal Nanoparticles? *ACS Energy Lett.* **2017**, *2* (7), 1641–1653.

(20) Zhang, Y. Theory of Plasmonic Hot-Carrier Generation and Relaxation. *J. Phys. Chem. A* **2021**, *125* (41), 9201–9208.

(21) Román Castellanos, L.; Hess, O.; Lischner, J. Single Plasmon Hot Carrier Generation in Metallic Nanoparticles. *Commun. Phys.* **2019**, *2* (1), 47.

(22) Christopher, P.; Moskovits, M. Hot Charge Carrier Transmission from Plasmonic Nanostructures. *Annu. Rev. Phys. Chem.* **2017**, *68* (1), 379–398.

(23) Khurgin, J. B. Hot Carriers Generated by Plasmons: Where Are They Generated and Where Do They Go from There? *Faraday Discuss.* **2019**, *214*, 35–58.

(24) Cortés, E.; Besteiro, L. V.; Alabastri, A.; Baldi, A.; Tagliabue, G.; Demetriadou, A.; Narang, P. Challenges in Plasmonic Catalysis. *ACS Nano* **2020**, *14* (12), 16202–16219.

(25) Satyapal, S.; Petrovic, J.; Read, C.; Thomas, G.; Ordaz, G. The U.S. Department of Energy's National Hydrogen Storage Project: Progress towards Meeting Hydrogen-Powered Vehicle Requirements. *Catal. Today* **2007**, *120* (3–4), 246–256.

(26) Luo, J.; Liu, J.-X.; Li, W.-X. H_2 Activation on Pristine and Substitutional $ZnO(10\bar{1}0)$ and Cr_2O_3 (001) Surfaces by Density Functional Theory Calculations. *J. Phys. Chem. C* **2022**, *126* (21), 9059–9068.

(27) Berdakin, M.; Douglas-Gallardo, O. A.; Sánchez, C. G. Interplay between Intra- and Interband Transitions Associated with the Plasmon-Induced Hot Carrier Generation Process in Silver and Gold Nanoclusters. *J. Phys. Chem. C* **2020**, *124* (2), 1631–1639.

(28) Wu, X.; Liu, B.; Frauenheim, T.; Tretiak, S.; Yam, C.; Zhang, Y. Investigation of Plasmon Relaxation Mechanisms Using Nonadiabatic Molecular Dynamics. *J. Chem. Phys* **2022**, *157* (21), 214201.

(29) Douglas-Gallardo, O. A.; Berdakin, M.; Frauenheim, T.; Sánchez, C. G. Plasmon-Induced Hot-Carrier Generation Differences in Gold and Silver Nanoclusters. *Nanoscale* **2019**, *11* (17), 8604–8615.

(30) Govorov, A. O.; Zhang, H. Kinetic Density Functional Theory for Plasmonic Nanostructures: Breaking of the Plasmon Peak in the Quantum Regime and Generation of Hot Electrons. *J. Phys. Chem. C* **2015**, *119* (11), 6181–6194.

(31) Brown, A. M.; Sundararaman, R.; Narang, P.; Goddard, W. A.; Atwater, H. A. Nonradiative Plasmon Decay and Hot Carrier Dynamics: Effects of Phonons, Surfaces, and Geometry. *ACS Nano* **2016**, *10* (1), 957–966.

(32) Scholl, J. A.; Koh, A. L.; Dionne, J. A. Quantum Plasmon Resonances of Individual Metallic Nanoparticles. *Nature* **2012**, *483* (7390), 421–427.

(33) Guidez, E. B.; Aikens, C. M. Theoretical Analysis of the Optical Excitation Spectra of Silver and Gold Nanowires. *Nanoscale* **2012**, *4* (14), 4190.

(34) Liu, Z.; Oviedo, M. B.; Wong, B. M.; Aikens, C. M. Plasmon-Induced Excitation Energy Transfer in Silver Nanoparticle Dimers: A Real-Time TDDFTB Investigation. *J. Chem. Phys* **2022**, *156* (15), 154705.

(35) Niehaus, T. A.; Suhai, S.; Della Sala, F.; Lugli, P.; Elstner, M.; Seifert, G.; Frauenheim, Th. Tight-Binding Approach to Time-Dependent Density-Functional Response Theory. *Phys. Rev. B* **2001**, *63* (8), 085108.

(36) Giri, S. K.; Schatz, G. C. Photodissociation of H_2 on Ag and Au Nanoparticles: Effect of Size and Plasmon versus Interband Transitions on Threshold Intensities for Dissociation. *J. Phys. Chem. C* **2023**, *127* (8), 4115-4123.

(37) Asadi-Aghbolaghi, N.; Rüger, R.; Jamshidi, Z.; Visscher, L. TD-DFT+TB: An Efficient and Fast Approach for Quantum Plasmonic Excitations. *J. Phys. Chem. C* **2020**, *124* (14), 7946–7955.

(38) Jamshidi, Z.; Asadi-Aghbolaghi, N.; Morad, R.; Mahmoudi, E.; Sen, S.; Maaza, M.; Visscher, L. Comparing the Nature of Quantum Plasmonic Excitations for Closely Spaced Silver and Gold Dimers. *J. Chem. Phys* **2022**, *156* (7), 074102.

(39) Hull, O. A.; Aikens, C. M. Theoretical Investigations on the Plasmon-Mediated Dissociation of Small Molecules in the Presence of Silver Atomic Wires. *J. Phys. Chem. A* **2023**, *127* (10), 2228–2241.

(40) Yan, L.; Ding, Z.; Song, P.; Wang, F.; Meng, S. Plasmon-Induced Dynamics of H_2 Splitting on a Silver Atomic Chain. *Appl. Phys. Lett.* **2015**, *107* (8), 083102.

(41) Wu, Q.; Zhou, L.; Schatz, G. C.; Zhang, Y.; Guo, H. Mechanistic Insights into Photocatalyzed H_2 Dissociation on Au Clusters. *J. Am. Chem. Soc.* **2020**, *142* (30), 13090–13101.

(42) Hull, O. A.; Lingerfelt, D. B.; Li, X.; Aikens, C. M. Electronic Structure and Nonadiabatic Dynamics of Atomic Silver Nanowire–N_2 Systems. *J. Phys. Chem. C* **2020**, *124* (38), 20834–20845.

(43) Herring, C. J.; Montemore, M. M. Mechanistic Insights into Plasmonic Catalysis by Dynamic Calculations: O_2 and N_2 on Au and Ag Nanoparticles. *Chem. Mater.* **2023**, *35* (4), 1586–1593.

(44) Idrobo, J. C.; Walkosz, W.; Yip, S. F.; Öğüt, S.; Wang, J.; Jellinek, J. Static Polarizabilities and Optical Absorption Spectra of Gold Clusters (Au_n , n = 2 – 14 and 20) from First Principles. *Phys. Rev. B* **2007**, *76* (20), 205422.

(45) Wang, J.; Wang, G.; Zhao, J. Density-Functional Study of Au_n (N= 2 –20) Clusters: Lowest-Energy Structures and Electronic Properties. *Phys. Rev. B* **2002**, *66* (3), 035418.

(46) Zhou, M.; Jin, R. Optical Properties and Excited-State Dynamics of Atomically Precise Gold Nanoclusters. *Annu. Rev. Phys. Chem.* **2021**, *72* (1), 121–142.

(47) Pandeya, P.; Aikens, C. M. Real-Time Electron Dynamics Study of Plasmon-Mediated Photocatalysis on an Icosahedral Al_{13}^{-1} Nanocluster. *J. Phys. Chem. A* **2021**, *125* (22), 4847–4860.

(48) Li, X.; Tully, J. C.; Schlegel, H. B.; Frisch, M. J. *Ab Initio* Ehrenfest Dynamics. *J. Chem. Phys* **2005**, *123* (8), 084106.

(49) Ding, F.; Goings, J. J.; Liu, H.; Lingerfelt, D. B.; Li, X. Ab Initio Two-Component Ehrenfest Dynamics. *J. Chem. Phys* **2015**, *143* (11), 114105.

(50) Kuda-Singappulige, G. U.; Aikens, C. M. Theoretical Insights into Excitation-Induced Oxygen Activation on a Tetrahedral Ag_8 Cluster. *J. Phys. Chem. A* **2021**, *125* (43), 9450–9458.

(51) Yabana, K.; Nakatsukasa, T.; Iwata, J.-I.; Bertsch, G. F. Real-Time, Real-Space Implementation of the Linear Response Time-Dependent Density-Functional Theory. *Phys. Status Solidi B* **2006**, *243* (5), 1121–1138.

(52) Goings, J. J.; Lestrange, P. J.; Li, X. Real-time Time-dependent Electronic Structure Theory. *WIREs Comput. Mol. Sci.* **2018**, *8* (1).

(53) Perdew, J. P.; Burke, K.; Ernzerhof, M. Generalized Gradient Approximation Made Simple. *Phys. Rev. Lett.* **1996**, *77* (18), 3865–3868.

(54) Rohrdanz, M. A.; Martins, K. M.; Herbert, J. M. A Long-Range-Corrected Density Functional That Performs Well for Both Ground-State Properties and Time-Dependent Density Functional Theory Excitation Energies, Including Charge-Transfer Excited States. *J. Chem. Phys* **2009**, *130* (5), 054112.

(55) Hay, P. J.; Wadt, W. R. *Ab Initio* Effective Core Potentials for Molecular Calculations. Potentials for K to Au Including the Outermost Core Orbitals. *J. Chem. Phys* **1985**, *82* (1), 299–310.

(56) Wadt, W. R.; Hay, P. J. *Ab Initio* Effective Core Potentials for Molecular Calculations. Potentials for Main Group Elements Na to Bi. *J. Chem. Phys* **1985**, *82* (1), 284–298.

(57) Hay, P. J.; Wadt, W. R. *Ab Initio* Effective Core Potentials for Molecular Calculations. Potentials for the Transition Metal Atoms Sc to Hg. *J. Chem. Phys* **1985**, *82* (1), 270–283.

(58) Gaussian Development Version, Revision I.13+, M. J. Frisch, G. W. Trucks, H. B. Schlegel, G. E. Scuseria, M. A. Robb, J. R. Cheeseman, G. Scalmani, V. Barone, G. A. Petersson, H. Nakatsuji, X. Li, M. Caricato, A. V. Marenich, J. Bloino, B. G. Janesko, R. Gomperts, B. Mennucci, H. P. Hratchian, J. V. Ortiz, A. F. Izmaylov, J. L. Sonnenberg, D. Williams-Young, F. Ding, F. Lipparini, F. Egidi, J. Goings, B. Peng, A. Petrone, T. Henderson, D. Ranasinghe, V. G. Zakrzewski, J. Gao, N. Rega, G. Zheng, W. Liang, M. Hada, M. Ehara, K. Toyota, R. Fukuda, J. Hasegawa, M. Ishida, T. Nakajima, Y. Honda, O. Kitao, H. Nakai, T. Vreven, K. Throssell, J. A. Montgomery, Jr., J. E. Peralta, F. Ogliaro, M. J. Bearpark, J. J. Heyd, E. N. Brothers, K. N. Kudin, V. N. Staroverov, T. A. Keith, R. Kobayashi, J. Normand, K. Raghavachari, A. P. Rendell, J. C. Burant, S. S. Iyengar, J. Tomasi, M. Cossi, J. M. Millam, M. Klene, C. Adamo, R. Cammi, J. W. Ochterski, R. L. Martin, K. Morokuma, O. Farkas, J. B. Foresman, and D. J. Fox, Gaussian, Inc., Wallingford CT, 2018.

(59) Wang, Y.; Aikens, C. M. Effects of Field Strength and Silver Nanowire Size on Plasmon-Enhanced N_2 Dissociation. *J. Phys. Chem. A* **2023**, *127* (27), 5609-5619

(60) Ding, F.; Guidez, E. B.; Aikens, C. M.; Li, X. Quantum Coherent Plasmon in Silver Nanowires: A Real-Time TDDFT Study. *J. Chem. Phys* **2014**, *140* (24), 244705.

(61) Liang, W.; Isborn, C. M.; Li, X. Laser-Controlled Dissociation of $C_2H_2^{2+}$: Ehrenfest Dynamics Using Time-Dependent Density Functional Theory. *J. Phys. Chem. A* **2009**, *113* (15), 3463–3469.

Chapter 6 - Implementation of energy and gradient for the TDDFT-approximate auxiliary function (aas) method

Yuchen Wang, Shana Havenridge, and Christine M. Aikens*
Department of Chemistry, Kansas State University, Manhattan, KS 66506, USA

*Email: cmaikens@ksu.edu

6.1 Abstract

In this work, we have implemented the TDDFT-aas method, which is an approximate TDDFT method. In this method, instead of calculating the exact two-center electron integrals in the *K* coupling matrix when solving the Casida equation, we approximate the integrals, thereby reducing the computational cost. Compared with the related TDDFT+TB method, a new type of gamma function is used when calculating the *K* coupling matrix, which does not depend on the tight binding parameters. The calculated absorption spectra of silver and gold nanoparticles using TDDFT-aas show good agreement with TDDFT+TB results. In addition, we have also implemented the analytical excited-state gradients for the TDDFT-aas method, which makes it possible to calculate the emission energy of the systems.

6.2 Introduction

Time-dependent density functional theory (TDDFT) has been successfully applied to calculate excited-state properties for small molecule, biomolecule, nanocluster, and solid-state systems.[1–4] TDDFT is built on DFT; however, since the classic Hohenberg-Kohn formulation of density functional theory is time-independent, DFT itself is not used for the excited state problem. Runge and Gross extended the theorem to excited states by incorporating a time-dependent external potential into the Hohenberg-Kohn DFT formalism.[5] Casida formulated the linear-response formalism of solving a time-dependent DFT equation, where the electron density experiences a linear response to an external potential perturbation.[6,7] In practice, the linear-

response formalism is sufficient to calculate the excitation spectrum of the system in response to a weak perturbation. Nowadays, the Casida formalism for TDDFT to solve for the excitation energies has been implemented in a variety of quantum chemistry calculation codes in order to calculate absorption spectra for systems of interest.

As the size of the system increases, the computational time and memory increase significantly for TDDFT calculations, in part because the *K* coupling matrix requires calculation of many two-electron integrals. Recently, some approximation methods to TDDFT have been proposed to reduce the computational cost, such as TD-DFTB,[8,9] sTDDFT,[10] sTDA,[11,12] TDDFT+TB,[13] TDDFT-as (TDDFT using auxiliary basis function s),[14] and TDDFT-ris.[15] To briefly review these approximation methods, TD-DFTB starts with semiempirical density functional tight-binding (DFTB) ground state calculations, where trial densities are applied instead of using actual densities. The trial density is a superposition of atomic contributions and needs to be parameterized; in general, DFTB calculations incorporate many parameters that must be determined in advance for each pair of atoms.[16,17] For TD-DFTB excited-state calculations, the *K* coupling matrix is calculated by using an approximation $K_{ia,jb} = \sum_{AB} q_{ia,A}\gamma_{AB}q_{jb,B}$ where q represents transition charges from a Mulliken population analysis, and the γ_{AB} function depends on both the distance between two atoms A and B (R_{AB}) and the tight-binding parameter for each element. To avoid the need for extensive parameterization, several recent methods have combined aspects of DFT and DFTB. For sTDA and sTDDFT, standard DFT is employed for the ground state calculations. Therefore, an approximation is only used in the excited state calculation. The related TDDFT+TB method is motivated by sTDA and sTDDFT; it also uses standard DFT for the ground state calculations. For these excited-state calculations, the *K* coupling matrix is calculated using the same equation as TD-DFTB, although Löwdin population analysis is used to calculate the q. Compared with sTDA and sTDDFT, TDDFT+TB does not take the Hartree-Fock exchange term into account when doing the approximations, which makes TDDFT+TB only applicable to pure functionals. Because the excited-state calculations are based on the actual density obtained from DFT calculations, TDDFT+TB can achieve more accurate results compared with TD-DFTB. By using this approximation, TDDFT+TB can address the computational limitations of calculating large molecules and nanoparticles.[18–21] The TDDFT-as method is similar to TDDFT+TB, and both of those two methods approximate the *K* coupling matrix when solving the linear Casida equation. However, the γ_{AB} function applied in the approximation is only

dependent on the distance between two atoms A and B (R_{AB}) and a single orbital exponent that can be varied. TDDFT-as has shown success in calculating absorption spectra specifically for silver nanoparticles.[14] TDDFT-ris method is an extension to the TDDFT-as method, where the exponent in γ_{AB} is related to the element types in the system. In addition, TDDFT-ris takes the Hartree-Fock exchange terms into account when doing the approximations.[14]

Linear-response TDDFT formalism calculations provide vertical excitation information that can be used to produce absorption spectra. To elucidate other optical properties such as photo-catalytic reaction pathways or photoluminescence, it is important to understand the excited state potential energy surface. Thus, gradient calculations (which are required for excited-state geometry optimizations) are needed to explore the potential energy surface and study optical properties such as photoluminescence. However, using TDDFT to perform excited-state gradient calculations is computationally expensive. Recently, the analytical gradient of the TDDFT+TB method has been derived, which enables speeding up the excited-state geometry optimization process.[22]

In this work, we develop a new TDDFT approximation method called TDDFT-aas (TDDFT- approximate auxiliary s function). The method resembles both TDDFT+TB and TDDFT-as methods. When the *K* coupling matrix is calculated using $K^{\mathrm{S}}_{ia,jb} = \sum_{AB}\ q_{ia,A}\gamma_{AB}q_{jb,B}$, we use Löwdin population analysis for the q and use the same type of γ_{AB} function as the TDDFT-as method. Therefore, the TDDFT-aas method is independent of chemical hardness parameters. We examine the absorption spectra for a variety of gold/silver nanoclusters using the new TDDFT-aas method. In addition to the energy calculation, we also implement the gradient for the TDDFT-aas method, which enables us to apply TDDFT-aas excited state geometry optimizations to calculate emission energies. After derivation and implementation of the TDDFT-aas energy and gradient, numerical and analytical gradients are calculated and compared to examine the accuracy of the analytical gradient. Emission energies for systems ranging from diatomic molecules to gold thiolate-stabilized nanoclusters are calculated. In addition, we also compare the computational costs between different approximation methods. Overall, because TDDFT-aas does not require tight-binding parameters, the method is easier to implement compared with other semi-empirical approximation methods.

6.3 Theory and code implementation

The linear formalism of TDDFT starts by solving the Casida equation,[6,7] which can be written as equation 6.1:

$$\begin{pmatrix} \mathbf{A} & \mathbf{B} \\ \mathbf{B}^* & \mathbf{A} \end{pmatrix} \begin{pmatrix} \mathbf{X} \\ \mathbf{Y} \end{pmatrix} = \boldsymbol{\omega} \begin{pmatrix} \mathbf{1} & \mathbf{0} \\ \mathbf{0} & \mathbf{-1} \end{pmatrix} \begin{pmatrix} \mathbf{X} \\ \mathbf{Y} \end{pmatrix} \quad \textbf{(Equation 6.1)}$$

where **A** and **B** represent rotational Hessian matrices and ω represents excitation energy. **X** and **Y** are eigenvectors that correspond to the excitation and deexcitation respectively. The linear Casida equation can be transformed into the formalism of $\mathbf{\Omega F} = \omega^2 \mathbf{F}$, where $\mathbf{F} = (\mathbf{A} - \mathbf{B})^{-\frac{1}{2}}(\mathbf{X} + \mathbf{Y})$ and $\mathbf{\Omega} = (\mathbf{A} - \mathbf{B})^{\frac{1}{2}}(\mathbf{A} + \mathbf{B})(\mathbf{A} - \mathbf{B})^{\frac{1}{2}}$.[6] To solve the equation, $\mathbf{A} + \mathbf{B}$ and $\mathbf{A} - \mathbf{B}$ need to be calculated, and the matrices have the following formulas:

$$\boldsymbol{A_{ia,jb} + B_{ia,jb} = \delta_{ab}\delta_{ij}(\epsilon_a - \epsilon_i) + 2(ia \mid jb) + 2(ia|f_{xc}|jb) - a_x((ij \mid ab) + (ib \mid ja)}$$ **(Equation 6.2)**

$$\boldsymbol{A_{ia,jb} - B_{ia,jb} = \delta_{ab}\delta_{ij}(\epsilon_a - \epsilon_i) - a_x((ij \mid ab) - (ib \mid ja))} \quad \textbf{(Equation 6.3)}$$

where *i, j* represent occupied orbitals and *a, b* represent virtual orbitals; $(\epsilon_a - \epsilon_i)$ represents the orbital energy difference between orbital index *i and a;* a_x is the amount of Hartree-Fock exchange; and $(ia \mid jb)$ and $(ia|f_{xc}|jb)$ are the usual two-electron integrals. If we only consider pure functionals, a_x = 0 and therefore $\mathbf{A} + \mathbf{B}$ and $\mathbf{A} - \mathbf{B}$ can be reduced to:

$$\boldsymbol{A_{ia,jb} + B_{ia,jb} = \delta_{ab}\delta_{ij}(\epsilon_a - \epsilon_i) + 2(ia \mid jb) + 2(ia|f_{xc}|jb)} \quad \textbf{(Equation 6.4)}$$

$$\boldsymbol{A_{ia,jb} - B_{ia,jb} = \delta_{ab}\delta_{ij}(\epsilon_a - \epsilon_i)} \quad \textbf{(Equation 6.5)}$$

The approximation TDDFT+TB has made is to approximate the two-center electron integrals calculations. In this way, instead of calculating the exact two-center electron integrals $(ia \mid jb)$ and $(ia|f_{xc}|jb)$, the approximation $K_{ia,jb} = \sum_{AB} q_{ia,A}\gamma_{AB}q_{jb,B}$ was used instead, where *A* and *B* are the two nuclei from which the two-center integrals arise, and *q* represents transition charges from a Löwdin population analysis that can be written as $q_{ia,A} = \sum_{\mu \in A} C'_{\mu i}C'_{\mu a}$, where $C' = S^{1/2}C$. In this equation, C represents the coefficient matrix of the Kohn-Sham orbitals; μ, ν, κ, and λ indicate atomic basis functions; and $S^{1/2}$ denotes the square root of the overlap matrix. The γ_{AB} function in TDDFT+TB depends on both the distance between two atoms *A* and *B* (R_{AB}) and the chemical hardness for each element.

For the TDDFT-aas method, we use the same γ_{AB} function as in TDDFT-as method, where $\gamma(R_{AB}) = \frac{\mathrm{erf}(R_{AB}\sqrt{\alpha/2})}{R_{AB}}$, and α is a parameter that needs to be tuned before using the method. In our code, the α value can be selected by the user at runtime.

To implement the excited state gradient of the TDDFT-aas method, we start with the full analytical gradient equation for TDDFT+TB,[22] where the equation can be written as:

$$\frac{d\mathrm{E}}{dR_A} = 2\sum_{\mu\in A,\nu\notin A}\frac{dh_{\mu\nu}}{dR_A}P_{\mu\nu} + 2\sum_{\mu,\lambda\in A,\nu,\kappa\notin A}\frac{d(\mu\nu|\lambda\kappa)}{dR_A}P_{\mu\nu}$$
$$+2\sum_{\mu\in A,\nu\notin A}\frac{dV^{XC}_{\mu\nu}}{dR_A}P_{\mu\nu} + 2\sum_{\mu\in A,\nu\notin A}S^{1/2}_{\mu\nu}\frac{dS^{1/2}_{\mu\nu}}{dR_A}(\Xi_A+\Xi_B)U_{\mu\nu} \qquad \textbf{(Equation 6.6)}$$
$$+4\sum_{\mu\in A,\nu\notin A}\frac{d\gamma_{AB}}{dR_A}U_AU_B - \sum_{\mu\in A,\nu\notin A}\frac{dS_{\mu\nu}}{dR_A}W_{\mu\nu}.$$

where $U_A = \sum_{ia}(X+Y)_{ia}q_{ia,A}$ and $\Xi_A = \sum_B \gamma_{AB}U_B$. From the gradient equation, the fourth and fifth terms involve the γ_{AB} function. Because the only difference between TDDFT+TB and TDDFT-aas is the form of γ_{AB}, we can use Equation 6.6 as the general TDDFT-aas gradient equation and adjust the new equation for the γ_{AB} related terms. We then also derive $\frac{d\gamma_{AB}}{dR_A}$:

$$\frac{d\gamma_{AB}}{dR_A} = \frac{\sqrt{\frac{2\alpha}{\pi}}*e^{-R_A^2\frac{\alpha}{2}}*R_A - \left(\mathrm{erf}\left(R_A\sqrt{\frac{\alpha}{2}}\right)\right)}{(R_A)^2} \qquad \textbf{(Equation 6.7)}$$

We have implemented the TDDFT-aas code in the Amsterdam Modeling Suite (AMS),[23] based on the TDDFT+TB gradient code.

6.4 Results and discussion

To validate the accuracy of the TDDFT-aas method energies and gradients, we performed test calculations using both linear-response TDDFT energy calculations and excited state geometry optimizations. All of the calculations were completed in a development version of the Amsterdam Density Functional (ADF) engine in the Amsterdam Modeling Suite (AMS).[23]

6.4.1 Optimized tuning parameter

Similar to the TDDFT-as method, the exponent (α) in γ_{AB} needs to be optimized before using the TDDFT-aas method. To tune the α parameter, optical absorption spectra were calculated for the Ag_{20} and Au_{20} tetrahedral nanoclusters with a range of different α values (0.16, 0.18, 0.2,

0.22, 0.24), and the absorption spectra results are plotted and shown in Figure 6.1. The calculations were performed at the PBE[24]/DZ level of theory. TDDFT and TDDFT+TB results calculated at the PBE/DZ level of theory are also included in the absorption spectra for comparison. In all cases, the overall shape of the spectrum and the approximate peak locations are well reproduced for all of the approximate methods. For the Ag_{20} nanocluster, the TDDFT-aas spectra show the best results when α is around 0.2, so α=0.2 is chosen as the default optimized value. The choice of α=0.2 also works well for the Au_{20} nanocluster. For the Ag_{20} nanocluster, the TDDFT-aas methods provide a closer approximation to the TDDFT oscillator strengths than the TDDFT+TB method; this is reversed for the Au_{20} nanocluster.

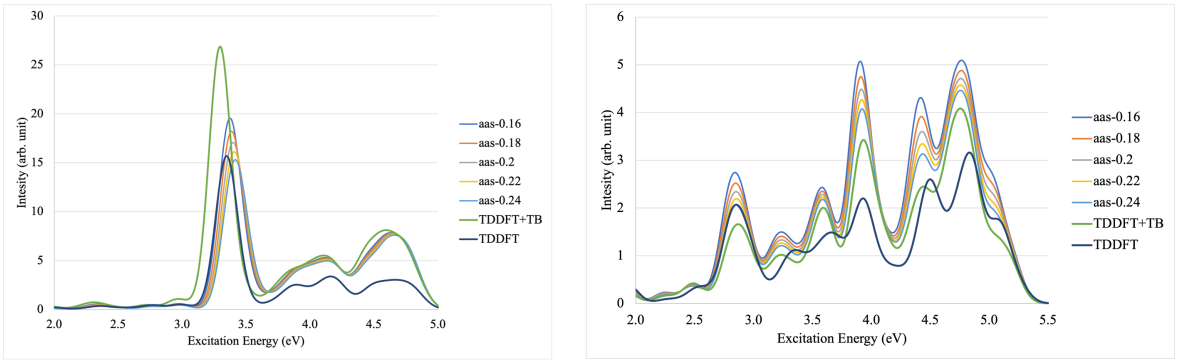
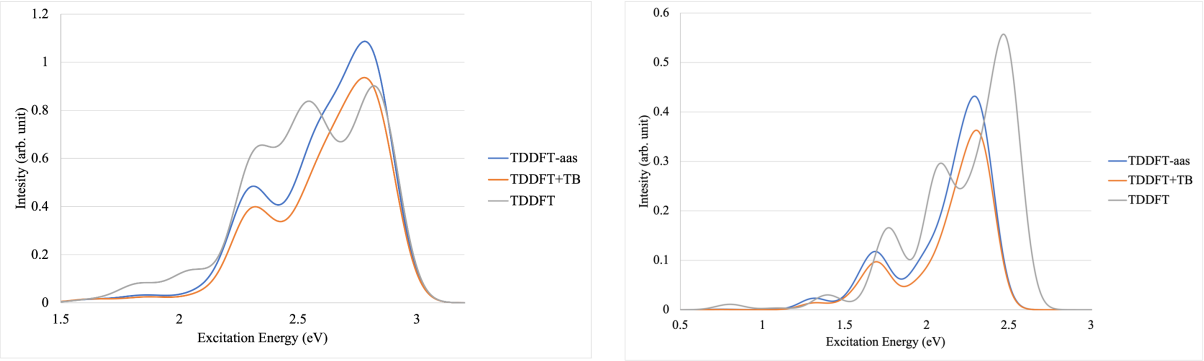


Figure 6.1 Absorption spectra for tetrahedral clusters A. Ag_{20} and B. Au_{20} calculated by the TDDFT-aas method with different α values. TDDFT and TDDFT+TB calculation results are included for comparison.

6.4.2 Comparison of methods for nanocluster absorption spectra

After examining the α parameter dependence for Ag_{20} and Au_{20}, we used 0.2 as the α value to calculate the absorption spectra for additional pure gold (Figure 6.2) and silver (Figure 6.3) nanoclusters. The absorption spectra result for the Au_{38}^{+4} system shows that both the TDDFT-aas and TDDFT+TB methods underestimate the absorption intensity at around 2.5 eV and overestimate the absorption intensity at around 2.7 eV. For the excitation at around 2.7 eV, both TDDFT-aas and TDDFT+TB show a slight redshift for the excitation energy. From the spectra

with a Gaussian broadening, it is hard to observe the peak around 2.5 eV in TDDFT-aas and TDDFT+TB compared with TDDFT results. Stick spectra are shown in the supporting information to better visualize each distinct excitation (Figure D.1); in general, the stick spectra have peaks in similar energy ranges, although the TDDFT-aas method predicts more splitting. For the Au_{55}^{+5} system, TDDFT-aas and TDDFT+TB show similar line shapes for their spectra, and they both underestimate the absorption intensities for excitation at around 1.8 eV and 2.5 eV compared with TDDFT results. The excitation at around 2.1 eV is not apparent in the two approximation methods but can be visualized more clearly from the stick spectra (Figure D.2). In summary, TDDFT-aas spectra show very similar line shapes to the TDDFT+TB spectra, and both agree with the excitation energies from TDDFT calculations well but have some issues when predicting the oscillator strengths.



A B

Figure 6.2 Comparison of the absorption results using TDDFT-aas and TDDFT+TB for pure gold nanoclusters. A. Au_{38}^{+4} B. Au_{55}^{+5}

The calculated spectra for representative silver nanoclusters are shown in Figure 6.3. For the Ag_{38}^{+4} system, the overall spectral line shapes show good agreement among TDDFT, TDDFT+TB, and TDDFT-aas results. TDDFT+TB shows an overestimate of the absorption intensity and redshift of the excitation energy for peaks at around 3.6 eV and 4.0 eV. TDDFT-aas shows relatively better agreement with TDDFT for both excitation energy and absorption intensity compared with TDDFT+TB. For the Ag_{55}^{+5} system, TDDFT-aas slightly underestimates the intensity for the peak located around 3.3 eV and TDDFT+TB overestimates the intensity for that peak compared with the TDDFT results. For the shoulder peak located around 2.9 eV, both two approximation methods show slight blueshifts compared with TDDFT.

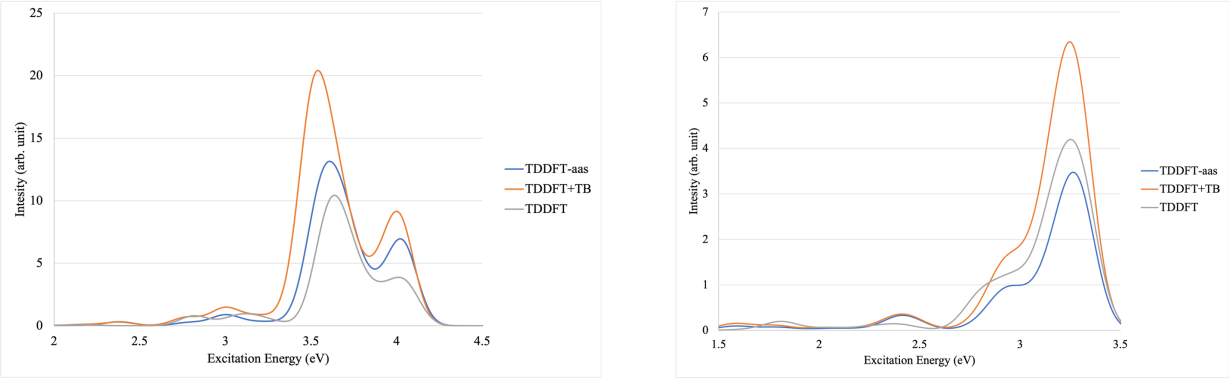


Figure 6.3 Comparison of the absorption results using TDDFT-aas to calculate pure gold nanoclusters. A. Ag_{38}^{+4} B. Ag_{55}^{+5}

Besides the pure metal nanoclusters, the absorption spectra of gold thiolate-protected nanoclusters were also calculated using the TDDFT-aas method, and the calculated spectra and comparison between TDDFT+TB and TDDFT results are shown in Figure 6.4. α=0.2 is applied for the calculations. Overall, TDDFT-aas shows good agreement with TDDFT for the excitation energies, while it slightly underestimates the oscillator strength of the first absorption peak. For the $Au_{25}(SCH_3)_{18}^-$ system, TDDFT-aas and TDDFT+TB overestimate the oscillator strength of the peak ranges between 3 eV and 4 eV. For the $Au_{38}(SCH_3)_{24}$ system, TDDFT-aas shows good agreement with the peaks around 2.5 eV and overestimates the oscillator strength of the peaks between 2.8 eV and 3.5 eV. Because α is set to be 0.2 for the system, which affects the S, C, and H atoms as well as Au, the absorption spectra results indicate that a generalized α is reasonable for these gold thiolate-protected nanocluster calculations. Overall, systems with less symmetry such as $Au_{25}(SCH_3)_{18}^-$ and $Au_{38}(SCH_3)_{24}$ provide a better match between the approximate TDDFT-aas and TDDFT+TB methods and the original TDDFT method compared to the pure nanoclusters such as Au_{38}^{+4} and Au_{55}^{+5}. This is likely due to the semiempirical approximations inherent in the methods, which reduce the number of integrals calculated, especially for highly symmetric systems.[13]

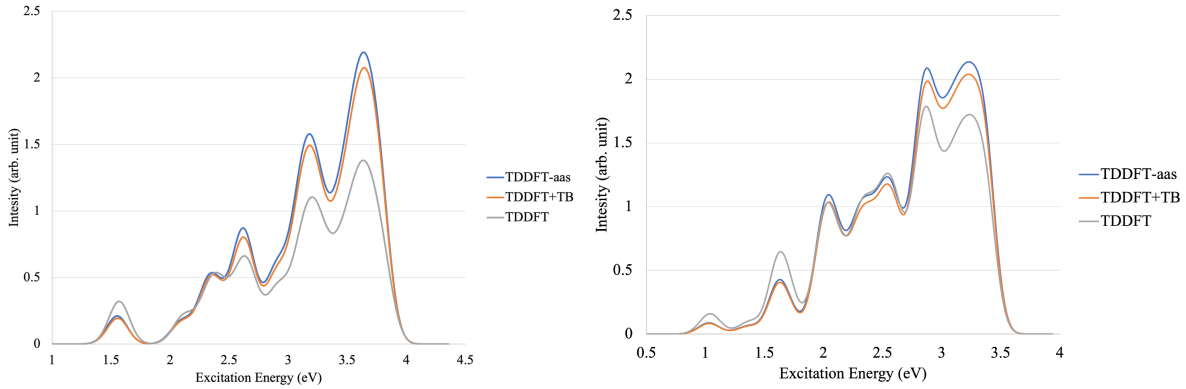


Figure 6.4 Comparison of the absorption results using TDDFT-aas to calculate thiolate-protected gold nanocluster. A. $Au_{25}(SCH_3)_{18}^-$ B. $Au_{38}(SCH_3)_{24}$

In addition to the PBE functional, the BP86 functional[25,26] was also applied to test the accuracy of TDDFT-aas calculations, and the results are shown in Figure D.3. The trends are similar to the PBE calculated results, where TDDFT-aas results show a very similar line shape with TDDFT+TB results; these methods overestimate the oscillator strength of peaks between 3.0 eV and 4.5 eV compared with TDDFT results but achieve very good agreement in excitation energies.

Overall, for the absorption spectra calculations, TDDFT-aas can obtain very similar results to TDDFT+TB calculations, and its excitation energies show good agreement with TDDFT. However, both approximate methods have some artifacts when predicting the oscillator strength.

6.4.3 Numerical and analytical gradients

As discussed in equations 6 and 7, the analytical gradients for TDDFT-aas have been derived in this work. To validate the TDDFT-aas gradient code implementation, we computed numerical and analytical gradients for selected systems and examined the results. For the numerical gradient, a finite difference is used with a step size of 0.001 Å in x, y, and z directions. The MAD (Mean Absolute Deviation) and RMS (Root Mean Square) results between the numerical and analytical gradient were calculated and are shown in Table 6.1. All MAD values are smaller than 2.11×10^{-4} Hartree/Å and all RMS values are smaller than 3.66×10^{-4} Hartree/Å.

These errors are similar to those for TDDFT+TB and TDDFT.[22] The results demonstrate the accuracy of the TDDFT-aas analytical gradient.

Table 6.1 Numerical vs. analytical gradient differences (Hartree/Å) for representative molecular systems.

	MAD	RMS
H_2	2.47×10^{-5}	4.22×10^{-5}
Li_2	1.50×10^{-5}	2.11×10^{-5}
N_2	2.11×10^{-4}	3.66×10^{-4}
Cl_2	1.87×10^{-5}	2.45×10^{-5}
HCl	1.66×10^{-5}	2.76×10^{-5}
Uracil	8.25×10^{-5}	1.11×10^{-4}
Ethene	1.23×10^{-4}	2.27×10^{-4}
Acetamide	1.53×10^{-4}	2.20×10^{-4}
Adenine	7.27×10^{-5}	1.04×10^{-4}
Pyrazine	4.00×10^{-5}	7.14×10^{-5}
Benzoquinone	2.94×10^{-5}	5.62×10^{-5}
Octatetraene	5.76×10^{-5}	2.12×10^{-4}
Benzene	1.30×10^{-5}	2.53×10^{-5}

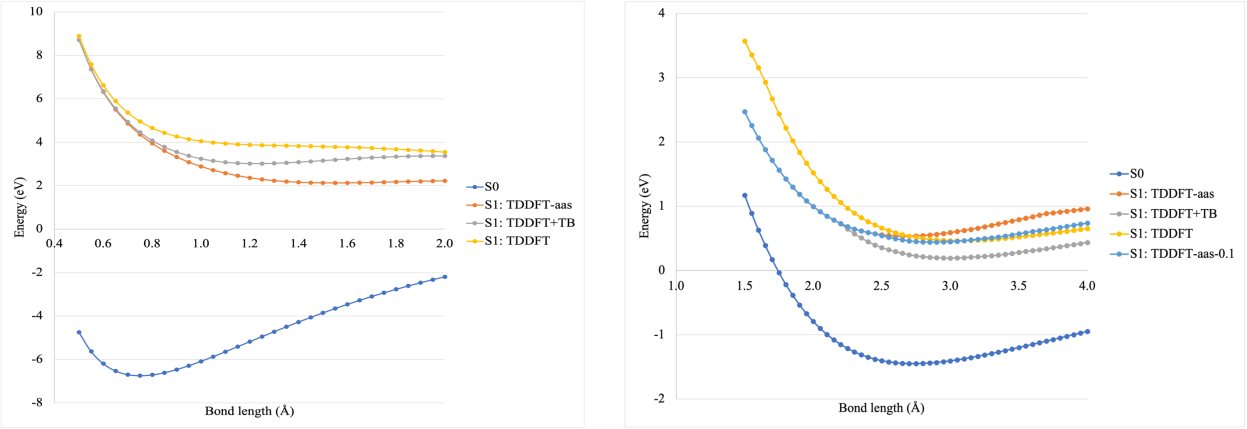
6.4.4 Excited state geometry optimization

Excited state geometry optimizations were then performed to evaluate the quality of the calculated emission energies. First, we perform excited-state geometry optimizations on several diatomic molecule systems at the PBE/TZP level of theory, and the results are shown in Table 6.2 and Table D.1. Diatomic molecules are known to be a challenging test case for approximate TDDFT methods due to the atomic transition charges' inability to model local transitions;[13] though a useful test of inherent errors, these approximate methods are not required for diatomic molecules because the standard TDDFT method is applicable for these systems.

Table 6.2 Emission energy for five diatomic molecules (unit: eV) calculated at different level of theories, TDDFT failed in calculating the emission energy of H_2.

	TDDFT	TDDFT-aas	TDDFT+TB
H_2	N/A	5.80	8.07
Li_2	1.85	1.98	1.60
N_2	6.45	6.97	6.97
Cl_2	1.19	0.94	0.94
HCl	1.71	1.51	1.51

For N_2, Cl_2, and HCl, TDDFT-aas and TDDFT+TB give the same emission energy results, where the energy difference between TDDFT-aas and TDDFT ranges from 0.20 eV to 0.52 eV. The TDDFT-aas method provides identical results to the TDDFT+TB method in these cases. To understand the H_2 and Li_2 cases, potential energy surfaces (PES) for these systems are plotted and shown in Figure 6.5.



A B

Figure 6.5 Potential energy surfaces for the A. H_2 and B. Li_2 systems. In the key, S0 represents the PES for the ground state. S1: TDDFT-aas represents the PES for the S_1 state using TDDFT-aas methods with α=0.2. S1: TDDFT-aas-0.1 represents the PES for the S_1 state using TDDFT-aas methods with α=0.1. S1: TDDFT+TB represents the PES for the S_1 state using TDDFT+TB methods. S1: TDDFT represents the PES for the S_1 state using TDDFT methods.

For the S_1 state, TDDFT did not calculate a minimum in the first excitation energy for H_2. The results agree with the reported potential energy surface for H_2,[27] in which there is not a local minimum for the S_1 state. Meanwhile, TDDFT+TB predicts a fairly shallow S_1 minimum geometry with an H-H bond length of 1.21 Å at 8.07 eV above the ground state energy. TDDFT-aas predicts

a very shallow S_1 minimum geometry at an H-H bond distance of 1.53 Å, with an energy of 5.80 eV above the ground state energy. Both of these two methods show long H-H distances for the S_1 minimum, which agree with the dissociative nature of the S_1 potential energy surface.

For Li_2, the S_1 state minima are calculated at 1.85 eV, 1.60 eV, and 1.98 eV for the TDDFT, TDDFT+TB, and TDDFT-aas(α=0.2) methods, respectively. From the PES, TDDFT+TB, and TDDFT-aas (for both α=0.2 and α=0.1) show the same S_1 PES when the Li-Li bond length is less than 2.2 Å; with the increased bond length, TDDFT-aas shows a higher potential energy surface than TDDFT+TB, and the TDDFT-aas PES crosses the TDDFT PES. The higher S_1 PES leads to a change in the order of the excited state compared with the other two methods. For the TDDFT+TB and TDDFT results, the S_1 state arises from a σ_g to σ_u transition, while in TDDFT-aas, the S_1 state shows σ_g to π_u transitions. However, if α is 0.1, the optimized excitation energy is 1.88 eV, and the corresponding transition arises from σ_g to σ_u. The results indicate that modifying the α value will change the order of the excitation in Li_2. Thus, tuning the α value may be helpful for systems of interest.

In addition to diatomic molecules, the emission energies for the Thiel test set[28] of organic molecules were examined using the TDDFT-aas method. The optimizations were performed at the PBE/TZP level of theory. The emission energy differences between TDDFT-aas, TDDFT+TB, and TDDFT are shown in Figure 6.6 and Table D.2.

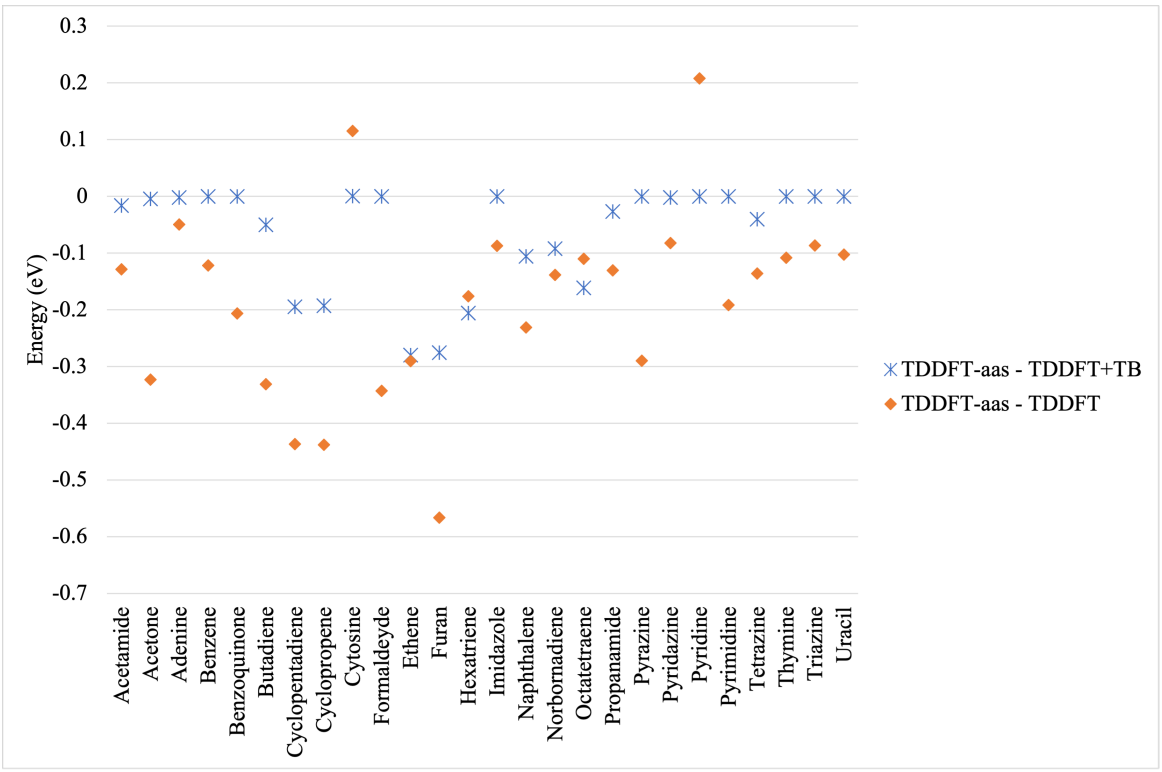


Figure 6.6 Emission energy differences among TDDFT-aas, TDDFT+TB, and TDDFT for organic molecules from the Thiel test set.

In general, the energy differences between TDDFT-aas and TDDFT+TB range from 0.00 to 0.29 eV, with both methods calculating the same optimized S_1 energy for many molecules. The similarity of these two methods is not surprising because the differences between the TDDFT-aas and TDDFT+TB gradient equations only arise in the fourth and fifth terms of equation 6. Ethene shows the highest energy difference between the TDDFT-aas and TDDFT+TB results at 0.29 eV. These results indicate that choosing 0.2 as the α value may still be reasonable for organic molecules.

For most systems, the agreement between TDDFT and TDDFT-aas is reasonable, ranging from 0.05 eV to 0.56 eV. However, a few cases occur that need further discussion. Furan shows the highest energy difference between TDDFT and TDDFT-aas. For the furan system, when the optimizations started from the same initial geometry, the energy at the S_1 minimum is calculated to be 5.56 eV, 4.70 eV, and 4.98 eV for the TDDFT, TDDFT-aas, and TDDFT+TB calculations, respectively. However, if furan were reoptimized using the TDDFT method starting from the final TDDFT-aas or TDDFT+TB S_1 optimized structure, the energy at the S_1 minimum is calculated to be 5.27 eV. If the reverse process is performed and furan is reoptimized starting from the original

TDDFT S_1 optimized structure, the S_1 excitation energy remains as 4.70 eV using the TDDFT-aas method or 4.98 eV using the TDDFT+TB method. For furan, TDDFT shows two optimized S_1 minima (corresponding to different excitation origins), whereas we have only been able to find one minimum point for TDDFT-aas and TDDFT+TB thus far.

For pyridazine, when the optimizations started from the same initial geometry, the energy at the S_1 minimum is calculated to be 1.71 eV, 2.27 eV, and 2.27 eV for the TDDFT, TDDFT-aas, and TDDFT+TB calculations, respectively. However, if the pyridazine were re-optimized starting from the TDDFT final optimized structure, the energy at the S_1 minimum is now calculated to be 1.63 eV for both TDDFT-aas and TDDFT+TB calculations. If the reverse process was performed and pyridazine was reoptimized starting from the TDDFT-aas or TDDFT+TB final optimized structure using the TDDFT method, the first excited state energy minimum is still calculated to be 1.71 eV. For pyridazine, TDDFT-aas and TDDFT+TB show two minimum points on the S_1 state surface, while TDDFT shows only one minimum point.

For tetrazine, when the optimizations started from the same initial geometry the energy at the S_1 minimum is calculated to be 2.28 eV, 3.06 eV, and 3.06 eV for the TDDFT, TDDFT-aas, and TDDFT+TB calculations, respectively. When tetrazine was reoptimized starting from the TDDFT final optimized structure, the energy at the S_1 minimum is now calculated to be 2.14 eV and 2.18 eV for TDDFT-aas and TDDFT+TB, respectively, which is quite close to the 2.28 eV calculated by TDDFT. If the reverse process is performed and tetrazine is reoptimized starting from the TDDFT-aas or TDDFT+TB final optimized structure using the TDDFT method, the energy at the S_1 minimum is now calculated to be 2.43 eV, which is a higher energy S_1 minimum. Thus for tetrazine, TDDFT-aas, TDDFT+TB, and TDDFT can find two excited state minima depending on the starting geometry; the initial minimum found is sensitive to the PES.

For the S_1 minimum state for ethene, the emission energies are calculated to be 5.58 eV, 6.71 eV, and 6.75 eV for the TDDFT-aas, TDDFT+TB, and TDDFT methods, respectively. For the electronic transition in the S_1 state, TDDFT-aas predicts that the π_u to π_g transition is responsible, whereas TDDFT+TB and TDDFT show that this state arises from the π_u to σ_u transition. When ethene was reoptimized starting from the TDDFT final optimized structure, the energy at the S_1 minimum is now calculated to be 5.58 eV and 6.73 eV for TDDFT-aas and TDDFT+TB, respectively. When ethene was reoptimized starting from the TDDFT-aas final optimized structure, the energy at the S_1 minimum is now calculated to be 5.89 eV for TDDFT+TB

and 6.17 eV for TDDFT. The results suggest that a second minimum may be possible for each method.

The results for the diatomic molecules and organic molecules indicated that TDDFT-aas shows good agreement with TDDFT+TB and TDDFT for most of the molecules. However, complications can arise when the excited state crosses with other states, and this can cause the excitation energy difference to be large between different computational methods. In addition, starting from different initial geometries could find different minima for some organic molecules, depending on the system.

Finally, we examine the emission energies for two gold nanoclusters at the PBE/DZ level of theory; the results are shown in Table 6.3. For the gold clusters, the TDDFT-aas emission energy results show good agreement with TDDFT+TB and TDDFT, with energy differences within 0.02 eV. To examine the effects of the α parameter, α was set to 0.1 and 0.3 respectively to carry out the calculations again, and the emission energy results are 0.754 eV and 0.758 eV respectively. The results indicate that α will slightly affect the results, but the general trends show that TDDFT-aas will very slightly underestimate the energy compared with TDDFT.

Table 6.3 Emission energy differences between TDDFT and TDDFT+TB for the gold nanoclusters.

	TDDFT-aas	TDDFT+TB	TDDFT
$Au_{25}(SCH_2CH_2CH_3)_{18}^{-1}$	0.75	0.76	0.77
Au_7^{+3}	1.90	1.91	1.93

6.4.5 Comparison between computational cost

In this section, we examine the efficiency of the TDDFT-aas code. First, we compare the computational cost between TDDFT-aas, TDDFT+TB, and TDDFT energy calculations (Table 6.4). For the uracil molecule, TDDFT-aas and TDDFT+TB show the same computational cost, which is sped up by around a factor of 4.3 compared with TDDFT. For the metal nanoclusters, both TDDFT-aas and TDDFT+TB finished energy calculations within 40 minutes using 8 cores; meanwhile, TDDFT needs more than 20 hours to finish using the same number of cores.

Table 6.4 Comparison between the computational time (minutes) for TDDFT-aas, TDDFT+TB and TDDFT energy calculations.

	TDDFT-aas	TDDFT+TB	TDDFT
uracil	0.17	0.17	0.73
Ag_{38}^{+4}	8.08	9.17	877.93
Au_{38}^{+4}	12.70	13.03	1544.75
Ag_{55}^{+5}	15.95	13.61	1311.25
Au_{55}^{+5}	39.03	34.98	638.50
$Au_{25}(SCH_3)_{18}^{-}$	6.05	6.39	362.23

We then examined the efficiency of the gradient calculations. The results for selected organic molecules and nanocluster systems are shown in Table 6.5 and Table 6.6, respectively (8 cores are used for all calculations).

Table 6.5 Comparison between the computational time (minutes) for TDDFT-aas, TDDFT+TB and TDDFT gradient calculations for three organic systems.

uracil	**TDDFT-aas**	**TDDFT+TB**	**TDDFT**
Computational time	1.1	1.1	5.2
Steps required to converge	6	6	6
furan	**TDDFT-aas**	**TDDFT+TB**	**TDDFT**
Computational time	0.52	0.53	2.65
Steps required to converge	5	5	4
ethene	**TDDFT-aas**	**TDDFT+TB**	**TDDFT**
Computational time	0.33	0.26	0.68
Steps required to converge	5	5	5

Table 6.6 Comparison between the computational time (minutes) for TDDFT-aas, TDDFT+TB and TDDFT gradient calculations for the $Au_{25}(SCH_2CH_2CH_3)_{18}^{-1}$ and Au_7^{3+} systems.

$Au_{25}(SCH_2CH_2CH_3)_{18}^{-1}$	**TDDFT-aas**	**TDDFT+TB**	**TDDFT**
Computational time	2098.48	1988.10	2604.37
Steps required to converge	56	53	50
Au_7^{3+}	**TDDFT-aas**	**TDDFT+TB**	**TDDFT**
Computational time	4.85	7.09	21.57
Steps required to converge	11	17	22

For the organic systems, all three methods require similar steps to converge the geometries; TDDFT-aas can speed up the calculation by an average factor of 4.1 compared with TDDFT. The time savings is similar to the TDDFT+TB method. For $Au_{25}(SCH_2CH_2CH_3)_{18}^{-1}$, TDDFT-aas needs slightly more steps to converge the geometry compared with the other two methods. For the gradient calculation, TDDFT-aas and TDDFT+TB still reduce the computational cost, but not as significantly compared with energy calculations. Our evaluation shows most of the computational costs are attributed to the calculation of the $\frac{dS_{\mu\nu}^{1/2}}{dR_A}$ term when solving the Z-vector equation. Improving the efficiency of the code is one of the directions for our future work.

6.5 Discussion

In summary, TDDFT-aas resembles the TDDFT-as method and the TDDFT+TB method: when solving the *K* coupling integrals in the excited state, an approximation is made instead of calculating the exact two-electron integrals. TDDFT-aas utilizes the γ_{AB} function from the TDDFT-as method via $K_{ia,jb} = \sum_{AB} q_{ia,A}\gamma_{AB}q_{jb,B}$ to calculate the coupling matrix. Because the γ_{AB} function is independent of tight binding parameters, TDDFT-aas will be easier to implement in codes that do not have tight binding parameters compared with TDDFT+TB. The performance of the TDDFT-aas method shows good agreement with TDDFT+TB and TDDFT, specifically for the metal nanocluster systems. For diatomic molecules and organic molecules, TDDFT-aas does not agree very well with TDDFT if state crossings are important; these types of systems should employ the standard TDDFT method or more advanced multireference methods. Overall, TDDFT-aas shares similar characteristics and considerations with TDDFT+TB: (1) As shown in equation 5, $\mathbf{A}-\mathbf{B}$ is a diagonal matrix, so the methods are currently available for pure functionals; sTDDFT[10] is an alternative option if hybrid functional calculation is expected. At the same time, since the approximation for the $\mathbf{A}-\mathbf{B}$ matrix violates the sum rule, both TDDFT+TB and TDDFT-aas have issues when predicting the oscillator strength for the excitation. (2) When approximating the coupling matrix, the monopole approximation is made, which leads to the issue that the atomic transition charges do not receive contributions from different atomic basis functions even if they are located on the same atom; for example, local excitations such as the σ_u to π_g

transition in N_2 system are not treated correctly.[13] It has been reported that doing an on-site correction to the TD-DFTB method[29] and sTDDFT method[30] can improve the excitation energy results compared with TDDFT. Therefore, implementing an on-site correction to the current TDDFT+TB and TDDFT-aas methods may improve the local excitations such as the σ_u to π_g transition in the N_2 system as well.

6.6 Conclusion

In this work, we implemented both the energy and gradient of the TDDFT-aas method. The TDDFT-aas method starts with a standard ground state DFT calculation to determine the density as well as the Kohn-Sham orbitals and orbital energies, and then approximates the two-electron integral terms when solving the Casida equations. When approximating the two- electron integrals, calculation of the *K* coupling matrix uses a formula that involves γ_{AB} and atomic transition charges. Compared with TDDFT+TB, γ_{AB} in TDDFT-aas is not dependent on tight-binding parameters such as chemical hardness. We found that the exponent (α) can be set to be 0.2 for most of the systems in the benchmark test set, which ranges from diatomic molecules, organic molecules, and gold nanoclusters. The absorption spectra and emission energy results indicate that TDDFT-aas will give similar results to TDDFT+TB, and they share similar computational costs. Overall, TDDFT-aas opens a new way to approximate the TDDFT method without using tight-binding parameters to calculate chemical systems, and the method shows good agreement with TDDFT results, specifically for gold and silver nanoclusters.

6.7 Acknowledgment

Y. W. and C.M.A. were supported by the National Science Foundation (Grant No. CHE-1955823) of the United States. The computing for this work was performed on the Beocat Research Cluster at Kansas State University, which is partially funded by the NSF (Grant Nos. CHE-1726332, CNS-1006860, EPS-1006860, and EPS-0919443). The authors thank Prof. Shane Parker for conversations that inspired this research.

6.8 References

(1) Adamo, C.; Jacquemin, D. The Calculations of Excited-State Properties with Time-Dependent Density Functional Theory. *Chem. Soc. Rev.* **2013**, *42* (3), 845–856.

(2) Dreuw, A.; Head-Gordon, M. Single-Reference Ab Initio Methods for the Calculation of Excited States of Large Molecules. *Chem. Rev.* **2005**, *105* (11), 4009–4037.

(3) Laurent, A. D.; Jacquemin, D. TD-DFT Benchmarks: A Review. *Int. J. Quantum Chem* **2013**, *113* (17), 2019–2039.

(4) Byun, Y.-M.; Sun, J.; Ullrich, C. A. Time-Dependent Density-Functional Theory for Periodic Solids: Assessment of Excitonic Exchange–Correlation Kernels. *Electron. Struct.* **2020**, *2* (2), 023002.

(5) Runge, E.; Gross, E. K. U. Density-Functional Theory for Time-Dependent Systems. *Phys. Rev. Lett.* **1984**, *52* (12), 997–1000.

(6) Casida, M. E. Time-Dependent Density Functional Response Theory for Molecules. In *Recent Advances in Computational Chemistry*; WORLD SCIENTIFIC, 1995; Vol. 1, pp 155–192.

(7) Casida, M. E.; Huix-Rotllant, M. Progress in Time-Dependent Density-Functional Theory. *Annu. Rev. Phys. Chem.* **2012**, *63* (1), 287–323.

(8) Niehaus, T. A.; Suhai, S.; Della Sala, F.; Lugli, P.; Elstner, M.; Seifert, G.; Frauenheim, Th. Tight-Binding Approach to Time-Dependent Density-Functional Response Theory. *Phys. Rev. B* **2001**, *63* (8), 085108.

(9) Trani, F.; Scalmani, G.; Zheng, G.; Carnimeo, I.; Frisch, M. J.; Barone, V. Time-Dependent Density Functional Tight Binding: New Formulation and Benchmark of Excited States. *J. Chem. Theory Comput.* **2011**, *7* (10), 3304–3313.

(10) Bannwarth, C.; Grimme, S. A Simplified Time-Dependent Density Functional Theory Approach for Electronic Ultraviolet and Circular Dichroism Spectra of Very Large Molecules. *Computational and Theoretical Chemistry* **2014**, *1040–1041*, 45–53.

(11) Grimme, S. A Simplified Tamm-Dancoff Density Functional Approach for the Electronic Excitation Spectra of Very Large Molecules. *J. Chem. Phys* **2013**, *138* (24), 244104.

(12) Risthaus, T.; Hansen, A.; Grimme, S. Excited States Using the Simplified Tamm–Dancoff-Approach for Range-Separated Hybrid Density Functionals: Development and Application. *Phys. Chem. Chem. Phys.* **2014**, *16* (28), 14408–14419.

(13) Rüger, R.; Van Lenthe, E.; Heine, T.; Visscher, L. Tight-Binding Approximations to Time-Dependent Density Functional Theory — A Fast Approach for the Calculation of Electronically Excited States. *J. Chem. Phys* **2016**, *144* (18), 184103.

(14) Giannone, G.; Della Sala, F. Minimal Auxiliary Basis Set for Time-Dependent Density Functional Theory and Comparison with Tight-Binding Approximations: Application to Silver Nanoparticles. *J. Chem. Phys* **2020**, *153* (8), 084110.

(15) Zhou, Z.; Della Sala, F.; Parker, S. M. Minimal Auxiliary Basis Set Approach for the Electronic Excitation Spectra of Organic Molecules. *J. Phys. Chem. Lett.* **2023**, *14* (7), 1968–1976.

(16) Porezag, D.; Frauenheim, Th.; Köhler, Th.; Seifert, G.; Kaschner, R. Construction of Tight-Binding-like Potentials on the Basis of Density-Functional Theory: Application to Carbon. *Phys. Rev. B* **1995**, *51* (19), 12947–12957.

(17) Seifert, G.; Porezag, D.; Frauenheim, Th. Calculations of Molecules, Clusters, and Solids with a Simplified LCAO-DFT-LDA Scheme. *Int. J. Quantum Chem.* **1996**, *58* (2), 185–192.

(18) Asadi-Aghbolaghi, N.; Rüger, R.; Jamshidi, Z.; Visscher, L. TD-DFT+TB: An Efficient and Fast Approach for Quantum Plasmonic Excitations. *J. Phys. Chem. C* **2020**, *124* (14), 7946–7955.

(19) Havenridge, S.; Aikens, C. M. Deciphering the Dual Emission in the Photoluminescence of $Au_{14}Cd(SR)_{12}$: A Theoretical Study Using TDDFT and TDDFT + TB. *J. Chem. Phys* **2021**, *155* (7), 074302.

(20) Baghdasaryan, A.; Besnard, C.; Lawson Daku, L. M.; Delgado, T.; Burgi, T. Thiolato Protected Copper Sulfide Cluster with the Tentative Composition $Cu_{74}S_{15}(2\text{-PET})_{45}$. *Inorg. Chem.* **2020**, *59* (4), 2200–2208.

(21) Sun, J.; Tang, X.; Liu, Z.-H.; Xie, Z.; Yan, B.; Yin, R.; Chaolumen, C.; Zhang, J.; Fang, W.; Wei, J.; Shen, H. Labile Ligands Protected Cu $_{50}$ Nanoclusters with Tailorable Optical Limiting Effect. *ACS Materials Lett.* **2024**, *6* (1), 281–289.

(22) Havenridge, S.; Rüger, R.; Aikens, C. M. Analytical Excited State Gradients for Time-Dependent Density Functional Theory plus Tight Binding (TDDFT + TB). *J. Chem. Phys* **2023**, *158* (22), 224103.

(23) te Velde, G.; Bickelhaupt, F. M.; Baerends, E. J.; Fonseca Guerra, C.; van Gisbergen, S. J. A.; Snijders, J. G.; Ziegler, T. Chemistry with ADF. *J. Comput. Chem.* **2001**, *22* (9), 931–967.

(24) Perdew, J. P.; Burke, K.; Ernzerhof, M. Generalized Gradient Approximation Made Simple. *Phys. Rev. Lett.* **1996**, *77* (18), 3865–3868.

(25) Perdew, J. P. Density-Functional Approximation for the Correlation Energy of the Inhomogeneous Electron Gas. *Phys. Rev. B* **1986**, *33* (12), 8822–8824.

(26) Becke, A. D. Density-Functional Exchange-Energy Approximation with Correct Asymptotic Behavior. *Phys. Rev. A* **1988**, *38* (6), 3098–3100.

(27) Kolos, W.; Roothaan, C. C. J. Accurate Electronic Wave Functions for the H_2 Molecule. *Rev. Mod. Phys.* **1960**, *32* (2), 219–232.

(28) Schreiber, M.; Silva-Junior, M. R.; Sauer, S. P. A.; Thiel, W. Benchmarks for Electronically Excited States: CASPT2, CC2, CCSD, and CC3. *J. Chem. Phys* **2008**, *128* (13), 134110.

(29) Domínguez, A.; Aradi, B.; Frauenheim, T.; Lutsker, V.; Niehaus, T. A. Extensions of the Time-Dependent Density Functional Based Tight-Binding Approach. *J. Chem. Theory Comput.* **2013**, *9* (11), 4901–4914.

(30) De Wergifosse, M.; Grimme, S. *The eXact Integral Simplified Time-Dependent Density Functional Theory (XsTD-DFT)*; preprint; Chemistry, 2024.

Chapter 7 - Effects of diglyme on Au nanocluster formation: mechanism, ^{1}H NMR, and bonding

Reprinted with permission from *J. Phys. Chem. A* 2022, 126, 42, 7598–7605. Copyright 2022 American Chemical Society

Yuchen Wang,[1] Alice Li,[1,2] Jacqueline Pinkerton,[1,3] Christine M. Aikens[1,*]

1. Department of Chemistry, Kansas State University, Manhattan, KS 66506, USA
2. Department of Chemistry and Biochemistry, Bates College, Lewiston, ME 04240, USA
3. Natural Sciences Programs, Pensacola Christian College, Pensacola, FL 32503, USA

7.1 Abstract

Recently, diglyme was applied as a solvent in the synthesis of a luminescent gold-thiolate nanocluster. However, the interactions between the diglyme and the gold nanocluster and the intrinsic mechanism of the diglyme-assisted nanocluster growth have not been examined. In this work, we use density functional theory (DFT) to propose a plausible pathway for diglyme-assisted Au(I)-thiolate synthesis; the reaction energies are found to be negative in every step. ^{1}H NMR calculations are applied to characterize how the environment arising from different gold motifs affects the chemical shifts of the protons on diglyme, which experience strong downfield shifts. Extended transition state - natural orbitals for chemical valence (ETS-NOCV) theory is also utilized to examine the interactions between diglyme and gold clusters as well as a $Au_{20}(SR)_{15}$ nanocluster. Our work demonstrates that diglyme can play an important role in the synthetic mechanism yielding gold nanoclusters and provides insights into the diglyme-nanocluster binding motifs and resulting NMR chemical shifts.

7.2 Introduction

Ligand-protected gold thiolate nanoclusters have shown several unique physical and chemical properties which can be applied to diverse areas such as photocatalysis,[1] biomedicine,[2] and chemical or biomedical sensors.[3] Most gold-thiolate nanoclusters are found to be "atomically

precise nanoclusters",[4] such as $Au_{20}(SR)_{16}$,[5,6] $Au_{25}(SR)_{18}^-$,[7–9] $Au_{38}(SR)_{24}$,[10,11] and $Au_{104}(SR)_{46}$.[12] The general structure of a gold-thiolate nanocluster consists of a gold kernel and gold-thiolate protecting motifs (of which the basic unit is SR-Au-SR).[13] The R group on the thiolate (SR) ligand can be SPh, SCH_2CH_2Ph (aka PET, phenylethanethiolate), *p*-MBA (*para*-mercaptobenzoic acid), etc.

The Brust–Schiffrin (B-S) method was one of the earliest methods to synthesize gold-thiolate nanoclusters. The B-S method starts with a Au(III) complex (such as $HAuCl_4$) and follows with a two solvent phase reduction to synthesize gold-thiolate nanoclusters.[14] Several modifications to the Brust–Schiffrin methods (i.e. changing the solvent, changing from two-phase to one-phase reactions) were then studied to refine the reaction process.[15,16] Recently, a mixture of diglyme (dg) and tetrahydrofuran (THF) solvents was applied to the gold-thiolate nanocluster self-assembly process, and diglyme can be observed as a ligand in the final generated product.[17–20] Diglyme was found to yield a gold-thiolate nanocluster dimer as well, which indicates that diglyme can mediate the gold nanoparticle assembly process.[18] Moreover, a $Au_{20}(SR)_{15}$-diglyme system was also found experimentally in which diglyme mediates dimerization of two nanoclusters to yield a photoluminescent cluster with a very high quantum yield.[21] Therefore, it is very important to investigate the interaction between diglyme and gold clusters which will help unravel the photoluminescent mechanism in these systems in the future.

With the growth of experimental research on ligand-protected gold nanoparticle synthesis,[14–16,22–25] the mechanisms involved in this process have also been investigated using quantum chemistry calculations.[26–30] A plausible reaction pathway from Au(III) chloride to Au(I) thiolate via the addition of thiols was first proposed by Barngrover and Aikens using the density functional theory (DFT) method in 2011, and the involved reaction pathways were demonstrated to be thermodynamically favorable.[26] Later, solvent effects and R group effects on the Au(III) to Au(I) reaction were examined theoretically.[27] The DFT method was also applied to study the Au nanoparticle growth pathway starting from gold halide complexes.[28] However, the previous discussions of the reaction mechanism were mainly focused on the original Brust–Schiffrin method. For the modified Brust–Schiffrin method that has diglyme as a solvent, the question arises: how does diglyme play a role in the gold nanocluster synthesis process?

In this work, we computationally model reasonable reaction pathways to generate Au(I)-containing species from the starting Au(III) complex. ^{1}H NMR spectra are calculated to examine the proton environment of the gold-diglyme system. The interactions between diglyme and gold-containing species are discussed using chemical bonding theory. In this way, a plausible mechanism for the diglyme-assisted Brust–Schiffrin synthesis can be proposed.

7.3 Computational Details

All calculations were performed with the Amsterdam Modeling Suite (AMS) 2021.102 software.[31] Geometry optimizations were performed at the BP86/TZP level of theory with a frozen core approximation (1s for C, 1s for O, 2p for S, 2p for Cl, 4f for Au), where BP86[32,33] is a generalized gradient approximation (GGA) exchange-correlation functional and TZP stands for the triple-zeta polarized basis set. Scalar relativistic effects were included by using the Zero Order Regular Approximation (ZORA).[34,35] Grimme3 parameters were added to correct for the dispersion interaction.[36,37] Solvent effects were taken into consideration using the Conductor-like Screening Model (COSMO).[38–40] All reaction pathways were modeled in diethyl ether solvent, which is similar in dielectric constant and functionality to the diglyme and tetrahydrofuran (THF) solvents used experimentally.

Because ^{1}H NMR spectra are sensitive to the atomic environment, NMR is a powerful experimental tool to characterize geometric structure. In our current work, ^{1}H NMR spectra for three featured molecular systems were calculated with respect to TMS (tetramethylsilane), because it is the standard reference for NMR spectra, both experimentally and theoretically. To examine the chemical shifts, single-point energy calculations were performed without the frozen core approximation in the basis set. Then, ^{1}H NMR calculations were performed on all protons in the diglyme molecule. Finally, ETS-NOCV theory[41–44] (see details in SI) was applied to analyze the bonding between the gold moiety and the diglyme molecule and to compare the differences between the gold-thiolate system and the gold-chloride system.

7.4 Results and discussion

A. Proposed reaction pathways

Previous theoretical work has suggested two different pathways that lead to the reduction of Au(III) to Au(I).[26] Our proposed reaction mechanisms are initially based on this previous work; however, our current proposed reaction pathway includes the diglyme molecule throughout the entire reaction pathway. The reaction mechanism consists of two main parts: 1. Au(III)-Au(III) linking in the presence of diglyme; 2. thiol addition reaction (including reduction of gold atoms).

1. Au(III)-Au(III) linking reactions:

For the proposed reaction mechanism, the first step is the binding between the gold-chloride complex and diglyme (dg). The reaction starts with a Au(III) complex (here we use $HAuCl_4$), which binds to the diglyme molecule, and the proton and one chloride from $HAuCl_4$ generate a HCl molecule and a $AuCl_3$ species that possesses a dative bond with diglyme (Reaction 1A, Figure 7.1A). Then, a second $HAuCl_4$ is added, which binds with the $(AuCl_3)$dg product to generate $(AuCl_3)_2$dg (Figure 7.1B) and release another HCl as well (Reaction 2A). The optimized structure of $(AuCl_3)_2$dg (Figure 7.1B) shows that two $AuCl_3$ moieties are bound to the diglyme, with two of the chlorides bridging the two gold atoms. The Au_2Cl_6 moiety is known to be the preferred structure for the $AuCl_3$ dimer.[45] The generated $(AuCl_3)_2$dg species can subsequently react with $HAuCl_4$ and generate a HCl and a $(AuCl_3)_3$dg species (Figure 7.1C, Reaction 3A). The reaction energies for 1A, 2A, and 3A are -0.90 eV, -0.46 eV, and -0.80 eV, respectively. These reaction energies indicate that the Au-Au linking reactions are thermodynamically favorable. Previous work has shown that transition states for similar reactions have barriers near 0.3 eV,[26] so we expect these reactions to have reasonable kinetics at room temperature, which is a common temperature for nanoparticle synthesis.[22,24] Due to the increased size of the present systems and the additional degrees of freedom with the addition of diglyme, transition state searches are not practical; however, the Au(III) and Au(I) species considered in this work are very close to those in Ref. 26. Due to the flexibility of the diglyme and PET ligands, it should be noted that the systems present experimentally may vary dynamically from the lowest energy isomers found in this work, but these calculations demonstrate that the reactions are thermodynamically feasible.

Reaction Scheme 1. Au(III)-Au(III) linking reactions

$HAuCl_4 + dg \rightarrow (AuCl_3)dg + HCl$ (1A)

$(AuCl_3)dg + HAuCl_4 \rightarrow (AuCl_3)_2dg + HCl$ (2A)

$(AuCl_3)_2dg + HAuCl_4 \rightarrow (AuCl_3)_3dg + HCl$ (3A)

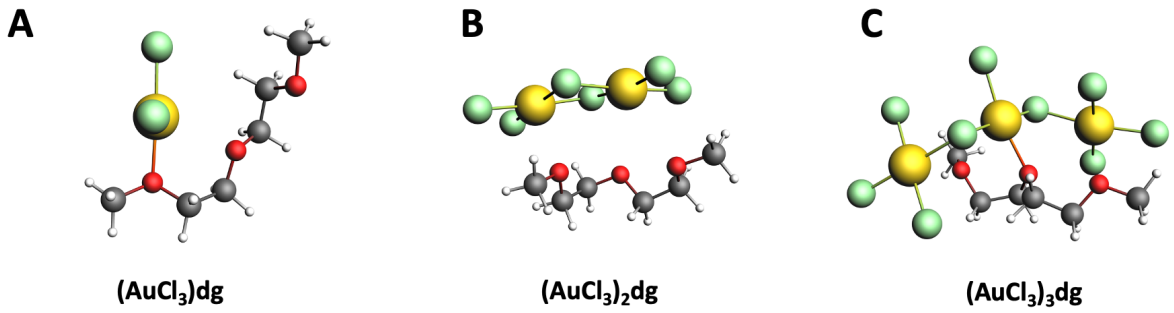


Figure 7.1 Three products in the Au-Au linking reactions. A. $(AuCl_3)dg$ B. $(AuCl_3)_2dg$ C. $(AuCl_3)_3dg$ Key: gold = gold, chlorine = green, carbon = grey, oxygen = red and hydrogen = white.

2. Thiol addition reactions:

For the thiol addition reactions, the $(AuCl_3)_2dg$ or $(AuCl_3)_3dg$ product can subsequently react with thiols to form a mixed Au(III)-Au(I) species. In this work, we focus on the species with two gold atoms as the simplest multi-atom species. 2-Phenylethanethiol (HPET, $HSCH_2CH_2Ph$) is used as the reactive thiol because it is the ligand used experimentally[18,19,21] in the formation of the known diglyme-containing nanoclusters. The added HPET reacts between the two Au atoms to bridge the two Au(III) species, and the proton on HPET reacts with one chloride to generate a $(AuCl_2)PET(AuCl_3)dg$ (Figure 7.2A) species and HCl (Reaction 1B), where PET is 2-phenylethanethiolate. The reaction energy for the first thiol addition is -0.97 eV, which is thermodynamically favorable. Then, the $(AuCl_2)PET(AuCl_3)dg$ species reacts with another thiol; the proton on the thiol reacts with a chloride to generate another HCl and product $(AuCl_2PET)_2dg$ (Figure 7.2B) with a reaction energy of -0.60 eV (Reaction 2B). Comparing between $(AuCl_3)_2dg$ and $(AuCl_2PET)_2dg$, we found that the gold chloride moieties tend to form a dimer and weakly bind to the diglyme molecule, whereas the mixed gold chloride-thiolate moieties tend to bind to the diglyme through coordinate covalent/dative bonding. The generated product $(AuCl_2PET)_2dg$ can continue to react with HPET to yield a disulfide $(PET)_2$ and the product $(AuCl_2)PET(AuCl)dg$

(Figure 7.2C) with a reaction energy of -0.79 eV (Reaction 3B). The resulting product, $(AuCl_2)PET(AuCl)dg$, is a mixed Au(III)-Au(I) species, in which one gold is in the +3 charge state and the other gold is in the +1 charge state. Formation of a disulfide is common in thiol-based reactions that reduce the oxidation state of gold.[15,26]

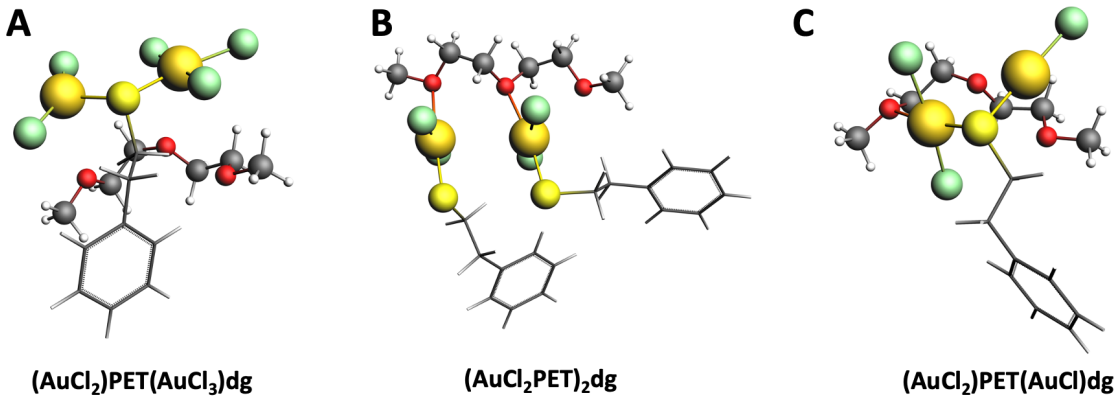


Figure 7.2 Three generated products for thiol addition reactions. The $-(CH_2)_2-Ph$ (phenylethane) group is shown using a stick model. A. $(AuCl_2)PET(AuCl_3)dg$ B. $(AuCl_2PET)_2dg$ C. $(AuCl_2)PET(AuCl)dg$ Key: gold = gold, sulfur = light yellow, chlorine = green, carbon = grey, oxygen = red and hydrogen = white.

Reaction Scheme 2. Thiol addition reactions in the presence of diglyme

$$(AuCl_3)_2dg + HPET \rightarrow (AuCl_2)PET(AuCl_3)dg + HCl \quad (1B)$$

$$(AuCl_2)PET(AuCl_3)dg + HPET \rightarrow (AuCl_2PET)_2dg + HCl \quad (2B)$$

$$(AuCl_2PET)_2dg + HPET \rightarrow (AuCl_2)PET(AuCl)dg + PET_2 + HCl \quad (3B)$$

To compare the differences between the reaction energy with diglyme participants and without diglyme participants, the thiol addition reactions were modeled without the presence of diglyme molecule as well (Reactions 1B', 2B', and 3B'). The products for these reactions are shown in Figure 7.3. Compared between the $(AuCl_2PET)_2dg$ (Figure 7.2B) and $(AuCl_2PET)_2$ (Figure 7.3B), we found the two $AuCl_2PET$ moieties will generate a dimer without the presence of the diglyme. The reaction energy results show that the reaction steps will be somewhat less energetically favorable when no diglyme is present in the molecular system (Table 7.1). These

results indicate that diglyme can increase the exothermicity of the reaction for the thiol addition process.

Reaction Scheme 3. Thiol addition reactions without the presence of diglyme

$(AuCl_3)_2$ + HPET → $(AuCl_2)PET(AuCl_3)$ + HCl (1B')

$(AuCl_2)PET(AuCl_3)$ + HPET → $(AuCl_2PET)_2$ + HCl (2B')

$(AuCl_2PET)_2$ + HPET → $(AuCl_2)PET(AuCl)$ + PET_2 + HCl (3B')

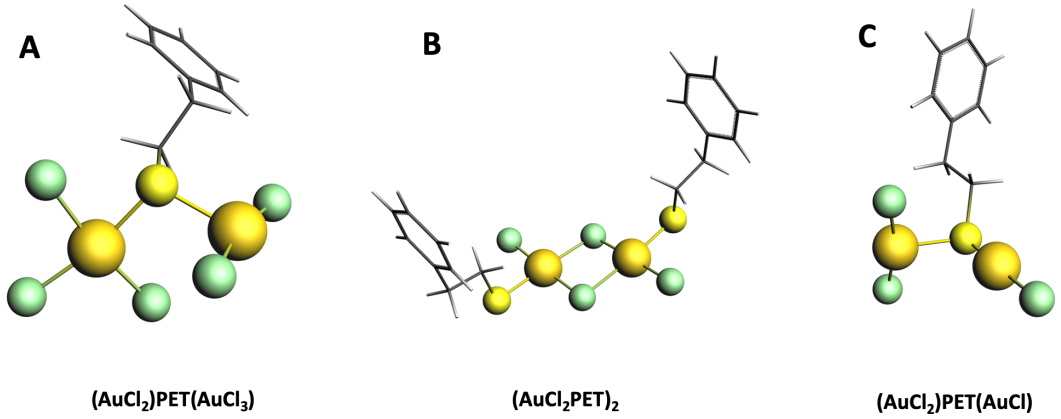


Figure 7.3 Three generated products for thiol addition reactions without diglyme; the -$(CH_2)_2$-Ph group is shown using a stick model. A. $(AuCl_2)PET(AuCl_3)$ B. $(AuCl_2PET)_2$ C. $(AuCl_2)PET(AuCl)$ Key: gold = gold, sulfur = light yellow and chlorine = green.

Table 7.1 Reaction energies for thiol addition steps (1B, 2B, 3B: diglyme present; 1B', 2B', 3B': no diglyme present).

Reaction index	Reaction energy (eV)	Reaction index	Reaction energy (eV)
1B	-0.97	**1B'**	-0.82
2B	-0.60	**2B'**	-0.26
3B	-0.79	**3B'**	-0.47

Next, the mixed Au(III)-Au(I) motif can continue to react with HPET to generate a motif that only contains Au(I) species. Two plausible pathways are considered as follows.

Reaction Scheme 4. Pathway 1

$(AuCl_2)PET(AuCl)dg + HPET \rightarrow (AuClPET)_2dg + HCl$ (1C)

$(AuClPET)_2dg + HPET \rightarrow (AuClPET)Au(PET)_2dg + HCl$ (2C)

$(AuClPET)Au(PET)_2dg + HPET \rightarrow (AuCl)PET(AuHPET)dg + PET_2$ (3C)

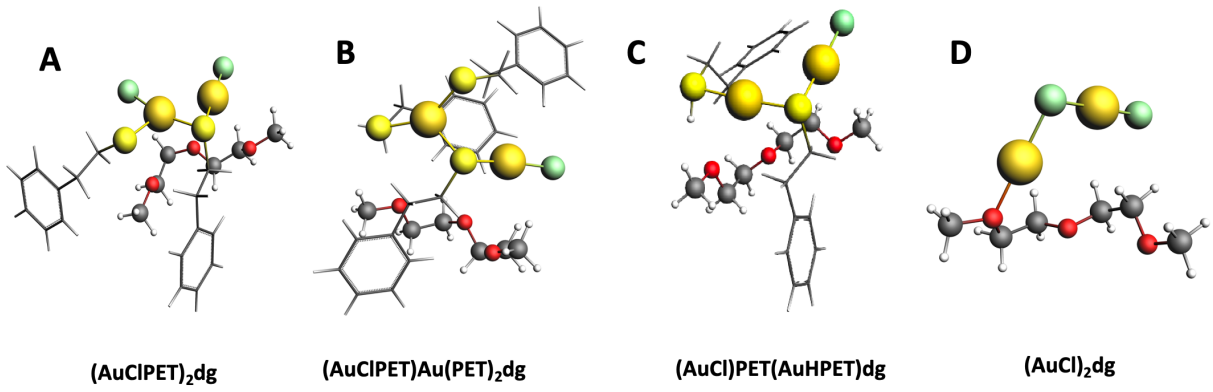


Figure 7.4 Four possible products formed in pathway 1 and pathway 2. The -$(CH_2)_2$-Ph group is shown using a stick model. A. $(AuClPET)_2dg$ B. $(AuClPET)Au(PET)_2dg$ C. $(AuCl)PET(AuHPET)dg$ D. $(AuCl)_2dg$ Key: gold = gold, sulfur = light yellow, chlorine = green, carbon = grey, oxygen = red and hydrogen = white.

Pathway 1 One potential pathway is that the mixed Au(III)-Au(I) species $(AuCl_2)PET(AuCl)dg$ (Figure 7.2C) reacts with HPET. A chloride on Au(III) and the proton from the HPET generate a HCl, and then the PET binds to the gold to form $(AuClPET)_2dg$ (Figure 7.4A). This reaction energy is -0.01 eV (Reaction 1C). Then, $(AuClPET)_2dg$ can subsequently react with an additional HPET, and that HPET substitutes for a second chloride on the Au(III) atom to yield $(AuClPET)Au(PET)_2dg$ (Figure 7.4B) with a reaction energy of -0.62 eV (Reaction 2C). $(AuClPET)Au(PET)_2dg$ then reacts with a third HPET and generates a PET_2 molecule and $(AuCl)PET(AuHPET)dg$ (Figure 7.4C, Reaction 3C). The reaction energy for this last step is -0.76 eV. The final product is a species that includes both Au(I)-thiolate and Au(I)-chloride motifs. Of note, the SR-Au-SR-Au-Cl moiety forms a V-shaped motif similar to the V-shaped staple motifs commonly found on the surface of gold nanoclusters.[4,46]

Reaction Scheme 5. Pathway 2

$$(AuCl_2)PET(AuCl)dg + HPET \rightarrow (AuCl)_2dg + PET_2 + HCl \quad (1D)$$

Pathway 2. Another pathway is that the Au(III)-Au(I)-mixed motif subsequently reacts with HPET to generate a disulfide (PET_2), HCl, and $(AuCl)_2dg$ (Figure 7.4D, Reaction 1D). Through this pathway, the mixed Au(III)-Au(I) motif can be transformed into a species with two Au(I)-chloride motifs. However, the calculated reaction energy is 1.13 eV, which indicates that the endothermicity for the reaction is relatively high. Disulfides (and the corresponding gold reduction) are unlikely to be formed in this manner.

The reaction energies for the mechanisms discussed in this work are summarized in Table 7.2. (Reaction free energies with zero-point energy and entropic corrections are shown in the SI.) Comparing these two distinct pathways, pathway 1 generates both Au(I)-thiolate and Au(I)-chloride motifs, while pathway 2 generates a gold-chloride motif. Pathway 1 exhibits negative reaction energies for each step and exhibits an overall exothermic process, which indicates that it is a more thermodynamically favorable reaction pathway than pathway 2. Compared with previous calculations for systems without diglyme,[26] the synthetic pathway in the presence of the diglyme molecule shows more negative reaction energies for each step, which consequently indicates that the Au(III)-chloride motif can be reduced to a Au(I) motif with the assistance of diglyme in an energetically favorable pathway. We note that in the experiment, diglyme is present in great excess as a solvent; Le Chatelier's principle will likely aid in the formation of the diglyme-bound $AuCl_3$ species. In this work, we only considered the binding of a single diglyme to the gold systems, in part because only 1 or at most 2 diglyme species have ligated experimental nanoclusters,[17–21] although future work could consider the binding of additional diglyme molecules.

Table 7.2 Calculated reaction energies (eV) for each step in the investigated reaction pathways.

Reaction Index	Reaction energy (eV)
1A	-0.90
2A	-0.46
3A	-0.80
1B	-0.97
2B	-0.60
3B	-0.79
1C	-0.01
2C	-0.62
3C	-0.76
1D	1.13

B. Chemical shift analysis

^{1}H NMR calculations of the protons on the diglyme ligand were performed on three different species to examine how the protons of this ligand are affected by environment. Similar calculations on the protons of the HPET moieties are discussed in the SI (Tables S1-S2, Figures S1-S2). The ^{1}H NMR spectra of the pure diglyme molecule was investigated previously and the theoretical chemical shifts lie in the range from 3.26 ppm to 3.98 ppm.[19] In $(AuCl_3)$dg (Figure 7.5A), $AuCl_3$ is a gold-chloride moiety with a +3 charge state for gold. The calculated ^{1}H NMR spectrum has chemical shifts that range from 3.35 ppm to 4.95 ppm (Table 7.3). Atom 13 has the highest chemical shift (δ = 4.95 ppm), and that proton is oriented close to a chloride on $AuCl_3$. Atom 10 shows a similar orientation to atom 13; its chemical shift is 4.60 ppm, which is the second-highest chemical shift. Atoms 21, 22, and 23 have the lowest chemical shifts; these three protons are located at the other terminal site of the diglyme molecule.

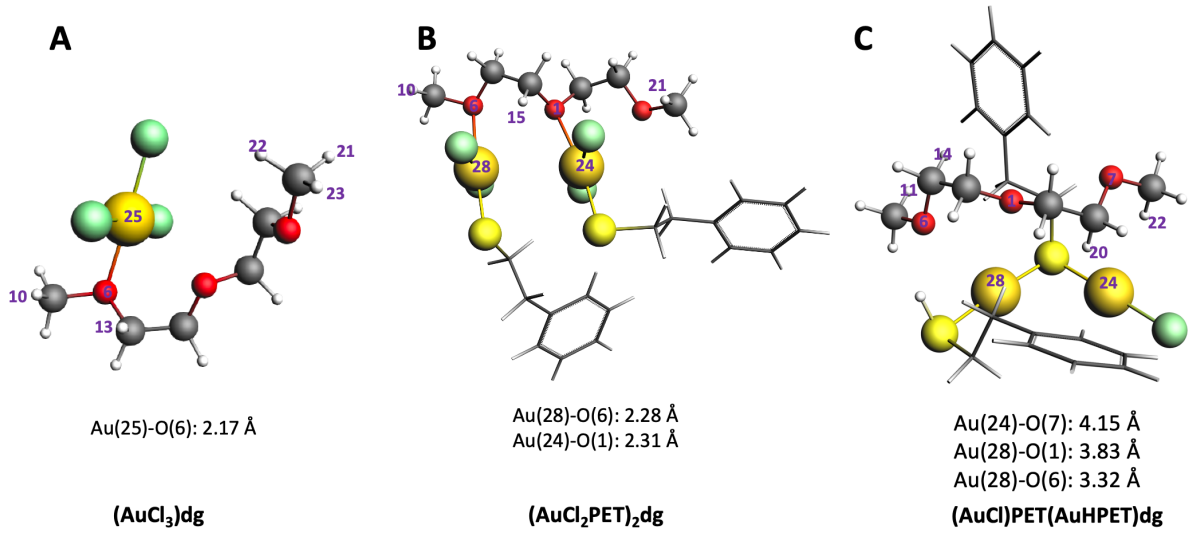


Figure 7.5 Optimized structures for A. $AuCl_3$dg, B. $(AuCl_2PET)_2$dg, and C. (AuCl)PET(AuHPET)dg. Selected geometric information and atom labels are also included. Full coordinates are given in the SI. Key: gold = gold, sulfur = light yellow, chlorine = green, carbon = grey, oxygen = red and hydrogen = white.

Table 7.3 Calculated NMR chemical shifts (ppm) for hydrogen atoms in diglyme ligand for $AuCl_3$dg, $(AuCl_2PET)_2$dg, and (AuCl)PET(AuHPET)dg.

$(AuCl_3)$dg		$(AuCl_2PET)_2$dg		(AuCl)PET(AuHPET)dg	
Atom Label	**δ (ppm)**	**Atom Label**	**δ (ppm)**	**Atom Label**	**δ (ppm)**
10	4.60	10	3.45	10	3.54
11	4.03	11	3.66	11	3.13
12	3.69	12	4.27	12	3.25
13	4.95	13	3.87	13	3.26
14	3.92	14	4.25	14	2.97
15	4.01	15	6.32	15	3.94
16	3.96	16	4.04	16	3.24
17	3.96	17	3.88	17	3.18
18	3.88	18	4.8	18	3.48
19	3.72	19	3.79	19	3.15
20	4.31	20	3.94	20	5.35
21	3.35	21	3.44	21	3.48
22	3.41	22	4.11	22	4.97
23	3.63	23	3.84	23	3.74

For $(AuCl_2PET)_2$dg (Figure 7.5B), two $AuCl_2PET$ motifs bind to two oxygen atoms of the diglyme molecule, and the two gold atoms are both in the +3 charge state. The ^{1}H NMR spectra have chemical shifts that range from 3.44 ppm to 6.32 ppm (Table 7.3). Atom 15 is located near two chlorides, and it has the highest chemical shift of 6.32 ppm. Atom 10 (δ = 3.45 ppm) and atom 21 (δ = 3.44 ppm) have the two lowest chemical shifts; these atoms are oriented away from the $AuCl_2PET$ moiety.

For the (AuCl)PET(AuHPET)dg system (Figure 7.5C), the two gold atoms are in the +1 charge state. The ^{1}H NMR spectra have chemical shifts ranging from 2.97 ppm to 5.35 ppm (Table 7.3). Atom 20, which is oriented towards the gold atom, has the highest chemical shift. Atom 22 has a very similar orientation to atom 20 and its calculated chemical shift is 4.97 ppm, which is the second-highest chemical shift. Atom 11 (δ = 3.13 ppm) and atom 14 (δ = 2.97 ppm) move upfield; both atoms are pointed towards the PET group.

Overall, by analyzing chemical shifts, the proton environment is observed to be strongly affected by the environment around diglyme. Protons that are oriented near gold and chloride will

shift downfield, whereas protons that are pointed towards the PET group will move upfield. It was found experimentally in the diglyme-protected $Au_{20}(PET)_{15}dg_2$ system that some of the protons on diglyme move downfield significantly, and theoretical results suggest that these protons are located near the gold atoms in the nanocluster.[19]

C. Chemical bonding analysis

Because the interaction between diglyme and the Au-containing moieties is of significant interest in this work, the metal-oxygen bond in the molecular system is investigated using the ETS-NOCV chemical bonding theory. Geometric information and binding energies of the three systems featured in Figure 7.5 are examined to provide insights into the diglyme-gold interaction for various oxidation states of gold.

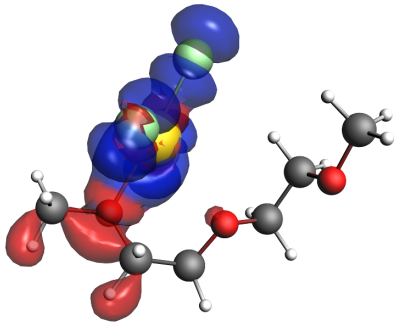
For the $(AuCl_3)dg$ system, the Au-O bond distance is 2.17 Å (Figure 7.5A). For the $(AuCl_2PET)_2dg$ system, two similar Au(III) moieties bind with diglyme, and the Au-O bond distances are calculated to be a little longer at 2.28 Å and 2.31 Å (Figure 7.5B). Compared with the mixed Au-thiolate and Au-chloride system $(AuCl_2PET)_2dg$, the pure Au-chloride $(AuCl_3)dg$ system binds more tightly with the diglyme. The (AuCl)PET(AuHPET)dg system consists of a (AuCl)PET(AuHPET) motif and a diglyme ligand. In this system, the gold motif (which contains Au(I) species only) shows a weak interaction with the diglyme molecule, and all Au-O distances are above 3 Å (Figure 7.5C).

For $AuCl_3dg$, the binding energy between $AuCl_3$ and diglyme is -179.5 kJ/mol (Table 7.4). The strongest contribution to the charge transfer is from the oxygen atom on diglyme to chlorides on $AuCl_3$ (Figure 7.6) based on ETS-NOCV theory, and the corresponding orbital interaction energy is -126.4 kJ/mol. The interaction between diglyme and $AuCl_3$ leads to a total of 0.30 electrons (e) transferred from diglyme to the gold moiety (Table 7.4).

Table 7.4 Binding energy (kJ/mol) calculated using Eq. (1) between diglyme molecule and the gold moiety for three featured molecular systems. Charge analysis for three gold-diglyme systems using ETS-NOCV theory. The system is split into two fragments: diglyme and gold motif.

Molecular System	Binding Energy (kJ/mol)	Charge on Fragment 1 (dg)	Charge on Fragment 2 (gold motif)
$(AuCl_3)dg$	-179.5	0.30	-0.30
$(AuCl_2PET)_2dg$	-209.1	0.39	-0.39
(AuCl)PET(AuHPET)dg	-106.5	0.06	-0.06
$Au_{20}(SCH_3)_{15}dg^+$	-176.3	0.24	0.76

$$E_{binding} = E_{(system)} - (E_{(Au\ motif)} + E_{(diglyme)}) \quad (1)$$



Orbital interaction: -126.4 kJ/mol

$(AuCl_3)dg$

Figure 7.6 Dominant ETS-NOCV deformation density contribution for diglyme and $AuCl_3$ interaction. The charge flux is red to blue (isovalue = 0.001 au). Key: gold = gold, chlorine = green, carbon = grey, oxygen = red and hydrogen = white.

For $(AuCl_2PET)_2dg$, the binding energy between the two $AuCl_2PET$ moieties and diglyme is -209.1 kJ/mol (Table 7.4), which is higher compared with $AuCl_3dg$. Two dominant orbital interactions lead to the charge transfer, and the orbital interaction energies for these interactions are -77.9 kJ/mol and -77.3 kJ/mol, respectively (Figure 7.7). The first interaction is between the exterior oxygen and the exterior gold moiety. The second interaction is between the center oxygen

and the center gold moiety. As a result, a total of 0.39 e was transferred from diglyme to the gold moieties (Table 7.4).

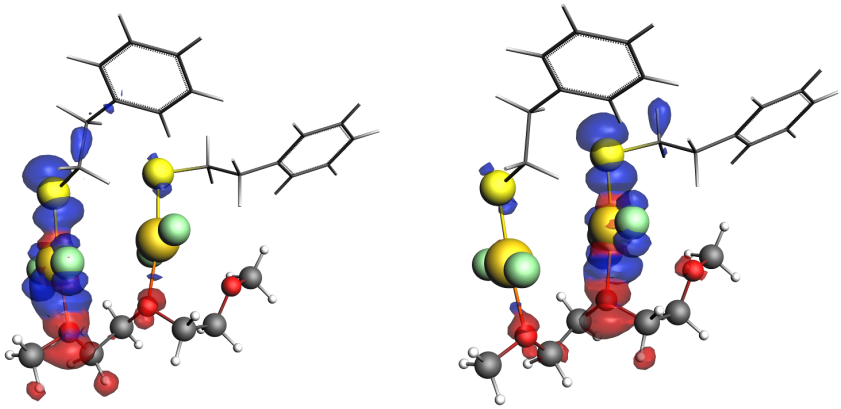


Figure 7.7 Dominant ETS-NOCV deformation density contributions for diglyme and $(AuCl_2PET)_2$ interaction. The charge flux is red to blue (isovalue = 0.001 au). Key: gold = gold, sulfur = light yellow, chlorine = green, carbon = grey, oxygen = red and hydrogen = white.

For (AuCl)PET(AuHPET)dg, the binding energy between the two fragments (diglyme and (AuCl)PET(AuHPET)) is -106.5 kJ/mol (Table 7.4), and only 0.06 e was transferred from diglyme to gold (Table 7.4). The dominant orbital interaction energy is -9.4 kJ/mol, which is relatively weak compared with the other two molecular systems (Figure 7.8). In this system, both Au atoms are in the +1 oxidation state and have two chloride or thiolate ligands, which causes the Au atoms to be less likely to accept electrons from the diglyme ligand.

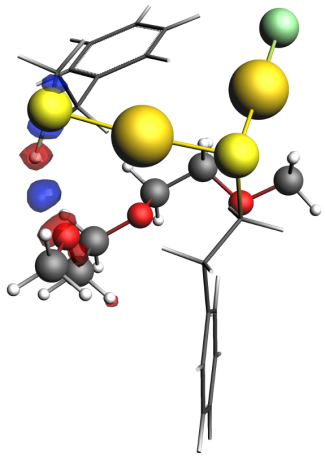
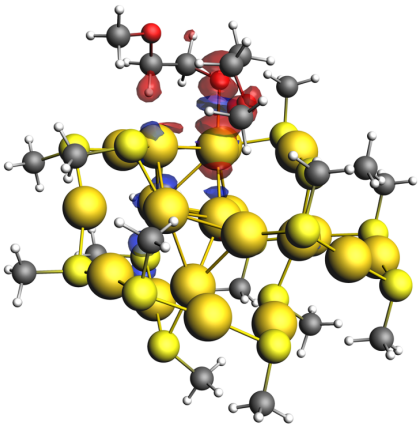


Figure 7.8 Dominant ETS-NOCV deformation density contribution for diglyme and (AuCl)PET(AuHPET) interaction. The charge flux is red to blue (isovalue = 0.001 au) Key: gold = gold, sulfur = light yellow, chlorine = green, carbon = grey, oxygen = red and hydrogen = white.

Since the diglyme has been found to have weak bonding with a gold nanocluster in experimental work,[18,19] the interaction between diglyme and $Au_{20}(SCH_3)_{15}^+$ was examined in the research as well. We started with the proposed $Au_{20}(SCH_3)_{15}dg^+$ computational model[19] and re-optimized the structure in diethyl ether solvent. The ETS-NOCV analysis shows a total of 0.24 electron (e) was transferred from diglyme to the gold nanocluster (Table 7.4). The dominant orbital interaction energy is -59.1 kJ/mol (Figure 7.9), and that orbital interaction energy is relatively weak compared with the interaction between the Au(III) species and diglyme.



Orbital interaction: -59.1 kJ/mol

$Au_{20}(SCH_3)_{15}dg^+$ system

Figure 7.9 Dominant ETS-NOCV deformation density contribution for diglyme and $Au_{20}(SCH_3)_{15}^+$ interaction. The charge flux is red to blue (isovalue = 0.001 au). Key: gold = gold, sulfur = light yellow, carbon = grey, oxygen = red and hydrogen = white.

For $(AuCl_3)$dg and $(AuCl_2PET)_2$dg, the gold atoms are all in the +3 charge state, while in (AuCl)PET(AuHPET)dg and gold motifs in $Au_{20}(SCH_3)_{15}dg^+$, the gold atoms are in the +1 charge state. Both the binding energy results and the charge transfer analysis indicate that Au(III) species have relatively strong orbital interaction with diglyme compared with Au(I), while Au(I) has a more intense dispersion interaction with diglyme (Table 7.5).

Energy decomposition results (Table 7.5) for the gold motifs show that $(AuCl_2PET)_2$dg has the highest total interaction energy while (AuCl)PET(AuHPET)dg has the lowest total interaction energy. $(AuCl_2PET)_2$dg has the highest orbital interaction energy, which accounts for the highest charge transfer value. (AuCl)PET(AuHPET)dg system has the highest dispersion correction interaction energy, which is related to the dispersion-based bonding between two fragments.

For the $Au_{20}(SCH_3)_{15}dg^+$ system, the dispersion interaction energy (-182.6 kJ/mol) is higher than the orbital interaction energy (-150.8 kJ/mol). The total interaction energy is -178.8 kJ/mol, which is lower than the interaction energy (-209.5 kJ/mol) between diglyme and two $AuCl_2PET$ moieties. Since the gold atoms on the ligand-protected motifs are all in +1 charge states, the energy decomposition results demonstrate that the bonding between diglyme and Au(I) is weaker than the bonding between diglyme and Au(III).

Table 7.5 Bonding energy decomposition results for selected systems.

	$(AuCl_3)dg$	$(AuCl_2PET)_2dg$	(AuCl)PET(AuHPET)dg	$Au_{20}(SCH_3)_{15}\ dg^+$
Pauli Repulsion Energy (kJ/mol)	399.3	566.5	181.4	397.2
Electrostatic Interaction Energy (kJ/mol)	-340.3	-465.0	-130.3	-262.6
Orbital Interaction Energy (kJ/mol)	-179.5	-219.5	-62.2	-150.8
Dispersion Interaction Energy (kJ/mol)	-61.3	-107.0	-130.1	-182.6
Solvation Energy (kJ/mol)	2.2	15.4	34.4	19.9
Total Interaction Energy (kJ/mol)	-179.5	-209.5	-106.8	-178.8

7.5 Conclusion

A series of experimental studies have previously demonstrated that diglyme can mediate the synthesis of gold nanoclusters and assist with the self-assembly of gold nanoparticles. This work represents the first investigation of the intrinsic mechanism of diglyme-assisted synthesis. In the current research, by exploring plausible reaction pathways and calculating the reaction energy for each step, we propose a reasonable reaction mechanism for synthesizing gold-thiolate motifs in the presence of diglyme. The negative reaction energy in each step theoretically demonstrates that diglyme can assist the synthesis process of the gold nanocluster in an energetically favorable pathway.

By analyzing the NMR spectrum, we found that the diglyme ligand interaction on the gold motif can be characterized by examining the chemical shifts. Protons that are pointed towards chloride have chemical shifts that are shifted downfield, and protons that are pointed to the PET group will have low chemical shifts that may even lie upfield from the bare diglyme molecule. The NMR results in this work can be a good reference for the experimental research.

Finally, we applied the ETS-NOCV method to examine the chemical bonding of the featured system. We found that the Au(III)-chloride system can bind strongly with diglyme through dative bonding, while the Au(I)-thiolate moiety tends to form dispersion-based bonding with diglyme. The highest dispersion interaction energy was found in the $Au_{20}(SCH_3)_{15}\ dg^+$ system, and that demonstrates the weak bonding between diglyme and nanocluster. Comparing between the three featured systems, we can determine that the interaction between diglyme and gold motif becomes weaker when the oxidation state of gold is reduced from Au(III) to Au(I).

7.6 Supporting Information

Supporting information provides information on NMR spectra of protons in HPET groups, theoretical background of the ETS-NOCV theory, isomer energies, graphical version of chemical shift results, reaction free energies, and coordinates of selected isomers.

7.7 Acknowledgements

The work was supported by the U.S. National Science Foundation (CHE-1905048). A.L. and J.P. were supported by the NSF REU program (CHE-1852182). The computing for this work was performed on the Beocat Research Cluster at Kansas State University, which is in part funded by the NSF (Grant Nos. CHE-1726332, CNS-1006860, EPS-1006860, and EPS-0919443).

7.8 References

(1) Chen, H.; Liu, C.; Wang, M.; Zhang, C.; Luo, N.; Wang, Y.; Abroshan, H.; Li, G.; Wang, F. Visible Light Gold Nanocluster Photocatalyst: Selective Aerobic Oxidation of Amines to Imines. *ACS Catal.* **2017**, *7* (5), 3632–3638.

(2) Dreaden, E. C.; Alkilany, A. M.; Huang, X.; Murphy, C. J.; El-Sayed, M. A. The Golden Age: Gold Nanoparticles for Biomedicine. *Chem. Soc. Rev.* **2012**, *41* (7), 2740–2779.

(3) Saha, K.; Agasti, S. S.; Kim, C.; Li, X.; Rotello, V. M. Gold Nanoparticles in Chemical and Biological Sensing. *Chem. Rev.* **2012**, *112* (5), 2739–2779.

(4) Jin, R.; Zeng, C.; Zhou, M.; Chen, Y. Atomically Precise Colloidal Metal Nanoclusters and Nanoparticles: Fundamentals and Opportunities. *Chem. Rev.* **2016**, *116* (18), 10346–10413.

(5) Pei, Y.; Gao, Y.; Shao, N.; Zeng, X. C. Thiolate-Protected $Au_{20}(SR)_{16}$ Cluster: Prolate Au_8 Core with New $[Au_3(SR)_4]$ Staple Motif. *J. Am. Chem. Soc.* **2009**, *131* (38), 13619–13621.

(6) Zeng, C.; Liu, C.; Chen, Y.; Rosi, N. L.; Jin, R. Gold–Thiolate Ring as a Protecting Motif in the $Au_{20}(SR)_{16}$ Nanocluster and Implications. *J. Am. Chem. Soc.* **2014**, *136* (34), 11922–11925.

(7) Zhu, M.; Aikens, C. M.; Hollander, F. J.; Schatz, G. C.; Jin, R. Correlating the Crystal Structure of A Thiol-Protected Au_{25} Cluster and Optical Properties. *J. Am. Chem. Soc.* **2008**, *130* (18), 5883–5885.

(8) Akola, J.; Walter, M.; Whetten, R. L.; Häkkinen, H.; Grönbeck, H. On the Structure of Thiolate-Protected Au_{25}. *J. Am. Chem. Soc.* **2008**, *130* (12), 3756–3757.

(9) Heaven, M. W.; Dass, A.; White, P. S.; Holt, K. M.; Murray, R. W. Crystal Structure of the Gold Nanoparticle $[N(C_8H_{17})_4][Au_{25}(SCH_2CH_2Ph)_{18}]$. *J. Am. Chem. Soc.* **2008**, *130* (12), 3754–3755.

(10) Lopez-Acevedo, O.; Tsunoyama, H.; Tsukuda, T.; Häkkinen, H.; Aikens, C. M. Chirality and Electronic Structure of the Thiolate-Protected Au_{38} Nanocluster. *J. Am. Chem. Soc.* **2010**, *132* (23), 8210–8218.

(11) Qian, H.; Eckenhoff, W. T.; Zhu, Y.; Pintauer, T.; Jin, R. Total Structure Determination of Thiolate-Protected Au_{38} Nanoparticles. *J. Am. Chem. Soc.* **2010**, *132* (24), 8280–8281.

(12) Dass, A.; Nimmala, P. R.; Jupally, V. R.; Kothalawala, N. $Au_{103}(SR)_{45}$, $Au_{104}(SR)_{45}$, $Au_{104}(SR)_{46}$ and $Au_{105}(SR)_{46}$ Nanoclusters. *Nanoscale* **2013**, *5* (24), 12082.

(13) Pei, Y.; Wang, P.; Ma, Z.; Xiong, L. Growth-Rule-Guided Structural Exploration of Thiolate-Protected Gold Nanoclusters. *Acc. Chem. Res.* **2019**, *52* (1), 23–33.

(14) Brust, M.; Walker, M.; Bethell, D.; Schiffrin, D. J.; Whyman, R. Synthesis of Thiol-Derivatised Gold Nanoparticles in a Two-Phase Liquid–Liquid System. *J. Chem. Soc., Chem. Commun.* **1994**, *0* (7), 801–802.

(15) Goulet, P. J. G.; Lennox, R. B. New Insights into Brust−Schiffrin Metal Nanoparticle Synthesis. *J. Am. Chem. Soc.* **2010**, *132* (28), 9582–9584.

(16) Shaltiel, L.; Shemesh, A.; Raviv, U.; Barenholz, Y.; Levi-Kalisman, Y. Synthesis and Characterization of Thiolate-Protected Gold Nanoparticles of Controlled Diameter. *J. Phys. Chem. C* **2019**, *123* (46), 28486–28493.

(17) Armstrong, J.; Ackerson, C. J. The $Au_{25}(PMBA)_{17}$Diglyme Cluster. *Molecules* **2021**, *26* (9), 2562.

(18) Compel, W. S.; Wong, O. A.; Chen, X.; Yi, C.; Geiss, R.; Häkkinen, H.; Knappenberger, K. L.; Ackerson, C. J. Dynamic Diglyme-Mediated Self-Assembly of Gold Nanoclusters. *ACS Nano* **2015**, *9* (12), 11690–11698.

(19) Anderson, I. D.; Wang, Y.; Aikens, C. M.; Ackerson, C. J. An Ultrastable Thiolate/Diglyme Ligated Cluster: $Au_{20}(PET)_{15}(DG)_2$. *Nanoscale* **2022**, *14* (25), 9134–9141.

(20) Herbert, P. J.; Yi, C.; Compel, W. S.; Ackerson, C. J.; Knappenberger, K. L. Relaxation Dynamics of Electronically Coupled $Au_{20}(SC_8H_9)_{15}$-*n*-Glyme-$Au_{20}(SC_8H_9)_{15}$ Monolayer-Protected Cluster Dimers. *J. Phys. Chem. C* **2018**, *122* (33), 19251–19258.

(21) Herbert, P. J.; Ackerson, C. J.; Knappenberger, K. L. Size-Scalable Near-Infrared Photoluminescence in Gold Monolayer Protected Clusters. *J. Phys. Chem. Lett.* **2021**, *12* (31), 7531–7536.

(22) Sokołowska, K.; Malola, S.; Lahtinen, M.; Saarnio, V.; Permi, P.; Koskinen, K.; Jalasvuori, M.; Häkkinen, H.; Lehtovaara, L.; Lahtinen, T. Towards Controlled Synthesis of Water-Soluble Gold Nanoclusters: Synthesis and Analysis. *J. Phys. Chem. C* **2019**, *123* (4), 2602–2612.

(23) Yao, Q.; Chen, T.; Yuan, X.; Xie, J. Toward Total Synthesis of Thiolate-Protected Metal Nanoclusters. *Acc. Chem. Res.* **2018**, *51* (6), 1338–1348.

(24) Chen, T.; Fung, V.; Yao, Q.; Luo, Z.; Jiang, D.; Xie, J. Synthesis of Water-Soluble $[Au_{25}(SR)_{18}]^{-}$ Using a Stoichiometric Amount of $NaBH_4$. *J. Am. Chem. Soc.* **2018**, *140* (36), 11370–11377.

(25) Qian, H.; Zhu, Y.; Jin, R. Size-Focusing Synthesis, Optical and Electrochemical Properties of Monodisperse $Au_{38}(SC_2H_4Ph)_{24}$ Nanoclusters. *ACS Nano* **2009**, *3* (11), 3795–3803.

(26) Barngrover, B. M.; Aikens, C. M. The Golden Pathway to Thiolate-Stabilized Nanoparticles: Following the Formation of Gold(I) Thiolate from Gold(III) Chloride. *J. Am. Chem. Soc.* **2012**, *134* (30), 12590–12595.

(27) Neidhart, S. M.; Barngrover, B. M.; Aikens, C. M. Theoretical Examination of Solvent and R Group Dependence in Gold Thiolate Nanoparticle Synthesis. *Phys. Chem. Chem. Phys.* **2015**, *17* (12), 7676–7680.

(28) Barngrover, B. M.; Manges, T. J.; Aikens, C. M. Prediction of Nonradical Au(0)-Containing Precursors in Nanoparticle Growth Processes. *J. Phys. Chem. A* **2015**, *119* (5), 889–895.

(29) Matus, M. F.; Malola, S.; Häkkinen, H. Ligand Ratio Plays a Critical Role in the Design of Optimal Multifunctional Gold Nanoclusters for Targeted Gastric Cancer Therapy. *ACS Nanosci. Au* **2021**, *1* (1), 47–60.

(30) Li, L.; Wang, P.; Pei, Y. Mechanism of Nucleation of Gold(I) Thiolate Oligomers into Gold–Thiolate Nanoclusters. *J. Phys. Chem. C* **2022**, *126* (13), 5980–5990.

(31) te Velde, G.; Bickelhaupt, F. M.; Baerends, E. J.; Fonseca Guerra, C.; van Gisbergen, S. J. A.; Snijders, J. G.; Ziegler, T. Chemistry with ADF. *J. Comput. Chem.* **2001**, *22* (9), 931–967.

(32) Perdew, J. P. Density-Functional Approximation for the Correlation Energy of the Inhomogeneous Electron Gas. *Phys. Rev. B* **1986**, *33* (12), 8822–8824.

(33) Becke, A. D. Density-Functional Exchange-Energy Approximation with Correct Asymptotic Behavior. *Phys. Rev. A* **1988**, *38* (6), 3098–3100.

(34) van Lenthe, E.; Ehlers, A.; Baerends, E.-J. Geometry Optimizations in the Zero Order Regular Approximation for Relativistic Effects. *J. Chem. Phys* **1999**, *110* (18), 8943–8953.

(35) Lenthe, E. van; Baerends, E. J.; Snijders, J. G. Relativistic Regular Two-component Hamiltonians. *J. Chem. Phys* **1993**, *99* (6), 4597–4610.

(36) Grimme, S.; Ehrlich, S.; Goerigk, L. Effect of the Damping Function in Dispersion Corrected Density Functional Theory. *J. Comput. Chem.* **2011**, *32* (7), 1456–1465.

(37) Grimme, S.; Antony, J.; Ehrlich, S.; Krieg, H. A Consistent and Accurate *Ab Initio* Parametrization of Density Functional Dispersion Correction (DFT-D) for the 94 Elements H-Pu. *J. Chem. Phys* **2010**, *132* (15), 154104.

(38) Klamt, A.; Schüürmann, G. COSMO: A New Approach to Dielectric Screening in Solvents with Explicit Expressions for the Screening Energy and Its Gradient. *J. Chem. Soc., Perkin Trans. 2* **1993**, No. 5, 799–805.

(39) Klamt, A. Conductor-like Screening Model for Real Solvents: A New Approach to the Quantitative Calculation of Solvation Phenomena. *J. Phys. Chem.* **1995**, *99* (7), 2224–2235.

(40) Klamt, A.; Jonas, V. Treatment of the Outlying Charge in Continuum Solvation Models. *J. Chem. Phys* **1996**, *105* (22), 9972–9981.

(41) Michalak, A.; DeKock, R. L.; Ziegler, T. Bond Multiplicity in Transition-Metal Complexes: Applications of Two-Electron Valence Indices. *J. Phys. Chem. A* **2008**, *112* (31), 7256–7263.

(42) Nalewajski, R. F.; Mrozek, J.; Michalak, A. Two-Electron Valence Indices from the Kohn-Sham Orbitals. *Int. J. Quant. Chem.* **1997**, *61* (3), 589–601.

(43) Mitoraj, M. P.; Michalak, A.; Ziegler, T. A Combined Charge and Energy Decomposition Scheme for Bond Analysis. *J. Chem. Theory Comput.* **2009**, *5* (4), 962–975.

(44) Mitoraj, M. P.; Michalak, A.; Ziegler, T. On the Nature of the Agostic Bond between Metal Centers and β-Hydrogen Atoms in Alkyl Complexes. An Analysis Based on the Extended Transition State Method and the Natural Orbitals for Chemical Valence Scheme (ETS-NOCV). *Organometallics* **2009**, *28* (13), 3727–3733.

(45) Hargittai, M.; Schulz, A.; Réffy, B.; Kolonits, M. Molecular Structure, Bonding, and Jahn−Teller Effect in Gold Chlorides: Quantum Chemical Study of $AuCl_3$, Au_2Cl_6, $AuCl_4^-$, AuCl, and Au_2Cl_2 and Electron Diffraction Study of Au_2Cl_6. *J. Am. Chem. Soc.* **2001**, *123* (7), 1449–1458.

(46) Wan, X.-K.; Tang, Q.; Yuan, S.-F.; Jiang, D.; Wang, Q.-M. Au_{19} Nanocluster Featuring a V-Shaped Alkynyl–Gold Motif. *J. Am. Chem. Soc.* **2015**, *137* (2), 652–655.

Chapter 8 - A Gaussian process approach to constructing transferable force fields for gold thiolate-protected nanoclusters

Yuchen Wang[1], D. Sulalith N. D. Samarasinghe[1], Hao Deng[2],
Bin Liu[2] and Christine M. Aikens[1,*]

1. Department of Chemistry, Kansas State University, Manhattan, KS 66506, USA
2. Tim Taylor Department of Chemical Engineering, Kansas State University, Manhattan, KS 66506, USA

* cmaikens@ksu.edu

8.1 Abstract

Gold nanoparticles can exhibit unique physical and chemical properties, such as plasmon resonances or photoluminescence. These nanoparticles have many atoms, which leads to high computational costs for density functional theory (DFT) calculations. In this work, we used the FLARE++ (Fast Learning of Atomistic Rare Events) code and incorporated an active learning algorithm to construct force fields for gold thiolate-protected nanoclusters. We started training the force field using $Au_{20}(SCH_3)_{16}$ as the initial structure and then applied the trained force field to perform molecular dynamics (MD) simulations. We then validated the machine learning force field using different types of gold nanoclusters as testing models. The test results were integrated into the existing database and re-trained again. The final force fields show success in predicting energies for nanoclusters not only in the training database but also outside the database. These tests revealed that the force field has achieved quantum mechanical level accuracy in some key performance metrics.

8.2 Introduction

Ligand-protected noble metal nanoclusters have found applications in various fields, such as photocatalysis, bioimaging, and light harvesting, because of their unique optical properties.[1–3]

The basic structure of gold thiolate-protected nanoclusters consists of a gold kernel in the inner shell and thiolate-stabilized motifs around the gold kernel such as RS-Au-SR and similar oligomers.[4,5] The gold kernel can be face-centered cubic (FCC), icosahedral, bi-icosahedral, etc. The SR ligand types of interest can include SH, SCH_3, SG = glutathione, SPh, SCH_2CH_2Ph, *p*-MBA (*para*-mercaptobenzoic acid), and so on. In 2008, the correctly predicted $Au_{25}(SR)_{18}$ structure opened up a new way of using DFT calculations to characterize the structures and properties of gold thiolate-protected nanoclusters.[6–8] Currently, DFT calculations have been successfully applied to study the geometric information, electronic structures, and optical properties of ligand-protected noble metal nanoclusters.[4,9–14] Properties such as catalysis and luminescence will vary depending on the size, shape, ligand types, and doping of the nanocluster.[15–17]

Both classical molecular dynamics (MD) and DFT molecular dynamics (DFT-MD) simulations have been successfully applied to investigate the dynamic picture of the gold nanoclusters.[11,18,19] Generally, DFT-MD yields accurate results; however, the relatively high computational costs of quantum chemistry calculations limit the simulation time scale and cluster size. Classical MD simulations are faster than DFT-MD simulations and can be considered to be an efficient sampling tool, especially if GPUs are used to accelerate the simulations. However, a set of pre-parameterized force fields needs to be available before performing classical MD simulations, and classical MD is usually not considered to be as accurate as DFT-MD. Therefore, we want to find a way to combine the advantages of those two approaches with the assistance of the machine learning toolbox.

Machine learning and data-driven methods have been used in analyzing the structure and properties of gold nanoclusters, which have been reported in recent literature.[20–24] In 2020, Pihlajamäki et al. applied a distance-based machine learning model to predict the structure of $Au_{38}(SCH_3)_{24}$.[21] The database was generated using DFT-MD simulations in their work, and the configuration space was explored using Monte Carlo simulations. Distance-based machine learning was applied to train the data points.[21] In another work reported by the same group, the orientation adaptive minimal learning machine (OAMLM) was utilized to perform geometry optimizations for both $Au_{25}(SCH_3)_{18}$ and $Au_{38}(SCH_3)_{24}$ nanoclusters.[20] In 2021, Baletto and co-workers applied the Gaussian process and unsupervised clustering methods to study the gold

nanoparticle melting process, and their theoretical prediction shows good agreement with the experimental results.[24]

For many of the traditional supervised machine learning approaches, the first step of the training process is to generate a training database that consists of enough labeled training data. The process of creating labeled training databases usually requires a lot of work, and we want to find a way to (1) create a database that contains most of the representative data points and (2) reduce the cost of labeling. Active learning (also known as on-the-fly learning), a type of self-supervised learning, provides new insights that make the training and database generation process work simultaneously. In that way, the active learning strategy will identify the most valuable datapoints for collection, allowing us to train more efficiently.

In our work, we applied an active learning strategy to develop a force field for gold thiolate-protected nanoclusters. We employed the FLARE++ code, which can perform both active and offline machine learning.[25,26] The developed machine learning force fields (ML-FFs) can be then applied to the molecular dynamics simulations (ML-MD). We started the active training with a relatively small gold nanocluster and used the trained force fields to perform molecular dynamics simulations on various nanoclusters with different sizes. Then we compared the energy from ML-MD simulations with DFT results. We then labeled those test results and integrated those new data points into the existing database and performed traditional Gaussian process training (aka offline training). We optimized the force fields by proceeding with several rounds of offline training and obtained the final force fields.

8.3 Theoretical background and computational details

Sparse Gaussian process FLARE++ employs the Gaussian process model to train the machine learning force fields. The detailed methodology can be found in the foundational FLARE paper.[25,26] As a summary, the Gaussian process model applies kernel function $k(\mathbf{d_1}, \mathbf{d_2})$ (Eq (8.1)) to quantify the similarity between two local environments, where $\mathbf{d}_i$ represents the descriptor vector

$$\boldsymbol{k(\mathbf{d_1}, \mathbf{d_2}) = \sigma^2 \left(\frac{\mathbf{d_1} \cdot \mathbf{d_2}}{d_1 d_2}\right)^{\xi}} \qquad \textbf{Equation 8.1}$$

where σ is a hyperparameter related to the variance in the learned local energy and was set to 2 eV at the beginning of the training. σ will be optimized during the training process. There are three

other hyperparameters related to noise: a force noise of $\sigma_F = 0.1$ eV/$\AA$, an energy noise of $\sigma_E = 50$ meV, and a stress noise of $\sigma_S = 0.1$ GPa. Those hyperparameters will be stored in a diagonal matrix and optimized during training.

In FLARE++, the atomic cluster expansion of Drautz was used as the descriptor to describe the local environment.[27] In general, a descriptor (c_i) for each atom was calculated by considering its neighboring atoms and analyzing the distances between them using a combination of radial basis functions and spherical harmonics as the basis functions. Then, this descriptor (c_i) was transformed into a rotationally invariant form (d_i) by keeping only the rotationally consistent parts of the result.

The dimension of the descriptor (n_{desc}) can be calculated using Eq (8.2):

$$\boldsymbol{n_{\text{desc}} = \frac{N_{\text{species}} N_{\text{rad}} \left(N_{\text{species}} N_{\text{rad}} + 1\right)(\ell_{\text{max}} + 1)}{2}} \qquad \textbf{(Equation 8.2)}$$

The dimensions are related to the number of species (N_{species}), the number of radial functions (N_{rad}), and the maximum value of ℓ in the spherical harmonics expansion (ℓ_{max}). To reach a balance between accuracy and computational cost, the N_{rad} and ℓ_{max} were set as 8 and 3 for all the training processes in this work.[25]

The sparse Gaussian process is available in the FLARE++ code, which can speed up the training process compared with the full Gaussian process. For the sparse Gaussian process, only the novel local environments will be added to the training data sets. An update threshold (Δ_{DFT}) was introduced as a criterion to determine whether a DFT call is needed. In general, the local environment will be added to the sparse sets only when $\Delta_{\text{sparse}} \leq \Delta_{\text{DFT}}$, which reduces the cost of the training. Therefore, this training process achieves a speed up compared with the full Gaussian process.

The gradient $\mathcal{L}$ was evaluated during the optimization process, as shown in Eq (8.3). Vector **y** encompasses training labels, which includes potential energies, forces, and stresses. $\mathbf{K}_{SF}$ is the matrix of kernel values between the sparse set S and the training set F, and $\mathbf{K}_{SS}$ is the matrix of kernel values between the sparse set S and itself.

$$\boldsymbol{\mathcal{L} = -\frac{1}{2}\log\left|\mathbf{K}_{SF}\mathbf{K}_{SS}^{-1}\mathbf{K}_{FS} + \Lambda\right| - \frac{1}{2}\mathbf{y}^{\top}\left(\mathbf{K}_{SF}\mathbf{K}_{SS}^{-1}\mathbf{K}_{FS} + \Lambda\right)^{-1}\mathbf{y} - \frac{N_{\text{labels}}}{2}\log\left(2\pi\right)} \textbf{(Equation 8.3)}$$

Active learning and offline training FLARE++ provides two different strategies for performing machine learning training. (1) Active learning does not require a prepared training data

set at the beginning, since training and generating database work in parallel. An initial starting geometry is used to perform a DFT calculation (DFT call) in VASP.[28–30] For the DFT calculations, the optPBE-vdW functional was applied to better describe the dispersion correction of the system.[31] The projector augmented wave (PAW) method was applied to describe the core electrons with a plane-wave basis set. The cutoff of energy was set as 450 eV.[32] Then, mapped Gaussian processes were applied to construct a Bayesian force field, and predicted variance was calculated to quantify the uncertainty of the force fields. If the uncertainty is lower than the tolerance value, the algorithm will proceed to the MD simulations section using the current trained force fields. Normally, DFT calculations will be frequently called in the beginning steps of the simulations, and DFT will be called infrequently when a relatively stable force field has been obtained. (2) The second strategy is offline training, which refers to the conventional Gaussian process in which a prepared database is needed before the start of training. In this work, we will apply both active learning and offline training to construct force fields. The details can be found in the following training procedure section.

Training procedure

For the training procedure, we first performed active learning starting with two different conformers of $Au_{20}(SCH_3)_{16}$ (called $Au_{20}(SCH_3)_{16}$: DFT[33] and $Au_{20}(SCH_3)_{16}$: crystal[34]); the structures are visualized in Figure 8.1.

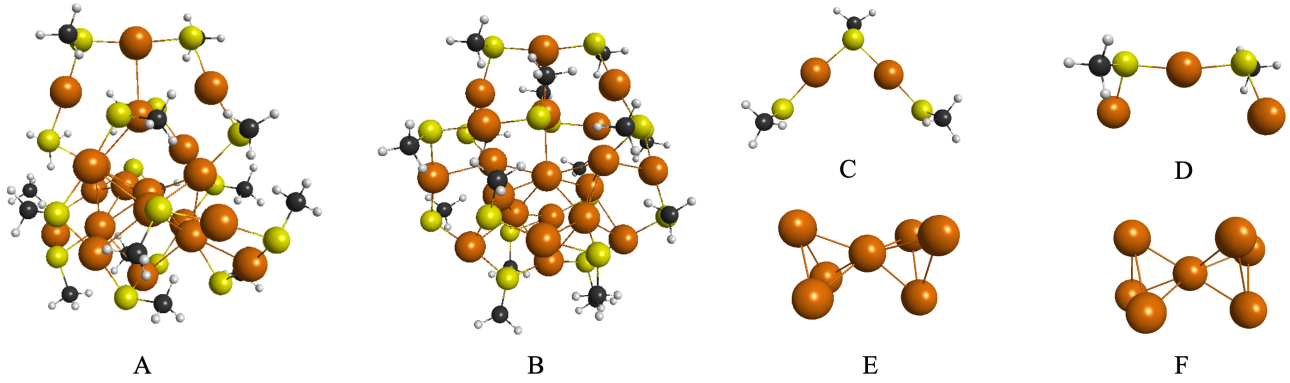


Figure 8.1 A. $Au_{20}(SCH_3)_{16}$: DFT. B. $Au_{20}(SCH_3)_{16}$: crystal. C. Basic motif in $Au_{20}(SCH_3)_{16}$ nanocluster. D. Basic motif in $Au_{20}(SCH_3)_{16}$ nanocluster. E. Au core in $Au_{20}(SCH_3)_{16}$: DFT structure. F. Au core in $Au_{20}(SCH_3)_{16}$: crystal structure. Color code: Gold = orange, carbon = gray, sulfur = yellow, and hydrogen = white.

After the two active learning processes (named otf-v1 and otf-v2, respectively) were finished, we combined all the data points obtained from the DFT calls together (structure and energy information are included in each labeled data) to create a database. We then performed an offline learning procedure using the prepared database (referred to as offline-v1). Then, the machine learning force fields were also applied to test gold nanoclusters other than $Au_{20}(SCH_3)_{16}$. Because active learning was initially performed at 300 K, when we validated the force fields at other temperatures (200 K and 400 K), the ML energy results did not agree well with the DFT calculations. To address the need for transferability across different temperatures, we labeled the test structures with the DFT-calculated energy and added them to the existing database. Adding the conformers at different temperatures thus expands the structure and energy space of the data points and improves the force field performance to better predict the energy of the novel conformers. A total of five rounds of offline training were undertaken (Table 8.1). In the first four rounds of offline trainings, the database contained information on $Au_{20}(SCH_3)_{16}$ and $Au_{25}(SCH_3)_{18}$. In the fifth round of the offline training, the database also contains information from $Au_{38}(SCH_3)_{24}$, $Au_{28}(SCH_3)_{20}$ and $Au_{36}(SCH_3)_{24}$ nanoclusters in addition to $Au_{20}(SCH_3)_{16}$ and $Au_{25}(SCH_3)_{18}$. The nanoclusters included in the database are visualized in Figure 8.2.[6,33–39] Overall, our training strategy aims at labeling the datapoints in an efficient way; the working flowchart that describes the training is shown in Figure 8.3.

Table 8.1 Database information for each round of the training procedure. The table contains information on the total number of data points in the database and the type of nanocluster included in the database.

	$Au_{20}(SCH_3)_{16}$: DFT	$Au_{20}(SCH_3)_{16}$: crystal	$Au_{25}(SCH_3)_{18}$	$Au_{38}(SCH_3)_{24}$	$Au_{28}(SCH_3)_{20}$	$Au_{36}(SCH_3)_{24}$	Total
otf-v1	122	0	0	0	0	0	122
otf-v2	0	97	0	0	0	0	97
offline_v1	122	97	0	0	0	0	219
offline_v2	122	119	22	0	0	0	263
offline_v3	122	119	44	0	0	0	285
offline_v4	122	140	66	0	0	0	338
offline_v5	122	173	98	33	33	33	492

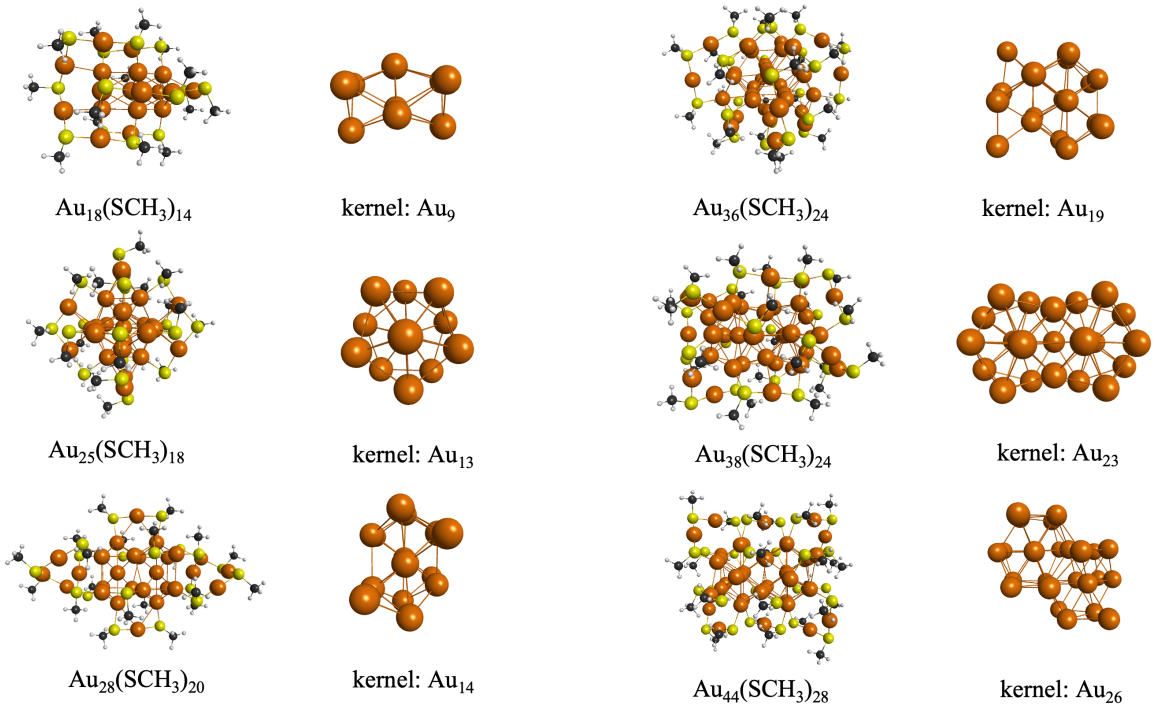


Figure 8.2 Visualization of the gold nanoclusters and their corresponding kernel structure.

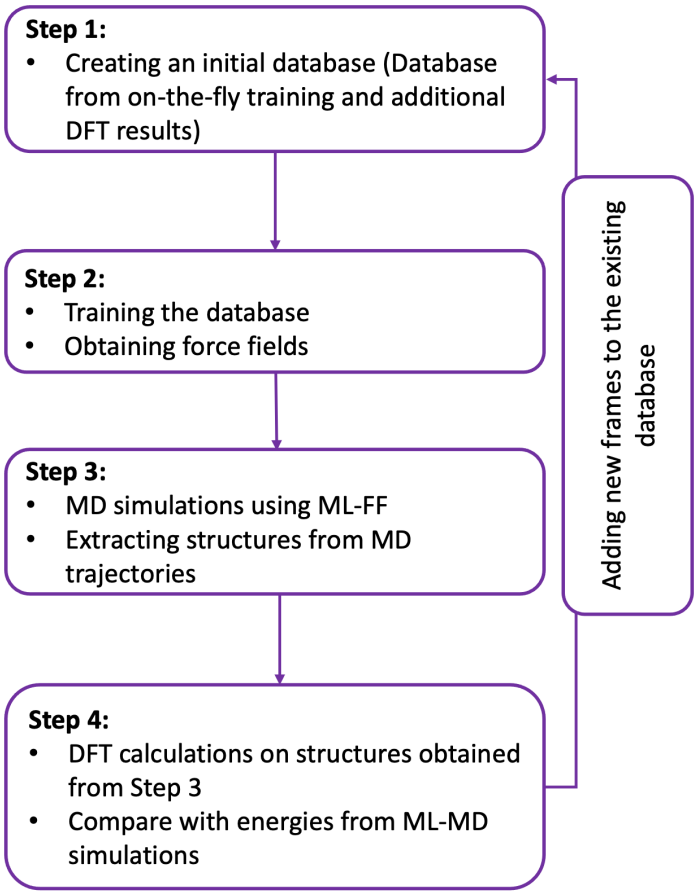


Figure 8.3 The training-testing-training working flowchart.

The parameter and hyperparameter information for each round of training is shown in Table 8.2. σ, σ_F, σ_E, and σ_S have been optimized during the training process. For the training process, we chose 5.0 Å as the cutoff value for the system; this value is chosen to achieve a balance between the computational cost and accuracy. For example, in a basic Au-S-Au motif (Figure 8.1C), the distance between Au atoms is around 3.6 Å, and the Au-S distance is approximately 2.4 Å. In that way, most of the featured local interactions will be included in the range of 5.0 Å.

Table 8.2 Parameters and hyperparameters for each round of the training procedure.

	Tolerance factor	σ	σ_F	σ_E	σ_S
otf-v1	0.05	1.6512	-0.046	-0.0310	0.0001
otf-v2	0.05	1.8765	0.0087	0.0310	0.0002
offline_v1	0.05	1.7185	-0.015	0.0334	-0.0001
offline_v2	0.01	-1.849	0.028	0.0551	0.0001
offline_v3	0.01	2.6239	0.1459	0.0523	0.0001
offline_v4	0.01	2.6117	-0.19	-0.053	0.0001
offline_v5	0.01	2.5840	-0.198	-0.048	-0.0001

LAMMPS molecular dynamics simulations The FLARE++-generated ML-FFs can be interfaced with LAMMPS[40] to perform molecular dynamics simulations.[41] The starting structures of the simulation were obtained from previously reported coordinates of gold thiolate-protected nanoclusters.[36]

For the LAMMPS simulation, the energy minimizations were performed for selected structures and the results were compared with the DFT geometry optimization results. A conjugate gradient (CG) algorithm was applied for the energy minimization, and the energy convergence criteria is 0.0001 (|ΔE|/E, where E is the final step's energy, and ΔE is the energy difference between the last step and the next-to-last step).

The production runs were performed using the NVT ensemble for 100 ps with a time step of 1 fs at 200 K, 300 K, and 400 K using a Nose-Hoover thermostat.[42–44] For all simulations, the simulation box size was chosen as 20 Å × 20 Å × 20 Å.

Analyzing the results of the machine learning calculations All the structural details corresponding to a single nanostructure are included in the cartesian coordinates of the atomic positions. Therefore, we employed an approach to measure different bonding parameters to characterize the surrounding environment of every atom. Our interest lies in different types of bonds, their bond lengths (minimum, maximum, and average), bond angles, dihedral angles, and coordination numbers of the atoms in the system. In this study, we are using a commercially available GitHub script[45] in conjunction with an in-house script to extract this information from the coordinates. The script helps to plot the desired graphs and calculate various components, such as coordination numbers and other structural details. Compared to the initial covalent radii given

in the script, we have increased the covalent radii by 14.85%, 25.00%, and 30.00% for this analysis. As the initial covalent radii parameter is not large enough to capture all bonds around the atoms, it needs to be increased. Therefore, increasing the covalent radii to 14.85% gives a significant result. To investigate the effect on the calculated Au coordination number, we have also tested with higher covalent radii (25.00% and 30.00%).

8.4 Results and discussion

After obtaining force fields from the offline_v5 training, we employed the force fields to perform geometry optimizations and molecular dynamics to examine the performance of the machine learning force fields.

Geometry optimization results

We first test the force fields on two nanoclusters that are not in the training database. For both $Au_{18}(SCH_3)_{14}$ and $Au_{44}(SCH_3)_{28}$, the visualized overlap between two geometries shows that LAMMPS energy minimization can obtain similar structures compared with DFT optimized structures (Figure 8.4). The geometric deviations between the two structures were quantified using the RMSD value (Eq 8.4)

$$\mathbf{RMSD} = \sqrt{\frac{\mathbf{1}}{\boldsymbol{N}}\sum_{\boldsymbol{i}}^{\mathbf{natom}} \left[(\boldsymbol{x_i} - \boldsymbol{x_i}')^{\mathbf{2}} + (\boldsymbol{y_i} - \boldsymbol{y_i}')^{\mathbf{2}} + (\boldsymbol{z_i} - \boldsymbol{z_i}')^{\mathbf{2}}\right]} \qquad \textbf{(Equation 8.4)}$$

where N is the number of atoms in the system, x_i and x_i' stand for the x-coordinate for atom i in the two compared structures, y_i and y_i' stand for the y-coordinate for atom i in the two compared structures, and z_i and z_i' stand for the z-coordinate for atom i in the two compared structures.

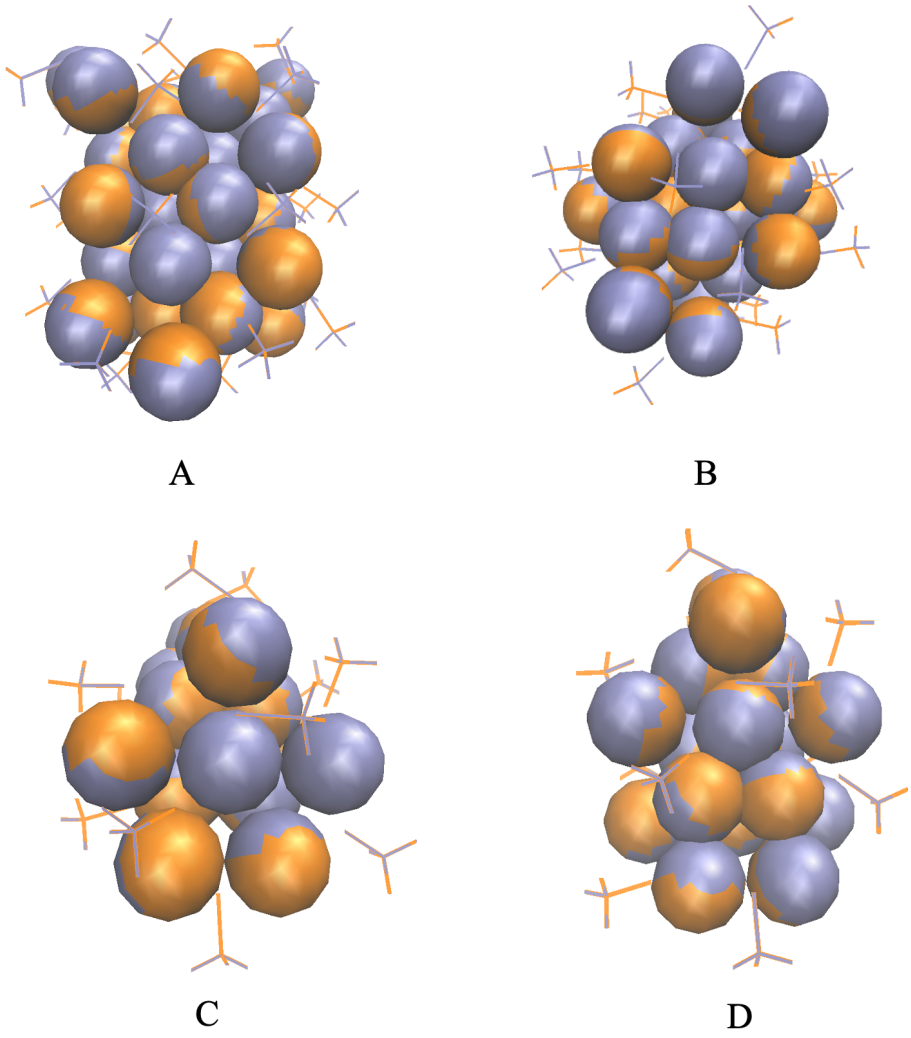


Figure 8.4 Overlap between the LAMMPS optimized and DFT optimized geometries. A. $Au_{18}(SCH_3)_{14}$ system front view. B. $Au_{18}(SCH_3)_{14}$ system side view. C. $Au_{44}(SCH_3)_{28}$ system front view. D. $Au_{44}(SCH_3)_{28}$ system side view. Color code: orange: DFT optimized geometry. Iceblue: LAMMPS optimized geometry.

The total RMSD value for the $Au_{18}(SCH_3)_{14}$ system is 0.015 Å and the RMSD for gold atoms is 0.017 Å. The total RMSD value for the $Au_{44}(SCH_3)_{28}$ system is 0.013 Å and the RMSD for gold atoms is 0.014 Å. The results indicate that machine learning force fields can reach a similar level of performance as DFT geometry optimization for the $Au_{18}(SCH_3)_{14}$ and $Au_{44}(SCH_3)_{28}$ systems.

Molecular dynamics at 300 K

To examine the performance of the machine-learned force fields, molecular dynamics for different types of nanoclusters were performed at 300 K using LAMMPS. We extracted structures every 10 ps during the ML-MD trajectories and performed DFT ground state single point energy calculations for these structures in order to compare their energy differences. Comparisons of the ML-MD energies and DFT results are shown in Figures 8.5-8.11.

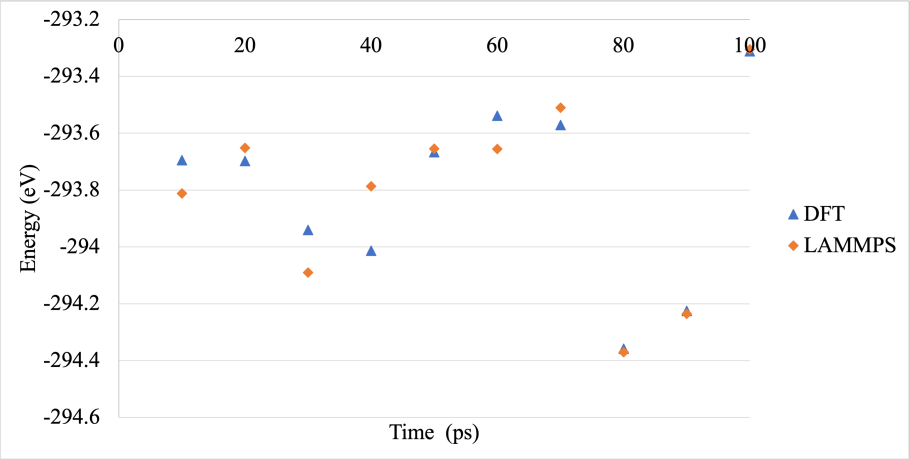


Figure 8.5 Comparison of the energy from the ML-MD LAMMPS simulation results and DFT calculated energy for the $Au_{18}(SCH_3)_{14}$ system.

For the $Au_{18}(SCH_3)_{14}$ system, the overall MAD (mean absolute deviation) for the examined structures is 0.0009 eV/atom (Figure 8.5). For the $Au_{20}(SCH_3)_{16}$: crystal system (Figure 8.6), the overall MAD for the examined structures is 0.0004 eV/atom. For the $Au_{25}(SCH_3)_{18}$ system, the overall MAD for the examined structures is 0.002 eV/atom. The results show that the ML-FF predicted energy will predict consistently lower energy compared with DFT calculated results for $Au_{25}(SCH_3)_{18}$ (Figure 8.7). If an offset value (0.184 eV) is applied to the ML-predicted results (Figure F.1), the overall MAD for the examined structures then becomes 0.0006 eV/atom. Because the offset is consistent across structures, relative energies are accurately predicted by the ML-FF. One notable point is the neutral $Au_{25}(SCH_3)_{18}$ system is an open-shell system whereas all other systems examined in this work are closed-shell systems, which may affect the predicted offset values.

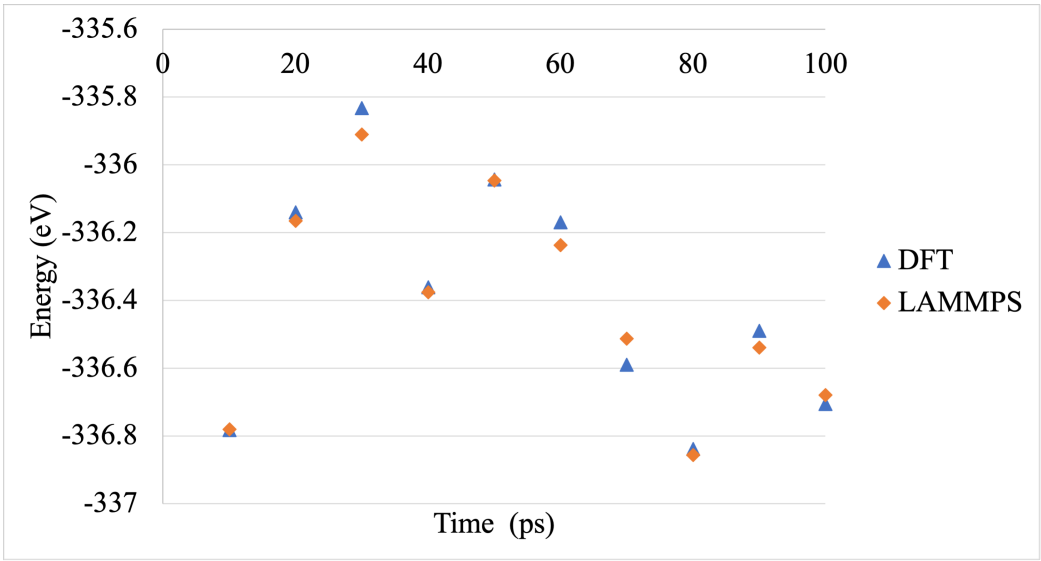


Figure 8.6 Comparison of the energy from the ML-MD LAMMPS simulation results and DFT calculated energy for the $Au_{20}(SCH_3)_{16}$ crystal system.

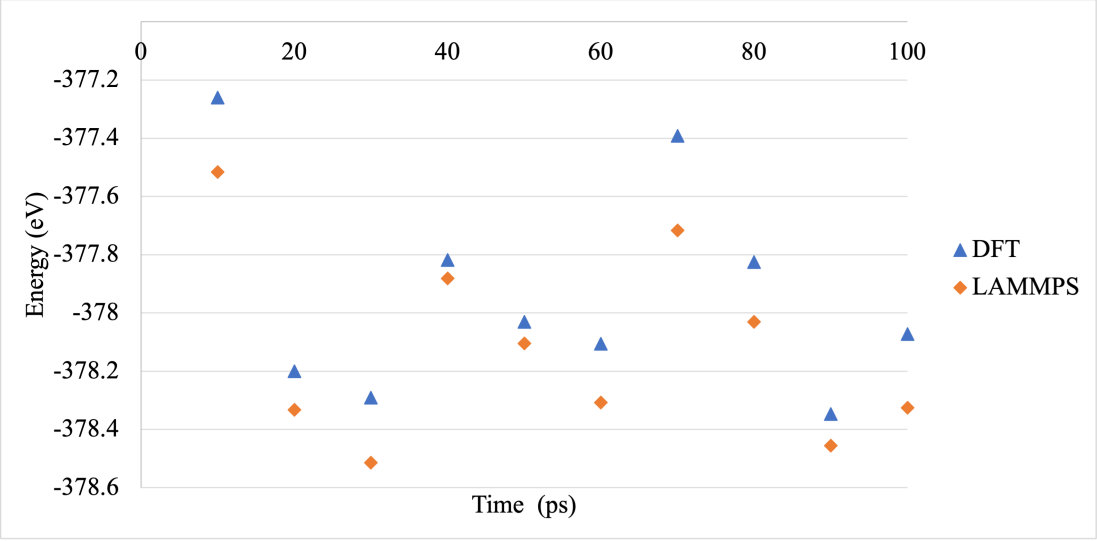


Figure 8.7 Comparison of the energy from the ML-MD LAMMPS simulation results and DFT calculated energy for the $Au_{25}(SCH_3)_{18}$ system.

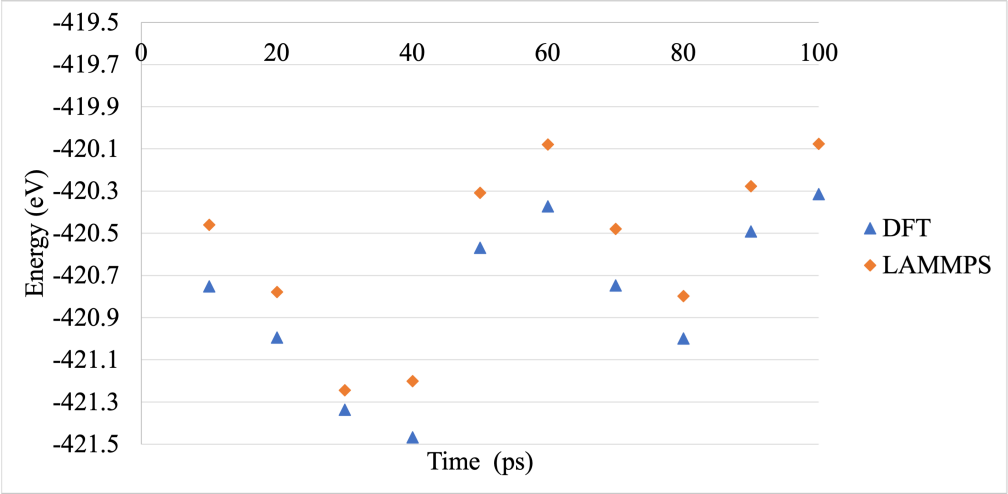


Figure 8.8 Comparison of the energy from the ML-MD LAMMPS simulation results and DFT calculated energy for the $Au_{28}(SCH_3)_{20}$ crystal system.

For the $Au_{28}(SCH_3)_{20}$ system, the overall MAD for the examined structures is 0.002 eV/atom (Figure 8.8). The results shows that the ML-predicted results tend to be higher compared with the DFT calculated results. If an offset value (-0.234 eV) is applied to the ML-predicted results (Figure F.2), the overall MAD for the examined structures is 0.0003 eV/atom. Again, the relative energies of these structures are accurately predicted by the machine-learned force field.

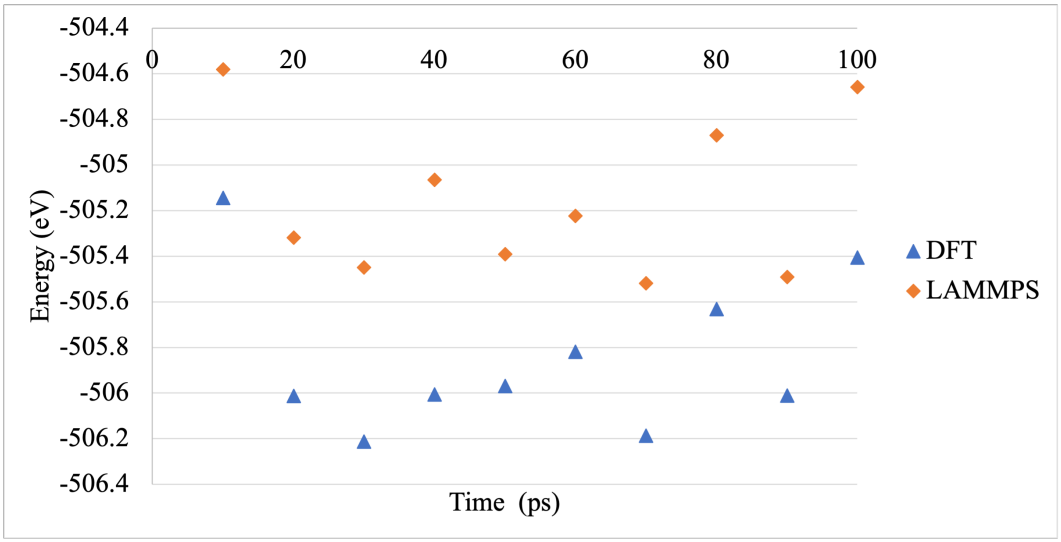


Figure 8.9 Comparison of the energy from the ML-MD LAMMPS simulation results and DFT calculated energy for the $Au_{36}(SCH_3)_{24}$ system.

For the $Au_{36}(SCH_3)_{24}$ system, the overall MAD for the examined structures is 0.0043 eV/atom (Figure 8.9). The results indicate that machine learning tends to overestimate the energy

compared with DFT calculated results. If an offset value (-0.682 eV) is applied to the ML-predicted results (Figure F.3), the overall MAD for the examined structures is 0.0006 eV/atom.

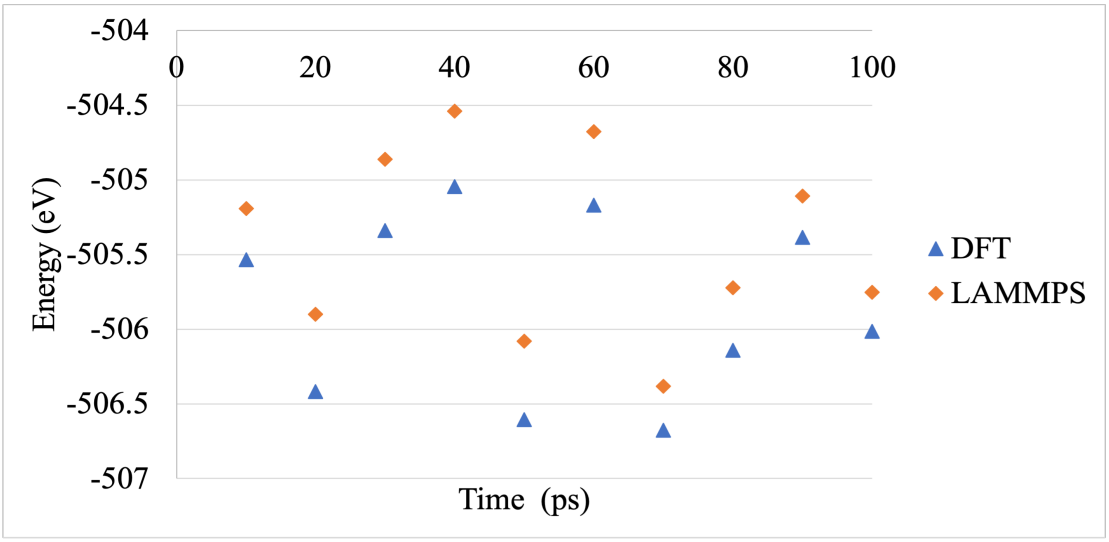


Figure 8.10 Comparison of the energy from the ML-MD LAMMPS simulation results and DFT calculated energy for the $Au_{38}(SCH_3)_{24}$ system. Simulation started without energy minimization.

For the $Au_{38}(SCH_3)_{24}$ system, the overall MAD for the examined structures is 0.0026 eV/atom (Figure 8.10). The results indicate that machine learning tends to overestimate the energy compared with DFT calculated results. If an offset value (-0.411 eV) is applied to the ML-predicted results (Figure F.4), the overall MAD for the examined structures is 0.0006 eV/atom.

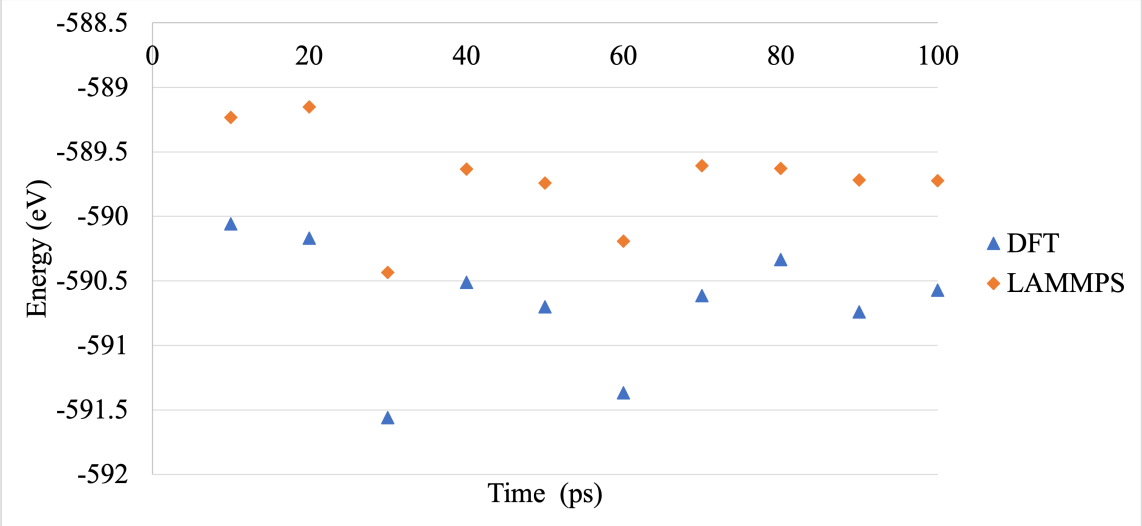


Figure 8.11 Comparison of the energy from the ML-MD LAMMPS simulation results and DFT calculated energy for the $Au_{44}(SCH_3)_{28}$ system.

For the $Au_{44}(SCH_3)_{28}$ system, the overall MAD for the examined structures during the simulations was 0.0051 eV/atom (Figure 8.11). Similar to $Au_{28}(SCH_3)_{20}$, $Au_{36}(SCH_3)_{24}$ and $Au_{38}(SCH_3)_{24}$, machine learning tends to overestimate the energy compared to the DFT calculated results. If an offset value (-0.956 eV) is applied to the ML-predicted results (Figure F.5), the overall MAD for the examined structures is 0.0006 eV/atom. As before, the relative energies are well-predicted for this system.

Overall, comparisons of the energies from the ML-predicted and DFT-calculated results for simulations at 300 K show low MAD values for the $Au_{18}(SCH_3)_{14}$ and $Au_{20}(SCH_3)_{16}$ systems. For the $Au_{25}(SCH_3)_{18}$, $Au_{28}(SCH_3)_{20}$, $Au_{36}(SCH_3)_{24}$, and $Au_{44}(SCH_3)_{28}$ systems, the MAD is less than 0.0006 eV/atom if a constant offset value is applied to the ML-predicted results. This indicates that machine learning force fields can successfully predict the relative energies for the systems. Notably, neither $Au_{18}(SCH_3)_{14}$ nor $Au_{44}(SCH_3)_{28}$ was included in the training database. Therefore, the machine learning force field shows good transferability in predicting the energies for nanoclusters outside the training database.

Molecular dynamics at different temperatures

The majority of data points in the training database come from the two active learning trajectories at 300 K, and only a small fraction of data points come from the high temperature conformer results. To examine the performance of the force fields at different temperatures, we next examined the molecular dynamics for nanoclusters at other temperatures. Representative results for $Au_{20}(SCH_3)_{16}$ at 400 K and $Au_{25}(SCH_3)_{18}$ at 200 K are shown in Figure 8.12 and Figure 8.13, respectively.

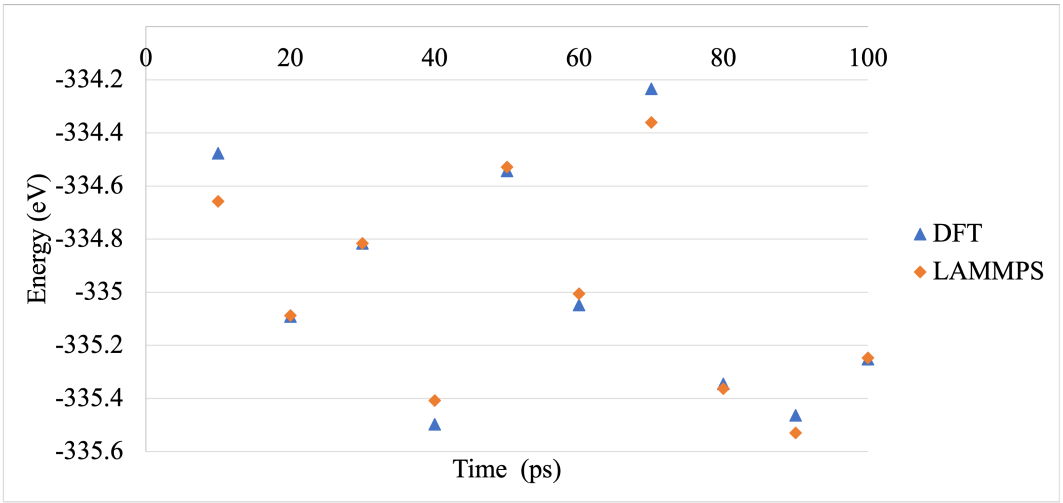


Figure 8.12 Comparison of the energy from the ML-MD LAMMPS simulation results and DFT calculated energy for the $Au_{20}(SCH_3)_{16}$ system at 400 K.

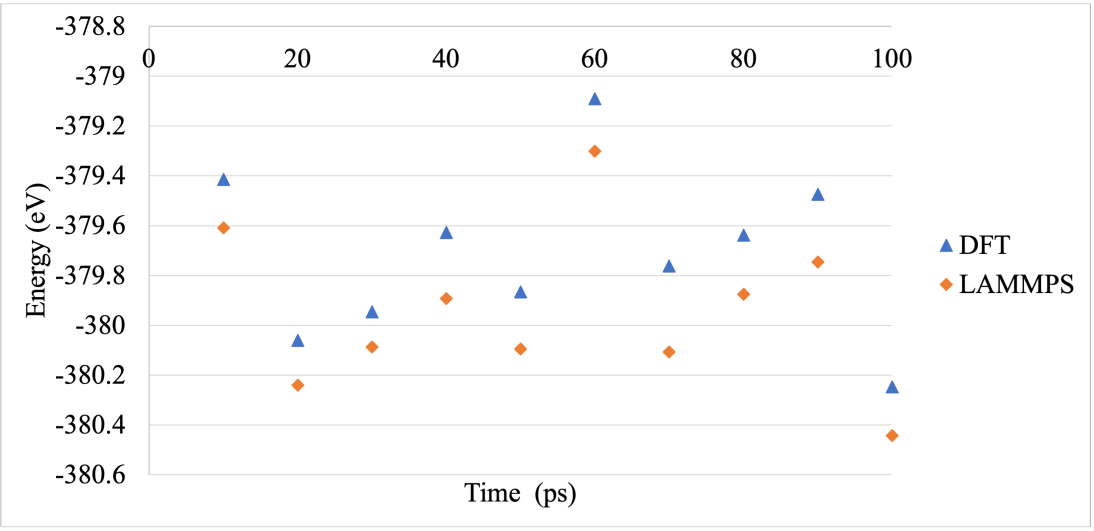


Figure 8.13 Comparison of the energy from the LAMMPS simulation results and DFT calculated energy for the $Au_{25}(SCH_3)_{18}$ system at 200 K.

For the $Au_{20}(SCH_3)_{16}$ system, the overall MAD for the examined structures is 0.0005 eV/atom. For the $Au_{25}(SCH_3)_{18}$ system, the overall MAD for the examined structures during the simulations is 0.0020 eV/atom. Similar to the $Au_{25}(SCH_3)_{18}$ simulation at 300 K, the ML force fields tend to underestimate the energy compared with the DFT. However, if the same offset value (0.184 eV) is applied to the ML-predicted results (Figure F.6), the overall MAD for the examined structures is 0.0006 eV/atom. Again, the general trends of the ML-predicted and DFT-calculated

energies show good agreement in relative energies. These results indicate that the force fields can also be applied for simulations at different temperatures.

Visualizing the results from machine learning calculations

Geometries from ML-MD trajectories can be analyzed in various ways. Geometrical parameters of various $Au_{20}(SCH_3)_{16}$ configurations at 400K are shown in Figure 8.14. The mean bond lengths between Au-Au, Au-S, S-C, and C-H bonds are depicted in Figure 8.14A. The C-S--S-C dihedral angle is one of the interesting features that can be explored in this system; there is a notable variation among the various configurations, with a preference for a dihedral angle larger than 100° (Figure 8.14B). Moreover, the coordination numbers of atoms, such as the Au-Au coordination, can be determined. Less than half of the Au atoms (8 atoms or less) in each system have a coordination number of six or higher throughout the simulation (Figure 8.14C). Finally, a thorough examination of these diverse bonding parameters through principal component analysis (PCA) shows that our training set expands throughout a significant portion of the feature space (Figure 8.14D).

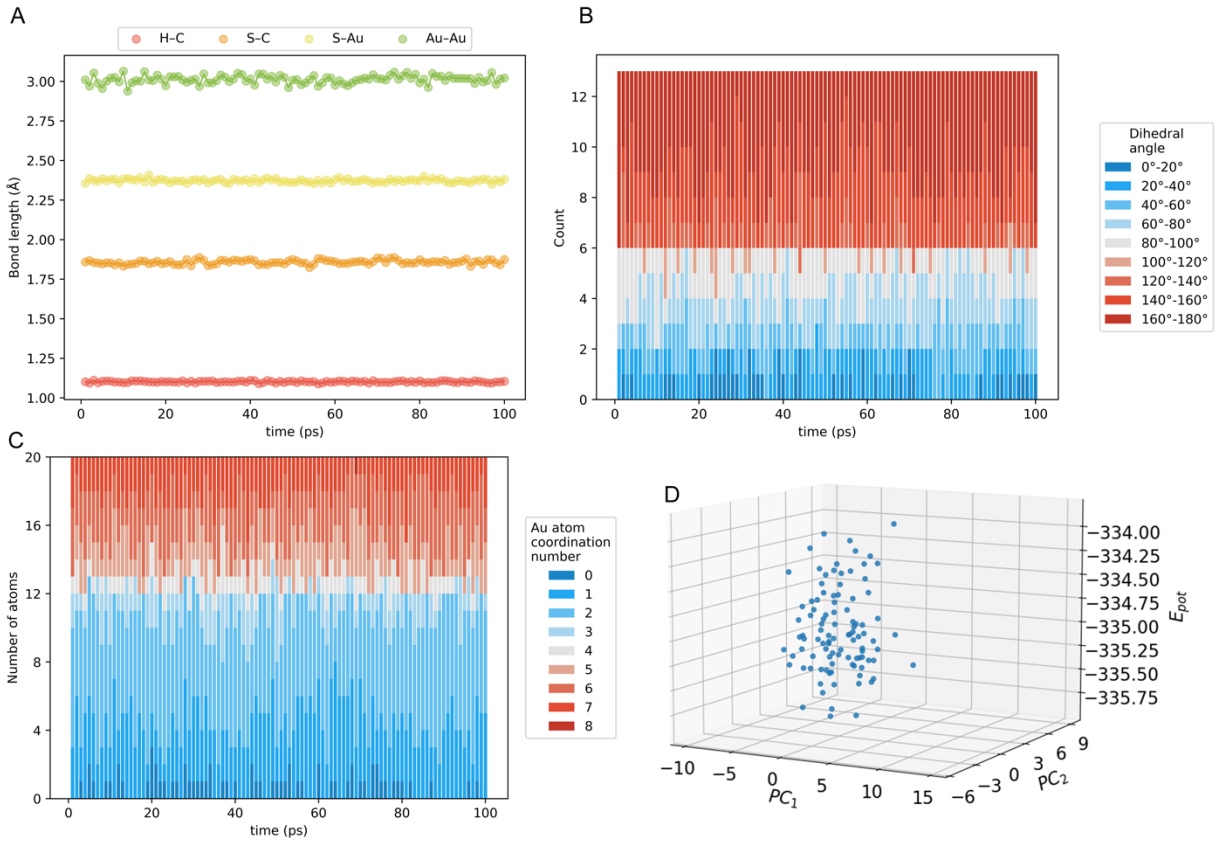


Figure 8.14 A. Mean bond length variation. B. C-S---S-C dihedral angle count for various angle ranges. C. Au atom count for each individual Au-Au coordination numbers. D. PCA visualization of the bonding parameters for different training configurations of $Au_{20}(SCH_3)_{16}$ at 400K (PC - principal component). Each graph demonstrates results from a hundred configurations (one snapshot per picosecond).

Geometrical parameters for $Au_{25}(SCH_3)_{18}$ at 200 K and $Au_{44}(SCH_3)_{28}$ at 300 K are shown in Figures 8.15 and 8.16, respectively, to demonstrate results for different nanoclusters at a variety of temperatures. The findings show that there is a notable shift in the mean bond lengths between Au-Au bonds in different gold configurations. For instance, Figure 8.15A shows that the mean bond length for $Au_{25}(SCH_3)_{18}$ is greater than 3 Å, while Figure 8.16A shows that the mean bond length for $Au_{44}(SCH_3)_{28}$ is much closer to 3 Å. $Au_{25}(SCH_3)_{18}$ and $Au_{44}(SCH_3)_{28}$ exhibit a lower C-S---S-C dihedral angle preference for angles greater than 100° and a higher Au-Au coordination in comparison to $Au_{20}(SCH_3)_{16}$ (Figures 8.15 and 8.16). These configurations are quite diverse, as shown by the PCA plots (Figure 8.15D and 8.16D). Overall, a 25.00% increase in covalent radii is used to analyze the results shown here. The supplemental material (Figures F7-F11) includes a

comparison of how the structure parameters change as the considered covalent radii are smaller (an increase of 14.85% compared to the default) or larger (an increase of 30.00%) compared to the 25.00% increase results shown in the main text.

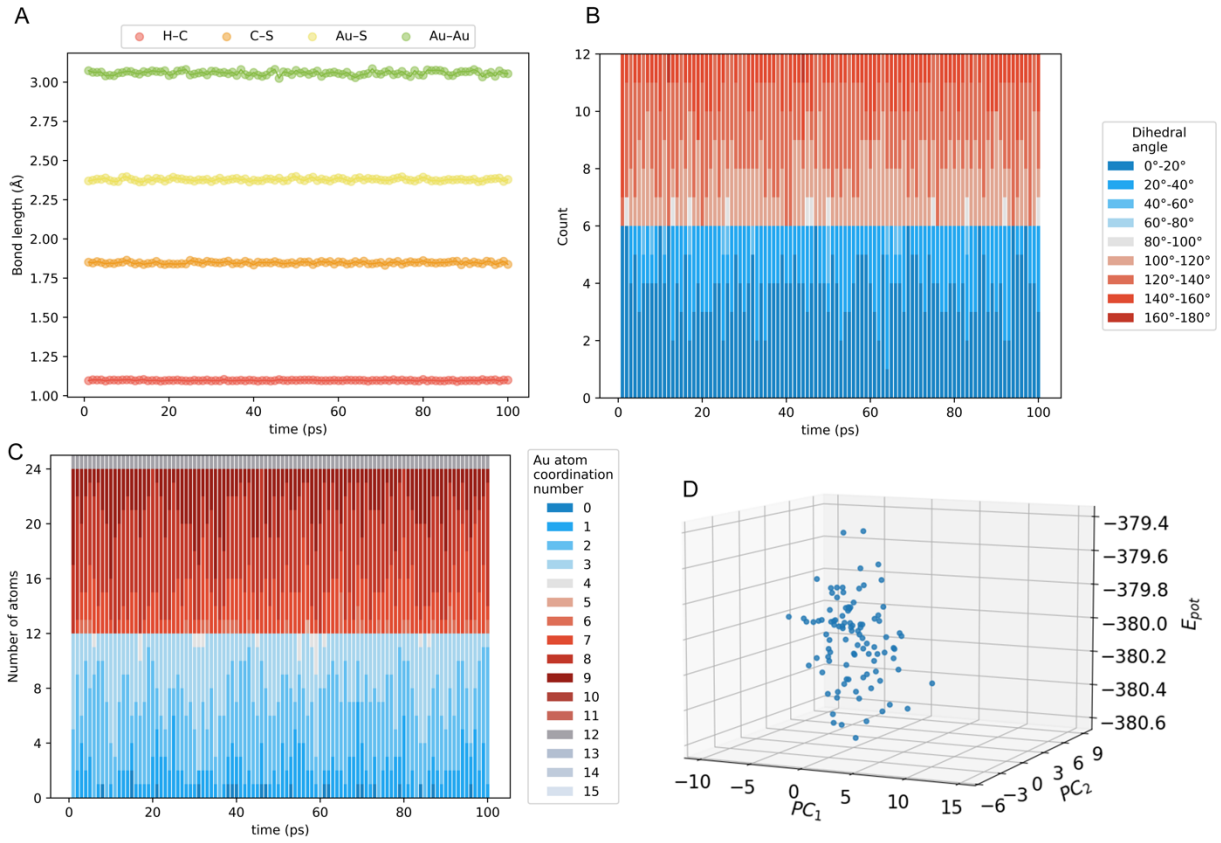


Figure 8.15 A. Mean bond length variation. B. C-S---S-C dihedral angle count for various angle ranges. C. Au atom count for each individual Au-Au coordination numbers. D. PCA visualization of the bonding parameters for different training configurations of $Au_{25}(SCH_3)_{18}$ at 200K (PC - principal component). Each graph demonstrates results from a hundred configurations (one snapshot per picosecond).

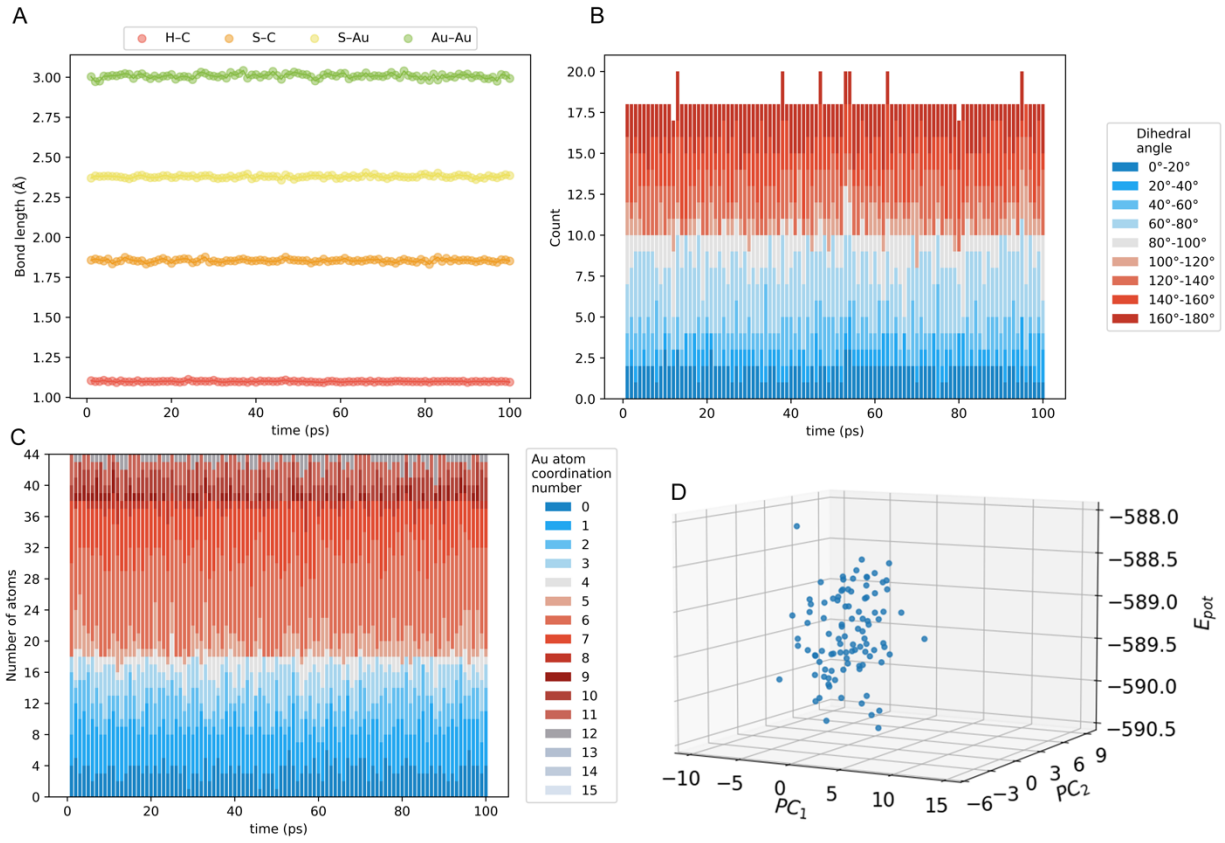


Figure 8.16 A. Mean bond length variation. B. C-S---S-C dihedral angle count for various angle ranges. C. Au atom count for each individual Au-Au coordination numbers. D. PCA visualization of the bonding parameters for different training configurations of $Au_{44}(SCH_3)_{28}$ at 300K (PC - principal component). Each graph demonstrates results from a hundred configurations (one snapshot per picosecond).

8.5 Conclusions

This work presents a machine-learning force field for gold thiolate-protected nanoclusters of the general formula $Au_x(SCH_3)_y$ that achieves DFT-level accuracy. The active learning strategy provides a way to efficiently sample the data points and automatically generate a training database. In our case, the active learning started with the $Au_{20}(SCH_3)_{16}$ structures and the resulting trained force field was initially used to simulate the $Au_{25}(SCH_3)_{18}$ system. In addition to active learning, we also applied offline training to incorporate all of the sampled data points into a single force field. During our offline learning steps, we incorporated a small amount of data from nanoclusters other than $Au_{20}(SCH_3)_{16}$ as well as data from higher and lower temperatures. We found that only adding a small number of the data points for the new systems significantly improves the predicted

results. The final force fields show good agreement not only in predicting energies and geometries for the structures in the database but can also correctly predict the energies and geometries for structures outside the database, which demonstrates good transferability of the force fields. Because the training database also includes high-temperature structures, the force fields can also be applied to high-temperature simulations and have been tested up to 400 K. Overall, the machine learning force fields can speed up MD simulations for gold thiolate-protected nanoclusters and extend molecular dynamics to larger-size gold nanoclusters.

8.6 Supporting information

Supporting information provides information on the energy difference between ML-predicted (constant offset applied) and DFT calculated results for the $Au_{25}(SCH_3)_{18}$, $Au_{28}(SCH_3)_{20}$, $Au_{36}(SCH_3)_{24}$, $Au_{38}(SCH_3)_{24}$, $Au_{44}(SCH_3)_{30}$ systems, and the analysis of the MD results with different covalent radii. The machine learning force field files (ML-FF.zip, which includes sparse_desc_lmp.flare, lmp.flare, and L_inv_lmp.flare), training data sets (all_dft.xyz) and a demonstration LAMMPS input file (lammps.in) are available via the Open Science Framework at https://osf.io/2sd8w/?view_only=3ad872a9704244e7bae58eaa0cb69001.

8.7 Conflicts

There are no conflicts of interest to declare.

8.8 Acknowledgment

The computing for this work was performed on the Beocat Research Cluster at Kansas State University, which is partially funded by the NSF (Grant Nos. CHE-1726332, CNS-1006860, EPS-1006860, and EPS-0919443). The authors thank Kansas State University for support of this research.

8.9 References

(1) Yuan, P.; Chen, R.; Zhang, X.; Chen, F.; Yan, J.; Sun, C.; Ou, D.; Peng, J.; Lin, S.; Tang, Z.; Teo, B. K.; Zheng, L.; Zheng, N. Ether-Soluble Cu_{53} Nanoclusters as an Effective Precursor of High-Quality CuI Films for Optoelectronic Applications. *Angew. Chem.* **2019**, *131* (3), 845–849.

(2) Kwak, K.; Choi, W.; Tang, Q.; Kim, M.; Lee, Y.; Jiang, D.; Lee, D. A Molecule-like $PtAu_{24}(SC_6H_{13})_{18}$ Nanocluster as an Electrocatalyst for Hydrogen Production. *Nat Commun* **2017**, *8* (1), 14723.

(3) Tang, Q.; Lee, Y.; Li, D.-Y.; Choi, W.; Liu, C. W.; Lee, D.; Jiang, D. Lattice-Hydride Mechanism in Electrocatalytic CO_2 Reduction by Structurally Precise Copper-Hydride Nanoclusters. *J. Am. Chem. Soc.* **2017**, *139* (28), 9728–9736.

(4) Lopez-Acevedo, O.; Tsunoyama, H.; Tsukuda, T.; Häkkinen, H.; Aikens, C. M. Chirality and Electronic Structure of the Thiolate-Protected Au_{38} Nanocluster. *J. Am. Chem. Soc.* **2010**, *132* (23), 8210–8218.

(5) Aikens, C. M. Electronic and Geometric Structure, Optical Properties, and Excited State Behavior in Atomically Precise Thiolate-Stabilized Noble Metal Nanoclusters. *Acc. Chem. Res.* **2018**, *51* (12), 3065–3073.

(6) Zhu, M.; Aikens, C. M.; Hollander, F. J.; Schatz, G. C.; Jin, R. Correlating the Crystal Structure of A Thiol-Protected Au_{25} Cluster and Optical Properties. *J. Am. Chem. Soc.* **2008**, *130* (18), 5883–5885.

(7) Heaven, M. W.; Dass, A.; White, P. S.; Holt, K. M.; Murray, R. W. Crystal Structure of the Gold Nanoparticle $[N(C_8H_{17})_4][Au_{25}(SCH_2CH_2Ph)_{18}]$. *J. Am. Chem. Soc.* **2008**, *130* (12), 3754–3755.

(8) Akola, J.; Walter, M.; Whetten, R. L.; Häkkinen, H.; Grönbeck, H. On the Structure of Thiolate-Protected Au_{25}. *J. Am. Chem. Soc.* **2008**, *130* (12), 3756–3757.

(9) Matus, M. F.; Häkkinen, H. Understanding Ligand-Protected Noble Metal Nanoclusters at Work. *Nat Rev Mater* **2023**, *8* (6), 372–389.

(10) Lopez-Acevedo, O.; Akola, J.; Whetten, R. L.; Grönbeck, H.; Häkkinen, H. Structure and Bonding in the Ubiquitous Icosahedral Metallic Gold Cluster $Au_{144}(SR)_{60}$. *J. Phys. Chem. C* **2009**, *113* (13), 5035–5038.

(11) Truttmann, V.; Loxha, A.; Banu, R.; Pittenauer, E.; Malola, S.; Matus, M. F.; Wang, Y.; Ploetz, E. A.; Rupprechter, G.; Bürgi, T.; Häkkinen, H.; Aikens, C.; Barrabés, N. Directing Intrinsic Chirality in Gold Nanoclusters: Preferential Formation of Stable Enantiopure Clusters in High Yield and Experimentally Unveiling the "Super" Chirality of Au_{144}. *ACS Nano* **2023**, *17* (20), 20376–20386.

(12) Xiong, L.; Pei, Y. Gold Nanoclusters with Atomic Precision: Optical Properties. In *Atomically Precise Nanoclusters*; Zhu, Y., Jin, R., Eds.; Jenny Stanford Publishing, 2021; pp 165–225.

(13) Sun, F.; Tang, Q.; Jiang, D. Atomically Precise Metal Nanoclusters as Electrocatalysts: From Experiment to Computational Insights. In *Atomically Precise Nanochemistry*; Jin, R., Jiang, D., Eds.; Wiley, 2023; pp 195–225.

(14) Weerawardene, K. L. D. M.; Häkkinen, H.; Aikens, C. M. Connections Between Theory and Experiment for Gold and Silver Nanoclusters. *Annu. Rev. Phys. Chem.* **2018**, *69* (1), 205–229.

(15) Li, S.; Du, X.; Liu, Z.; Li, Y.; Shao, Y.; Jin, R. Size Effects of Atomically Precise Gold Nanoclusters in Catalysis. *Precision Chemistry* **2023**, *1* (1), 14–28.

(16) Lopez-Acevedo, O.; Kacprzak, K. A.; Akola, J.; Häkkinen, H. Quantum Size Effects in Ambient CO Oxidation Catalysed by Ligand-Protected Gold Clusters. *Nature Chem* **2010**, *2* (4), 329–334.

(17) Havenridge, S.; Aikens, C. M. Understanding the Ligand-Dependent Photoluminescent Mechanism in Small Alkynyl-Protected Gold Nanoclusters. *J. Phys. Chem. A* **2023**, *127* (47), 9932–9943.

(18) Juarez-Mosqueda, R.; Malola, S.; Häkkinen, H. Ab Initio Molecular Dynamics Studies of $Au_{38}(SR)_{24}$ Isomers under Heating. *Eur. Phys. J. D* **2019**, *73* (3), 62.

(19) Sabooni Asre Hazer, M.; Malola, S.; Häkkinen, H. Isomer Dynamics of the $[Au_6(NHC\text{-}S)_4]^{2+}$ Nanocluster. *Chem. Commun.* **2022**, *58* (19), 3218–3221.

(20) Pihlajamäki, A.; Malola, S.; Kärkkäinen, T.; Häkkinen, H. Orientation Adaptive Minimal Learning Machine: Application to Thiolate-Protected Gold Nanoclusters and Gold-Thiolate Rings. *10.48550/ARXIV.2203.09788* **2022**.

(21) Pihlajamäki, A.; Hämäläinen, J.; Linja, J.; Nieminen, P.; Malola, S.; Kärkkäinen, T.; Häkkinen, H. Monte Carlo Simulations of $Au_{38}(SCH_3)_{24}$ Nanocluster Using Distance-Based Machine Learning Methods. *J. Phys. Chem. A* **2020**, *124* (23), 4827–4836.

(22) Li, J.; Chen, T.; Lim, K.; Chen, L.; Khan, S. A.; Xie, J.; Wang, X. Deep Learning Accelerated Gold Nanocluster Synthesis. *Advanced Intelligent Systems* **2019**, *1* (3), 1900029.

(23) Pihlajamäki, A.; Malola, S.; Kärkkäinen, T.; Häkkinen, H. Graphs and Kernelized Learning Applied to Interactions of Hydrogen with Doped Gold Nanoparticle Electrocatalysts. *J. Phys. Chem. C* **2023**, *127* (29), 14211–14221.

(24) Zeni, C.; Rossi, K.; Pavloudis, T.; Kioseoglou, J.; De Gironcoli, S.; Palmer, R. E.; Baletto, F. Data-Driven Simulation and Characterisation of Gold Nanoparticle Melting. *Nat Commun* **2021**, *12* (1), 6056.

(25) Vandermause, J.; Xie, Y.; Lim, J. S.; Owen, C. J.; Kozinsky, B. Active Learning of Reactive Bayesian Force Fields Applied to Heterogeneous Catalysis Dynamics of H/Pt. *Nat Commun* **2022**, *13* (1), 5183.

(26) Vandermause, J.; Torrisi, S. B.; Batzner, S.; Xie, Y.; Sun, L.; Kolpak, A. M.; Kozinsky, B. On-the-Fly Active Learning of Interpretable Bayesian Force Fields for Atomistic Rare Events. *npj Comput Mater* **2020**, *6* (1), 20.

(27) Drautz, R. Atomic Cluster Expansion for Accurate and Transferable Interatomic Potentials. *Phys. Rev. B* **2019**, *99* (1), 014104.

(28) Kresse, G.; Hafner, J. *Ab Initio* Molecular Dynamics for Liquid Metals. *Phys. Rev. B* **1993**, *47* (1), 558–561.

(29) Kresse, G.; Furthmüller, J. Efficiency of Ab-Initio Total Energy Calculations for Metals and Semiconductors Using a Plane-Wave Basis Set. *Computational Materials Science* **1996**, *6* (1), 15–50.

(30) Kresse, G.; Furthmüller, J. Efficient Iterative Schemes for *Ab Initio* Total-Energy Calculations Using a Plane-Wave Basis Set. *Phys. Rev. B* **1996**, *54* (16), 11169–11186.

(31) Klimeš, J.; Bowler, D. R.; Michaelides, A. Chemical Accuracy for the van Der Waals Density Functional. *J. Phys.: Condens. Matter* **2010**, *22* (2), 022201.

(32) Kresse, G.; Joubert, D. From Ultrasoft Pseudopotentials to the Projector Augmented-Wave Method. *Phys. Rev. B* **1999**, *59* (3), 1758–1775.

(33) Pei, Y.; Gao, Y.; Shao, N.; Zeng, X. C. Thiolate-Protected $Au_{20}(SR)_{16}$ Cluster: Prolate Au_8 Core with New $[Au_3(SR)_4]$ Staple Motif. *J. Am. Chem. Soc.* **2009**, *131* (38), 13619–13621.

(34) Zeng, C.; Liu, C.; Chen, Y.; Rosi, N. L.; Jin, R. Gold–Thiolate Ring as a Protecting Motif in the $Au_{20}(SR)_{16}$ Nanocluster and Implications. *J. Am. Chem. Soc.* **2014**, *136* (34), 11922–11925.

(35) Nimmala, P. R.; Knoppe, S.; Jupally, V. R.; Delcamp, J. H.; Aikens, C. M.; Dass, A. $Au_{36}(SPh)_{24}$ Nanomolecules: X-Ray Crystal Structure, Optical Spectroscopy, Electrochemistry, and Theoretical Analysis. *J. Phys. Chem. B* **2014**, *118* (49), 14157–14167.

(36) Kuda-Singappulige, G. U.; Aikens, C. M. Geometrical and Electronic Structure, Stability, and Optical Absorption Spectra Comparisons between Thiolate- and Chloride-Stabilized Gold Nanoclusters. *J. Phys. Chem. A* **2019**, *123* (45), 9712–9720.

(37) Zeng, C.; Chen, Y.; Iida, K.; Nobusada, K.; Kirschbaum, K.; Lambright, K. J.; Jin, R. Gold Quantum Boxes: On the Periodicities and the Quantum Confinement in the Au_{28}, Au_{36}, Au_{44}, and Au_{52} Magic Series. *J. Am. Chem. Soc.* **2016**, *138* (12), 3950–3953.

(38) Qian, H.; Eckenhoff, W. T.; Zhu, Y.; Pintauer, T.; Jin, R. Total Structure Determination of Thiolate-Protected Au_{38} Nanoparticles. *J. Am. Chem. Soc.* **2010**, *132* (24), 8280–8281.

(39) Tian, S.; Li, Y.-Z.; Li, M.-B.; Yuan, J.; Yang, J.; Wu, Z.; Jin, R. Structural Isomerism in Gold Nanoparticles Revealed by X-Ray Crystallography. *Nat Commun* **2015**, *6* (1), 8667.

(40) Thompson, A. P.; Aktulga, H. M.; Berger, R.; Bolintineanu, D. S.; Brown, W. M.; Crozier, P. S.; In 'T Veld, P. J.; Kohlmeyer, A.; Moore, S. G.; Nguyen, T. D.; Shan, R.; Stevens, M. J.; Tranchida, J.; Trott, C.; Plimpton, S. J. LAMMPS - a Flexible Simulation Tool for Particle-Based Materials Modeling at the Atomic, Meso, and Continuum Scales. *Comput. Phys. Commun.* **2022**, *271*, 108171.

(41) Xie, Y.; Vandermause, J.; Sun, L.; Cepellotti, A.; Kozinsky, B. Bayesian Force Fields from Active Learning for Simulation of Inter-Dimensional Transformation of Stanene. *npj Comput Mater* **2021**, *7* (1), 40.

(42) Nosé, S. A Unified Formulation of the Constant Temperature Molecular Dynamics Methods. *J. Chem. Phys* **1984**, *81* (1), 511–519.

(43) Hoover, W. G. Canonical Dynamics: Equilibrium Phase-Space Distributions. *Phys. Rev. A* **1985**, *31* (3), 1695–1697.

(44) Nosé, S. Constant Temperature Molecular Dynamics Methods. *Prog. Theor. Phys. Suppl.* **1991**, *103*, 1–46.

(45) Dechert, S. Xyz2tab Https://Github.Com/Radi0sus/Xyz2tab.Git.

Chapter 9 - Final conclusion and outlook

The major focus of this dissertation is employing both quantum chemistry and machine learning approaches to study the ground state and excited state properties of noble metal nanoclusters.

In the first part (chapters 3, 4 and 5), we are interested in the plasmon-induced photocatalytic process. In these three chapters, by employing mean-field Ehrenfest dynamics, we can watch the motion of nuclei and electrons varying with time in the presence of the applied electric fields.

Firstly, in chapter 3, the effects of the electric field strengths and silver nanowire length on N_2 dissociation were studied. Our investigation shows that stronger field strengths lead to plasmon-enhanced N_2 dissociation in general; however, the N_2 dissociation or activation ability does not always monotonically increase with the field strength, which might be related to the nonlinear electronic and population transition properties arising from different electric field strengths.

Secondly, in chapter 4, we are interested in how the doping affects photo-catalytic properties of silver nanowire on N_2 dissociation. Interestingly, we found that the excited state dynamics results do not have a direct correlation with the ground state binding energy between the wire and the N_2 molecule. We also found that although Au and Cu are in the same group in the periodic table, Ag_5Au showed the best plasmon-enhanced catalysis properties for N_2 dissociation with longitudinal excitation, while the Ag_5Cu system shows quite weak plasmon-enhanced properties for N_2 dissociation with the longitudinal excitation. The differences in plasmon-enhanced properties can be due to the differences in the electronic structure and potential energy surfaces for doped systems.

In both chapters 3 and 4, we applied a continuous wave field to the system. In chapter 5, we want to learn how a static field interacts with the system and how it affects the system differently from a continuous wave field, as well as giving fundamental insights into the effects at the maximum positive and negative values for a continuous wave field. We found that the applied static electric field affects the coupling between the bonding/antibonding interaction of the H_2 σ orbital with the Au/Ag cluster, with the negative z direction field strengthening the coupling. When applying continuous wave fields to the system, Ehrenfest dynamics results indicate that the H_2 activation not only depends on the frequencies of the excitation, but also depends on the

configuration between the Ag/Au cluster and the H_2 molecule. In addition, linear response TDDFT results show that Ag has more intense peaks than Au; however, both of these systems show similar trends in H_2 activation with selected excitations. The results indicate that oscillator strength is not the only factor that determines the activation properties, and the nuclear motions play an important role in this excitation-induced process.

In chapter 6, we implemented both the energy and gradient of the TDDFT-aas method. The TDDFT-aas method starts with a standard ground state DFT calculation to determine the density as well as the Kohn-Sham orbitals and orbital energies and then approximates the two-electron integral terms when solving the Casida equations. When approximating the two-electron integrals, TDDFT-aas calculates the K coupling matrix with a formula that involves γ_{AB} and atomic transition charges. Compared with TDDFT+TB, the γ_{AB} in TDDFT-aas is not dependent on tight-binding parameters such as chemical hardness. The absorption spectra and emission energy results indicate that TDDFT-aas will give similar results to TDDFT+TB, and they share similar computational costs. In addition, TDDFT-aas results show good agreement with TDDFT results, specifically for gold and silver nanoclusters.

In chapter 7, we have applied the DFT method to propose a nanoparticle growth mechanism starting from an Au(III)-chloride system. By applying ETS-NOCV theory, we found that the Au(III)-chloride system can bind strongly with diglyme through dative bonding, while the Au(I)-thiolate moiety tends to form dispersion-based bonding with diglyme. Based on our investigations, we can determine that the interaction between diglyme and gold motif becomes weaker when the oxidation state of gold is reduced from Au(III) to Au(I).

In chapter 8, we developed a type of machine-learning force field for the thiolate-protected gold nanocluster. The force fields show good agreement not only in predicting energies and geometries for the $Au_x(SCH_3)_y$ structures in the database but also in correctly predicting the energies and geometries for $Au_x(SCH_3)_y$ structures outside the database, which demonstrates good transferability of the force fields. In addition, the force fields can also be applied to high-temperature (up to 400 K) simulations.

Overall, in this dissertation, we applied electronic structure calculations and non-adiabatic dynamics to study the plasmon-induced process of the nanowire/nanocluster system. Our studies demonstrated that nonadiabatic dynamics is an advanced and useful technique to study the excited state properties of the system. The development of efficient nonadiabatic dynamics methods is a

fast-growing topic in the community, and future directions can be (1) Developing efficient approximation methods to simulate larger systems; (2) Developing more exact methods to better describe the quantum effects of the system; (3) Developing new tools to study strong light-matter interactions, for example, cavity techniques. In the TDDFT-aas project, we have shown the importance of developing approximation methods when studying larger-size nanoclusters to reduce computational costs. In the last project, we successfully incorporated the machine learning model into molecular dynamics, and our future directions are to explore the potential to improve our training process more efficiently and to improve our force fields to the level of reactive force fields.

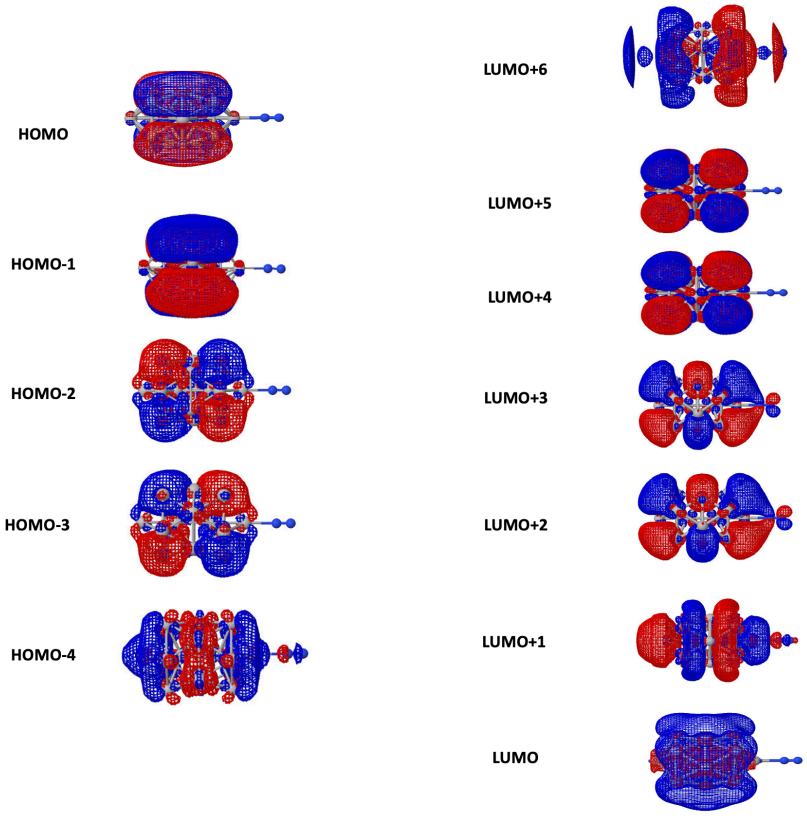
Appendix A - Supporting information for: Effects of field strength and silver nanowire size on plasmon-enhanced N_2 dissociation

Yuchen Wang, Christine M. Aikens*

Department of Chemistry, Kansas State University, Manhattan, KS 66506, USA

*Email: cmaikens@ksu.edu; Phone: 1-785-532-0954

Selected molecular orbitals of $Ag_{19}N_2^{+1}$



Appendix Figure A.1 Selected molecular orbitals (HOMO-4 to LUMO+6) of $Ag_{19}N_2^{+1}$.

Electronic transitions information for two main excitations of $Ag_{19}N_2^{+1}$systems

Appendix Table A.1 Dominant electronic transitions for two excitations in the $Ag_{19}N_2^{+1}$systems from LR-TDDFT calculations.

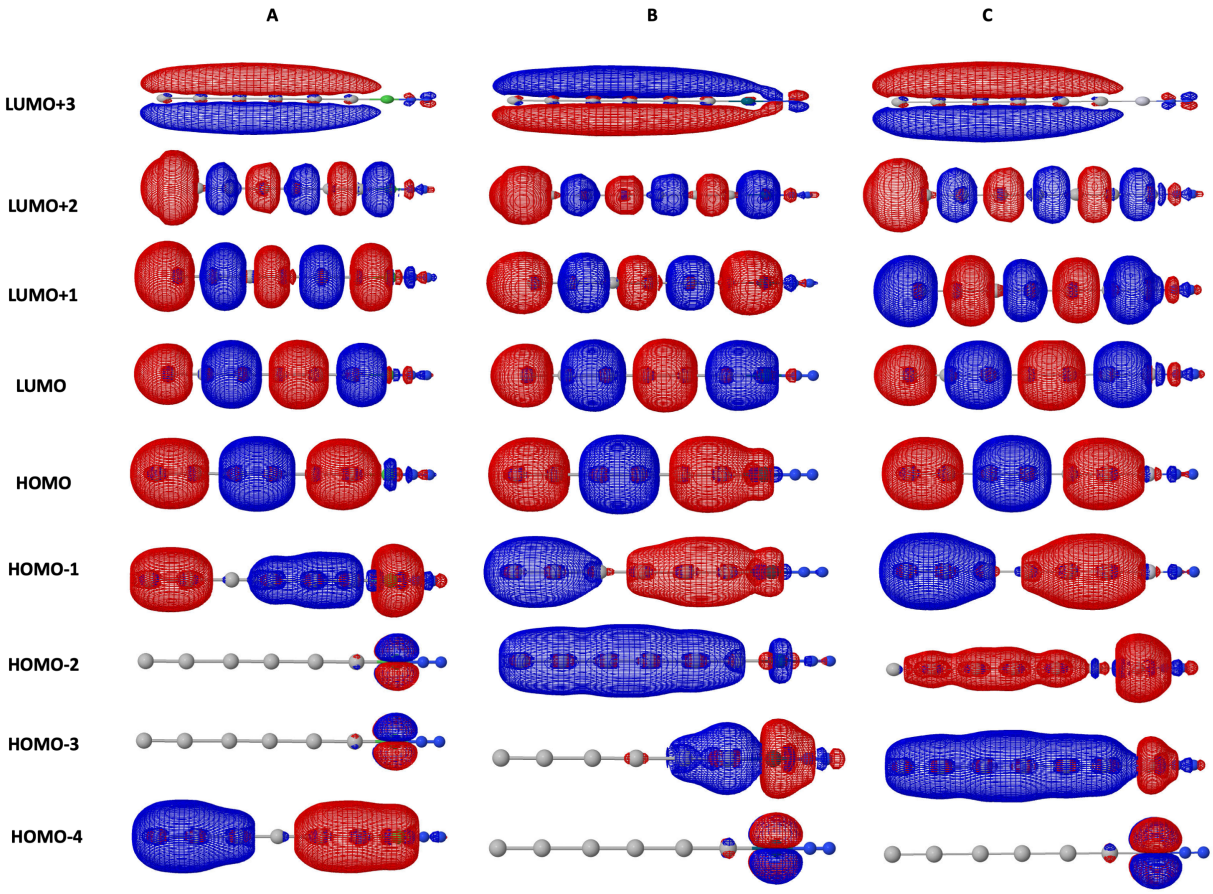
Excitation Energy (eV)		Main Electronic transitions	Contribution
3.86 eV	degenerate A	HOMO-2->LUMO+6	32.07%
		HOMO-3 ->LUMO+5	10.11%
		HOMO-2->LUMO+4	10.11%
	degenerate B	HOMO-3 ->LUMO+6	32.06%
		HOMO-2 ->LUMO+5	10.11%
		HOMO-3 ->LUMO+4	10.11%
3.94 eV		HOMO-3 ->LUMO+2	22.74%
		HOMO-2->LUMO+3	22.74%
		HOMO-4 ->LUMO+1	21.08%

Appendix B - Supporting information for: Effects of nanowire doping on plasmon-enhanced N_2 dissociation

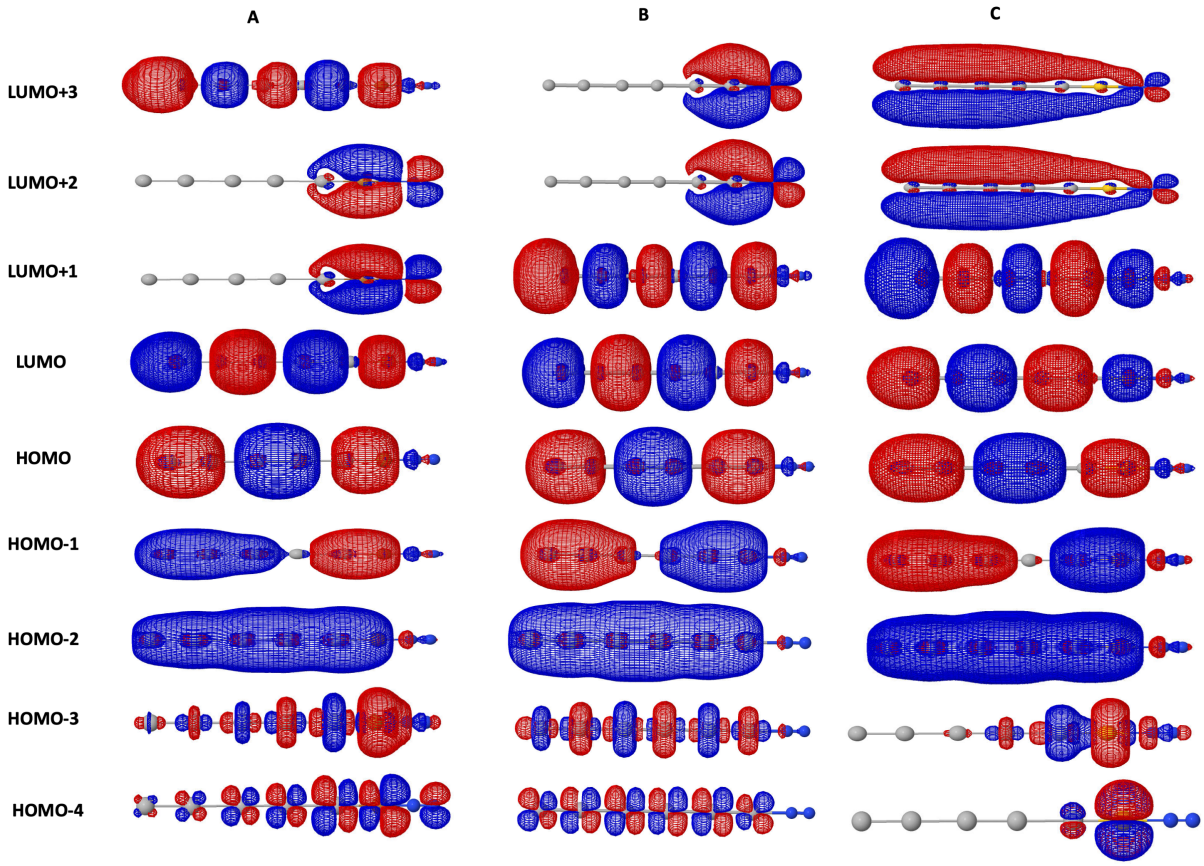
Yuchen Wang, Christine M. Aikens*

Department of Chemistry, Kansas State University, Manhattan, KS 66506, USA

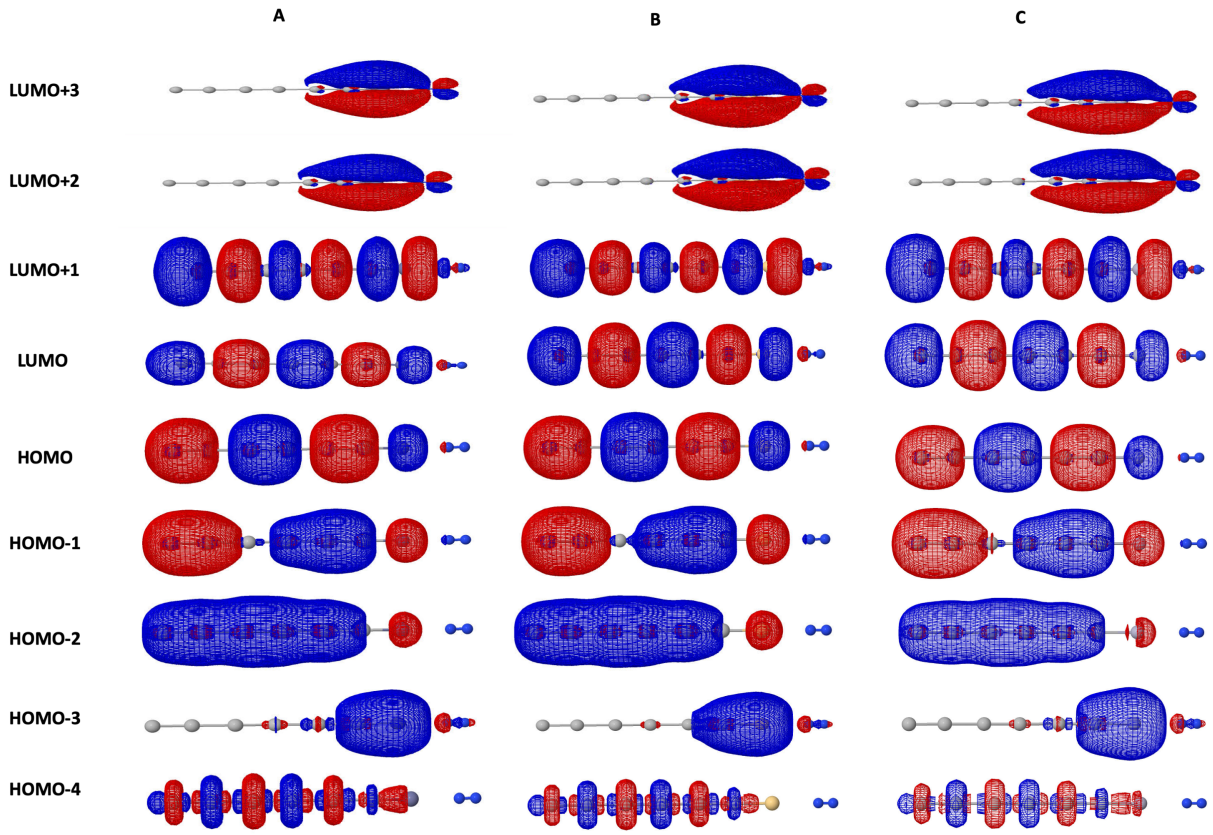
*Email: cmaikens@ksu.edu



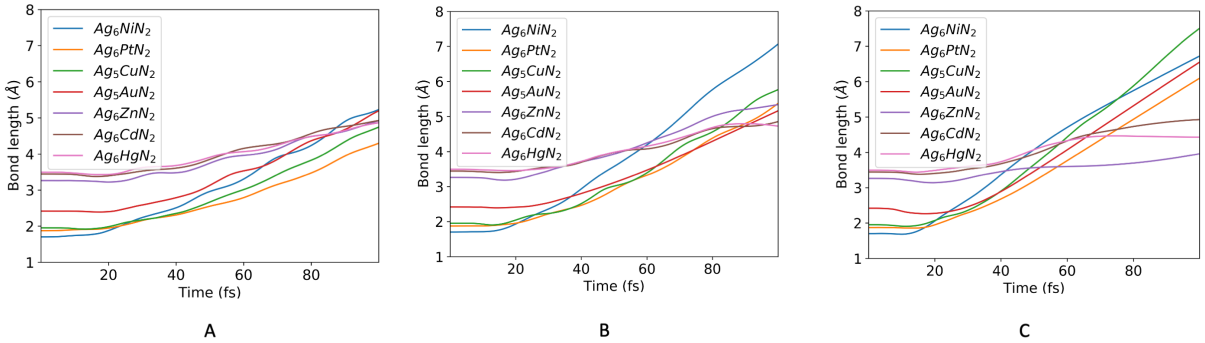
Appendix Figure B.1 Selected molecular orbitals (from HOMO-4 to LUMO+3) for A. Ag_6NiN_2; B. Ag_6PdN_2; C. Ag_6PtN_2 (isovalue =0.01).



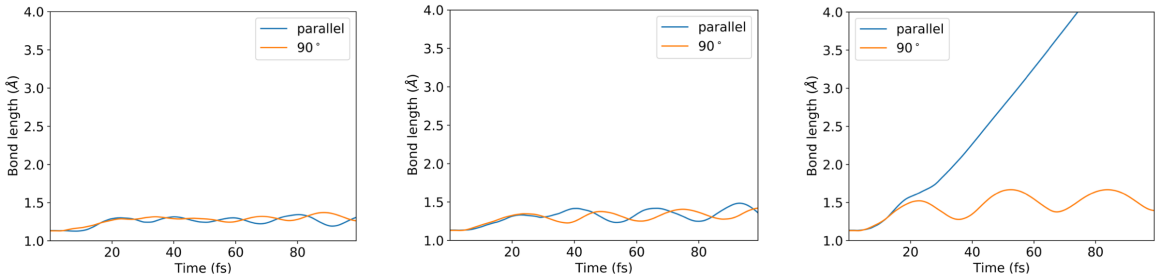
Appendix Figure B.2 Selected molecular orbitals (from HOMO-4 to LUMO+3) for A. Ag_5CuN_2; B. Ag_6N_2; C. Ag_5AuN_2 (isovalue =0.01).



Appendix Figure B.3 Selected molecular orbitals (from HOMO-4 to LUMO+3) for A. Ag_6ZnN_2; B. Ag_6CdN_2; C. Ag_6HgN_2. (isovalue =0.01).



Appendix Figure B.4 Variation of the doped metal-N1 distance during nonadiabatic dynamics using the A. 0.03 au, B. 0.04 au, and C. 0.05 au electric fields with frequencies corresponding to the longitudinal excitation of each parallel system.



Appendix Figure B.5 Comparison of Ehrenfest dynamics results between parallel structure and 90º structure of Ag_6PtN_2 system with A. 0.03 au, B. 0.04 au, and C. 0.05 au electric field strengths excited at the longitudinal excitation energy.

Appendix C - Supporting information for: Connectivity between static field and continuous wave field effects on excitation-induced H_2 activation

Yuchen Wang, Christine M. Aikens*

Department of Chemistry, Kansas State University, Manhattan, KS 66506, USA

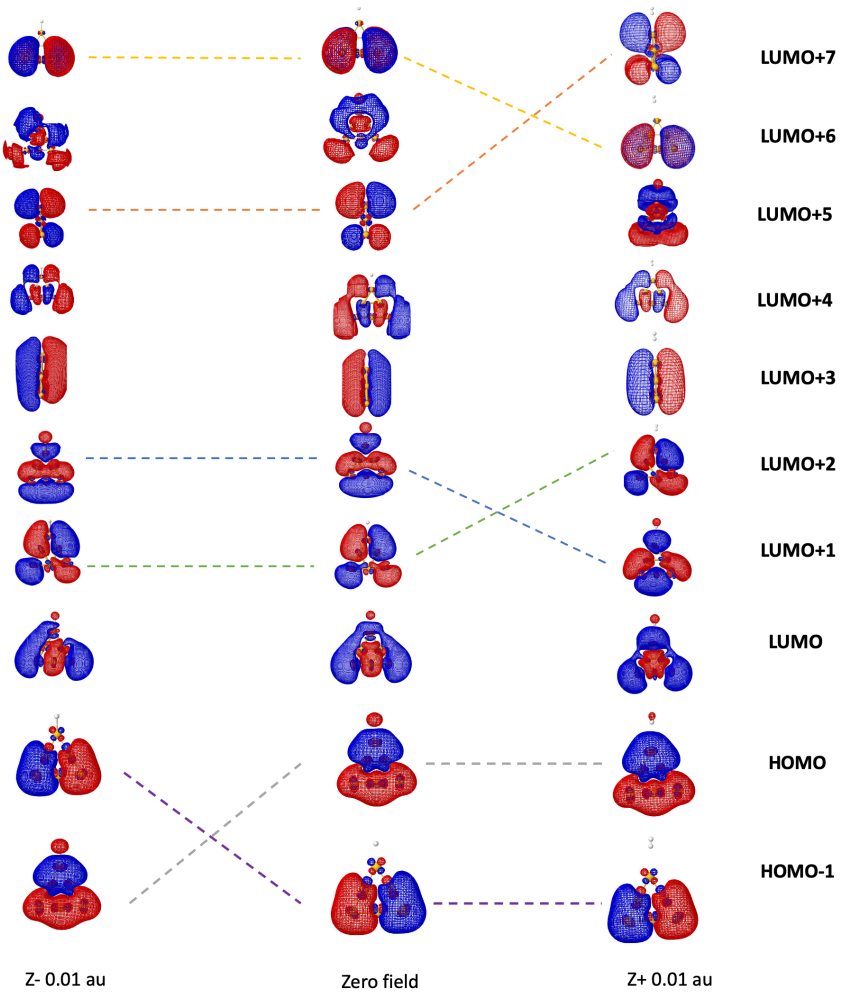
*Email: cmaikens@ksu.edu; Phone: 1-785-532-0954

Comparison between PBE and LC-ωPBE functionals

Appendix Table C.1 Selected bond lengths (Å) after ground state geometry optimizations using PBE and LC-ωPBE functionals.

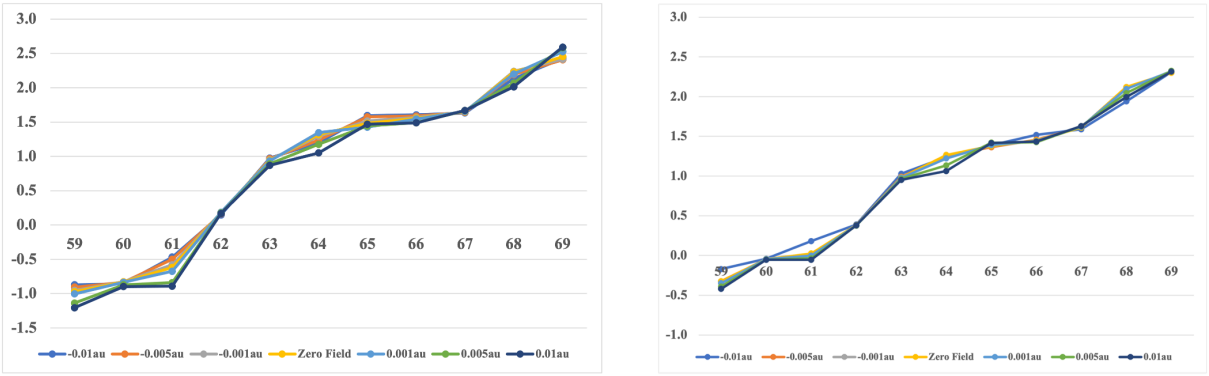
		PBE			LC-ωPBE		
		- 0.01 au	Zero field	0.01 au	- 0.01 au	Zero field	0.01 au
	H1-H2	0.76	0.76	0.76	0.77	0.75	0.75
Au_6H_2	Au6-H1	2.38	2.60	2.40	2.1	2.41	3.27
	Au6-H2	2.70	2.60	2.68	2.1	2.41	4.02
	H1-H2	0.76	0.75	0.75	0.76	0.75	0.74
Ag_6H_2	Ag6-H1	2.36	3.07	4.49	2.34	3.22	4.93
	Ag6-H2	2.36	3.07	4.49	2.34	3.22	4.93

Correlated MO diagram of Au_6H_2 system



Appendix Figure C.1 Selected molecular orbitals of optimized Au_6H_2 under different static applied electric fields. (All molecular orbitals are oriented using a front view, except the orbitals involving H_2 σ*, which are oriented using the side view for the sake of clarity.)

Orbital energies of selected orbitals

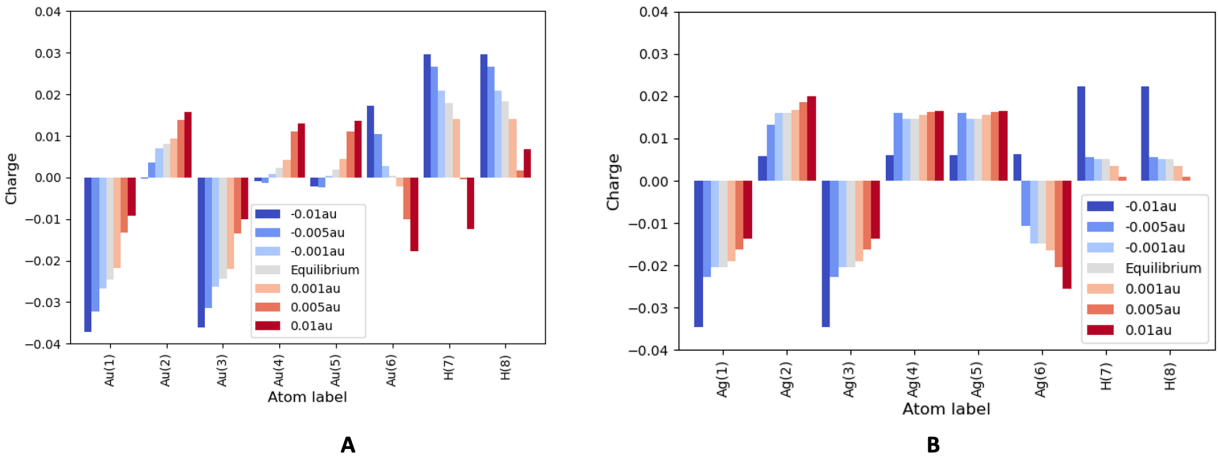


Appendix Figure C.2 Selected unoccupied orbital energies (59 denotes LUMO; 69 denotes LUMO+10) for A. Au_6H_2 and B. Ag_6H_2.

Appendix Table C.2 Selected orbital energies (in eV) for two systems. "Bonding" denotes the orbital that shows bonding character for the interaction between H_2 and the cluster. "Antibonding" denotes the orbital that shows antibonding character for the interaction between H_2 and the cluster. Electric fields are given in atomic units.

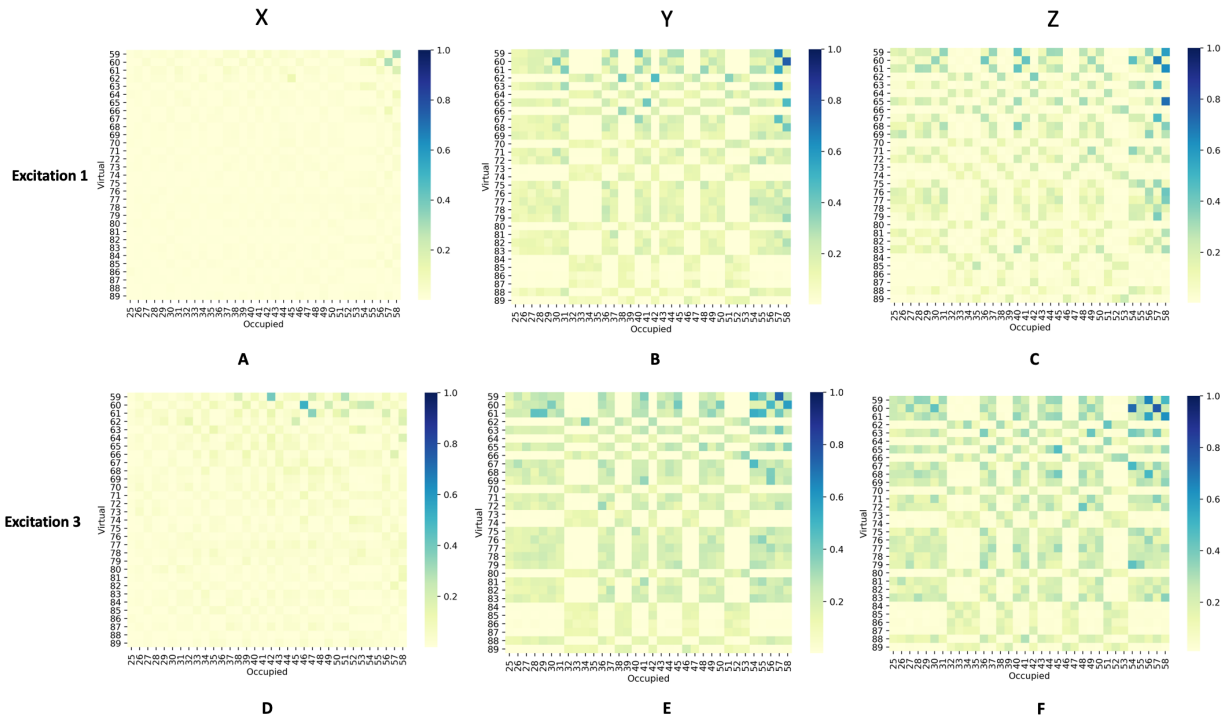
		Bonding	Antibonding	HOMO	LUMO
Au_6H_2	Z -0.01	-18.00	-8.53	-8.48	-0.87
	Z -0.005	-17.67	-8.54	-8.52	-0.90
	Z -0.001	-17.14	-8.56	-8.56	-0.95
	Zero field	-16.90	-8.58	-8.58	-0.97
	Z +0.001	-16.59	-8.60	-8.60	-1.00
	Z +0.005	-15.61	-8.67	-8.67	-1.14
	Z +0.01	-15.43	-8.67	-8.67	-1.21
		Bonding	**Antibonding**	**HOMO**	**LUMO**
Ag_6H_2	Z -0.01	-16.83	-6.88	-6.79	-0.17
	Z -0.005	-15.65	-6.97	-6.92	-0.32
	Z -0.001	-15.63	-6.95	-6.95	-0.33
	Zero field	-15.63	-6.95	-6.95	-0.33
	Z +0.001	-15.51	-6.95	-6.95	-0.35
	Z +0.005	-15.32	-6.94	-6.94	-0.39
	Z +0.01	-15.21	-6.91	-6.91	-0.42

Hirshfeld charge analysis

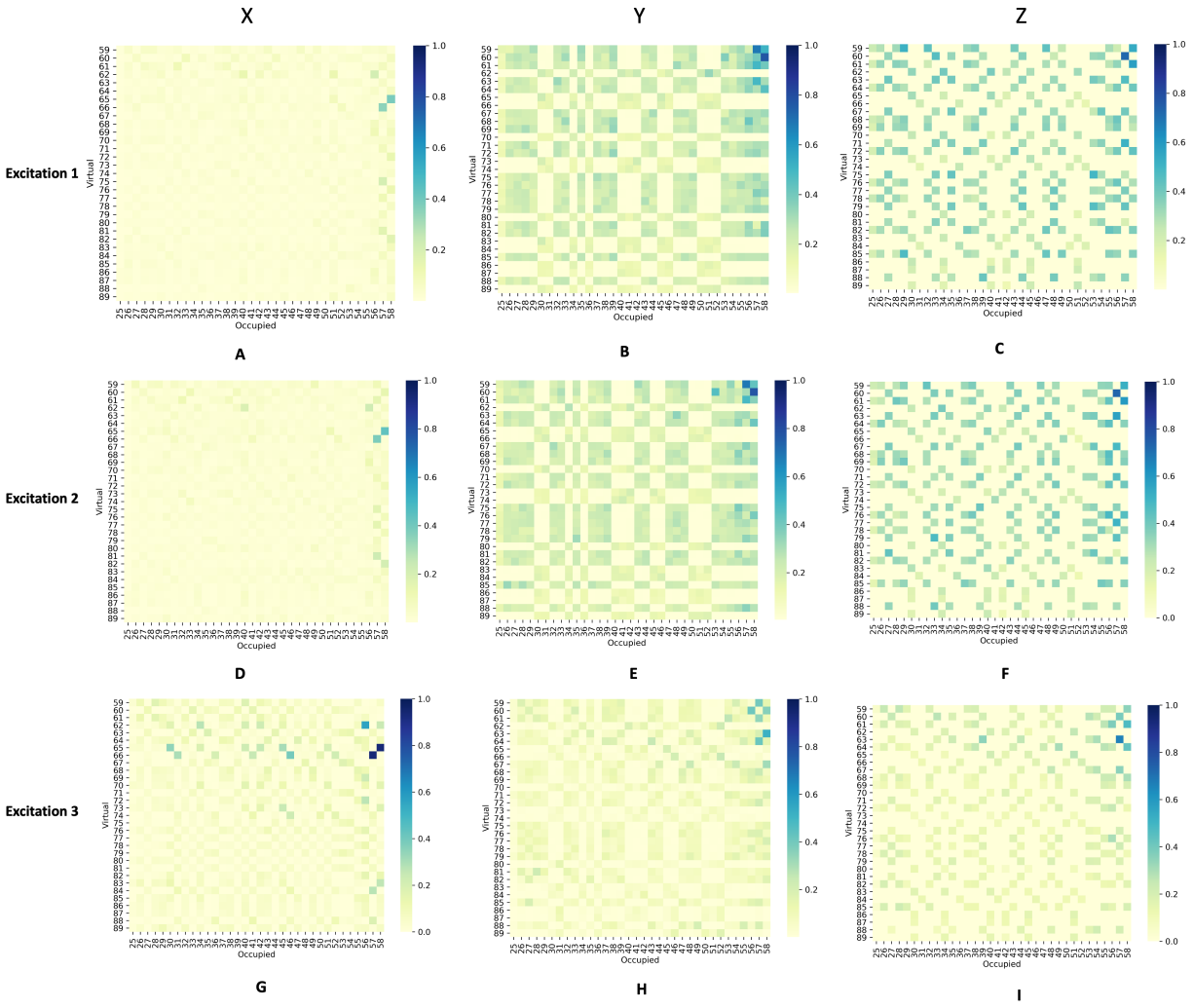


Appendix Figure C.3 Hirshfeld charge analysis for A. Au_6H_2 B. Ag_6H_2.

Electronic transitions in RT-TDDFT simulations



Appendix Figure C.4 Off-diagonal elements (Pov) analysis for Au_6H_2 in RT-TDDFT simulations; the x-axis represents the occupied orbital number and the y-axis represents the virtual orbital number. The color represents the maximum number of the Pov (MPov) during the electron dynamics in the first 40fs. The dark-blue color shows a relatively strong transition, while the light-yellow color shows a weak transition.



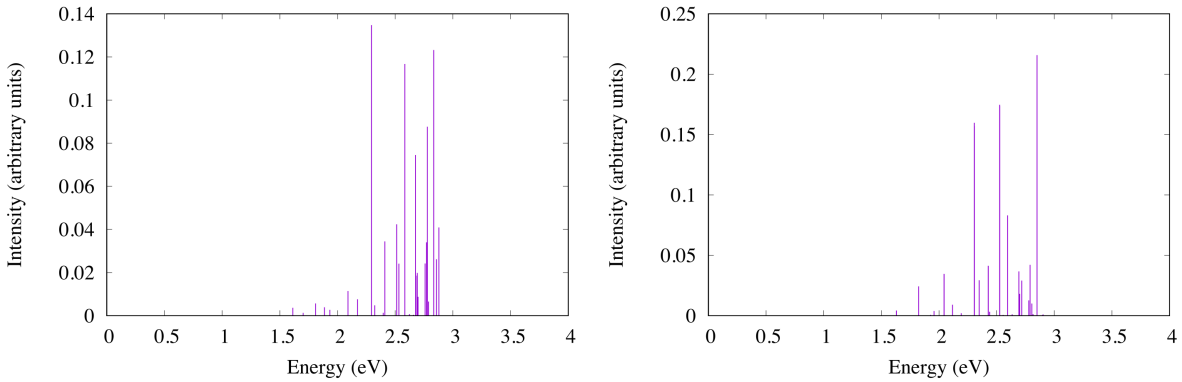
Appendix Figure C.5 Off-diagonal elements (Pov) analysis of Ag_6H_2 system in RT-TDDFT simulations; the x-axis represents the occupied orbital number and the y-axis represents the virtual orbital number. The color represents the maximum number of the Pov (MPov) during the electron dynamics in the first 40fs. The dark-blue color shows a relatively strong transition, while the light-yellow color shows a weak transition.

Appendix D - Supporting information for: Implementation of energy and gradient for the TDDFT- approximate auxiliary function (aas) method

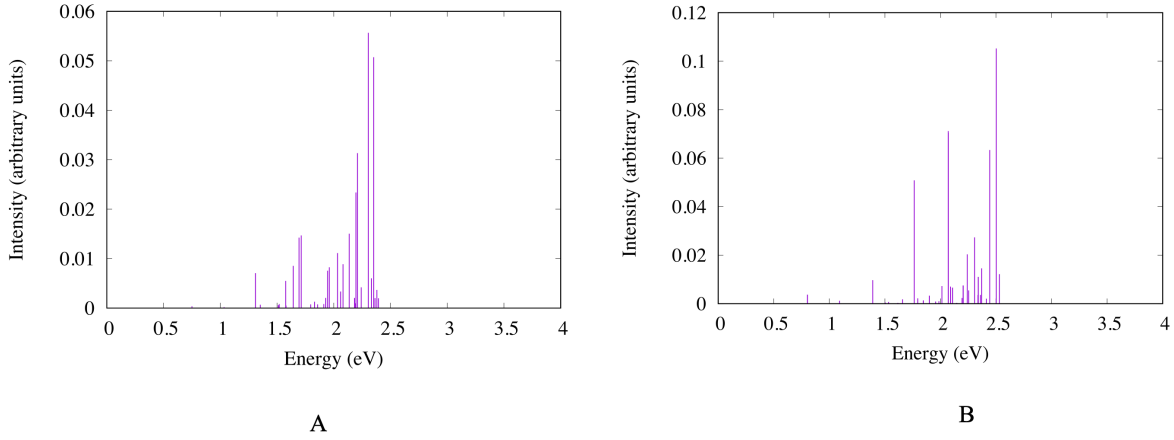
Yuchen Wang, Shana Havenridge, and Christine M. Aikens*

Department of Chemistry, Kansas State University, Manhattan, KS 66506, USA

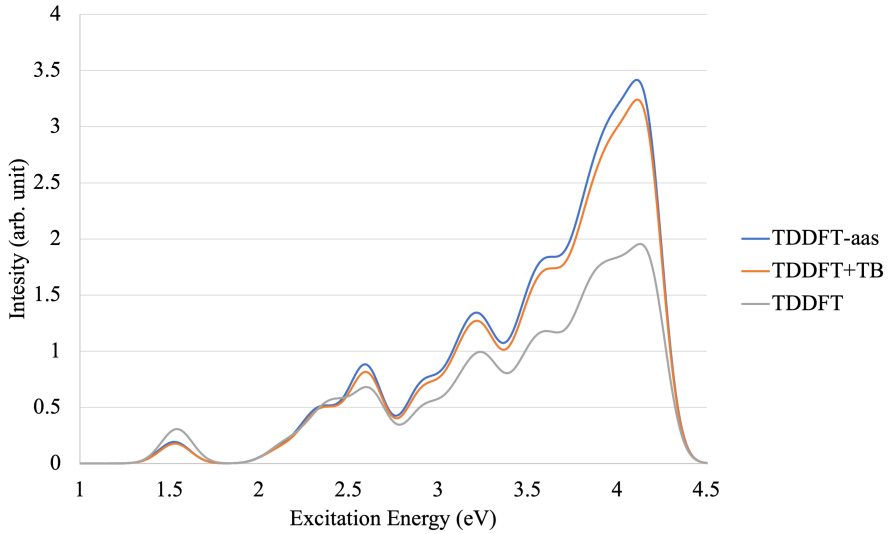
*Email: cmaikens@ksu.edu



Appendix Figure D.1 Stick spectra for the Au_{38}^{+4} system A. TDDFT-aas calculated results; B. TDDFT calculated results.



Appendix Figure D.2 Stick spectra for the Au_{55}^{+5} system A. TDDFT-aas calculated results; B. TDDFT calculated results.



Appendix Figure D.3 BP86 calculated results using TDDFT-aas, TDDFT+TB and TDDFT for the $Au_{25}(SCH_3)_{18}^-$ system.

Appendix Table D.1 Emission energy differences for five diatomic molecules (unit: eV) calculated at different level of theories; TDDFT failed in calculating the emission energy of H_2.

	Energy (TDDFT-aas) – Energy (TDDFT+TB)	Energy (TDDFT-aas) – Energy (TDDFT)
H_2	-2.27	N/A
Li_2	0.38	0.13
N_2	0.00	0.52
Cl_2	0.00	-0.25
HCl	0.00	-0.20

Appendix Table D.2 Emission energy differences among TDDFT-aas, TDDFT+TB, and TDDFT for organic molecules from the Thiel test set. Unit: eV

	TDDFT	TDDF-aas	TDDFT+TB	Energy (TDDFT-aas) – Energy (TDDFT+TB)	Energy (TDDFT-aas) – Energy (TDDFT)
Acetamide	1.13	1.00	1.02	-0.02	-0.13
Acetone	2.84	2.52	2.52	0.00	-0.32
Adenine	3.09	3.04	3.05	0.00	-0.05
Benzene	4.98	4.86	4.86	0.00	-0.12
Benzoquinone	1.71	1.51	1.51	0.00	-0.21
Butadiene	3.64	3.30	3.35	-0.05	-0.33
Cyclopentadiene	3.85	3.41	3.60	-0.19	-0.44
Cyclopropene	3.85	3.41	3.60	-0.19	-0.44
Cytosine	1.47	1.58	1.58	0.00	0.12
Ethene	6.18	5.89	6.17	-0.28	-0.29
Formaldeyde	3.21	2.86	2.86	0.00	-0.34
Furan	5.27	4.70	4.98	-0.28	-0.57
Hexatriene	4.11	3.93	4.14	-0.21	-0.18
Imidazole	2.13	2.05	2.05	0.00	-0.09
Naphthalene	3.63	3.40	3.50	-0.11	-0.23
Norbornadiene	1.85	1.71	1.80	-0.09	-0.14
Octatetraene	3.52	3.41	3.57	-0.16	-0.11
Propanamide	1.15	1.02	1.05	-0.03	-0.13
Pyrazine	3.37	3.08	3.08	0.00	-0.29
Pyridazine	1.71	1.63	1.63	0.00	-0.08
Pyridine	3.10	3.31	3.31	0.00	0.21
Pyrimidine	2.96	2.77	2.77	0.00	-0.19
Tetrazine	2.28	2.14	2.18	-0.04	-0.14
Thymine	2.69	2.58	2.58	0.00	-0.11
Triazine	2.43	2.35	2.35	0.00	-0.09
Uracil	2.55	2.45	2.45	0.00	-0.10

Appendix E - Supporting Information for: Effects of diglyme on Au nanocluster formation: mechanism, ^{1}H NMR, and bonding

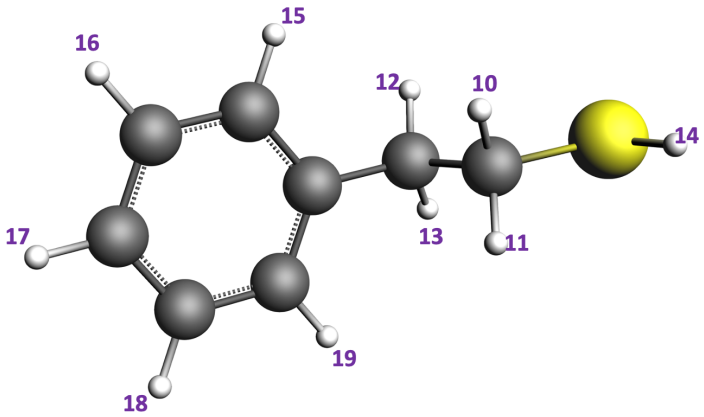
Yuchen Wang,[1] Alice Li,[1,2] Jacqueline Pinkerton,[1,3] Christine M. Aikens[1,*]

4. Department of Chemistry, Kansas State University, Manhattan, KS 66506, USA
5. Department of Chemistry and Biochemistry, Bates College, Lewiston, ME 04240, USA
6. Natural Sciences Programs, Pensacola Christian College, Pensacola, FL 32503, USA

NMR spectra results

1. *Pure HPET*

Chemical shifts of protons on a pure HPET molecule (Figure E.1) were calculated at the same level of theory as diglyme. NMR spectra results show that chemical shifts of protons on the CH_2SH group are located from 2.58 ppm to 2.85 ppm, with the CH_2 protons centered at 2.8 ppm, and chemical shifts of protons on the phenyl group range from 7.41 ppm to 7.57 ppm (Table E.1). The experimental ^{1}H NMR spectrum of free HPET has signals located from 2.75 ppm to 3.25 ppm and 7.00 ppm to 7.50 ppm.[1] The calculated results show a good agreement with the experimental results.



Appendix Figure E.1 Labeled hydrogen atoms on HPET. Key: sulfur = light yellow, carbon = grey, and hydrogen = white.

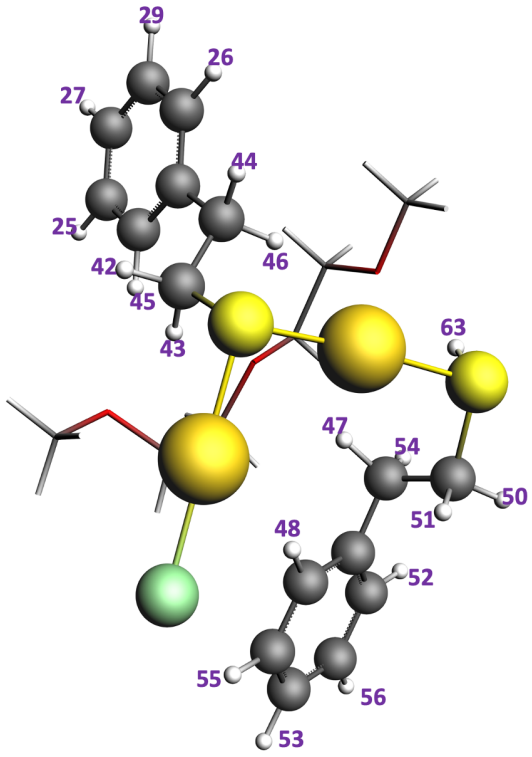
Appendix Table E.1 Calculated ^{1}H NMR results for hydrogen atoms in HPET.

Atom Label	δ (ppm)
10	2.85
11	2.83
12	2.79
13	2.76
14	2.58
15	7.57
16	7.52
17	7.41
18	7.52
19	7.55

2. PET/HPET on the gold motif

NMR calculations of protons on PET and HPET in the gold-containing species (AuCl)PET(AuHPET)]dg (Figure E.2) were investigated as well. The ^{1}H NMR spectra show that protons on the CH_2 group are calculated to have chemical shifts ranging from 2.86 ppm to 4.81 ppm, which are more downfield than pure HPET, and that downfield shift can be observed in experimental ^{1}H NMR as well.[1] Protons on the phenyl group have chemical shifts ranging from 7.37 ppm to 8.87 ppm (Table E.2). The SH proton has a chemical shift of 6.25 ppm, which is significantly shifted from that of pure HPET. Atom 42 shows the lowest chemical shift, and it is located on the CH_2 group in PET. Atom 44 and atom 51 show a calculated chemical shift of 2.98 ppm, and both are located on the CH_2 group in HPET/PET as well. Atom 45, 48, and 55 have calculated chemical shifts above 8 ppm, and they are all located in the phenyl group. Atom 45 is oriented towards the oxygen, atom 48 is oriented towards the gold atom and atom 55 is pointed to the chloride atom. We can observe the downfield shift of protons in the phenyl group compared with the ^{1}H NMR spectrum of pure HPET; however, the downfield shift of phenyl protons was not observed in the experimental ^{1}H NMR spectrum of the gold nanocluster. This might be due to two reasons: 1. The chloride atom on (AuCl)PET(AuHPET)]dg will affect the chemical shifts, but chloride is not present on the larger nanocluster.[1] 2. The gold motif and gold nanocluster will show different ligand environments that lead to the differences in their ^{1}H NMR spectra. Overall, both the calculated ^{1}H NMR spectra of pure HPET and HPET in the gold motif show a reasonable

agreement with the reported experimental ^{1}H NMR spectra results considering the difference in environment between the PET groups in these species.[1]



Appendix Figure E.2 Hydrogen atoms on PET and HPET in (AuCl)PET(AuHPET)]dg. Diglyme is displayed with a stick model. Key: gold = gold, sulfur = light yellow, chlorine = green, carbon = grey, oxygen = red and hydrogen = white.

Appendix Table E.2 Calculated ^{1}H NMR results for hydrogen atoms on PET and HPET in (AuCl)PET(AuHPET)]dg.

Atom Label	δ (ppm)
25	7.49
26	7.4
27	7.37
29	7.46
42	2.86
43	4.68
44	2.98
45	8.52
46	3.81
47	4.81
48	8.87
50	3.19
51	2.98
52	7.42
53	7.51
54	3.33
55	8.19
56	7.49
63	6.25

ETS-NOCV theory

The principal idea of extended transition state - natural orbitals for chemical valence (ETS-NOCV) theory[2–5] is the decomposition of total bonding energy into each specific interaction between two fragments. Initially, the molecular system will be split into two fragments. In our research, the molecular system will be divided into the diglyme part and the gold-containing part.

The interaction energy between two fragments can be considered as the sum of electrostatic interaction (ΔE_{elstat}), Pauli repulsion (ΔE_{Pauli}), orbital interaction (ΔE_{orb}), dispersion interaction correction (ΔE_{disp}), and solvation energy (ΔE_{solv}) because the Grimme3 correction[6,7] and Conductor-like Screening Model (COSMO)[8–10] have been added in our DFT calculations (Eq S1).

$$\Delta E_{\text{int}} = \Delta E_{\text{elstat}} + \Delta E_{\text{Pauli}} + \Delta E_{\text{orb}} + \Delta E_{\text{disp}} + \Delta E_{\text{solv}} \qquad \text{(S1)}$$

To calculate the orbital interaction (ΔE_{orb}), the Natural Orbitals for Chemical Valence (NOCV) approach can be derived from Nalewajski-Mrozek valence theory.[2–5]

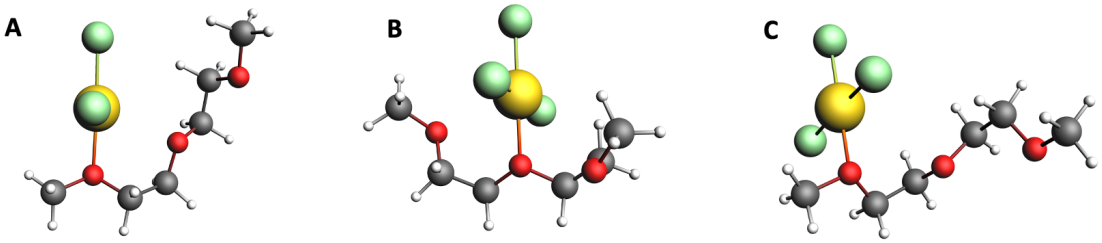
The orbital interaction energy can be written as Eq S2:

$$\Delta E_{\text{orb}} = \sum \Delta E_k^{\text{orb}} = \sum \nu_k (-F_{-k}^{TS} + F_k^{TS}) \qquad \text{(S2)}$$

where $-F_{-k}^{TS}$ and F_k^{TS} are diagonal transition-state Fock matrix elements (Kohn-Sham matrix elements for DFT), and $-\nu_k$ and ν_k denote their corresponding eigenvalues.

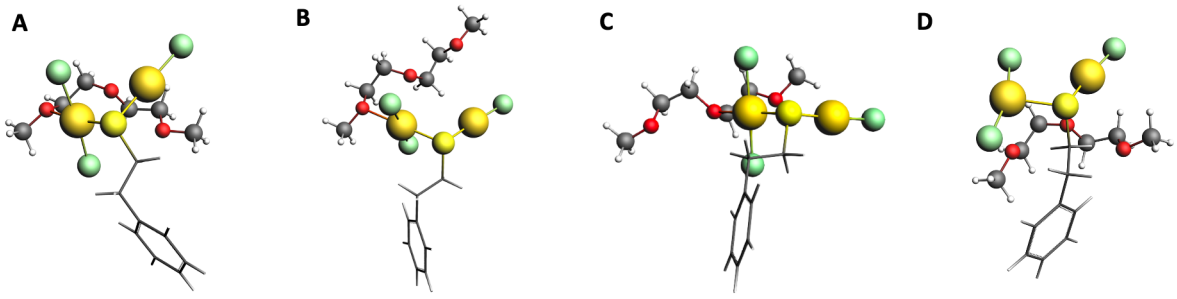
Isomers

Adding diglyme into the modeled systems increases the number of degrees of freedom. Therefore, we performed geometry optimizations starting with various initial structures. The results are shown as below, and the lowest energy isomers are considered in the reaction pathway. Due to the flexibility of the diglyme and PET ligands, it should be noted that the systems present experimentally may vary dynamically from the lowest energy isomer found here.



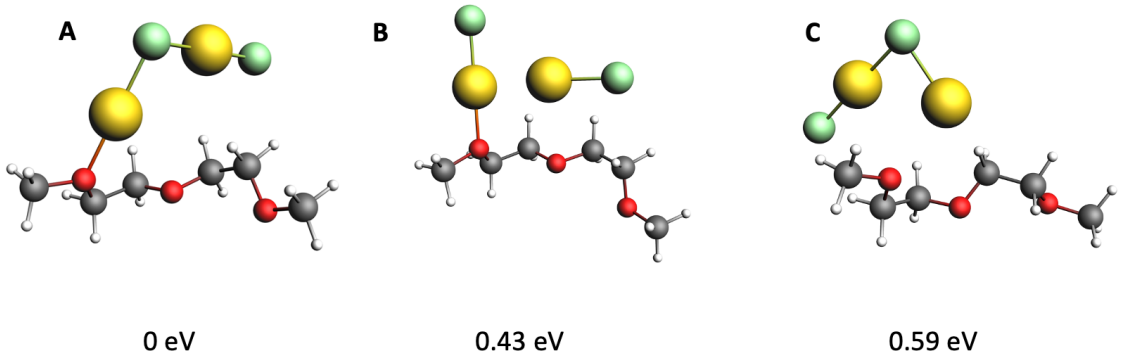
0 eV 0.002 eV 0.16 eV

Appendix Figure E.3 Optimized geometries for ($AuCl_3$)dg isomers and their relative energies.

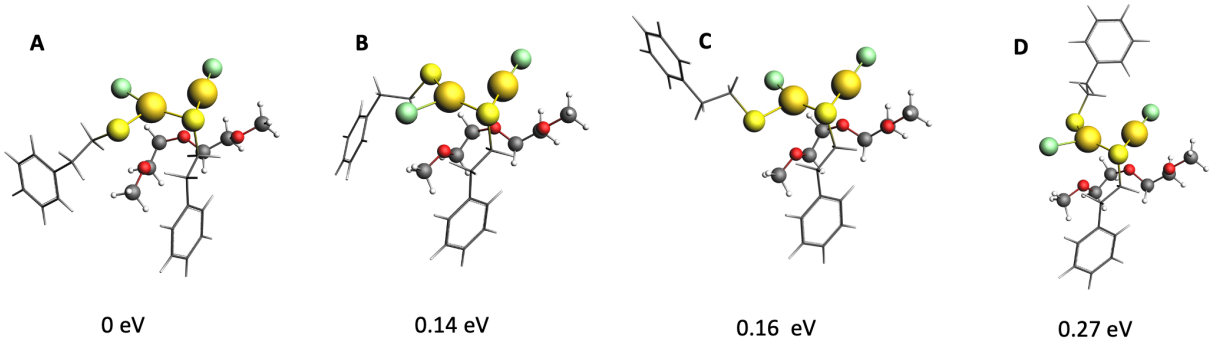


0 eV 0.19 eV 0.20 eV 0.53 eV

Appendix Figure E.4 Optimized geometries for $(AuCl_2)PET(AuCl)dg$ isomers and their relative energies.

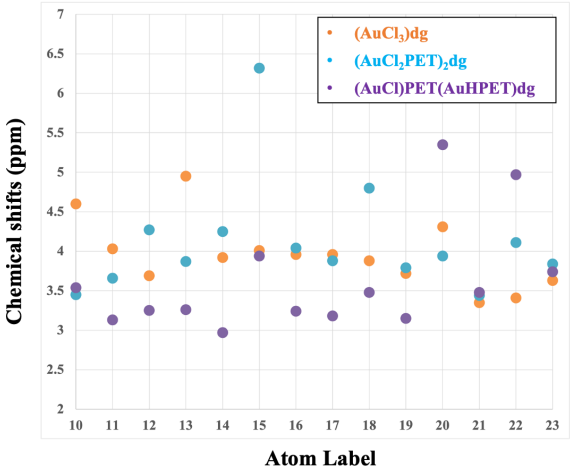


Appendix Figure E.5 Optimized geometries for $(AuCl)_2dg$ isomers and their relative energies.



Appendix Figure E.6 Optimized geometries for $(AuClPET)_2dg$ isomers and their relative energies.

Graphical version of chemical shift results



Appendix Figure E.7 Graphical form of chemical shift results for $(AuCl_3)dg$ (orange), $(AuCl_2PET)_2dg$ (blue) and (AuCl)PET(AuHPET)dg (purple) systems.

Reaction free energies

The reaction free energy calculations are summarized in Table E.3. Pathway 1 shows more negative reaction energies than Pathway 2, which is consistent with Table 7.2. However, reaction free energy for 1C shows a slightly positive reaction energy compared with the reaction energy for 1C in Table 7.2. This reaction may be affected by explicit interactions with solvent or other species in the reaction, concentration effects, etc.

Appendix Table E.3 Calculated free energies (eV) at 298.15 K for each step in the investigated reaction pathways.

Reaction Index	Free energy (eV)
1A	-0.60
2A	-0.31
3A	-0.53
1B	-0.77
2B	-0.34
3B	-1.36
1C	0.16
2C	-0.38
3C	-0.88
1D	0.44

References

(1) Anderson, I. D.; Wang, Y.; Aikens, C. M.; Ackerson, C. J. An Ultrastable Thiolate/Diglyme Ligated Cluster: $Au_{20}(PET)_{15}(DG)_2$. *Nanoscale* **2022**, *14* (25), 9134–9141.

(2) Michalak, A.; DeKock, R. L.; Ziegler, T. Bond Multiplicity in Transition-Metal Complexes: Applications of Two-Electron Valence Indices. *J. Phys. Chem. A* **2008**, *112* (31), 7256–7263.

(3) Nalewajski, R. F.; Mrozek, J.; Michalak, A. Two-Electron Valence Indices from the Kohn-Sham Orbitals. *Int. J. Quant. Chem.* **1997**, *61* (3), 589–601.

(4) Mitoraj, M. P.; Michalak, A.; Ziegler, T. A Combined Charge and Energy Decomposition Scheme for Bond Analysis. *J. Chem. Theory Comput.* **2009**, *5* (4), 962–975.

(5) Mitoraj, M. P.; Michalak, A.; Ziegler, T. On the Nature of the Agostic Bond between Metal Centers and β-Hydrogen Atoms in Alkyl Complexes. An Analysis Based on the Extended Transition State Method and the Natural Orbitals for Chemical Valence Scheme (ETS-NOCV). *Organometallics* **2009**, *28* (13), 3727–3733.

(6) Grimme, S.; Ehrlich, S.; Goerigk, L. Effect of the Damping Function in Dispersion Corrected Density Functional Theory. *J. Comput. Chem.* **2011**, *32* (7), 1456–1465.

(7) Grimme, S.; Antony, J.; Ehrlich, S.; Krieg, H. A Consistent and Accurate *Ab Initio* Parametrization of Density Functional Dispersion Correction (DFT-D) for the 94 Elements H-Pu. *J. Chem. Phys* **2010**, *132* (15), 154104.

(8) Klamt, A.; Schüürmann, G. COSMO: A New Approach to Dielectric Screening in Solvents with Explicit Expressions for the Screening Energy and Its Gradient. *J. Chem. Soc., Perkin Trans. 2* **1993**, No. 5, 799–805.

(9) Klamt, A. Conductor-like Screening Model for Real Solvents: A New Approach to the Quantitative Calculation of Solvation Phenomena. *J. Phys. Chem.* **1995**, *99* (7), 2224–2235.

(10) Klamt, A.; Jonas, V. Treatment of the Outlying Charge in Continuum Solvation Models. *J. Chem. Phys* **1996**, *105* (22), 9972–9981.

Coordinate information

($AuCl_3$)dg

O	-0.44767796	-1.30679516	1.33525185
C	0.49704620	-1.86992499	2.26763170
C	-1.53802503	-2.19020682	1.05652907
C	-2.22691979	-1.70742837	-0.19443758
C	1.66057776	-0.91752742	2.40244672
O	-1.38553428	-2.04923299	-1.36308987
O	1.23448552	0.27060677	3.08068080
C	-2.08221612	-1.79260019	-2.63100368
C	2.24259250	1.28929721	3.02545920
H	-2.30501482	-0.72464526	-2.73332649
H	-1.41079077	-2.13280594	-3.42417773
H	-2.99993150	-2.39213610	-2.62189743
H	-2.39346599	-0.62094824	-0.18745266
H	-3.17546323	-2.23953455	-0.34402137
H	-1.17586659	-3.22159122	0.90096312
H	-2.26614599	-2.19467591	1.88739821
H	0.86779825	-2.83557554	1.88131330
H	0.00965334	-2.03715827	3.24420191
H	2.47232478	-1.41673604	2.96507215
H	2.04688047	-0.66885129	1.39741298
H	3.18136989	0.95539463	3.50203663
H	2.45750783	1.57868154	1.98176172
H	1.85216970	2.15766679	3.56908941
Cl	2.73378630	-0.31265237	-1.36761558
Au	0.59957905	-1.16594054	-1.31992719
Cl	1.41080149	-3.34664224	-1.07706899
Cl	-0.33851798	0.95802354	-1.57598267

$(AuCl_2PET)_2$dg

O	-0.44724737	0.49483346	-0.29115063
C	0.47290801	1.43717213	0.35056030
C	-0.84226960	-0.62361786	0.55380243
C	-2.05664034	-0.28767357	1.38994310
C	1.90740391	0.95684249	0.29244037
O	-3.13240552	0.26698594	0.57556980
O	2.38064486	1.12073714	-1.05021046
C	-4.39606330	0.27203284	1.30527073
C	3.58354519	0.36984016	-1.28371971
H	-4.24130237	0.76510556	2.27387876
H	-4.75214028	-0.75727795	1.44747907
H	-5.09961502	0.84884356	0.69799335
H	-2.39241236	-1.21659493	1.87700770
H	-1.84113524	0.46679236	2.16159577
H	-1.05708596	-1.45740438	-0.11895102
H	-0.01983440	-0.92761110	1.21646468
H	0.14590715	1.58347032	1.38806305
H	0.35243798	2.37324366	-0.20688076
H	2.52217590	1.54910634	0.99431468
H	1.97096444	-0.10476683	0.59293359
H	4.36903266	0.64153711	-0.55917380
H	3.38114977	-0.71251889	-1.22735974
H	3.92353137	0.62735051	-2.29252872
Au	0.04773686	-0.00479445	-2.49146671
H	7.42534285	2.17979472	-6.71447388
Cl	-0.49928934	2.21257997	-2.97218574
Cl	0.85497212	-2.11414028	-1.89678291
Au	-3.41534796	-0.23808026	-1.62937816
H	5.50712340	3.59039434	-7.46306177
Cl	-4.02429003	2.00028814	-1.83413782

Cl	-3.12824581	-2.52791209	-1.20906187
H	7.02491295	0.30445210	-5.11803323
C	4.90319189	0.67332452	-4.97540448
C	6.19311152	0.92802123	-5.44944635
C	6.41874237	1.97958520	-6.34465300
C	5.34343398	2.76953397	-6.76306575
C	4.05394488	2.50856252	-6.28819099
C	3.81373217	1.46154122	-5.38519840
C	2.41491232	1.20001860	-4.87249276
C	1.95681771	-0.24598219	-5.10551554
S	0.19229117	-0.56529925	-4.75083662
H	2.02503559	-0.50327620	-6.17700311
H	2.56870071	-0.97074039	-4.55280665
H	1.70437415	1.88715241	-5.35127324
H	2.35762041	1.41704050	-3.79331496
H	4.74693090	-0.15500520	-4.28205055
H	3.21934702	3.12863703	-6.62170356
H	-1.41678410	5.04178741	-8.78318506
H	0.07184723	3.93398984	-7.11353888
H	-3.65148787	4.05758180	-9.28839096
C	-3.40865471	2.40669693	-7.91584177
C	-2.99346107	3.57723159	-8.56246510
C	-1.74048226	4.12976732	-8.27952702
C	-0.90572749	3.50635397	-7.34326944
C	-1.32208793	2.34010253	-6.69915288
C	-2.57527741	1.77188999	-6.98455492
C	-3.01151489	0.51217043	-6.26501705
C	-3.33306132	0.84888652	-4.79341556
S	-3.53314651	-0.74190743	-3.89671930
H	-2.49539348	1.39194172	-4.34197344
H	-4.24426893	1.45157140	-4.71413522

H	-2.19753104	-0.22745989	-6.30038802
H	-0.67963670	1.85920510	-5.95824488
H	-3.88839196	0.07024770	-6.75862152
H	-4.38832742	1.97974625	-8.14083840

(AuCl)PET(AuHPET)dg

O	-2.57751799	-1.32032001	-3.55246806
C	-1.67308700	-2.20769811	-2.87339211
C	-3.46674204	-0.69798201	-2.61936688
C	-4.32974720	0.32684100	-3.31409907
C	-0.73316598	-2.83358407	-3.87370205
O	-5.20019197	-0.31916001	-4.25998688
O	0.23967899	-1.85723400	-4.27141714
C	-5.98577690	0.63873702	-4.98293781
C	1.15164006	-2.38513207	-5.24355698
H	-6.56188822	0.08256600	-5.73268318
H	-5.34092093	1.36939597	-5.50000811
H	-6.67548418	1.17876303	-4.31223202
H	-4.92586184	0.86265600	-2.55231690
H	-3.69273901	1.06239998	-3.83473206
H	-4.09961319	-1.46098804	-2.12779593
H	-2.89236808	-0.17761999	-1.82976103
H	-2.23431993	-3.00645804	-2.35556197
H	-1.09215200	-1.65093100	-2.11459899
H	-0.24070700	-3.71317911	-3.41963696
H	-1.30055404	-3.19249797	-4.75483608
H	1.70828199	-3.24960589	-4.84235001
H	0.61732298	-2.71116400	-6.15524197
H	1.85065997	-1.58002305	-5.49737215
Au	-1.42989004	-3.91072989	-7.46611500
H	0.21554799	2.15671110	-3.10656810

H	-2.98249698	3.18564892	-6.76795578
H	-0.45653099	4.52022886	-3.53766203
Au	-4.44267893	-2.42129207	-6.72117281
H	-2.06145692	5.02622890	-5.38207483
C	-4.51590204	-4.04901981	-3.58901691
C	-5.63217497	-4.51707602	-4.52751303
C	-2.28073406	2.95737004	-5.96246481
C	-1.76360095	3.99561310	-5.18122196
C	-0.86394203	3.71297193	-4.14832878
C	-0.48814401	2.38649607	-3.90870094
C	-1.01061702	1.34848404	-4.68549395
C	-1.91910195	1.62202001	-5.72276211
C	-2.56882906	0.51345003	-6.52438688
C	-1.64271605	-0.65635598	-6.84093809
S	-2.50829291	-1.90669799	-7.92642403
Cl	-0.36661300	-5.93496418	-7.02679586
H	-0.75953501	-0.34536001	-7.41422081
H	-1.31977797	-1.15709496	-5.92607212
H	-2.99083900	0.92795199	-7.45236683
H	-0.72383499	0.31891501	-4.46891880
H	-3.41508198	0.10549500	-5.94480991
H	-3.90145206	-3.29723310	-4.10934401
H	-2.54364896	-5.25315809	-5.01926517
S	-6.35711813	-3.12394691	-5.53011322
H	-6.46512222	-4.98547220	-3.98883295
H	-5.25897980	-5.22019815	-5.28199387
H	-4.50174713	-5.37630510	-1.17621005
H	-1.26672995	-8.09575462	-2.04699707
H	-4.96404219	-3.54561305	-2.72031808
H	-1.04647303	-7.07768822	-4.33147383
H	-3.00507402	-7.23635578	-0.48030999

C	-3.75093508	-5.76051378	-1.87049997
C	-2.65758204	-5.68993521	-4.02390909
C	-1.80775595	-6.72532511	-3.63375092
C	-2.90563393	-6.80447912	-1.47756803
C	-1.93085897	-7.28747797	-2.35718489
C	-3.63311601	-5.19090891	-3.14592910
H	-6.24699879	-2.16028690	-4.55905390

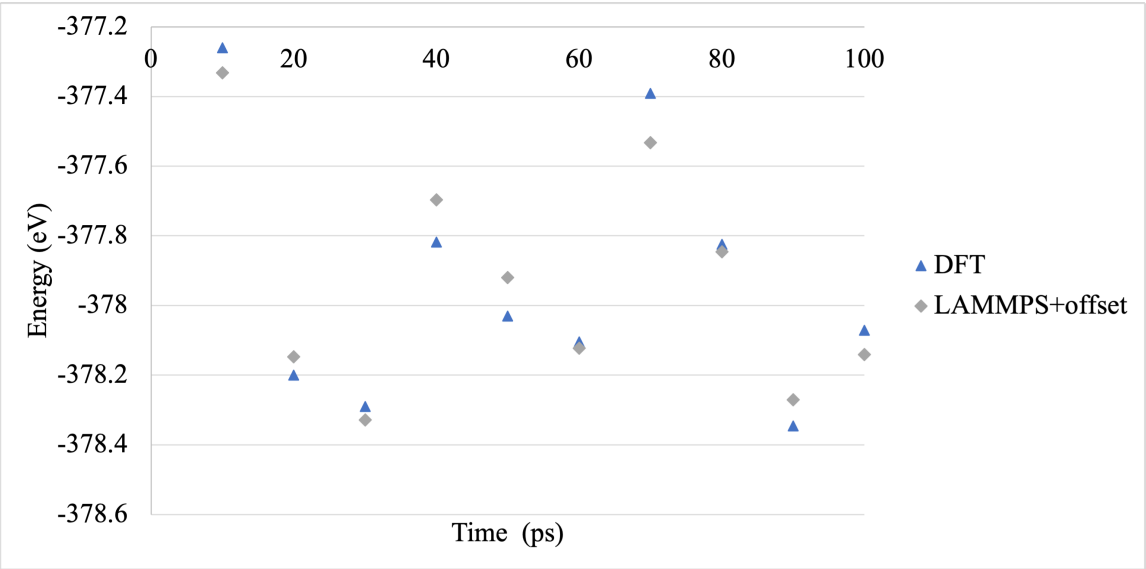
Appendix F - Supporting information for: A Gaussian process approach to constructing transferable force fields for gold thiolate-protected nanoclusters

Yuchen Wang[1], D. Sulalith N. D. Samarasinghe[1], Hao Deng[2], Bin Liu[2] and Christine M. Aikens[1,*]

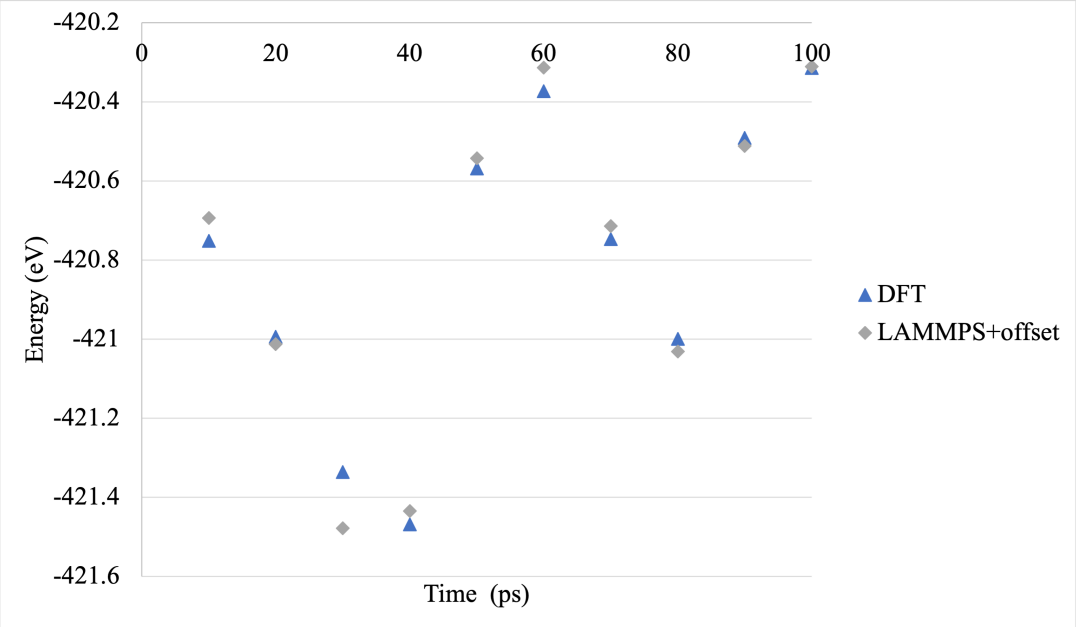
1. Department of Chemistry, Kansas State University, Manhattan, KS 66506, USA
2. Tim Taylor Department of Chemical Engineering, Kansas State University, Manhattan, KS 66506, USA

* cmaikens@ksu.edu

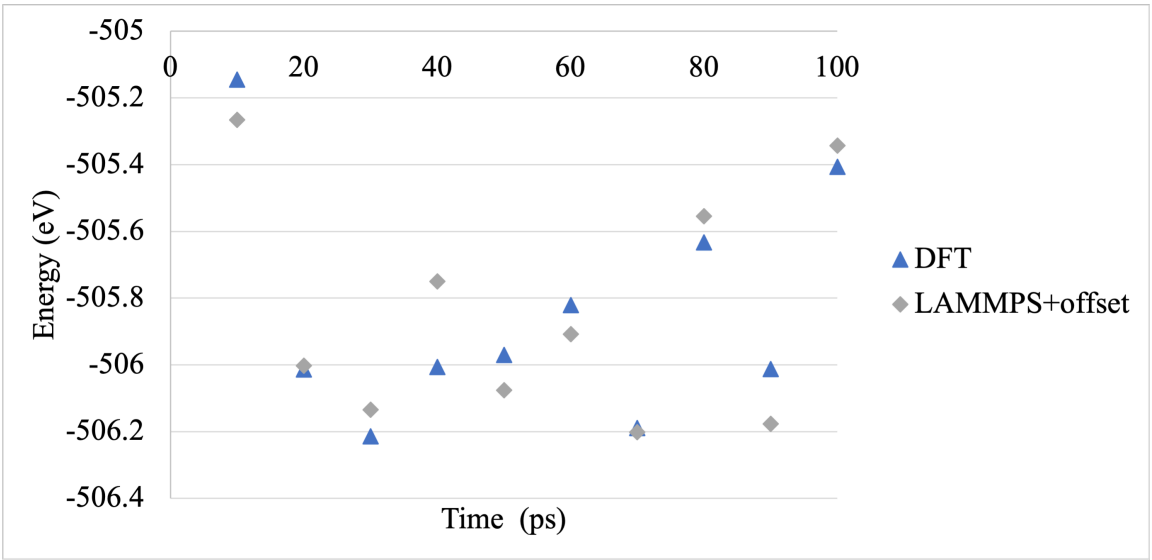
Molecular dynamics at 300 K



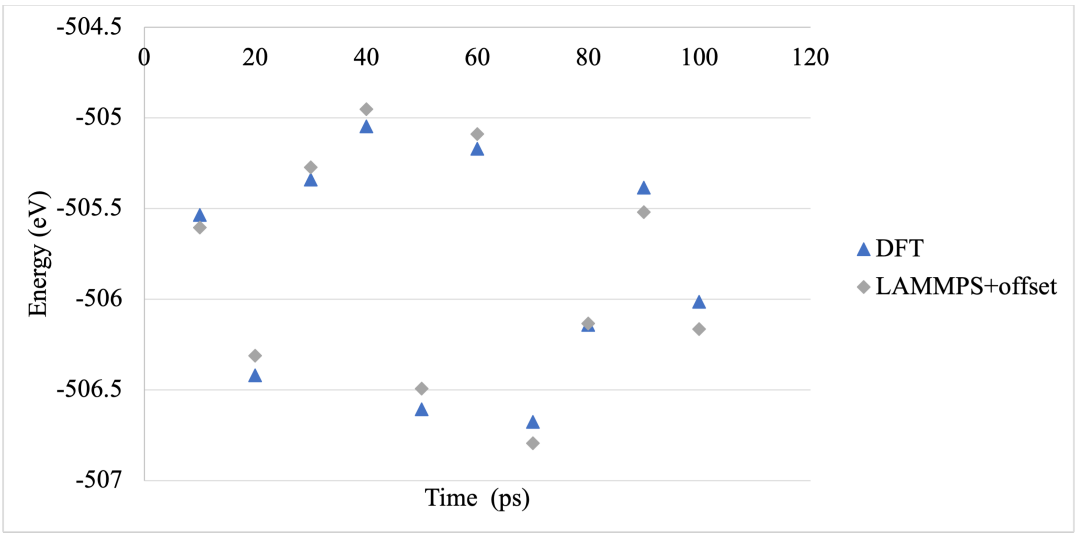
Appendix Figure F.1 Comparison of the energy from the ML-MD LAMMPS simulation results and DFT calculated energy for the $Au_{25}(SCH_3)_{18}$ system at 300 K.



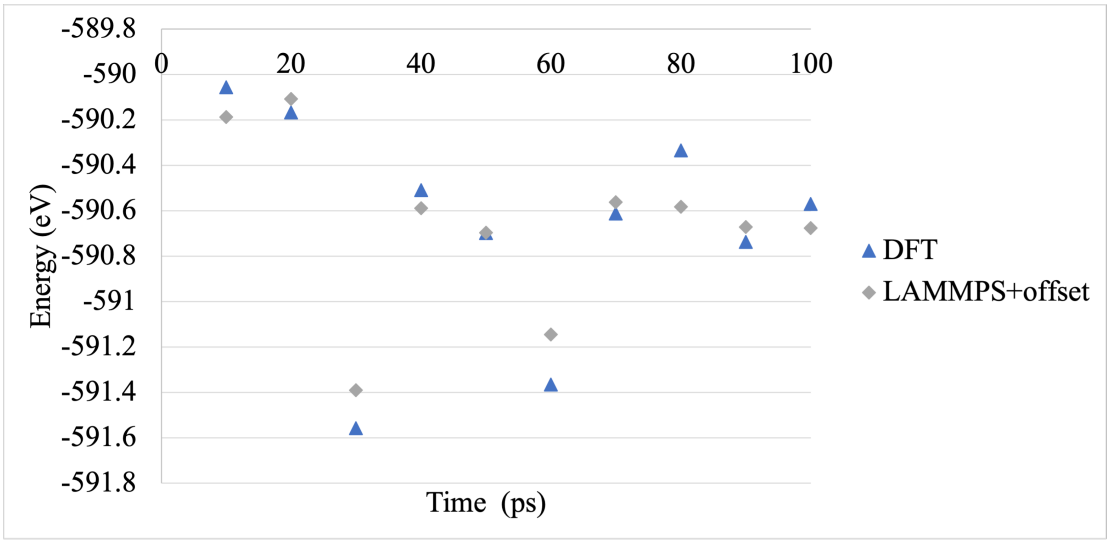
Appendix Figure F.2 Comparison of the energy from the ML-MD LAMMPS simulation results and DFT calculated energy for the $Au_{28}(SCH_3)_{20}$ system at 300 K.



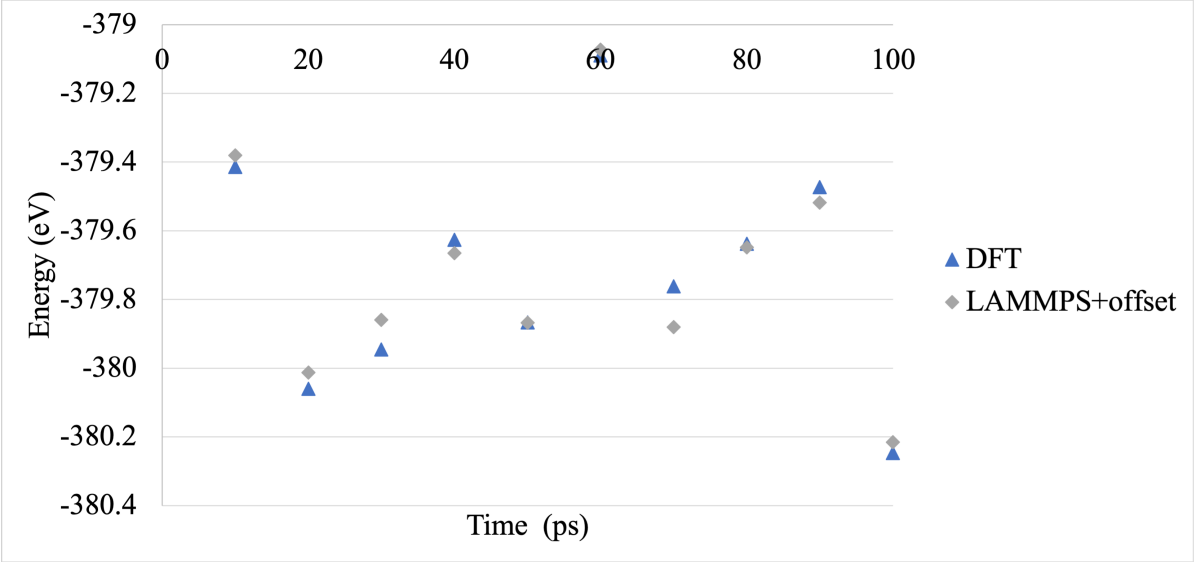
Appendix Figure F.3 Comparison of the energy from the ML-MD LAMMPS simulation results and DFT calculated energy for the $Au_{36}(SCH_3)_{24}$ system at 300 K.



Appendix Figure F.4 Comparison of the energy from the ML-MD LAMMPS simulation results and DFT calculated energy for the $Au_{38}(SCH_3)_{24}$ system at 300 K.

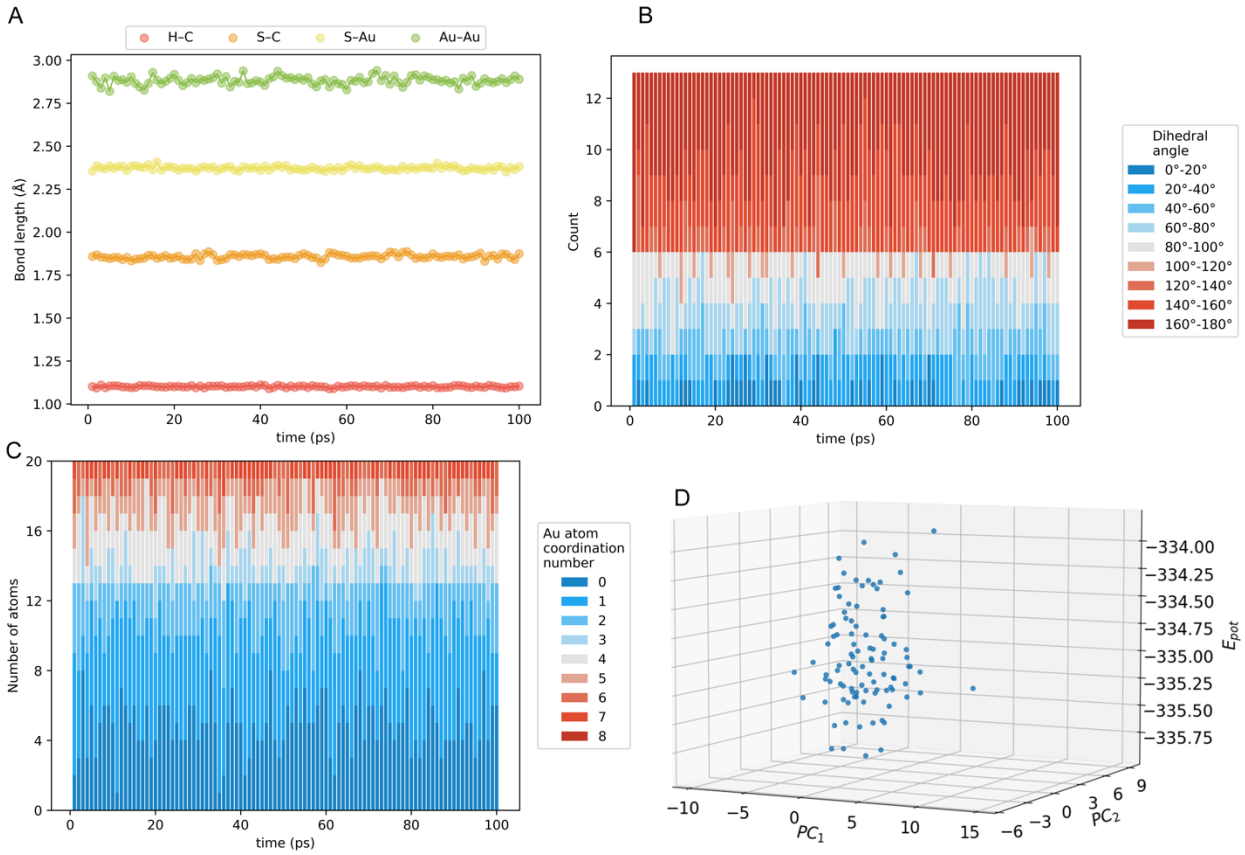


Appendix Figure F.5 Comparison of the energy from the ML-MD LAMMPS simulation results and DFT calculated energy for the $Au_{44}(SCH_3)_{30}$ system at 300 K.

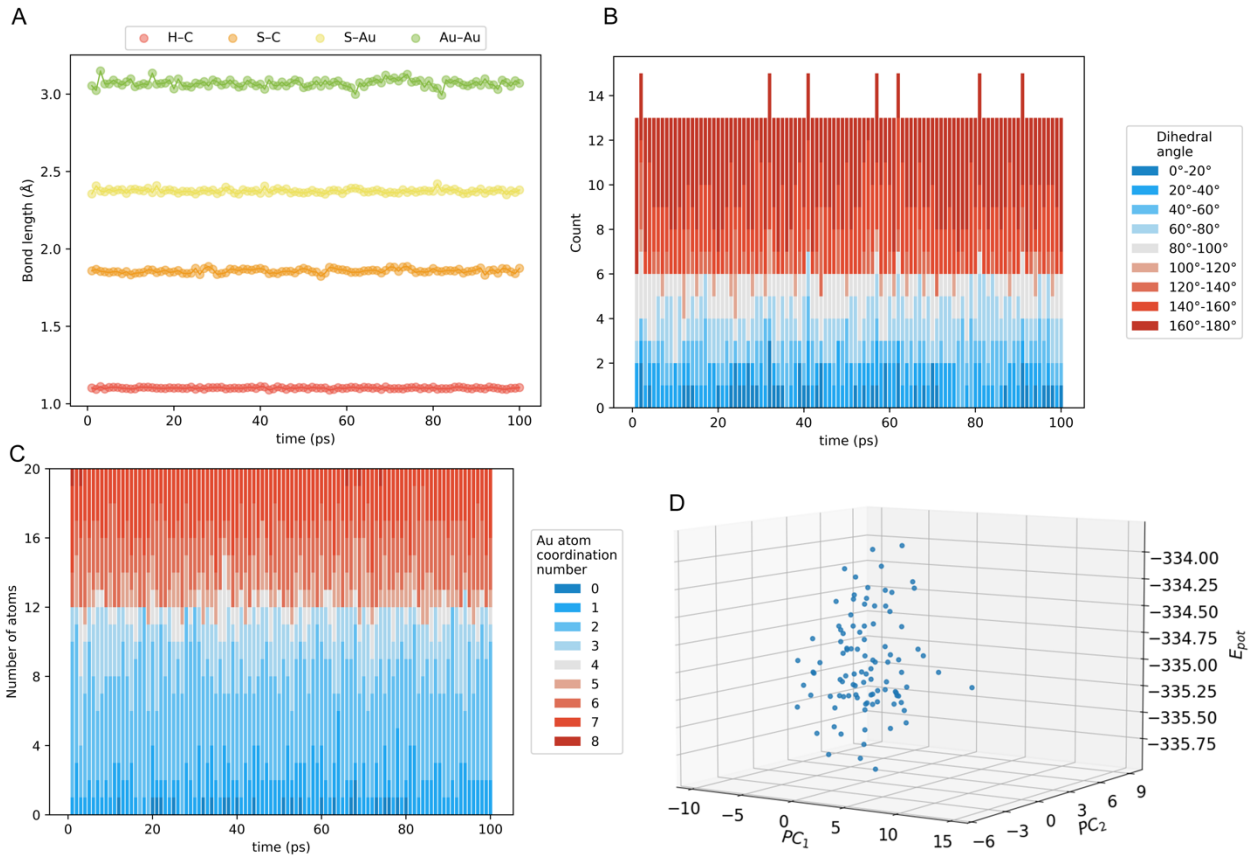


Appendix Figure F.6 Comparison of the energy from the ML-MD LAMMPS simulation results and DFT calculated energy for the $Au_{25}(SCH_3)_{18}$ system at 200 K.

Visualizing the results from machine learning calculations for $Au_{20}(SCH_3)_{16}$ at 400K

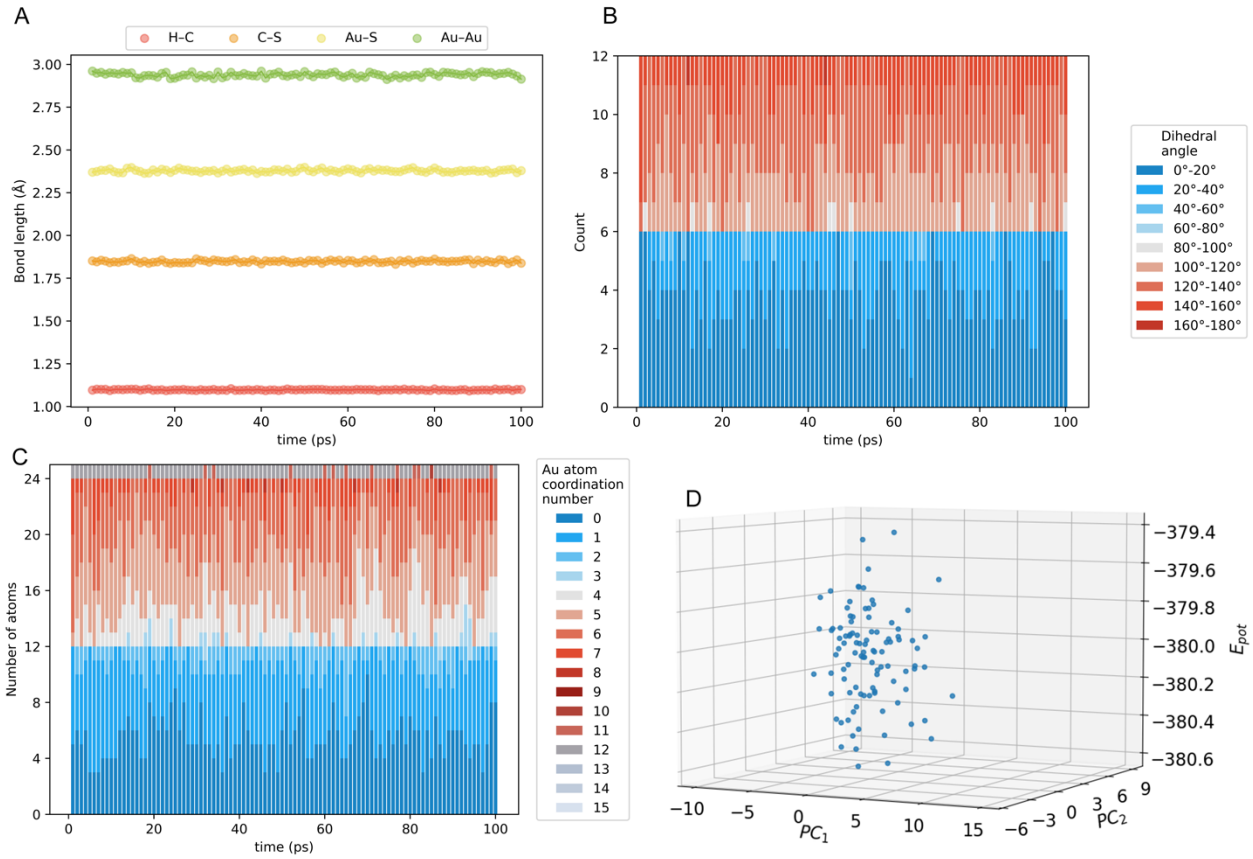


Appendix Figure F.7 A. Mean bond length variation. B. C-S---S-C dihedral angle count for various angle ranges. C. Au atom count for each individual Au-Au coordination numbers. D. PCA visualization of the bonding parameters for different training configurations of $Au_{20}(SCH_3)_{16}$ at 400K (using a 14.85% increase in covalent radii). Each graph demonstrates results from a hundred configurations (one snapshot per picosecond).

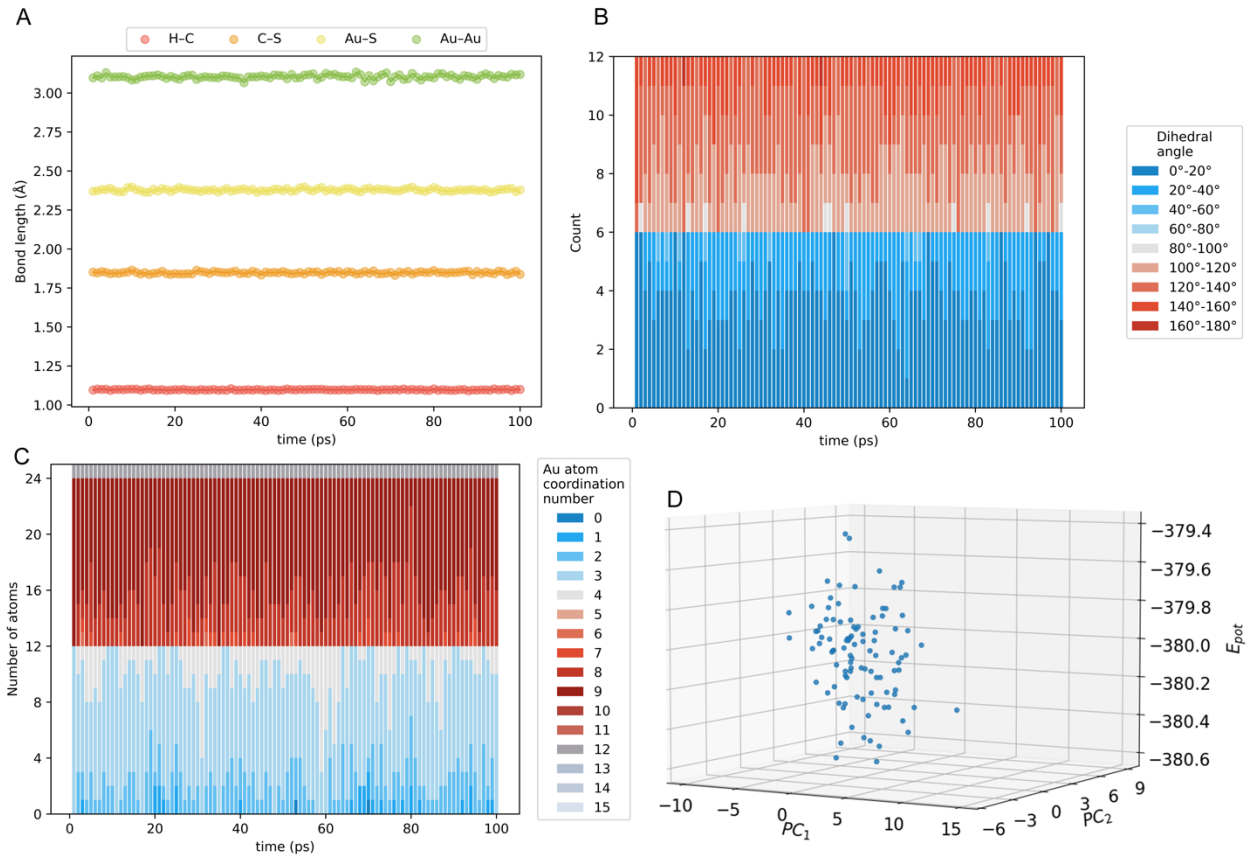


Appendix Figure F.8 A. Mean bond length variation. B. C-S---S-C dihedral angle count for various angle ranges. C. Au atom count for each individual Au-Au coordination numbers. D. PCA visualization of the bonding parameters for different training configurations of $Au_{20}(SCH_3)_{16}$ at 400K (using a 30.00% increase in covalent radii). Each graph demonstrates results from a hundred configurations (one snapshot per picosecond).

Visualizing the results from machine learning calculations for $Au_{25}(SCH_3)_{18}$ at 200K

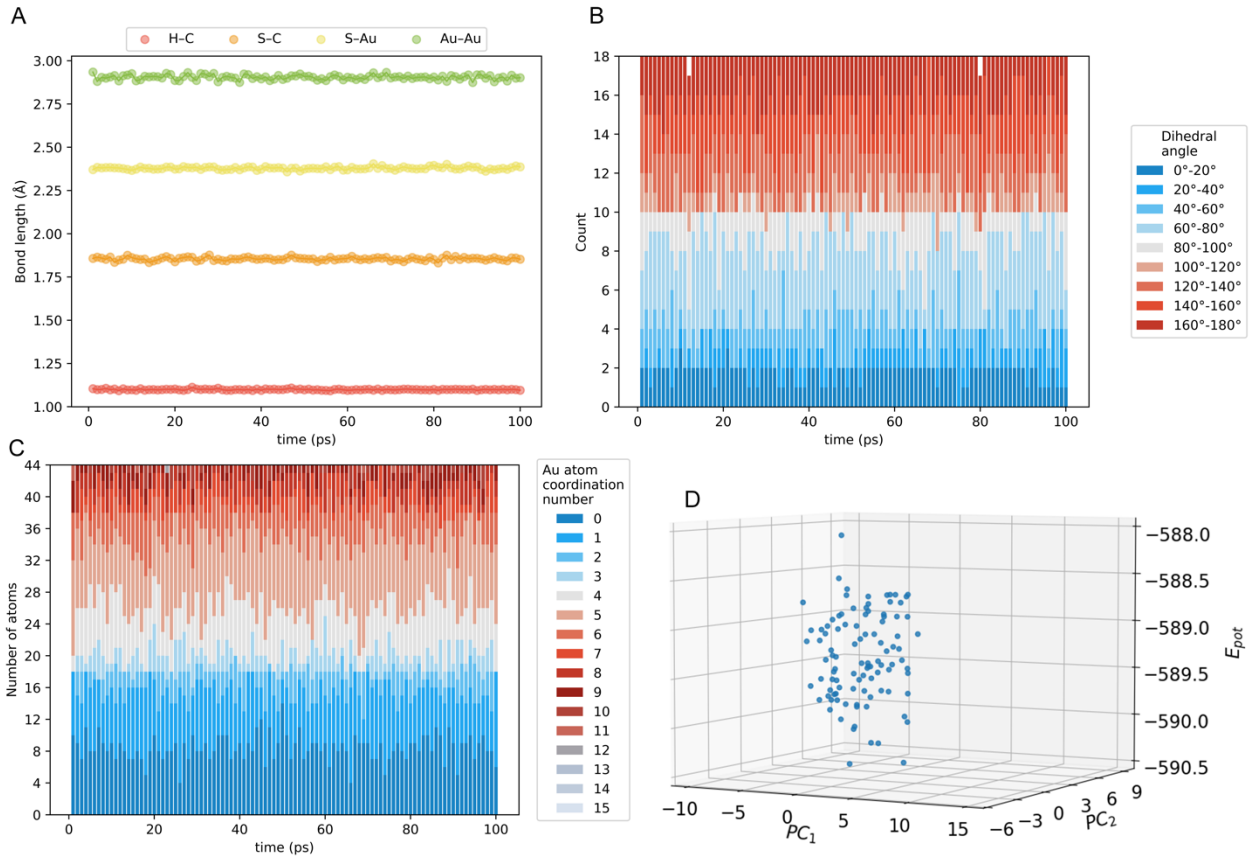


Appendix Figure F.9 A. Mean bond length variation. B. C-S---S-C dihedral angle count for various angle ranges. C. Au atom count for each individual Au-Au coordination numbers. D. PCA visualization of the bonding parameters for different training configurations of $Au_{25}(SCH_3)_{18}$ at 200K (using a 14.85% increase in covalent radii). Each graph demonstrates results from a hundred configurations (one snapshot per picosecond).



Appendix Figure F.10 A. Mean bond length variation. B. C-S---S-C dihedral angle count for various angle ranges. C. Au atom count for each individual Au-Au coordination numbers. D. PCA visualization of the bonding parameters for different training configurations of $Au_{25}(SCH_3)_{18}$ at 200K (using a 30.00% increase in covalent radii). Each graph demonstrates results from a hundred configurations (one snapshot per picosecond).

Visualizing the results from machine learning calculations for $Au_{44}(SCH_3)_{28}$ at 300K



Appendix Figure F.11 A. Mean bond length variation. B. C-S---S-C dihedral angle count for various angle ranges. C. Au atom count for each individual Au-Au coordination numbers. D. PCA visualization of the bonding parameters for different training configurations of $Au_{44}(SCH_3)_{28}$ at 200K (using a 14.85% increase in covalent radii). Each graph demonstrates results from a hundred configurations (one snapshot per picosecond).